

# **Computational Fluid Dynamic Modelling for Arterial Diseases Assessment**

**Mohammad AL-Rawi**

A thesis submitted to Auckland niversity of Technology  
in fulfilment of the degree of  
Doctor of Philosophy



Auckland, New Zealand

**Institute of Biomedical Technologies**

Primary Supervisor: Prof Ahmed AL-Jumaily

October, 2012

*Dedicated to*  
*my wife Annette Al-Rawi*  
*and daughter*  
*Summer Al-Rawi*

## **ACKNOWLEDGEMENTS**

There are many people I wish to formally thank for their contribution to this thesis. First of all, I would like to express my appreciation and gratitude to my supervisor, Professor Ahmed Al-Jumaily director of Institute of Biomedical Technologies (IBTec). He is such a knowledgeable, patient and helpful person. Without his invaluable support, consistent encouragement and push, I would not have finished this research.

I would like to acknowledge the funds contributed by IBTec for my scholarship, conference attendance and experimental work.

I would like also to thank my second supervisor, Dr. Andrew Lowe for his generous technical guidance, constructive criticism and continuous support throughout my endeavour. I wish to thank Dr. Jun Lu, for training and technical support in guiding me in the performance of the animal experiments.

Warmest thanks to David Parker and Prachi Redey for correcting this thesis. They provided lots of help and valuable suggestions about writing. I acknowledge Catriona Carruthers for her services as a proof-reader. To my colleagues and friends at IBTec, it has felt like being in a family. To Gijs, Miguel, Mohammed and Hai Lan, thank you for your help and advice.

I wish to give my most sincere appreciation to my parents Ayad Al-Rawi and Atyaf Al Waally. They have always stood behind me and supported me. Without their support and encouragement, this thesis would not have been possible.

Finally, I would also like to acknowledge ethical approval from the University of Auckland Ethics Committee approval number R915 approved on 15 August 2011.

## ABSTRACT

One of the leading causes of death is cardiovascular disease, being 30% of all deaths worldwide and 40% of those in New Zealand. In other words, every 90 minutes a New Zealander dies due to cardiovascular disease. Cardiovascular mortality is higher in New Zealand than Australia, but the reasons for this are not clear. Although Australia and New Zealand are similar politically, culturally, and socioeconomically, mortality from cardiovascular disease is about 25% higher in New Zealand than in Australia.

In recent years, engineers and scientists have collaborated with the medical community to find new methods and approaches for assessing and investigating the development of cardiovascular diseases such as abdominal aortic aneurysm and atherosclerosis. In this thesis, atherosclerosis and aneurysm diseases are investigated and analysed using computational fluid dynamic/finite element (CFD/FE) methods. These models are validated against the *in vivo* and *in vitro* experiments performed on animals. The experimental models are also investigated; the assessment of arterial blockages using blood pressure waveforms obtained invasively at the right femoral artery.

The animal experiments are performed following appropriate ethical protocols (R915) on Wistar rats weighing between 250-350g. An arterial blockage is created surgically within the abdominal aorta of healthy animals to create an unhealthy condition. Blood pressure waveforms are measured by injecting catheter into the right femoral artery of the rat. These measurements are taken at the baseline (healthy condition) and at four different severities of arterial blockage of the abdominal aorta for the same specimen. *In vivo* and *in vitro* measurements of the arterial diameter and wall thickness are also taken using Magnetic Resonance Imaging (MRI) and microscopic techniques, respectively.



These data are then input onto CFD/FE models in order to develop a new, non-invasive method of assessing arterial blockage. The experimental and computational results indicate that arterial blockages occurring within the abdominal aorta could be assessed, and the development of the disease diagnosed, very clearly and non-invasively at the right femoral artery. The findings of the animal model are then implemented in the human model for screening atherosclerosis and aneurysm at the brachial artery. These diseases are modelled and simulated in a 3D CFD/FE aorta geometry using the fluid–structure interaction (FSI) approach on the commercial software ANSYS®14.0. Literature blood flow waveform datum is assumed at the inlet and invasive catheter pulsatile pressure waveforms data is imposed at the four outlets of the aorta (provided by Green Lane Hospital under ethic approval number NTX/09/11/109). Correlations between the stress phase angle (SPA), augmentation index (AI), lumen diameter and blood pressure waveforms for various scenarios of diseased models are made and compared to the control model. The results show that CFD/FE models with different radii and thicknesses at the abdominal aorta significantly influence blood pressure waveforms, high negative SPA values, and high AI detected at the brachial artery.

# TABLE OF CONTENTS

<b>ACKNOWLEDGEMENTS.....</b>	<b>iii</b>
<b>ABSTRACT .....</b>	<b>iv</b>
<b>TABLE OF CONTENTS.....</b>	<b>vi</b>
<b>STATEMENT OF ORIGINALITY .....</b>	<b>xv</b>
<b>LIST OF UNITS, SYMBOLS AND ABBREVIATIONS .....</b>	<b>xvi</b>
<b>Chapter 1 Overview .....</b>	<b>1</b>
1.1 Introduction .....	1
1.2 Background .....	1
1.3 The Physiology of the Human Circulatory System.....	3
1.4 Arterial Structure.....	5
1.5 Cardiovascular Diseases .....	6
1.5.1 Atherosclerosis .....	7
1.5.2 Aneurysm.....	8
1.6 Diagnostic Methods for Cardiovascular Disease .....	10
1.6.1 Magnetic Resonance Imaging (MRI) .....	10
1.6.2 Computed Tomography (CT) .....	12
1.6.3 Blood Pressure Monitors .....	12
1.6.4 Doppler Ultrasound .....	14
1.7 Computational Fluid Dynamics Method.....	15
1.8 Closure .....	15
<b>Chapter 2 Literature Review.....</b>	<b>17</b>
2.1 Introduction .....	17
2.2 The Pulse Wave Mechanism in Cardiovascular Disease .....	18
2.2.1 The Mechanics of Atherosclerosis .....	22
2.2.2 The Mechanics of Aneurysm .....	24
2.3 Computational Fluid Dynamics in Arteries .....	25
2.3.1 Assumptions in Modelling Blood Flow .....	26
2.3.2 Complex Mechanical Interaction.....	30
2.3.3 Structure of the Arterial Wall.....	32
2.3.4 Wave Propagation in the Arterial System.....	33
2.4 Model Outputs.....	35
2.4.1 Wall Shear Stress .....	35
2.4.2 Circumferential Strain .....	37
2.4.3 Stress Phase Angle .....	38
2.5 Summary of the Literature .....	40
2.6 Research Objectives .....	41
2.7 Thesis Outline .....	43
<b>Chapter 3 Computational Fluid Dynamics Modelling.....</b>	<b>46</b>
3.1 Introduction .....	46
3.2 Mechanism of Arterial Structure.....	48
3.2.1 Model Geometries .....	49
3.2.2 Artery Wall Characteristics .....	52
3.2.3 Arterial Length.....	54
3.2.4 Cross-Section .....	55
3.3 Computational Meshes.....	56
3.4 Fluid-Structure Interaction Method .....	57
3.4.1 Two-Way FSI.....	58
3.4.2 Arbitrary Lagrangian Eulerian Method .....	62

3.5	Governing Equations.....	62
3.5.1	Blood Flow Equations.....	63
3.5.2	Elastic Vessel Wall Modelling .....	68
3.6	Closure .....	71
<b>Chapter 4</b>	<b>Animal Model .....</b>	<b>72</b>
4.1	Introduction .....	72
4.2	Animal Model Background.....	73
4.3	Animal Model .....	74
4.4	Data Collection .....	75
4.4.1	In vivo Investigations .....	76
4.4.1.1	Experimental Design.....	76
4.4.1.2	Experimental Setup .....	82
4.4.1.3	Measurement Data .....	84
4.4.2	In vitro Investigations .....	89
4.5	Computational Modelling .....	90
4.5.1	Abdominal Aorta Geometry .....	90
4.5.1.1	Transient Structure Mechanic.....	91
4.5.1.2	Computational Fluid Dynamic.....	94
4.5.2	Mesh Generation.....	97
4.5.3	Material Properties and Boundary Conditions .....	98
4.5.4	Fluid-Structure Interaction .....	98
4.6	Validation and Results .....	99
4.6.1	In vivo Results .....	99
4.6.2	CFD/FE Results .....	102
4.7	CFD/FE Model Validation.....	107
4.8	Closure .....	108
<b>Chapter 5</b>	<b>The Human Model .....</b>	<b>109</b>
5.1	Introduction .....	109
5.2	Model Development.....	111
5.2.1	Aorta Geometry.....	111
5.2.1.1	Atherosclerosis.....	115
5.2.1.2	Abdominal Aortic Aneurysm .....	117
5.2.2	Transient Structure Mechanics .....	119
5.2.2.1	Mesh Generation.....	119
5.2.2.2	Material Properties.....	121
5.2.3	Computational Fluid Dynamic and Command Field Exercise.....	122
5.2.3.1	Mesh Generation.....	123
5.2.3.2	Boundary Conditions .....	125
5.2.3.3	Fluid-Structure Interaction Model.....	127
5.2.4	Two-way FSI .....	128
5.3	Stress Phase Angle .....	129
5.4	CFD/FE Results and Analysis.....	133
5.4.1	Atherosclerosis.....	135
5.4.1.1	Stress and Strain .....	135
5.4.1.2	Stress Phase Angle .....	143
5.4.1.3	Artery Stiffness Variations .....	145
5.4.2	Abdominal Aortic Aneurysm .....	148
5.4.2.1	Stress and Strain .....	152
5.4.2.2	Stress Phase Angle .....	154
5.4.2.3	Arterial Wall Stiffness Variation.....	156
5.5	Closure .....	158

<b>Chapter 6 Discussion and Analysis.....</b>	<b>159</b>
6.1 Introduction .....	159
6.2 Atherosclerosis Development Formula.....	159
6.2.1 Atherosclerosis Group-One .....	160
6.2.2 Atherosclerosis Group-Two .....	162
6.2.3 Atherosclerosis Group-Three.....	164
6.2.4 Atherosclerosis Risk Assessment.....	167
6.3 Abdominal Aortic Aneurysm Formula .....	169
6.3.1 Abdominal Aortic Aneurysm Assessment.....	171
6.4 Assessing Arterial Blockages Using Animal Models .....	173
6.4.1 Arterial Blockage Formula Based on Animal Model Validations .....	176
6.5 Closure .....	177
<b>Chapter 7 Conclusion and Future Work .....</b>	<b>178</b>
7.1 Summary .....	178
7.2 Conclusions .....	179
7.3 Future Work .....	182
7.3.1 Blood Pressure Device.....	182
7.3.2 Improving the CFD/FE Model.....	183
<b>REFERENCES.....</b>	<b>185</b>
<b>APPENDIX.....</b>	<b>191</b>
Appendix I.....	192
Appendix II .....	196
Appendix III.....	198

## LIST OF FIGURES

Figure 1-1 <i>Human circulatory system. Red indicates oxygenated blood; blue indicates deoxygenated blood [5]</i> .....	4
Figure 1-2 <i>Cross-sectional view of an artery showing the three distinct layers [6]</i> .....	6
Figure 1-3 <i>Atherosclerosis disease within the artery [18]</i> .....	8
Figure 1-4(a) <i>Healthy abdominal aorta and (b) Abdominal aortic aneurysm (AAA) [29]</i> .....	9
Figure 1-5 <i>MRI Phase Contrast Flow Quantification in the ascending aorta (a) magnitude (b) the phase images and (c) mean blood flow in ascending aorta [39]</i> .....	11
Figure 1-6 <i>Fetus in week 18 (a) Ultrasound of blood flow at abdominal aorta, (b) colour heart function and (c) normal heart function</i> .....	14
Figure 2-1 <i>Reflection of the arterial pulse wave along the aorta and its reflection at the iliac bifurcation (adapted from [7])</i> .....	19
Figure 2-2 <i>A typical healthy arterial pulse waveform showing the systolic pressure, dirotic notch, mean pressure and the diastolic pressure</i> .....	19
Figure 2-3 <i>Pulse type correlated to physiological cause and possible diseases with their pulse wave shape (images were taken from [42])</i> .....	21
Figure 2-4 <i>Stresses (wall shear stress and circumferential strain) affecting a healthy artery and an artery with atherosclerosis</i> .....	23
Figure 2-5 <i>Healthy abdominal aorta and unhealthy abdominal aortic aneurysm in three stages of aneurysms devlopment (images were taken from [23, 63])</i> .....	25
Figure 2-6 <i>Selection of models for arterial flow analysis (adapted from [34])</i> .....	28
Figure 2-7 <i>Non-invasively ascending and right femoral pressure waveforms (adapted from [9])</i> .....	34
Figure 2-8 <i>Stress Phase Angle</i> .....	39
Figure 3-1 <i>Flow chart of CFD/FE modelling showing the process followed for modelling the artery wall and the blood flow bodies</i> .....	47
Figure 3-2 <i>Three different meshed geometries: (a) cuboid, (b) T-shape cylindrical and (c) cylindrical geometry</i> .....	49
Figure 3-3 <i>Stages of constructing aorta geometry from two dimensional images and the idealized aorta in both blood and artery bodies</i> .....	51
Figure 3-4 <i>Arterial wall in a (a) healthy artery and (b) diseased artery (atherosclerosis) showing the inner and outer diameters, the change of the thickness in both healthy and unhealthy conditions and how the length of the artery changes in atherosclerosis</i> .....	53
Figure 3-5 <i>Different types of arterial length condition: (a) healthy condition; (b) unhealthy condition with same length, <math>L</math>; and (c) unhealthy condition with shorter length, <math>L1</math></i> .....	54
Figure 3-6 <i>Three different cross sections for the geometries in Figure 3-2 using different types of mesh methods</i> .....	55
Figure 3-7 <i>Computational mesh methods for three-dimensional domains in ANSYS®: (a) sweep method for cuboid; (b) tetrahedrons method for cuboid; and (c) multi-zone method for cylindrical</i> .....	57
Figure 3-8 <i>Flow chart of Aorta CFD/FE modelling using ANSYS® showing the steps followed to model any artery</i> .....	60
Figure 3-9 <i>Blood flow-artery wall interaction: (a) mesh generation and (b) total deformation</i> .....	61
Figure 3-10 <i>Inlet and outlet blood flow through the artery</i> .....	64
Figure 3-11 <i>Engineering strain of deformation for a sample of the artery wall</i> .....	67

Figure 3-12 Analysis of shear stresses, normal strain rate and strain rate of deformation analysis of the artery wall for (right) diastolic and (left) systolic deformations ....	70
Figure 4-1 Cardiovascular system for rat (left) and for human (right) localizing the area of interest in this investigation (adapted from [118]) .....	78
Figure 4-2 Localizing the abdominal aorta, iliac bifurcation and right femoral artery	79
Figure 4-3 Plastic cable for creating arterial blockages at the abdominal aorta .....	80
Figure 4-4 MRI images for rat using MRI-4.7T illustrating (a) cross-sectional image showing the iliac bifurcation, (b) the abdominal aorta, (c) the longitudinal section illustrating the right and left femoral arteries and (d) the abdominal aorta .....	81
Figure 4-5 Block diagram of the experimental set up to perform in vivo experiments on rats .....	83
Figure 4-6 Lab Chart viewer showing the calibrated blood pressure measurement in mmHg .....	84
Figure 4-7 Blood pressure for healthy condition and four different arterial blockages representing the unhealthy conditions for the same rat (P-H: healthy blood pressure) and (P-U: unhealthy blood pressure) .....	85
Figure 4-8 Setup of the speed camera for measuring the deformation of the arterial wall. ....	86
Figure 4-9 Artery wall deformation for systolic and diastolic pulse and the stresses affecting the artery wall .....	87
Figure 4-10 Speed Camera Technique for measuring the deformation of the arterial wall in vivo experiments .....	88
Figure 4-11 Stress vs Strain for the artery wall at the abdominal aorta .....	88
Figure 4-12 The in vitro measurement of (a) the descending aorta, abdominal aorta and right femoral artery in cross section and (b) the whole aortic body .....	89
Figure 4-13 Flowchart of the Transient Structure Mechanic (TSM) .....	92
Figure 4-14 Abdominal aorta, iliac bifurcation and femoral arteries in healthy and unhealthy (20%, 50%, 80% and 100%) conditions .....	93
Figure 4-15 Flowchart structure of ANSYS CFX [90] .....	95
Figure 4-16 Flowchart of Computational Fluid Dynamic method using CFX .....	96
Figure 4-17 3D model of unhealthy abdominal aorta (a) the artery wall and (b) the blood body (top view) and (c) the side view of the blood body .....	97
Figure 4-18 Two-way FSI using ANSYS® 14.0 [90] .....	99
Figure 4-19 Blood pressure at the abdominal aorta for four different rats in a healthy condition, using catheter method .....	100
Figure 4-20 The healthy blood pressure and four unhealthy blood pressures measured invasively at right femoral artery for rats weighing (a) 350g and (b) 300g .....	101
Figure 4-21 Blood pressure measured invasively at the abdominal aorta compared to the CFD/FE results .....	102
Figure 4-22 The blood pressure at the right femoral artery for both the simulated (CFD) simulation results and the in vivo experiments (Invasive) .....	103
Figure 4-23 Blood pressure at the abdominal aorta for four arterial blockages compared with a healthy condition for 300g rat from CFD/FE results (P = pressure and Unh = Unhealthy) .....	104
Figure 4-24 Augmentation Index (AI %) at the abdominal aorta for a group of rats 310-350g and a group 270-300g .....	105
Figure 4-25 WSS and CS for 50% Arterial blockage at (a) the abdominal aorta and (b) the right femoral artery [H=Healthy and U=Unhealthy] .....	106
Figure 4-26 WSS for the FSI for atherosclerosis of 50% severity at the abdominal aorta at different times (0.3, 0.5 and 0.8s) .....	106

Figure 4-27 CS of the artery wall for atherosclerosis of 50% severity at the abdominal aorta at different times (0.3, 0.5 and 0.8s).....	107
Figure 4-28 Comparison between the CFD/FE models against the experimental data.....	107
Figure 5-1 Block diagram of WSS and CS affecting the arterial wall .....	110
Figure 5-2 A realistic 3D aorta geometry in healthy condition .....	113
Figure 5-3 Aorta geometry of the artery wall and blood body for atherosclerosis (a) and (b), respectively; and abdominal aortic aneurysm (c) and (d), respectively .....	114
Figure 5-4 Aorta geometry and the scenarios of decreasing the diameter of the aorta to simulate atherosclerosis development for Group one.....	115
Figure 5-5 Aorta geometry for the scenario of reducing the length of the diseased portion .....	116
Figure 5-6 Aorta geometry and the scenario of increasing the thickness of atherosclerosis .....	117
Figure 5-7 Design of the study of healthy and unhealthy aorta; (a) the healthy aorta measurement locations and (b) the unhealthy aorta.....	118
Figure 5-8 Mesh generation for the aorta wall (a) at the aortic arch for an atherosclerosis condition and (b) for an the abdominal aortic aneurysm condition .....	120
Figure 5-9 Mesh generation for the aortic arch and three branches (a) blood flow in case of atherosclerosis and (b) in the case of abdominal aortic aneurysm .....	124
Figure 5-10 Boundary condition for the blood flow and pressure; (a) blood flow waveform at the ascending aorta; (b) blood pressure at the brachial artery; (c) at the iliac artery; and (d) a free body diagram of the boundary conditions .....	126
Figure 5-11 FSI approach effects on the wall-blood interaction for the atherosclerosis model (right) and abdominal aortic aneurysm (left).....	128
Figure 5-12 Stress Phase Angle (SPA); (a) in the case of atherosclerosis condition and (b) in the case of aneurysm condition .....	130
Figure 5-13 SPA for the (a) abdominal aorta when atherosclerosis occurs and (b) an abdominal aortic aneurysm .....	132
Figure 5-14 Flow Rate validations (for healthy condition) with literature data (black dotted) [17] and CFD model (blue) .....	133
Figure 5-15 Validation of the pressure wave forms located the renal artery against the clinical trials: P invasive (solid) and P CFD/FE (dotted) in healthy condition .....	134
Figure 5-16 The Max WSS (blue) and the max CS (red), at the brachial artery (right) and at the abdominal aorta (left) for: (a) Group One; (b) Group Two and; (c) Group Three .....	137
Figure 5-17 WSS and CS comparison between healthy condition and (a) Group One, (b) Group Two and (c) Group Three of unhealthy conditions. The upper left graphs represent the healthy data at the abdominal aorta and the lower left graphs represent these data at the brachial artery. The middle graphs represent unhealthy condition (5) and the right graphs represent unhealthy condition (8).....	140
Figure 5-18 WSS-FSI for two unhealthy conditions ( $D_i = 2.5$ mm and 12.5 mm) compared to the healthy condition, keeping the thickness constant .....	141
Figure 5-19 CS at the abdominal aorta showing the development of arterial blockages in two unhealthy conditions as compared with the healthy condition .....	142
Figure 5-20 The DFT of healthy and unhealthy WSS and ESI for Group One at (a) the abdominal aorta and (b) at the brachial artery (see Appendix II) .....	144
Figure 5-21 Simulated abdominal aorta pressure waveform for an unhealthy young adult (45 years old from Green Lane Hospital data).....	146

Figure 5-22 Simulated brachial artery pressure waveform for an unhealthy young adult (45 years old from Green Lane Hospital data) .....	146
Figure 5-23 Augmentation Indices at the abdominal aorta and brachial artery for Group One, changing the inner diameter of the abdominal aorta. AI-A (Abdominal Aorta) and AI-B(Brachial artery) .....	147
Figure 5-24 Augmentation Indices at the abdominal aorta and brachial artery for Group Two, changing the length of the atherosclerosis disease along the abdominal aorta. AI-A (Abdominal Aorta) and AI-B(Brachial artery) .....	147
Figure 5-25 Augmentation Indices at the abdominal aorta and brachial artery for Group Three, changing the thickness of the atherosclerosis disease along the abdominal aorta. AI-A (Abdominal Aorta) and AI-B(Brachial artery) .....	148
Figure 5-26 Systolic blood pressures along the left subclavian artery: Unhealthy ( $Di=24$ mm) and unhealthy ( $Di=26$ mm) conditions .....	150
Figure 5-27 Pressure contour at the aortic arch and along the branches (left subclavian artery) to the brachial artery for an unhealthy ( $Di=26$ mm) and time =0.3s.....	150
Figure 5-28 Diastolic blood pressures along the branch as shown in Figure 5-7: for healthy ( $Di=20$ mm) and unhealthy ( $Di=22$ mm) conditions .....	151
Figure 5-29 WSS (solid) mmHg and CS (dotted) in terms of $\Delta t$ for (a) healthy and (b) unhealthy models at location 10 brachial artery (c) or healthy and (d) for unhealthy model at location 11 abdominal aorta .....	153
Figure 5-30 Amplitude and phase angle vs. frequency at (a) location 10 brachial artery (b) location 11abdominal aorta: WSS-healthy (-o-), WSS-unhealthy (-I-), CS-healthy ('+') and CS-unhealthy (solid).....	155
Figure 5-31 Augmentation Indices (AI) for the twenty abdominal aortic aneurysm developments at the abdominal aorta (A) and at the brachial artery.....	157
Figure 5-32 Systolic blood pressures at the abdominal aorta (A) and at the brachial artery (B).....	157
Figure 6-1 Correlating brachial blood pressure with the lumen diameter, AI and SPA (at the abdominal aorta) for Group One of Atherosclerosis diseases .....	161
Figure 6-2 Diagram illustrating the amount of risk for developing atherosclerosis through narrowing the abdominal aorta .....	162
Figure 6-3 Correlating brachial blood pressure with the length of the disease along the abdominal aorta, AI and SPA calculated at the abdominal aorta for Group Two of Atherosclerosis diseases with $Di=10$ mm, $Do=14$ mm and $L= 60$ .....	163
Figure 6-4 Diagram illustrating the risk of developing atherosclerosis from changing the length of atherosclerosis condition at the abdominal aorta .....	164
Figure 6-5 Systolic blood pressure at the brachial artery for unhealthy conditions (a) $Di=7.5$ mm, (b) $Di=10$ mm, (c) $Di=15$ mm and (d) $Di=17.5$ mm .....	166
Figure 6-6 Diagram illustrating the risk of developing atherosclerosis through change to the thickness of the abdominal aorta in four unhealthy conditions with different lumen diameters .....	167
Figure 6-7 Correlation between the $Di$ , AI (at the abdominal aorta) against the systolic blood pressure at the cuff for atherosclerosis.....	168
Figure 6-8 Correlating systolic brachial blood pressure with arterial wall thickness, AI % and SPA at the abdominal aortic aneurysm.....	170
Figure 6-9 Diagram illustrating the high risk of developing abdominal aortic aneurysm by changing the lumen diameter of the abdominal aorta for twenty unhealthy conditions .....	171
Figure 6-10 Correlation between the $Di$ , AI (at the abdominal aorta) with systolic blood pressure at the cuff for abdominal aortic aneurysm .....	172



Figure 6-11 <i>Blood pressure measurement at the right femoral artery for five rats with high body fat compared with the severity of abdominal aorta blockages, AI'% and SPA at the abdominal aorta</i> .....	173
Figure 6-12 <i>Blood pressure measurement at the right femoral artery for five rats with low body fat compared with the severity of abdominal aorta blockages, AI'% and SPA at the abdominal aorta</i> .....	174
Figure 6-13 <i>Diagram illustrating the assessment of arterial blockages in ten rats divided into two groups of 5 high body fat rats and 5 low body fat rats of Wistar strain</i> .....	175
Figure 6-14 <i>Comparison between animal models and the CFD/FE models</i> .....	177

## LIST OF TABLES

Table 4-1 <i>The different controlled arterial blockages at the Abdominal Aorta</i>	80
Table 4-2 <i>The measured in vitro data</i>	90
Table 5-1 <i>The material and boundary conditions of the arterial wall in healthy conditions and unhealthy (atherosclerosis and aneurysm) conditions (adapted from [9, 23])</i>	122
Table 5-2 <i><math>\Delta t</math> for the three groups of atherosclerosis diseases compared with the healthy condition</i>	138
Table 5-3 <i>SPA for the three groups at the abdominal aorta and brachial artery as compared to the healthy condition</i>	145

## **STATEMENT OF ORIGINALITY**

‘I hereby declare that this submission is my own work and that, to the best of my knowledge and belief, it contains no material previously published or written by another person nor material which to a substantial extent has been accepted for the qualification of any other degree or diploma of a university or other institution of higher learning, except where due acknowledgment is made in the acknowledgments.’

..... (signed)

..... (date)

## LIST OF UNITS, SYMBOLS AND ABBREVIATIONS

Symbol	Unit
Hz	Hertz
ml	Millilitre
mm	Millimetre
mmHg	Millimetre of mercury, unit for pressure
Pa	Pascal
s	Second
V	Volt
Description	
$D_i$	Inner diameter of the abdominal aorta
$d_i$	Inner diameter of the brachial artery
$dn_j$	Differential Cartesian components of the outward normal surface vector
$D_o$	Outer diameter of the abdominal aorta
$d_o$	Outer diameter of the brachial artery
$E$	Young's modulus
$F_i$	Body force acting on the solid
$f$	Frequency
$G$	Shear modulus of the artery wall
$I$	Unit tensor
$\bar{I}$	First invariant of the left Cauchy-Green deformation tensor
$\bar{I}'$	Unit tensors for solid

$J$	Ratio of the deformed elastic volume over the un-deformed volume
$k$	Bulk modulus of the arterial wall
$L$	Length of the disease at the abdominal aorta
$P$	Pressure
$p'$	Hydrostatic pressure
$P_d$	Diastolic pressure
$P_i$	Inflection pressure
$P_s$	Systolic pressure
$r$	Radial coordinate
$Re$	Reynolds number
$s$	Surface region of integration
$S_{ij}$	Second Piola-Kirchhoff stress tensor
$t$	Thickness
$T$	Time
$U$	Displacement vector of computational grid-points
$V$	Volume of regions of integration
$\vec{v}$	Velocity vector
$W$	Strain energy
$\mathbf{W}$	Velocity of the control volume boundary
$x$	Axial coordinate
$\dot{\gamma}$	Shear rate
$\varepsilon$	Strain tensor
$\varepsilon_{ij}$	Green-Lagrange strain tensor
$\eta$	Function of all three invariants of the rate-of-deformation tensor $\left(\frac{\partial u_j}{\partial x_i} + \frac{\partial u_i}{\partial x_j}\right)$

$\mu$	Viscosity
$\nu$	Poisson's ratio
$\rho$	Density
$\rho_w$	Arterial density
$\sigma$	Stress
$\sigma_{Von Mises}$	Von Mises stress
$\tau$	Shear stress

### **Abbreviations**

2D	Two-Dimensional
3D	Three-Dimensional
A	Abdominal Aorta Location
AAA	Abdominal Aortic Aneurysm
AI	Augmentation Index
ALE	Arbitrary Lagrangian Eulerian
B	Brachial Artery Location
BC	Brachiocephalic artery
BP	Blood Pressure
CFD	Computational Fluid Dynamics
CFX	Command Field Exercise
CS	Circumferential Strain
CT	Computed Tomography
DFT	Discrete Fourier Transform
DM	DesignModeler
EC	Endothelial Cell

FFT	Fast Fourier Transform
FE	Finite Element
FSI	Fluid-Structure Interaction
FV	Finite -Volume
H	Healthy
IDAO	Institutional Drug Administration Order
IPA	Impedance Phase Angle
LCC	Left Common Carotid
LS	Left Subclavian
MRI	Magnetic Resonance Imaging
SPA	Stress Phase Angle
SST	Shear Stress Transport
SOBE	Second Order Backward Euler
TSM	Transient Structural Mechanic
U	Unhealthy
VJU	Vernon Jansen Unit (at the University of Auckland)
WSS	Wall Shear Stress

# **Chapter 1 Overview**

## **1.1 Introduction**

The main objective of this thesis is to investigate the possibility of developing a non-invasive approach for the detection of cardiovascular diseases. This chapter provides background information on related subject matter. It provides a general description of the physiology of the circulatory system (Section 1.3), followed by a description of blood vessel structure (Section 1.4). Section 1.5 discusses the development of cardiovascular disease (atherosclerosis and aneurysm). Currently available devices for non-invasive diagnostic are discussed in Section 1.6. Computer Fluid Dynamics/Finite Element (CFD/FE) methods, which play an important role in analysing cardiovascular diseases, are discussed in Section 1.7. The specific objectives of the research are discussed at the end of the literature review in Chapter 2.

## **1.2 Background**

Annually cardiovascular diseases account for 40% of deaths in New Zealand. Statistics from Auckland Hospital show that, every day, 16 patients in New Zealand die from cardiovascular diseases [1-4]. The Heart Foundation of New Zealand claims that many conditions causing these deaths are difficult to diagnose in their early stages and complications from cardiovascular disease occur suddenly [1-4]. Recent studies have therefore focused on the investigation and development of new technologies and methods for early, non-invasive diagnosis of cardiovascular diseases.



The fundamental causes and diagnosis of cardiovascular diseases have occupied researchers' efforts for many years. Diagnostic methods have been developed with varying degrees of success; and yet, cardiovascular disease cannot be detected or screened in its early stages. Even with the best new medical devices and technologies, cardiovascular diseases still manifest in patients suddenly and in a critical, high risk stage. Moreover, a large proportion of patients do not experience or respond to pain until their condition has reached a near-fatal stage [1-4]. This can be largely attributed to limited understanding of the physiology circulatory system. The circulatory system is highly complex in structure, and can malfunction in many different ways. Regardless of the various biomechanical or biological circulatory system factors which can lead to cardiovascular disease, the result is arterial blockages or rupture [1-4]. Consequently, investigating the mechanism of the circulatory system is of vital importance in researching arterial diseases.

This research focuses on investigating new hypothesis in non-invasive diagnostic tools for cardiovascular diseases using CFD and FE methods validated through *in vivo* experiments. These methods are low cost compared to current devices available (e.g. MRI). The main aim of this research is to investigate the relative contribution of hemodynamic stress behaviour in the assessment and detection of cardiovascular diseases. This involves a detailed investigation of propagated blood pressure waveform and flow in non-disease and disease conditions. A deeper understanding of the development of hemodynamic stress in diseased arteries may lead to advances in non-invasive techniques. Moreover, correlating those stresses with specific diseases may provide a crucial context for early diagnosis.

### **1.3 The Physiology of the Human Circulatory System**

The circulatory system is divided into three major parts: the heart; the blood and the blood vessels as shown in Figure 1-1 [5]. The heart represents the pump which circulates the blood to keep the cardio-transport system running. The blood leaves the heart, carrying essential substances (nutrients, oxygen and hormones) to the cells. The blood travels through various kinds of vessels: arteries, veins or capillaries. For example, waste produced from cellular metabolism, harmful chemicals and carbon dioxide are transported away from the organs by veins as shown in Figure 1-1. There is an exchange station for the oxygen (lungs) which is carried by arteries and the carbon dioxide which is carried by veins. The heart circulates five litres of blood which are distributed to all parts of the body. The blood is circulated through the body in a pulsatile flow and propagates pulse pressure waveforms which travel along the arterial system. The measurement and calculation of these waves in living beings depend upon an understanding of their physiological principles.

With age, major changes occur in the arteries such as dilation and become stiffen due to fragmentation of the elastin lamella of the artery wall, leading to increase collagen recruitment. This increases the development of blockages or aneurysms. Therefore, the main objective of this chapter is to perform a comparison of cardiovascular systems in the absence or presence of cardiovascular disease.

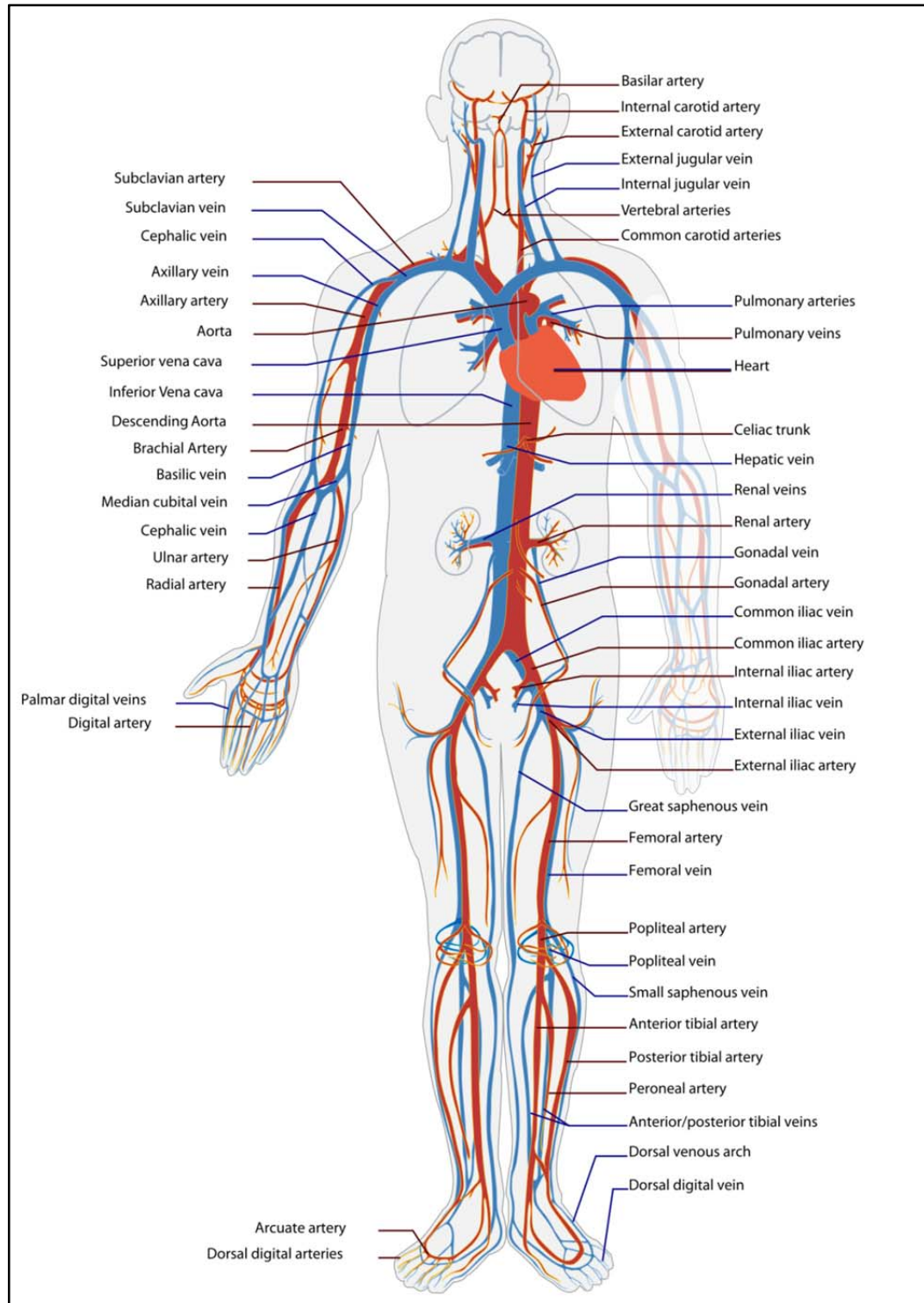


*Figure 1-1: Human circulatory system. Red indicates oxygenated blood; blue indicates deoxygenated blood [5]*

## **1.4 Arterial Structure**

Blood vessels are classified into arteries, arterioles, capillaries, venules and veins. The arteries and veins are bigger than the capillaries and venules (reaches the smallest organs in the body) [7, 8]. The cross-sectional structure for any artery consists of three layers being stronger than those of veins as blood pressure is lower in the veins. The layers of the artery are the intima, the media and the adventitia, as shown in Figure 1-2 [6]. The intima layer is composed of a monolayer of endothelial cells on a base membrane. The intima serves several purposes: it is responsible for the antithrombogenic behaviour of the vascular wall, vasoregulation, control of smooth muscle cell proliferation and control of the transport of water, solutes, macromolecules and cells across the vessel wall [7-9]. The media forms the thickest layer and is composed of smooth muscle cells and connective tissue, mainly collagen and elastin, with both cells and matrix fibres circumferentially oriented [7-9]. The media layer provides structural integrity while the smooth muscle inside this layer allows for control of arterial diameter [7-9]. The adventitia forms the outer layer and is mainly composed of connective tissue and axially-oriented collagen fibres. This layer provides mechanical support to the other two layers [7-9].

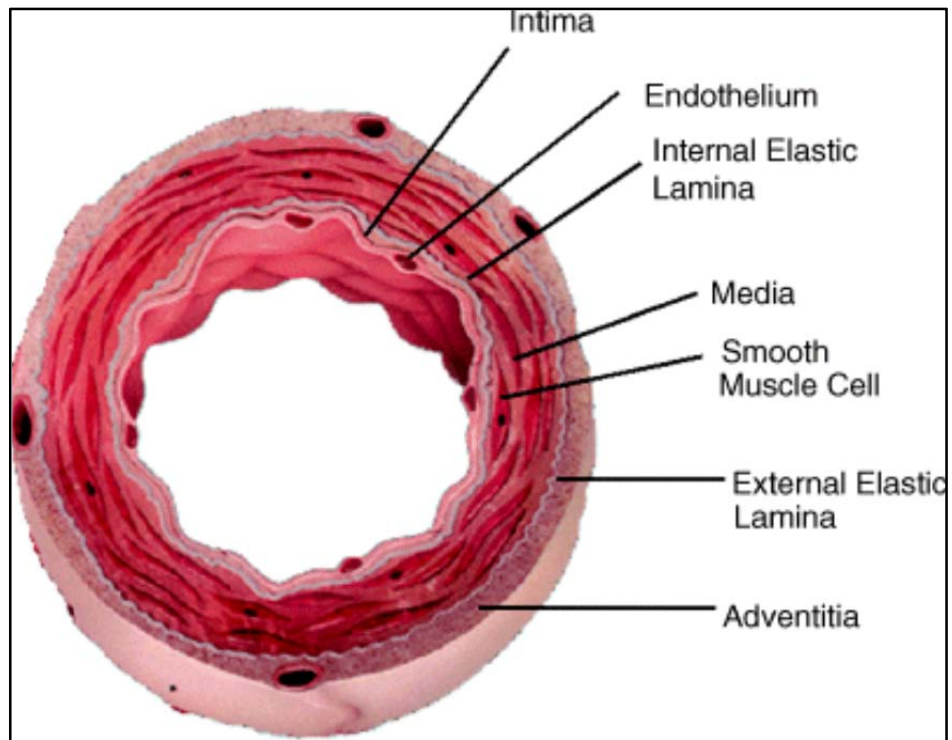


*Figure 1-2: Cross-sectional view of an artery showing the three distinct layers [6]*

## **1.5 Cardiovascular Diseases**

High risk of cardiovascular disease is most prevalent in western countries and involves damage to the heart and major arteries, such as the aorta. There are many risk-factors which play important roles in the development of cardiovascular diseases. Some of these are: (I) family history of the disease, (II) smoking, (III) stress, (IV) high blood pressure, (V) high cholesterol and (VI) diabetes [9]. An intensive study is undertaken in this thesis, to investigate a new, non-invasive method for diagnosing cardiovascular disease. There are many different forms of cardiovascular disease such as stroke, heart failure, atherosclerosis, aneurysm, etc, but the focus of this investigation is on two kinds of cardiovascular disease: atherosclerosis and aneurysm, which most commonly occur at the aorta.

### **1.5.1 Atherosclerosis**

Atherosclerosis is a fatal cardiovascular disease that affects both the heart as well and disturbs the blood flow through the circulatory system. In this condition the artery wall thickens, causing narrowing of the artery and increased resistance to blood flow [9-12, 16]. Arterial narrowing results in decreased blood flow and reduced oxygen supply to dependent tissues [8-12].

Atherosclerosis originates from a small injury to the artery wall, which results in scar tissue forming at the injury site and a local thickening of the wall. This local thickening in turn results in a self-reinforcing process whereby progressively more material is deposited, causing the blood passage to become increasingly narrow [9, 12, 16] as shown in Figure 1-3. The deposited material mostly consists of fats, cholesterol, platelets, cellulose products and calcium, and is referred to as plaque [13-21].

The clinical data suggest that injury to the endothelial cell layer of arteries can be caused by diabetes, hypertension, hyperlipidaemia and certain infections such as herpes viruses.

In terms of hemodynamic stresses, this plaque will cause turbulent flow and will result in increasing the hemodynamic stresses which affects the arterial wall. Wall shear stress (WSS) is a common stress caused by turbulent flow and it is believed to be a significant factor in injury to the intima of the artery. However, presently, there is no clear medical evidence quantifying the range of critical WSS values for different cardiovascular diseases [13-24].

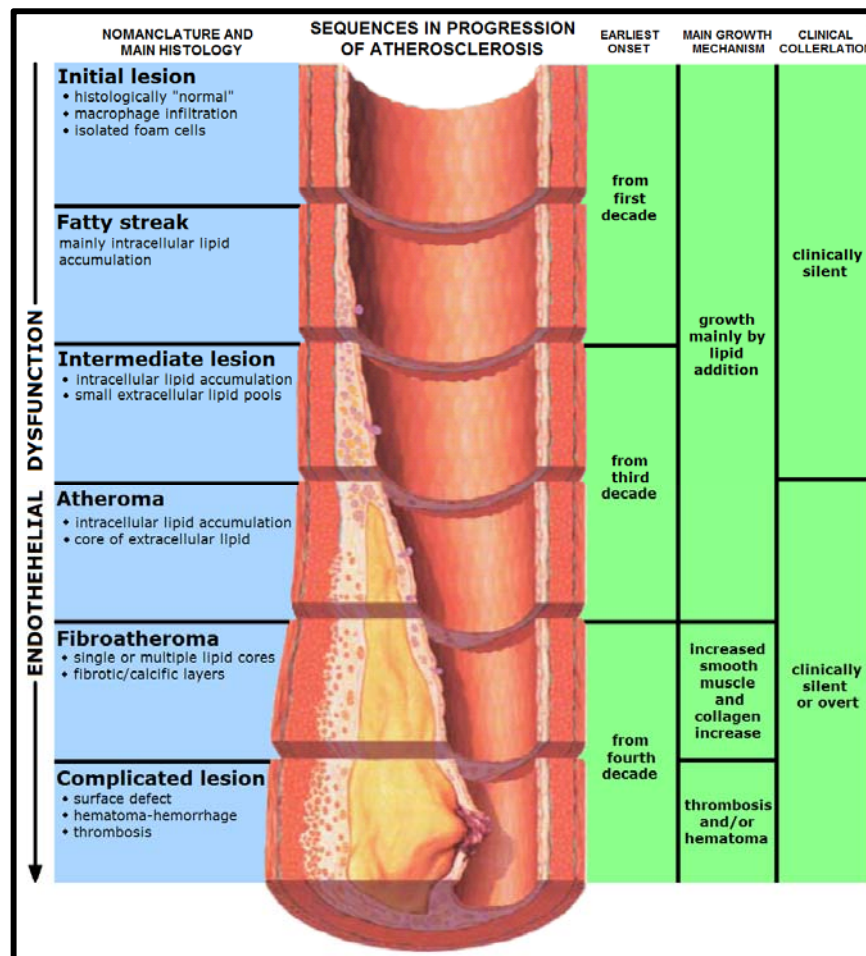


Figure 1-3: Atherosclerosis disease within the artery [15]

### 1.5.2 Aneurysm

Aneurysm is an abnormal widening or ballooning of a portion of an artery due to weakness in the wall of the blood vessel. Aneurysm causes changes to the inner and outer diameters of the artery and to the thickness of the artery wall [8, 23-26] as shown in Figure 1-4 [27]. It has been clinically observed that an increase in the size of the aneurysm by 50% has a rupture risk equal to 1.5 times that of its original artery diameter [23-26]. Aneurysm size also varies from one patient to another, depending on factors such as age, gender, weight and other physiological circumstances. Aneurysms result from a weakening in a section of the arterial wall, and may be caused by

hereditary conditions, atherosclerosis, hypertension, smoking or obesity [25-28]. Arterial rupture can occur in various locations, such as the abdominal aorta, causing a massive haemorrhage into the abdominal cavity, which is fatal [8, 23-26].

In terms of mechanical stresses, aneurysm growth and rupture are caused by an interaction of hemodynamic forces and blood vessel wall biology and the resulting impact on the wall's mechanical properties, such as its elasticity and density [23-26]. The rupture can be determined by setting the wall stress against wall strength; however measurement of wall strength *in vivo* is not possible [23-26]. On the other hand, using CFD/FE methods with *in vitro* clinical data, it is possible to measure and estimate the strength value at any point in time.

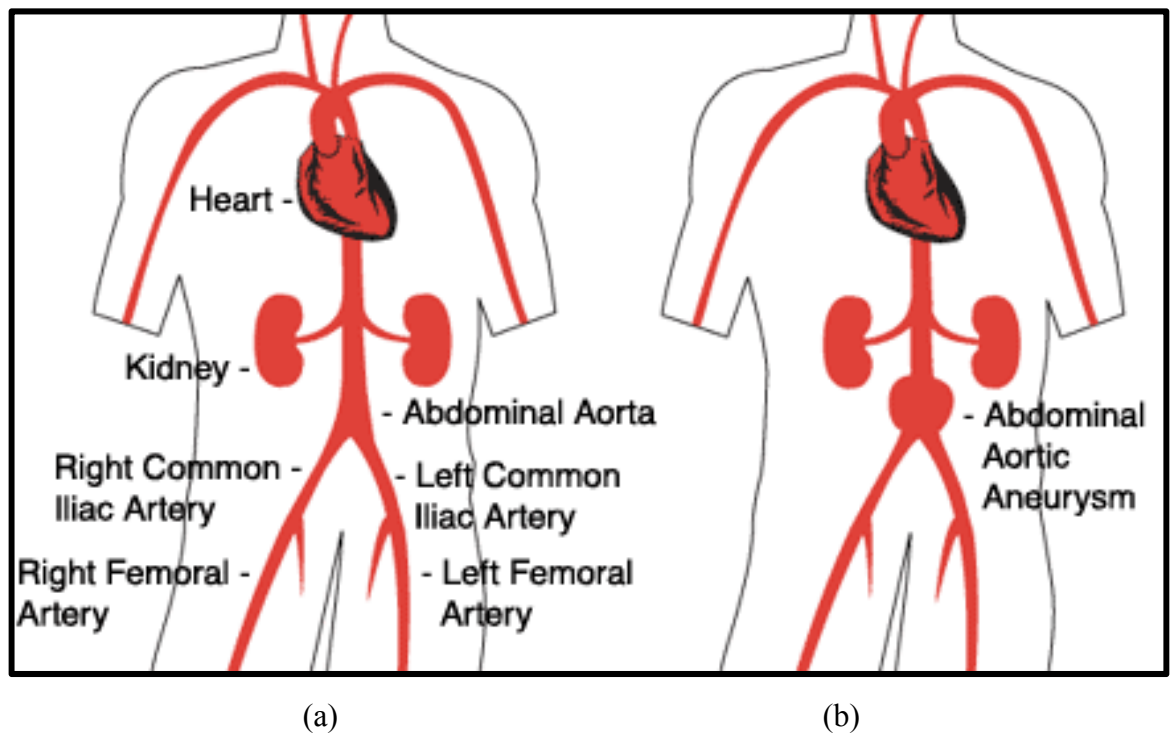


Figure 1-4: (a) Healthy abdominal aorta and (b) Abdominal aortic aneurysm (AAA) [27]



## **1.6 Diagnostic Methods for Cardiovascular Disease**

The devices and methods used for the diagnosing and screening of cardiovascular diseases (atherosclerosis and aneurysm) are discussed in this section in detail. The current non-invasive devices are Magnetic Resonance Imaging (MRI), Doppler Ultrasound, Computed Tomography (CT) scan and blood pressure monitors. All of these play an important role in examining and diagnosing cardiovascular diseases in detail: These devices can examine the size of organs in more depth to investigate their characteristics. In general, cardiovascular diseases are detected by a physical examination usually available at hospitals which includes X-rays, Ultrasound, CT or MRI. These are costly devices for examination and are not available to all patients who may need them.

### **1.6.1 Magnetic Resonance Imaging (MRI)**

MRI is a non-invasive medical imaging technology for identifying and locating unhealthy medical conditions [9]. MRI scanning of a disease location gives cross-sectional images that are presented as slices to the radiologist [9, 28-31]. The procedure for acquiring an MRI scan is as follows:

- I. A patient, lying on a table inside the MRI machine, is subjected to a radio frequency wave. The frequency of these waves is selected such that the hydrogen atoms of water molecules are disturbed.
- II. A strong magnetic field is applied, which causes these hydrogen atoms to line up in parallel. Subsequently a strong pulse of radio waves is applied to the body, which will knock the nuclei out of their parallel alignment and produce detectable radio signals.

III. These radio signals are converted into grey-scale images, with the tone representing the water content at the specific location.

The advantage of using MRI compared to other imaging techniques (such as CT, ultrasound and X-ray) is that it does not use ionizing radiation and provides an image with much higher contrast between tissue types [28-31]. MRI allows the physician to accurately determine geometric parameters such as the size of each blood vessel, spatial location, branch position and direction of bifurcation [31]. It can also measure velocity components non-invasively with phase contrast techniques as shown in Figure 1-5 [31], allowing physicians to evaluate various parts of the body and determine the presence of certain diseases that may not be assessed adequately through other the imaging methods [9, 28-31].

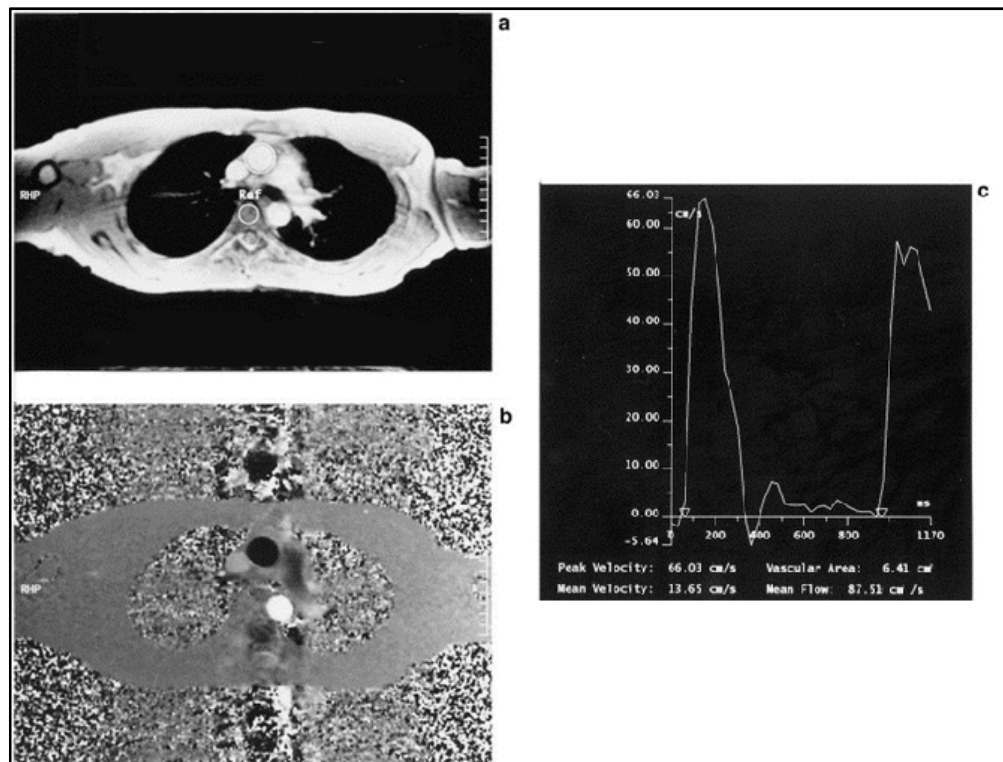


*Figure 1-5: MRI Phase Contrast Flow Quantification in the ascending aorta (a) magnitude (b) the phase images and (c) mean blood flow in the ascending aorta [31]*

### **1.6.2 Computed Tomography (CT)**

CT scanning is a non-invasive device which combines X-ray techniques and sophisticated computers to produce multiple images, in four-dimensional form, of the bones, soft tissue and blood vessels. These images are taken as cross-sections of the scanned object inside the body [9].

The CT scan has many advantages over MRI, for example: CT is less sensitive to patient movement and is able to scan implanted medical devices. CT scan images are acquired at high frame rates alluring for the capture of the arterial deformation. The disadvantage of CT scanning is that it is not suitable for early cardiovascular disease diagnostics. It does not provide information about and detail of arterial wall layers which is important to assess and determine arterial disease [9].

### **1.6.3 Blood Pressure Monitors**

Blood pressure is the force exerted by circulating blood per unit area on the walls of the blood vessels [9]. From a fluid dynamics point of view, blood pressure is necessary to generate flow through the cardiovascular system. The amount of blood pressure needed depends on the resistance of the blood vessels. Small arteries and arterioles provide the largest resistance to flow and this results in a large drop in pressure further away from the heart [32-36].

The sphygmomanometer is a device used to non-invasively measure the blood pressure within the brachial artery [32-36]. This device operates by placing a cuff closely around the upper arm. The cuff is inflated until the artery is completely occluded [32-36]. The pressure in the cuff is slowly released while placing a stethoscope close to the brachial

artery at the inner surface of the elbow. When blood flow is detected as a pounding sound from the stethoscope, this pressure is recorded as the systolic pressure. Subsequently, the pressure is further released until the sound disappears, and this pressure is recorded as the diastolic pressure. Systolic pressure is associated with contraction of the heart's ventricles, while diastolic pressure occurs when the heart's ventricles are at their maximum blood volume [32]. Systolic and diastolic pressure values in healthy adult males are around 120 and 75 mmHg respectively [32-36]. These values vary, not only between patients, but also over time within the same patient. There are many reasons for these variations, including circadian rhythm, exercise, stress, nutritional factors, drugs or disease [36].

**Pulse wave analysis.** The pulse wave is formed as a non-sinusoidal waveform resulting from the contraction by the heart of a volume of blood flow into the aorta. This pulse travels along the aorta and is recognized and analysed by medical doctors as a combination of forward and backward waves. The forward wave results from the heart's contraction; however, the backward wave is the reflective wave created by the resistance of the arteries which travels towards the heart. This pulse is used as a measure of arterial wall compliance and intensity to screen for unhealthy conditions such as hypertension. Therefore, an investigation is carried out in this thesis to correlate the shape of this pulse wave at the brachial artery to the one at site of the disease.

#### 1.6.4 Doppler Ultrasound

Doppler ultrasound is a non-invasive medical device used to diagnose diseases inside the body. This device measures blood flow velocity in healthy and unhealthy conditions, as shown in Figure 1-6. This measurement is made by transmitting an ultrasonic beam into the body i.e. the circulatory system at a certain frequency detecting wave. This wave travels inside the body and is reflected in the body [37-38]. The body causes this reflection and deflection as it is moving in relation to the ultrasonic transducer, so that the frequency of the received wave will be different from that of the transmitted one. The frequency difference is proportional to the relative difference between the object inside the body and the ultrasonic transducer [37-38].

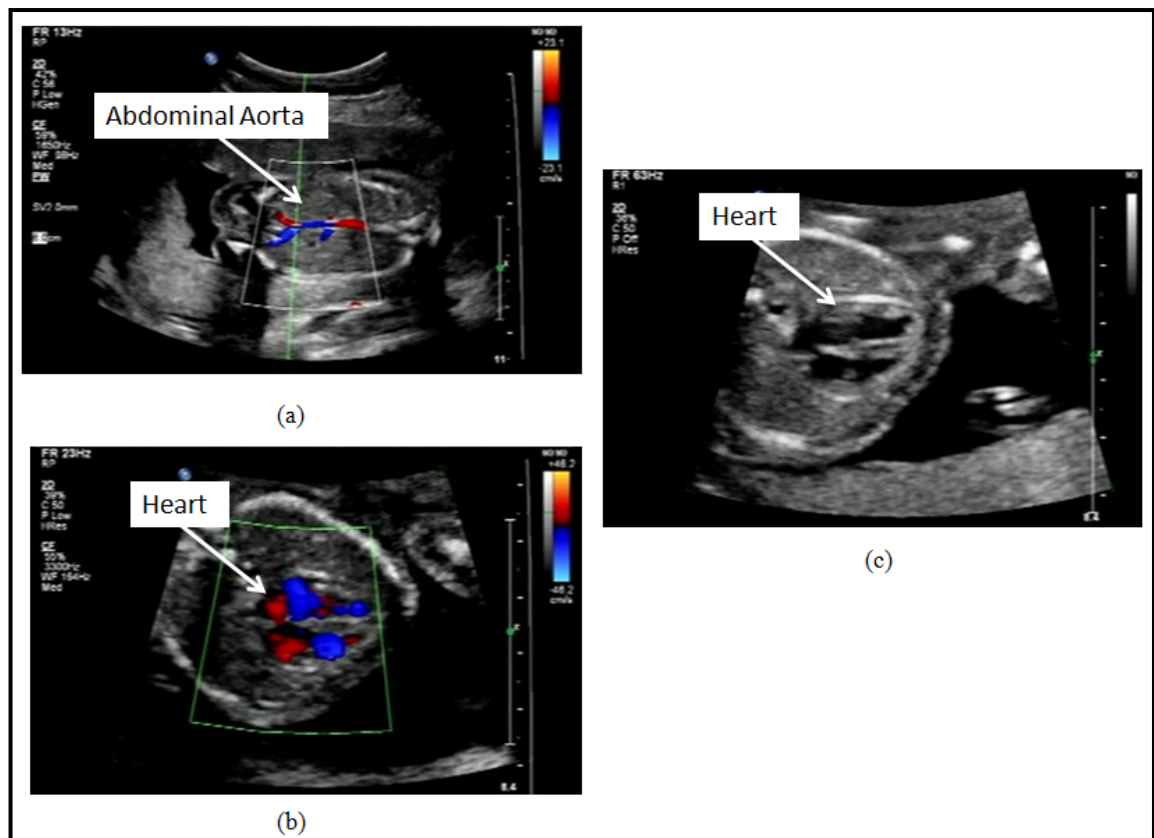


*Figure 1-6: Fetus in week 18 (a) Ultrasound of blood flow at abdominal aorta, (b) colour heart function and (c) normal heart function*

## **1.7 Computational Fluid Dynamics Method**

The CFD method is a promising approach for developing a new non-invasive diagnostic tool in biomedical research. For example, analysis of the components of the blood flow through arteries can be investigated using CFD modelling. This is based on solving fluid dynamic equations such as the continuity and conservation of energy equations. CFD can also be used to develop and optimise devices and system design, to improve existing equipment and reduce costs. Therefore, biomedical engineers and scientists are increasingly employing CFD models to examine the circulatory system on both human and animal subjects to obtain valuable information that is difficult to determine clinically.

CFD methods can also accurately simulate the stresses affecting the artery wall and the dynamic behaviour of the blood flow in its pulsatile form. Therefore, the outputs from CFD analysis can be used to reduce the risk of disease complication and enable a better understanding of the effects of hemodynamic stresses [39-43, 101].

## **1.8 Closure**

This chapter presented background information on the cardiovascular system in both healthy and diseased conditions. This chapter also described the non-invasive diagnostic devices used for detecting cardiovascular disease, most of which are expensive and not available to all doctors. In this thesis we are investigating two kinds of cardiovascular diseases: atherosclerosis and aneurysm. To understand how these diseases develop, it is necessary to understand the hemodynamic stresses which influence blood flow through

the arteries, and what role atherosclerosis and aneurysm play. The next chapter will discuss the current available models and their ability to describe the hemodynamic characteristics of cardiovascular diseases as they develop in terms of wave propagation.

## **Chapter 2 Literature Review**

### **2.1 Introduction**

There are many factors which contribute to cardiovascular disease, such as obesity, diabetes, high blood pressure and smoking, as well as a family history. In order to understand these contributions, an intensive investigation of artery wall mechanism and blood flow is required. This enquiry will formalise the theories and analytical techniques used to develop the new approach used in the computational and numerical modelling in this thesis and will be discussed in this chapter. Therefore, this chapter illustrates the effect of the hemodynamic characteristics of blood pressure waveforms and the mechanical properties of the arterial wall during cardiovascular disease.

The main focus of this chapter is to understand how blood pressure waveforms are associated with disease development. This chapter is based on investigating the mechanism and physiology of the pulse wave correlated for both atherosclerosis and aneurysm. This correlation will be used to assess the development of the diseases based on the systolic and diastolic blood pressures. There will follow a review of the computational modelling process, used to analyse the pulse wave, is correlated with the mechanical arterial wall stresses. This chapter also highlights the limitations of the existing models in the literature in determining the risk of cardiovascular disease.



For a complete understanding of the field, several related topics will be discussed in this chapter to analyse the development of aneurysm and atherosclerosis. The pulse wave mechanism in cardiovascular diseases is discussed for atherosclerosis and aneurysm in the aorta (Section 2.2).

This chapter also covers the CFD modelling for the arterial system (Section 2.3). Model outputs from the CFD results are discussed in Section 2.4. Sections 2.5 and 2.6 provide a summary of the literature and the research objectives, respectively. Section 2.7 presents the thesis outline.

## **2.2 The Pulse Wave Mechanism in Cardiovascular Disease**

An investigation into cardiovascular disease requires a comprehensive understanding of the mechanism of propagation of the pulse wave as it travels through the cardiovascular system in healthy and diseased conditions. In a healthy body, the heart contracts and generates a uniformly contoured wave called the arterial pulse wave. This wave travels along the arterial tree where it partially reflects at various bifurcations, particularly at the iliac bifurcation [9, 44-47] as shown in Figure 2-1 [47].

The shape of the reflected pulse wave is directly dependent on the stiffness and compliance of the artery. Stiff arteries can result in the reflected iliac wave returning to the heart in the systolic phase as shown in Figure 2-2, which results in an increase in pressure. It has also been observed that, with age, both the forward and reflected pulse waves increase [44-47]. This can result in a higher total pressure and the reflected wave coinciding with the forward wave at the heart and thereby a higher pressure.

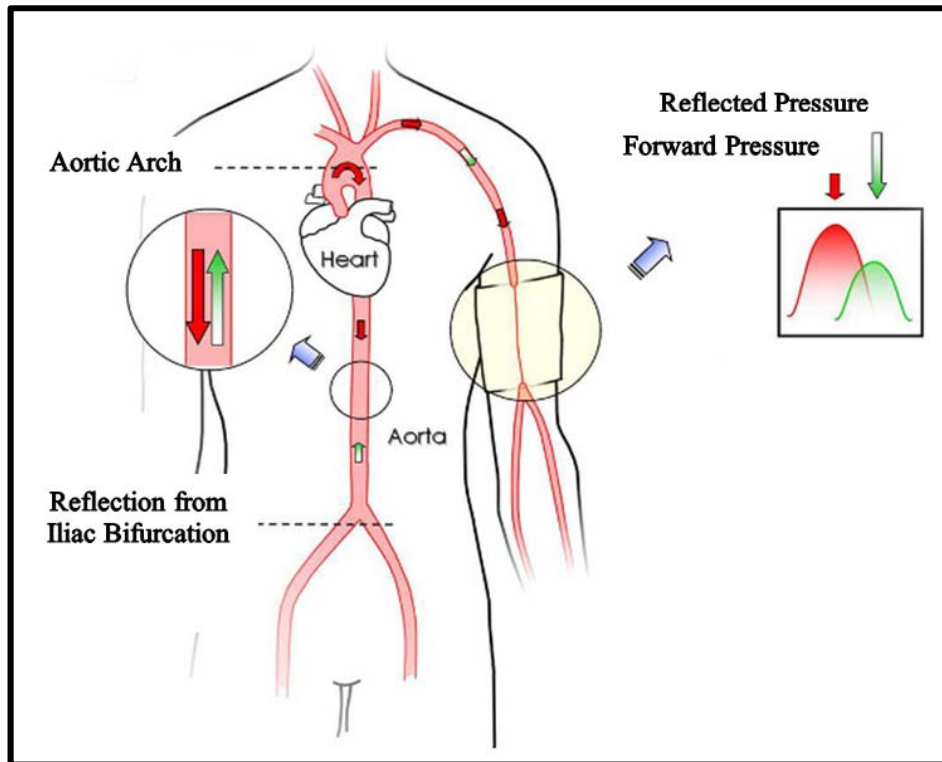


Figure 2-1: Reflection of the arterial pulse wave along the aorta and its reflection at the iliac bifurcation (adapted from [47])

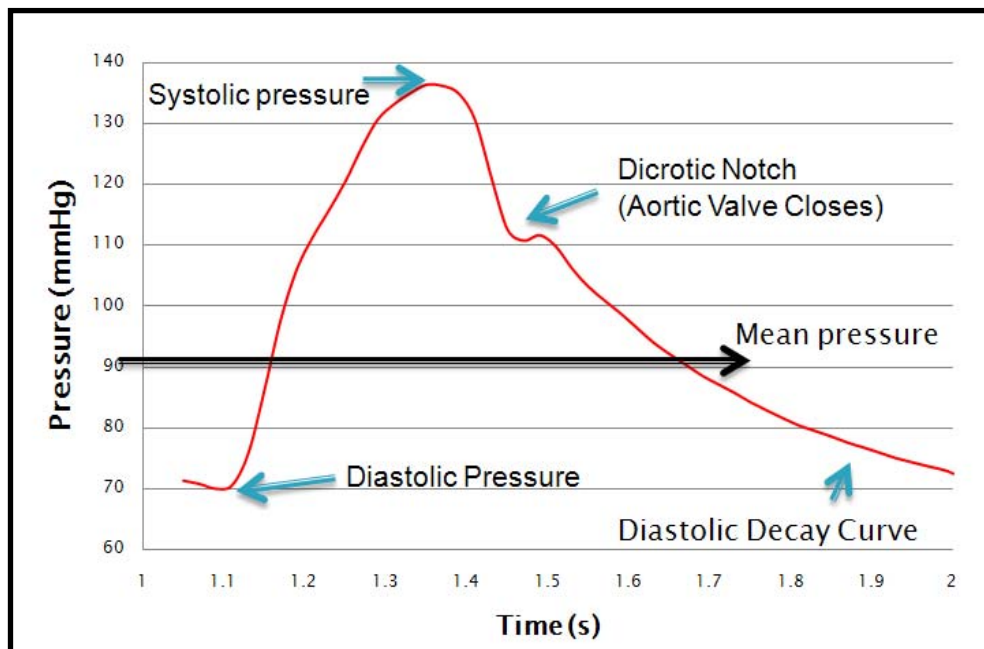


Figure 2-2: A typical healthy arterial pulse waveform showing the systolic pressure, diastolic pressure, mean pressure and diastolic pressure

Arterial wave reflection propagated along the aorta is a characteristic alteration of the pressure pulse. The magnitude and timing of these waves are important in understanding their underlying physiology and hemodynamic characteristics, as shown in Figure 2-3. This figure shows different pulse shapes corresponding to various diseases, based on physiological causes [44-47]. For example, small and weak pulses accompanied by increased peripheral resistance results from three possible causes: (i) heart failure, (ii) hypovolemia, or (iii) severe aortic stenosis and are low-peaked compared to normal pulse waves. This figure shows the combined pulse of the forward and backward waves correlated to a physiological cause and possible disease.

At any location within the arterial system, the net resultant wave is the superposition of the propagated and the reflected waves at that location. A wave returning to the heart during systole would increase the ventricular after-load. If this wave is subtracted from the forward pulse wave, it diminishes the net forward flow. This is disadvantageous to ventricular ejection volume and the heart has to overcome it by applying higher pressure and energy [33, 48-51].





Pulse type	Physiological cause	Possible disease	Abnormalities of the Arterial Pulse
Small & weak Pulses	Decreased stroke volume	Heart failure, hypovolemia, severe aortic stenosis	 <p>Normal pulses</p> <p>Small and weak pulses</p>
	Increased peripheral resistance		
Large & bounding Pulses	Increased stroke volume	Fever, anaemia, hyperthyroidism, aortic regurgitation, bradycardia, heart block, atherosclerosis	 <p>Large &amp; bounding pulses</p>
	Decreased peripheral resistance		
	Decreased compliance		
Bisferiens Pulse	Increased arterial pulse with double systolic peak	Aortic regurgitation, aortic stenosis and regurgitation, hypertrophic cardiomyopathy	 <p>Bisferiens pulses</p>
Pulsus Alternans	Pulse amplitude varies from peak to peak, rhythm basically regular	Left ventricular failure	 <p>Pulsus alternans</p>

Figure 2-3: Pulse type correlated to physiological cause and possible diseases with their pulse wave shape  
(images were taken from [33])

Symptoms of cardiovascular diseases such as atherosclerosis and aneurysm depend on location of the disease. These diseases often have no outward symptoms but can be detected with X-rays, MRI, CT scan or ultrasound during a routine examination [48-51] as discussed in Chapter 1 (Section 1.5). For example, when symptoms do occur, they could include a pulsing sensation, pain, difficulty in swallowing, coughing or hoarseness [33]. These side effects are ambiguous and do not occur in the early stages. However, it is hypothesised that the mechanical stresses which affect the artery wall are the main cause of disease development and are present at the earliest stages of the disease. Identifying these mechanical stresses is the aim of this thesis.

The literature indicates that the shape of blood pressure waveforms measured at the brachial artery changes with the severity (compliance) of the disease [48-51]. Therefore, in this thesis the shape of these waves will be investigated against the geometrical dimensions of the diseases.

### **2.2.1 The Mechanics of Atherosclerosis**

As mentioned in Chapter 1, atherosclerosis is a circulatory disease which causes lesions and plaques in arteries and results in blood being prevented from flowing uniformly. This non-uniform blood flow further damages the artery wall at the endothelium layer due to an excessive inflammatory response from the inner artery wall [52-55]. The role of the thin endothelium layer is to form an interface between blood flow and the artery wall. The intima layer also reduces flow turbulence of the blood around the circulatory system and regulate blood flow [55-58]. This is a protection against high wall shear stress (WSS) on the artery wall, because endothelium cells create a prothrombotic and antifibrinolytic microenvironment [55-58]. However, there is another stress affecting

the elasticity of the arterial wall, called the circumferential strain (CS), which is shown in Figure 2-4. This figure illustrates the different stresses affecting the artery wall in laminar blood flow (during healthy artery) and turbulent flow (during diseased artery). Due to the narrowing of the artery channel, there is an increase in the shear-stress force of the blood flow towards the wall. This shear stress exacerbates the development of atherosclerosis, which leads to arterial blockage [57-58].

The literature indicates a strong relationship between these different kinds of stresses resulting from turbulent blood flow in the case of atherosclerosis. However, the correlation between the stresses attacking the artery wall and disease development is missing. This correlation could be used in establishing a new method for early diagnosis of atherosclerosis, which is one of the main objectives of this thesis.

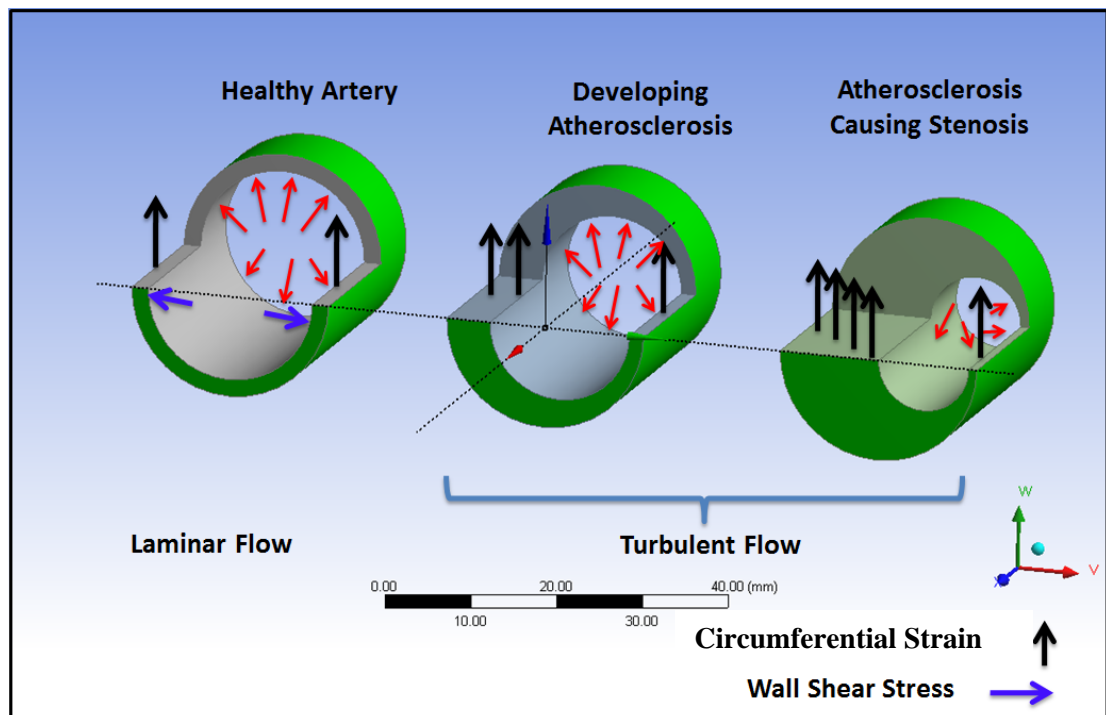


*Figure 2-4: Stresses (wall shear stress and circumferential strain) affecting a healthy artery and an artery with atherosclerosis*

### **2.2.2 The Mechanics of Aneurysm**

Aneurysm is a very serious disease affecting the circulatory system [8, 23, 59] causing a widening in the artery which originates from a weakness or local absence of the media layer in the artery wall [23, 59-61] and is affected by different mechanical stresses. The pulse pressure of the circulating blood within the artery stretches the weakened part of the arterial wall causing a swelling in the artery wall. Ultimately, this leads to serious and potentially fatal complications from either the compression of surrounding tissue structures or from rupture of the artery leading to haemorrhage. This may occur in any part of the aorta or the major arteries (the ascending aorta, aortic arch, descending aorta and abdominal aorta) [23, 56-64]. When the rupture occurs in the abdominal aorta this is called an abdominal aortic aneurysm (AAA). AAA is a disease where the abdominal aorta experiences an increase in the lumen diameter to around double the diameter of a healthy aorta, and presents a high risk of rupture. Figure 2-5 shows the different stages of a developing aneurysm in the abdominal aorta [23].

Previous studies [59-64] show that abdominal aorta rupture could occur in older patients (aged 60-70) due to their arterial wall stiffness and compliance increasing with age in both genders [23, 59-64]. From the mechanical perspective, Young's modulus at the location of the disease reaches high values compared with a healthy artery. These high values result in reducing WSS and CS, which could cause rupture in some patients; however, other patients have a rupture when the aorta wall is more elastic [23, 59-64].

This finding leads us to investigate the changes in the mechanical characteristics of the abdominal aorta wall to achieve a clear idea of why and when rupture occurs. These data can be transferred, using a correlation of wall stresses, to the brachial artery for non-invasive measurement.

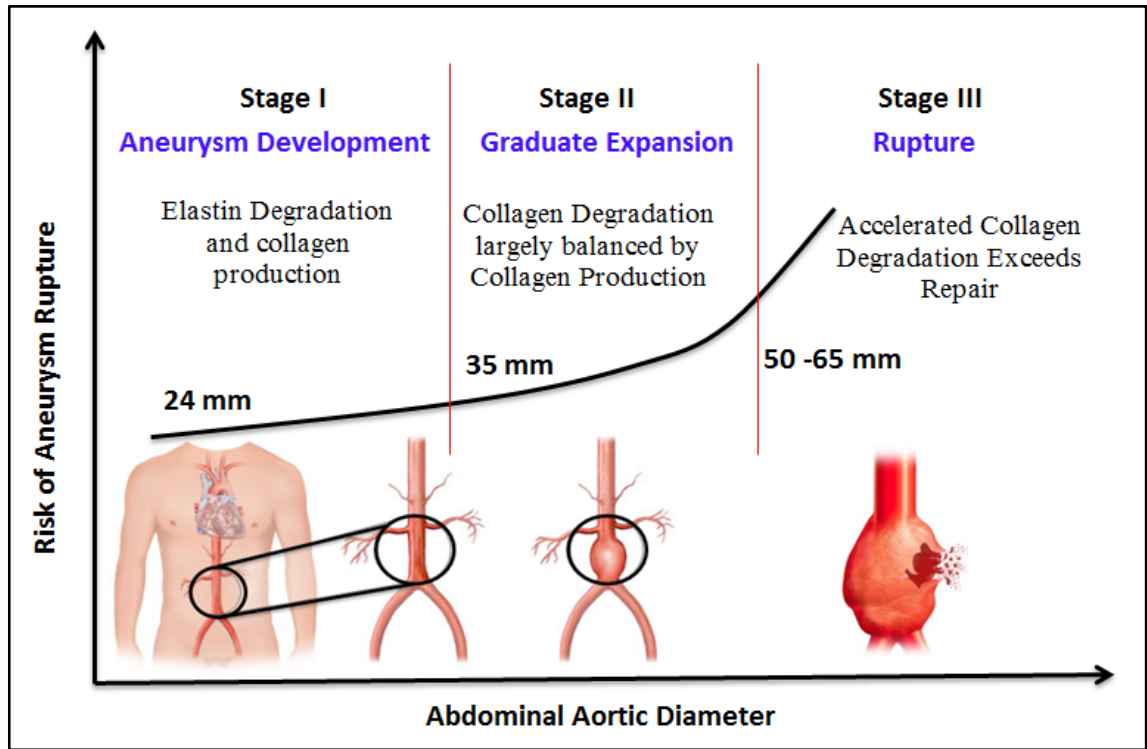


Figure 2-5: Healthy abdominal aorta and unhealthy abdominal aortic aneurysm in three stages of aneurysm development (images were taken from [23,63])

### 2.3 Computational Fluid Dynamics in Arteries

Computational fluid dynamics (CFD) is an appropriate approach to studying and investigating blood flow in arteries as it requires less time and money. CFD is a numerical method, based on solving mathematical equations involved in fluid-solid motion. This modern method is considered a powerful approach to solving complicated



simulations which can be run on a personal computer within a reasonable period of time.

There are many advantages to using the CFD method, in particular:

- I. It has a simple feasibility of design and develops theoretical models compared to experimental methods.
- II. It enables better clinical decisions by identifying the risk of cardiovascular diseases prior to surgery or other clinical procedures.
- III. It is a fast tool that can be used to make clinical decisions.

This section discusses the available models of blood flow and arterial wall interaction. The defining assumptions for the blood flow models are introduced first. Next, modelling the coupling between blood flow properties and arterial wall mechanics is discussed, using the two-way fluid-structure interaction (FSI) method. Finally, wave propagation and reflection in the cardiovascular system are examined.

### **2.3.1 Assumptions in Modelling Blood Flow**

The modelling of blood flow is based on solving the theoretical dynamics models of flow and arterial geometries. Those theories have been developed on idealized biomedical (cardiovascular) conditions such as atherosclerosis and aneurysms for specific patient geometries. The results of these simplified models have influenced the investigation of the mechanisms of cardiovascular disease development. These simplified models have been improved and refined by the development of CFD modelling methods which has resulted in realistic models based on *in vivo* anatomical data.

The literature shows that different types of modelling assumptions are used in blood flow simulation and analysis. Figure 2-6 shows the different types of models, from the simplest combination of a steady, one dimensional, laminar viscous flow of a Newtonian fluid in a long straight tube of constant cross-section, to the most complicated model of an unsteady, three dimensional, non-Newtonian, pulsatile flow in a short, tapered tube with a flexible wall [41, 65-71]. Each of these assumptions influences the pulsatile flow and the calculated arterial wall characteristics [80-85]. Early models assumed laminar, continuous, non-pulsatile flow when modelling blood flow [68-72]. However, later studies found that pulsatile flow in arteries tends to be non-laminar, with a flattening velocity profile during systole and a more parabolic velocity profile during diastole [68-72]. Evidently, changing the modelling assumptions can significantly influence blood flow parameters, especially for diseased arteries. It has been observed that with atherosclerosis and aneurysms, the blood flow profile acts as transitional or turbulent flow patterns [68-72]. This observation requires the intensive investigation of blood formation.

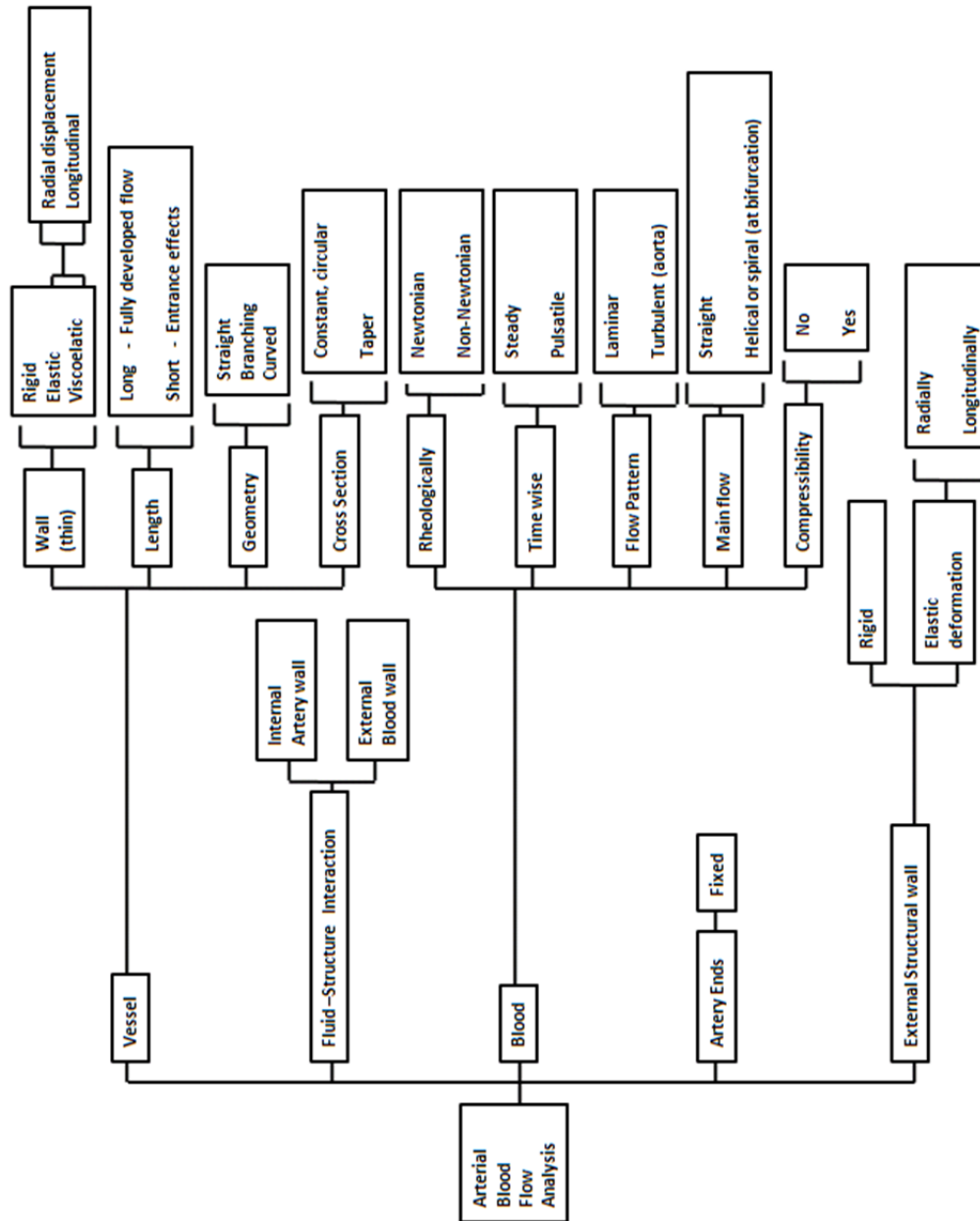


Figure 2-6: Selection of models for arterial flow analysis (adapted from [41])

The blood is formed by red blood cells, white blood cells and platelets which are suspended in plasma. This formulation has viscosity that allows the blood layers to slide over one another in smooth layer paths creating laminar flow in healthy blood vessels. However, in diseased blood vessels, the velocity increases, causing interference between the different layers due to different inertia and frictions close to the artery wall and results in turbulent flow. An assumption of either laminar or turbulent flow in diseased arteries, assuming a rigid artery wall, has been used in computer simulations to compare its accuracy with *in vivo* measurements [73-75]. The turbulence assumption showed better agreement with clinical data with respect to the velocity profile in atherosclerotic arteries [67-75]. It was concluded that the transition from laminar to turbulent flow in arteries occurs at a relatively low Reynolds number (Re) [8, 9] using Equation 2-1.

$$Re = \frac{\text{Inertia Forces}}{\text{Viscous Forces}} = \frac{D\rho V}{\mu} \quad (2-1)$$

The velocity (V), diameter (D), density ( $\rho$ ) and viscosity ( $\mu$ ) indicate the shear stress at the artery wall. For example, a low Re with a value less than 2300 for internal flow, indicates laminar flow. However, at  $Re = 2300$ , the flow enters a transitional period and at  $Re > 2300$ , it becomes turbulent flow [8, 9]. In the transitional and turbulent regimes, the fluid particles become erratic and time dependent in nature which fits with the pulsatile flow in diseased arteries. Abraham *et al.* [21] analysed a three-dimensional, pulsatile flow model of blood flow in complex tubular geometries using a representation of a plaque-narrowed artery. They found that removal of the plaque led to a 2.5 magnitude increase in the blood flow for both the systole and diastole portions of the

cardiac cycle [76]. To apply this model in complex geometries, the blood flow through the artery with plaque is solved under specific assumptions. The Finite-Volume (FV) numerical method can be used for these flow calculations [53]. However, it is very difficult to simulate the flow and generate the coordinate system for these complex geometries [41, 54]. Many computational analyses assume the plaque to be rigid. This is a passive assumption regarding the lumen of the artery wall where the blood flows through a less streamlined conduit [41, 77].

The literature lacks a model of the arterial wall with realistic material properties such as the non-linearity of its material properties. Therefore, in this thesis, non-linear properties will be considered and analysed by the two-way FSI.

### **2.3.2 Complex Mechanical Interaction**

Arterial wall-blood flow modelling is a challenging process in computational and numerical simulation due to the effects of divers feedback. For example, low stiffness of the artery compared to viscosity of the blood results in a strong coupling of blood flow and arterial wall mechanics [60-64, 78-79]. However, the pulsatile blood flow deforms the artery wall and results changes in the blood flow profile [54]. To address this coupling, an FSI method has been developed which combines a constitutive model describing the stress distribution in the vessel wall with a computational analysis of blood flow [60, 64]. This method allows for the solution of fluid and solid phase coupled problems by accounting for both instantaneous fluid mechanical forces on the artery wall, such as pressure and WSS, and the effects of wall movement on fluid motion. Li *et al.* [78] used this approach to investigate the flow and stress fields for different diseases, particularly atherosclerosis and aneurysm. They found that

atherosclerosis and aneurysm result in significant wall motion and, consequently, increase blood velocities and decrease WSS [79].

From a mechanical perspective, changes in arterial geometry compliance represent the clinical manifestations of an induced force exceeding the strength of the artery wall where disease is located. Wall stress is quantified as either the maximum principal stress or the Von Mises stress, resulting from a force exerted along the diseased arterial wall [76]. The impinging normal force exerted on the arterial wall is the dominant stress producing the distributed wall deformation. Scotti *et al.* [64] and Leung *et al.* [60] studied the effect of wall stress and fluid dynamics in an abdominal aortic aneurysm using the Finite Element (FE) method. They found that, when applying a transient FSI approach, the maximum abdominal aortic aneurysm WSS result was higher than that under the rigid wall assumption. Subsequently, in a comparison between models of an aortic arch with and without aneurysm using FSI, stresses were found to be much higher at the inflection points in the model with aneurysm [60]. Furthermore, stresses on the media layer are higher for stiffer arterial walls. In a subsequent study, this required the simulation to be performed considering artery layer thickness that is modelled as a non-linear hyperelastic material [61]. When modelling the artery wall as individual layers, it was found that stresses in the media layer are the highest, particularly at the outer edge near the adventitia layer [56]. This may explain why tears in the artery wall often originate in the media near the adventitia [56].

### **2.3.3 Structure of the Arterial Wall**

In modelling arteries, one of the most important decisions to make is what type of artery wall assumptions are necessary [56]. The structure of the arterial wall is anisotropic, multilayered and nonlinearly elastic, thereby making its material properties highly nonlinear [57, 61].

Previous modelling studies were carried out under the rigid wall assumption which does not take into account the quantitative influence of arterial wall motion under pulsatile flow [60-67]. This has an effect on flow conditions in both healthy and diseased arteries and on the regions downstream of severe constrictions such as poststenotic regions [57]. This results in a change in hemodynamics pressure and WSS values [57]. Consequently, to optimize the accuracy and applicability of mathematical models for atherosclerosis and aneurysms, an investigation into the effects of different arterial wall assumptions is required. The mathematical modelling of development of arterial blockage or aneurysm rupture at the abdominal aorta requires material properties of the aorta wall when a constitutive equation of blood flow is required due to consideration of hemodynamic factors. Those hemodynamic and mechanical properties of biological soft tissues are nonlinear, elastic properties and have a stress-strain relationship that can be mathematically described as an approximately exponential function [64-65]. These stresses and forces are caused by the pulsatile blood pressure and flow on the arterial wall causing deformation. The amount of deformation depends on the pulsatile blood flow rate and temperature of the body. For example, for a small deformation with no heat transfer (adiabatic system), the material elasticity of the arterial wall returns to its original configuration after removing the extra blood flow.

### **2.3.4 Wave Propagation in the Arterial System**

Analysis of blood flow and pressure wave propagation in arteries is helpful in exploring the mechanisms associated with the regulation and control of blood circulation in the human body in healthy and diseased conditions [80-89]. With respect to atherosclerosis and aneurysms, changes in the blood flow patterns around the diseases location are of particular interest. As these diseases lead to changes in the arterial wall characteristics, considerable changes in blood flow patterns can be expected [84-89]. Some studies [84-89] have analysed the aorta using a simple model of a uniform elastic tube with a constant diameter. This simplification seems warranted for certain sections of the aorta and shows a close agreement with clinical quantities with respect to pulse wave propagation [87-89].

Progress in computing technology has improved modelling using CFD to investigate the effects of blood flow parameters on the arterial wall [87-89]. These models measure the pressure gradient using more realistic assumptions than previous simple assumptions, which assumed pressure wave propagation as finite [87-89]. Some of these assumptions include; realistic wall geometry, Newtonian, viscous incompressible fluid with non-linear viscoelastic behaviour and wall tissue with orthotropic material behaviour [83-86]. These are incorporated by employing the equation of motion for the fluid and using the equation of continuity for the wall. These are then numerically solved to determine the variation of the phase velocities and the transmission coefficients with frequencies for different transmission pressures and initial stress [83-89]. Thus, mathematical analysis has the potential to enhance understanding of velocity and pressure wave related to change in arterial wall properties, such as thickness and diameter, that affect blood flow.



Pulse waves carry a lot of information about the cardiovascular system and if captured in the right context, they may help in identifying changes in the dimension and material properties of that system [9] as shown in Figure 2-7.

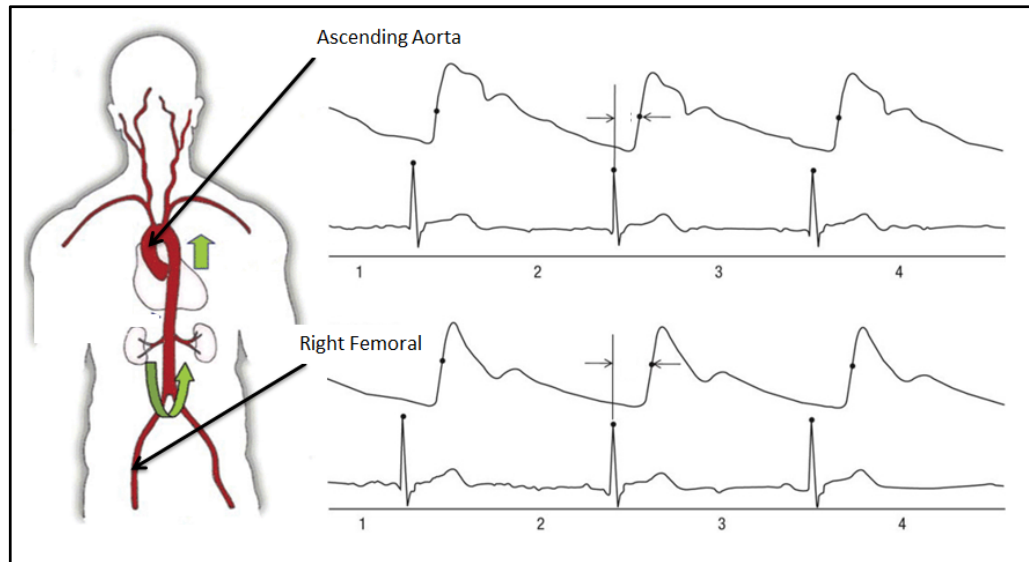


Figure 2-7: Non-invasively measured ascending and right femoral pressure waveforms (adapted from [9])

Figure 2-7 shows blood pressure waveforms measured at the ascending aorta compared with those at the right femoral artery. These waveforms show the forward and backward waves and are correlated with the reflection coefficient using *in vitro* data [9]. This coefficient is affected by blood flow and the material properties of the artery wall and or is impacted by cardiovascular disease. A previous study [9] shows that cardiovascular diseases affect the backward waves, arterial wall stiffness and thickness. The results show that these diseases change blood flow and pressure waveforms by reducing the pulsatility of the distal waves. This finding could enable us to establish a novel, quantitative method of diagnosing cardiovascular diseases non-invasively.

## 2.4 Model Outputs

In this study, for any modelling process, the final outputs are obtained by finding and solving equations which are input into the software package ANSYS® 14.0 [90]. This section describes the computational and numerical model outputs, such as WSS, which result from blood pressure. This section also illustrates the stress phase angle (SPA), which results from correlating WSS and CS.

### 2.4.1 Wall Shear Stress

Wall shear stress (WSS) is the main mechanical characteristic that links flow to any changes in the artery wall and cardiovascular disease lesions [91-95]. An increased WSS comes from a remodelling of the vascular wall which is instigated through mechano-sensitive pathways in the wall. The calculated WSS values are greatly influenced by flow condition as given by Equation 2-2.

$$\tau = \mu \sqrt{\left(\frac{\partial u_i}{\partial x_j} + \frac{\partial u_j}{\partial x_i}\right)} \quad (2-2)$$

where  $\tau$  represents the WSS,  $\mu$  represents the viscosity and  $\left(\frac{\partial u_i}{\partial x_j} + \frac{\partial u_j}{\partial x_i}\right)$  represents the second invariant of the rate of deformation as described by Tada et.al [108].

The majority of literature assumes that blood flow is laminar, incompressible, Newtonian and pulsatile, which for the analysis of WSS, was found to be quite accurate [21, 90]. Morris *et al.* [95] and Stroud *et al.* [96] simulated a 3D model for the human aorta which was obtained using clinical data. The results show that maximum WSS occurs along the inner wall of the bend of the aortic arch. However, this maximum

value depends on whether the flow is assumed to be steady or pulsatile [91-93]. Valencia *et al.* [79] found that the pulsatile flow in an artery with atherosclerosis disease is numerically characterized by high WSS and pressure at the diseased location with a recirculation zone. The size of the recirculation zone varies during one cardiac pulse and the recirculation length depends on the degree of severity of the disease, for example stenosis [56].

To contribute to the identification of the earliest stages of cardiovascular disease, there are some predictions that have significant implications for understanding local hemodynamic characteristics. In areas of small curvature and high flow, assuming a non-Newtonian fluid may be more appropriate. This is due to the fact that increased red blood cell density on the inner radius of curvature is associated with low WSS [95-97]. Jung *et al.* [98] found that the red blood cell build up is a result of complex recirculation patterns, oscillatory flow with flow reversal, and vessel geometry which results in a prolonged particulate residence time especially at the end of the diastole cycle. These lead to an increase in initial plasma viscosity causing lower WSS [91-98]. These findings are of importance as areas of low WSS have been associated with a build-up of fatty materials on the artery wall (atherogenesis) [95-99]. WSS is, therefore, an important factor in the development or the retardation of a plaque layer [99]. Hence, in a diseased condition, where low WSS occurs in the poststenotic area, this area actually represents the narrowing region for the stenosis [99]. A small region of low WSS can still be seen as a small irregularity on the inside of the curve of the artery [100-102]. In addition, WSS greatly depends on the position of the artery wall, as expected in an arterial geometry with significant primary and secondary curvature [103-05].

The studies discussed above have indicated that WSS significantly affects the intima and media layers of the artery wall, which is the main cause of disease of the artery layers. However, presently there is no clear medical evidence quantifying the range of changes in WSS for different cardiovascular diseases. Moreover, there is insufficient information on the critical values of this stress for diagnosing atherosclerosis and aneurysm medically.

#### 2.4.2 Circumferential Strain

The mechanical characteristics of arteries are defined by the pulsatile blood pressure, flow and the compliance of the artery wall. One of the stresses affecting the cells of the arterial wall is called circumferential strain (CS) [104-107] and is governed by Equation 2-3.

$$\varepsilon_{ij} = \frac{1}{2} \left( \frac{\partial U_i}{\partial x_j} + \frac{\partial U_j}{\partial x_i} \right) \quad (2-3)$$

where  $U = U_1, U_2, U_3$  represents the displacement vector of computational grid-points of the artery wall in tensor axis.  $ij$  represent the tensor directions.

By adjusting the pressure and flow rate while the artery is held at a constant axial stretch ratio, it is possible to independently control CS in perfusion organ culture experiments. CS is related by the equations of equilibrium, the flow equation and the pressure-diameter response of the artery wall. For example, equilibrium in the radial direction causes CS within the arterial wall at a given time, this is where the pulsatile pressure affects the outer diameter and thickness of the arterial wall as shown in Figure 2-8. It is believed that CS could be correlated with the development of cardiovascular

disease and thereby establishes a new relationship as discussed in the next section [104-107].

### **2.4.3 Stress Phase Angle**

Most *in vivo* and *in vitro* studies to date have focused on either WSS or CS but not on their interaction [105, 108-109], which is believed to play a considerable role in determining arterial wall displacement and the development of arterial disease [105,107-109].

Recently, research has shown that concomitant WSS and CS affect endothelial cells in a biochemical response which is modulated by a phase angle called the stress phase angle (SPA) [106-109]. The SPA is used to characterize the dynamic mechanical stimuli experienced by the endothelial cell monolayer which expresses as a waveform of stresses. An endothelial cell is simultaneously exposed to the mechanical forces of fluid WSS imposed by blood flow and solid CS induced by the blood vessel's elastic response to the pressure pulse [107]. Tada *et al.* [108] found experimentally that these combined forces induce unique endothelial biomolecular reactions which are characterised as the driving force in modulating an endothelial response [110].

SPA may influence vascular remodelling and play a role in the localization of cardiovascular disease in the arteries. This angle is highly radian negative at sites that are prone to atherosclerosis [104, 111]. For a better illustration of the SPA, a typical transverse arterial cross-section is shown in Figure 2-8. Pulsatile flow in the axial direction induces pressure and WSS on the endothelium cell lined vascular wall. Pressure imposes a normal radial stress on the wall from the lumen [108-109].

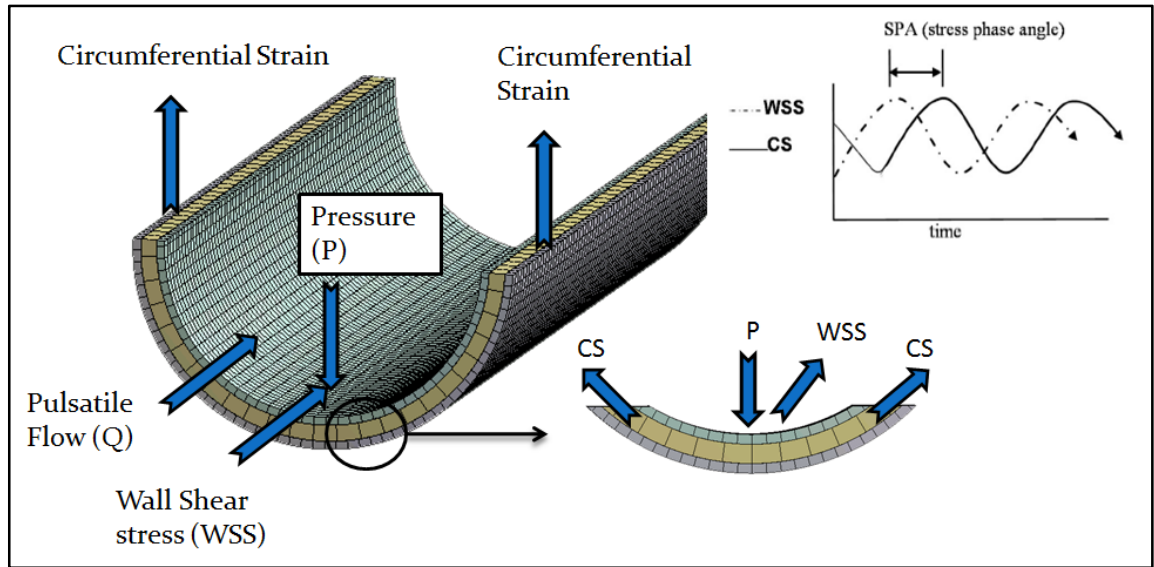


Figure 2-8: Stress Phase Angle

Previous studies have shown how the SPA can be used to indicate disease location. Tada *et al.* [112] simulated 3D, pulsatile flow in a carotid bifurcation model with atherosclerosis. They found a negative SPA on the outer wall of the carotid sinus where disease was localized [112]. Torii *et al.* [110] also investigated the effect of changes in flow velocity waveform and arterial wall geometry before and after coronary intervention in the right coronary artery using the CFD/FE method. The results suggested that SPA measures the degree of asynchrony between pressure and flow waveforms and that it is the only parameter that combines WSS and CS (Figure 2-8) [110].

In *in vivo* studies, Dancu *et al.* [107] found that blood vessel endothelial cells are subjected to simultaneous pulsatile WSS and CS, which act in approximately perpendicular directions to each other. In addition, they found that the phase angle between pressure and flow represents the impedance phase angle (IPA). They suggested

that there is a possible correlation between stress and impedance phase angles, which may help in non-invasive screening for cardiovascular diseases [107].

## **2.5 Summary of the Literature**

Since some cardiovascular diseases can be identified by the SPA, correlation can be established between this angle and the information carried by the propagated pulse wave. It has been shown that the negative values for the phase angle indicate presence of the development of atherosclerosis or aneurysm disease in arteries. Our research [49-51] has indicated that hemodynamic characteristics may be predicted from pressure wave signals gathered at the brachial or femoral arteries. This is anticipated to be a practical approach for diagnosing or screening for atherosclerosis and aneurysm from blood pressure waveform measurements at the brachial and femoral arteries.

The FSI scheme provides realistic results that are possible to validate clinically using an animal model. Therefore, it is important to include both the dynamics of blood flow and the wall motion response associated with the pulsatile nature of the flow to accurately represent an aneurysm or atherosclerosis disease model. However, current models lack the ability to consider the arterial wall thickness and changes in its material properties in the healthy and diseased conditions. Therefore, this research considers non-linear arterial wall properties with pulsatile blood flow.

This chapter gives a thorough and comprehensive literature survey to summarise many different types of theoretical and experimental models which have been developed to investigate the possibility of a correlation between the SPA and the development of atherosclerosis and aneurysm at the abdominal aorta. The applied material classification

and material properties used were proven to be valid. The above literature indicates the following:

- I. Intensive modelling research has been conducted on the cardiovascular system in general and the arteries in particular with the objective of determining blood flow characteristics. This research has resulted in correlations between these characteristics and changes in arterial geometry and physical condition caused by various diseases.
- II. Intensive research, including that at the Institute of Biomedical Technologies at the Auckland University of Technology [54-56], has been conducted on pulse wave propagation and how the information carried by these waves can be translated in various diagnostic tools.
- III. The literature lacks any correlation between the blood flow modelling and the wave propagation modelling. It is believed that if such a correlation is established, many arterial diseases can be identified using pressure wave propagation. This will be one of the main outcomes of this thesis.

## **2.6 Research Objectives**

The current research forms part of a larger effort by the Institute of Biomedical Technologies at the Auckland University of Technology to investigate the potential of altering current diagnostic techniques and that of non-invasive diagnosis of cardiovascular diseases. A detailed understanding of the role of developing diseases and in particular, hemodynamic stresses and blood pressure are a key feature of this research. To identify and formulate a technique for diagnosing atherosclerosis and aneurysm, it is



essential to understand how the disease affects the artery wall and disturbs the blood pressure waveform. Hence the main objectives of the current research are to:

- 1- To investigate hemodynamic stresses in both atherosclerosis and aneurysm affected samples and healthy samples.
- 2- To discover the correlation between the stress phase angle (SPA) and the development of atherosclerosis and aneurysm.
- 3- To investigate arterial wall compliance and severity in both diseased and healthy conditions.
- 4- To investigate the hypothesis of non-invasively assessing the risk of arterial blockages and aneurysm, based on systolic and diastolic blood pressure measurement from the cuff, using pulse wave transmission.

Three components to detect cardiovascular diseases are identified: blood pressure wave forms, arterial compliance and stress phase angles (SPA) using a two-way FSI approach. Comprehensive CFD/FE and *in vivo* models used to investigate these components and their interaction can reveal the role each process plays in the development of disease. Such a model also allows for a more targeted investigation of the differences between healthy and diseased aorta geometries, which could lead to the development of new methodologies for screening for these diseases.

The literature review indicates that there is currently no model that can fully explain when and where abdominal aorta blockage develops or the factors leading to rupture occur. Specifically, none of the models is able to quantitatively predict the disease establishment using parameters such as WSS or blood flow and pressure measurements.

## 2.7 Thesis Outline

To address these issues, the methodology of this thesis includes:

- 1- Presenting a suitable CFD/FE theory for circulatory system modelling (Chapter 3)

Chapter 3 describes the theory behind the modelling of CFD/FE geometries as well the involvement of modelling the interaction between the blood flow and arterial wall deformation.

- 2- Simulating 3D-CFD/FE atherosclerosis disease in animal models (Chapter 4)

Since it is difficult, if not impossible, to validate a CFD/FE model on human subjects, animal models are considered for this stage of the investigation.

To have more insight into CFD/FE modelling on a human model requires ascertaining the accuracy of the CFD/FE results on live specimens. Therefore, Chapter 4 investigates the validity of the CFD/FE modelling process in living body data using animals. The test of this validity involves comparing the *in vivo* and *in vitro* experimental results to those of the CFD/FE models. Chapter 4 describes the results of the animal experimental models in which atherosclerosis was created in the abdominal aorta in Wistar rats. The animal experimental and computational models are investigated as follows:

- a) Measure blood pressure, lumen diameter, arterial length and thicknesses of the following arteries: (i) abdominal aorta, (ii) iliac bifurcation and (iii) right femoral artery in healthy specimens.

- b) Narrowing the abdominal aorta for the animals in group (a) at four different severities of atherosclerosis development and re-measure blood pressure.
- c) Generate 3D-CFD/FE models adapted from the animal experiments and validate their results against the *in vivo* measurements.
- d) Correlate the blood pressure waveforms at the right femoral artery with the degree of severity of the disease.

### 3- Simulating 3D-CFD/FE cardiovascular diseases at the abdominal aorta in the human model (Chapter 5)

Using CFD/FE, we determine the effect of geometric and physical changes, caused by cardiovascular diseases such as atherosclerosis and aneurysm growth, on the propagation of pulsatile blood flow and pressure waveform characteristics.

Part of this investigation, i.e. the literature survey of available data, has been covered in this chapter. The lack of quantitative data concerning the development of cardiovascular diseases necessitates a preliminary CFD/FE investigation on healthy arteries prior to the development of unhealthy conditions in those arteries. This preliminary CFD/FE investigation will focus on the propagation of the blood flow and pressure response to the WSS and CS stresses at the artery wall. Similarly, the unhealthy conditions will be assessed by subjecting these arteries to changes in the lumen diameter, thickness and length to investigate the instantaneous WSS and CS changes and the Augmentation Index (AI). Changing diameter, thickness and length of the arterial wall will be analysed to provide a bridge between a single event response and the development and growth of atherosclerosis and aneurysm. The CFD/FE models are developed through the following steps:

- i. Simulations of 3D Newtonian pulsatile flow through an ideal artery system with bifurcation for three different aorta models are generated for healthy, atherosclerosis and aneurysm conditions within abdominal aorta.
- ii. In the three models, clinical pulse waves are imposed as input and outputs boundary conditions.

#### 4- Quantifying cardiovascular disease stresses (Chapters 4, 5 and 6).

After completion of objective one, the relationship between the SPA and the disease location and growth in both the animal and human models are determined. The predominant diseases of the cardiovascular system, atherosclerosis and aneurysm, will be analysed in terms of SPA, to assess disease growth from non-invasive measurements taken at farther locations, such as the brachial artery. This study will investigate whether the SPA is an appropriate indicator to diagnose the growth of cardiovascular diseases occurring at the abdominal aorta by measurements taken at the brachial artery. Lastly an empirical SPA relationship will be generated in an effort to expedite the process of diagnosing cardiovascular disease parameters by physicians.

#### 5- Discussion and Analysis (Chapter 6)

Chapter 6 illustrates the formula for assessing cardiovascular diseases non-invasively either from the brachial artery or from the right femoral artery. This assessment is based on determination of the systolic and diastolic blood pressures correlated to the diseases' development and arterial wall compliance. Chapter 6 also discusses the CFD/FE results of the animal and human models in detail.

## **Chapter 3 Computational Fluid Dynamics Modelling**

### **3.1 Introduction**

This chapter describes a series of CFD modelling methods which were selected to increase the understanding of the hemodynamic behaviour of atherosclerosis and aneurysm at the abdominal aorta. While there is a significant amount of data on cardiovascular disease (Chapters 1 and 2), little has been reported on diagnosing those diseases non-invasively, particularly with regards to pressure pulse propagation and arterial wall compliance.

Recently, CFD methods have been proven to solve very complex problems in many modern engineering fields, and have been successfully applied in many areas of fluid mechanics [90]. CFD is used for simulation and analysis of fluid flow and provides a qualitative and quantitative prediction using computer-based simulations which require high processor speeds.

CFD modelling in biomedical applications is used to solve, analyse and optimize many medical devices as well as to investigate many physiological problems. This modelling also predicts the physical parameters related to the blood flow in arteries and FSI. The artery wall is modelled using FE methods using the Transient Structural Mechanic (TSM) scheme. TSM provides the ability to simulate solid bodies in their linear, nonlinear, static and transient form [90].

This chapter aims to provide a description of the governing mathematical equations and algorithms developed for the mechanism of the arterial structure (Section 3.2). The computational mesh methods are discussed in Section 3.3. Section 3.4 of this chapter deals with the FSI coupling method, followed by the governing equations in Section 3.5.

A schematic of the CFD/FE approach is given in Figure 3-1. This figure will be discussed in further detail in the following sections.

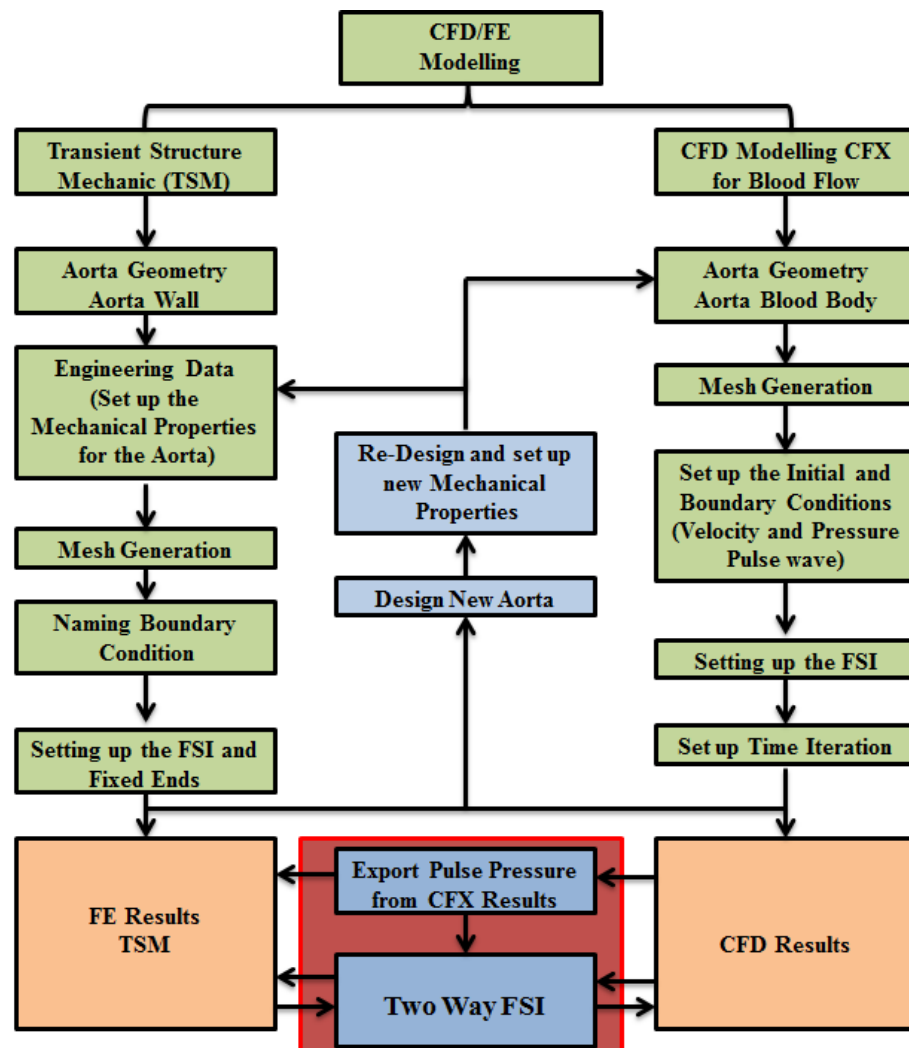


Figure 3-1: Flow chart of CFD/FE modelling showing the process followed for modelling arterial wall and blood flow

### **3.2 Mechanism of Arterial Structure**

Modelling a healthy blood vessel is a complex process because the artery provides non-thrombogenic branching for blood flow [9, 12-13]. In addition, arteries transport oxygen from the heart at higher physiologic pressures than other blood vessels [9, 12-13]. This physiologic feature must be taken into account when forming the initial conditions of the model.

To construct the aorta model (3D geometry), both the solid component for a structural analysis and the fluid volume for a blood analysis, the ANSYS DesignModeler (DM) is used to transfer 2D sketches to 3D models of bodies and parts. The DM tool is available under ANSYS® 14.0 and allows adjustment and updating the design of the geometry as well as removal of particular features to simplify the geometry using different tools such as draw, modify, dimensions, constraints and settings toolboxes. There are advanced features and tools used for special cases such as separating the solid body from the fluid body using the fill, named selection, freeze and unfreeze features of the software. Fill is used to fill the whole inside of the solid body with a new body representing the fluid volume while the solid body is frozen which allows for the separation of the new body. This technique is helpful for performing two-way FSI analysis between the artery wall and blood flow.

Diseased arteries show changes in the structure of the geometry and mechanical properties of the wall. These changes occur at the diseased location and manifest as non-linear mechanical properties along the arterial wall segment [9, 12-13, 19]. Modelling these non-linear properties using TSM is complicated; therefore a number of simplifying assumptions are made.

This section outlines the parameters used to model arterial wall characteristics in healthy and unhealthy conditions. These parameters describe the arterial geometric shape and complexity, artery wall, length of the diseased portion and cross-sectional area of the artery in FE modelling.

### 3.2.1 Model Geometries

The TSM method is used to model a variety of simple (straight) geometries and complex (branching or curved) geometries. The shape of these geometries determines the specific mesh generation and FSI scheme used to model them. Figure 3-2 illustrates three different meshed geometries (including their solid body, fluid body and FSI interface). Each of these would require a different procedure and method for meshing and solving their FSI coupling equations, which are discussed in Sections 3.3 and 3.4.

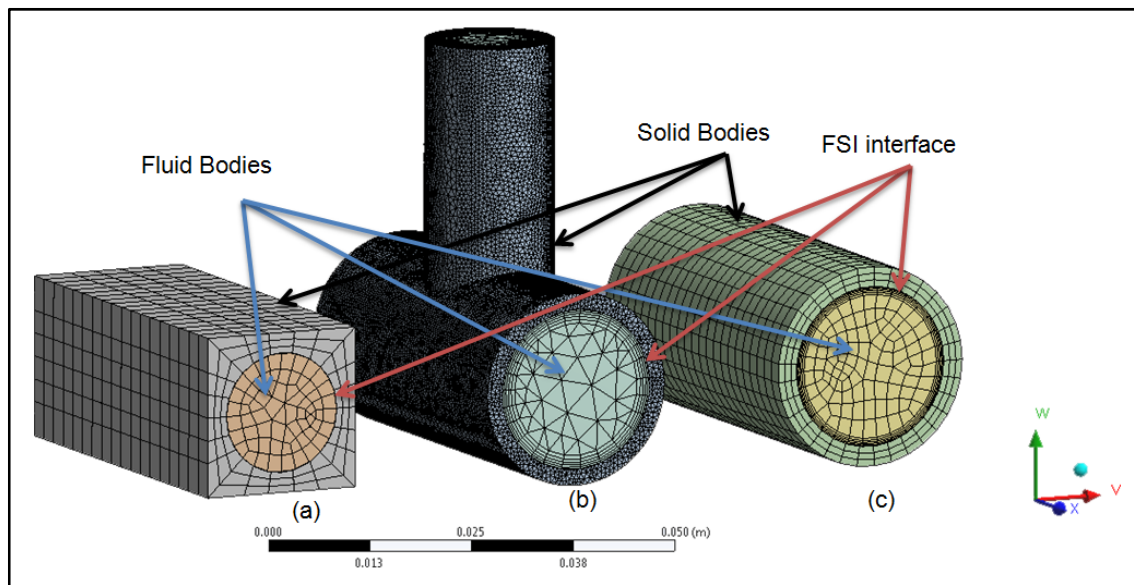


*Figure 3-2: Three different meshed geometries: (a) cuboid, (b) T-shaped cylindrical and (c) cylindrical geometry*



In this thesis we investigate the aorta's geometry which is classified as a complex geometry. The aorta has three main branches: Brachiocephalic (BC); Left Common Carotid (LCC); and Left Subclavian (LS), which are all connected to the aortic arch [9-16] as shown in Figure 3-3. In constructing and modelling this geometry, it is necessary to consider the thickness of the artery wall and incorporate the bifurcation and branches. This simulation of the bifurcation and branches takes a long time; however, this can be reduced with a faster processor. Previous studies [9-16] modelled the aorta with simplified assumptions which give rise to minor divergences between the model and clinical trials. However, these differences are minimal and the results can still be validated against clinical trials. Therefore, an idealized model is acceptable.

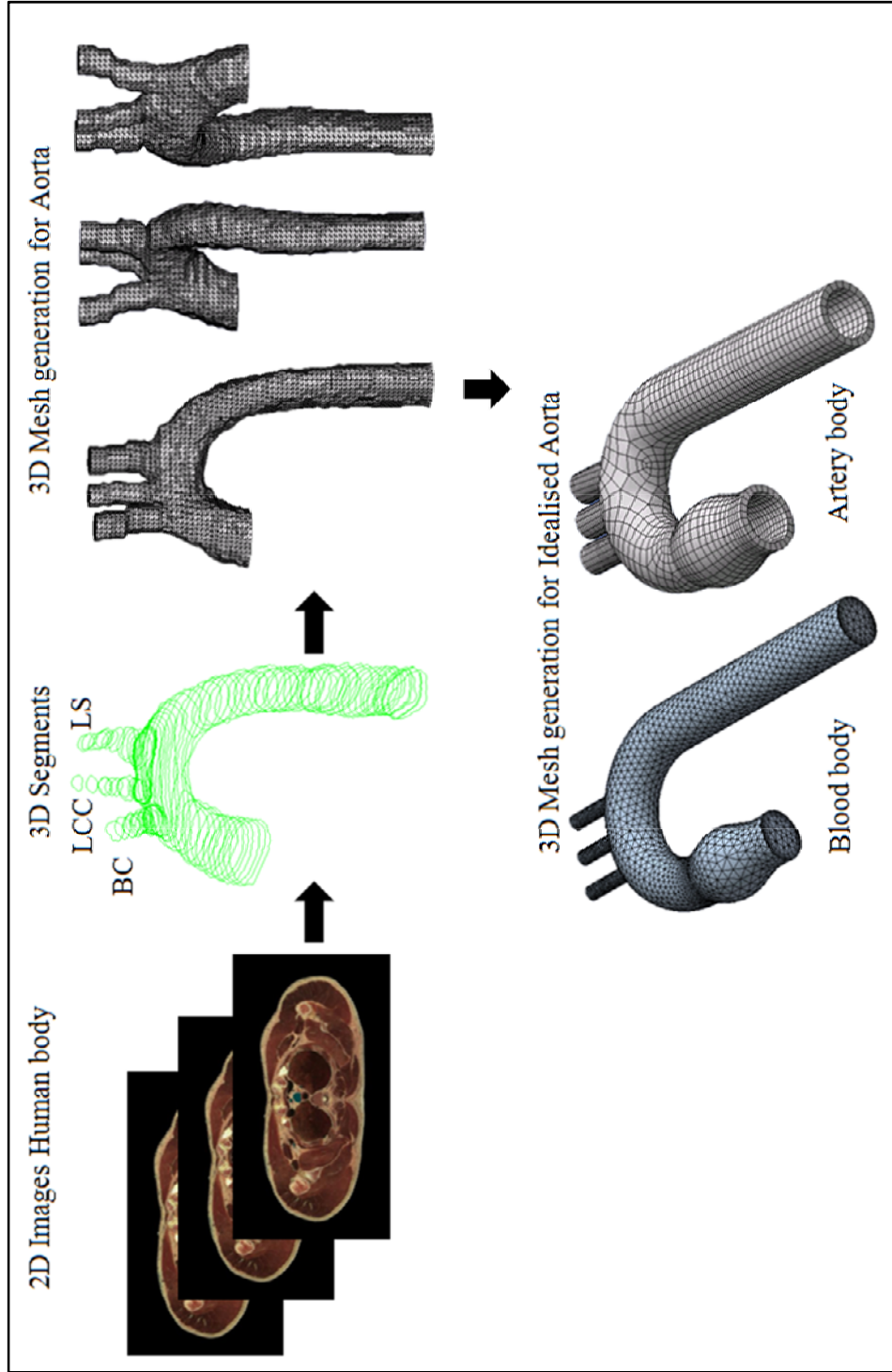


Figure 3-3: Stages of constructing aorta geometry from two dimensional images and the idealized aorta in both blood and artery bodies

### 3.2.2 Artery Wall Characteristics

As discussed in Chapter 2, the arterial wall is composed of three layers called the *intima*, *media* and *adventitia* [9-13]. The *intima* consists of an endothelial cell (EC) monolayer that prevents blood and other elements from adhering to the lumen surface [9-13, 112, 107]. The *media* is the thick middle layer composed of smooth muscle and elastic tissue in varying proportions [9-13, 107, 112]. The *adventitia* is the outer covering layer which is composed of collagenous tissue [9-13]. The construction of these three arterial layers using TSM modelling presents a challenge due to the difficulty in setting up their non-linear material properties. Recent studies [9-13] assumed that the artery wall thickness is equal to that of the endothelium layer. Simulating an unhealthy arterial wall (atherosclerosis and aneurysm) was performed by altering the mechanical properties (such as elasticity and rigidity) of the *intima* layer adapted from *in vitro* experiments [9-13].

Figure 3-4 shows the different kinds of arterial construction, depicting the arterial wall in both healthy (a) and unhealthy (b) conditions following the idealised construction of arteries. These models are acceptable because they are capable of investigating the effect of blood flow on the arterial wall [41].

Many studies [59-64, 78] modelled the artery wall as either rigid, elastic or viscoelastic. The most suitable assumption is the elastic, single-layer wall (representing the *intima*). Although this simplifies the model, the assumption of a flexible wall is most closely aligned with clinical data.

The arterial wall's material properties are assumed to be similar to those of silicon rubber, which agrees with the *in vitro* data, and is suitable for flexible wall modelling. Studies which have considered the wall rigid [59-64] provide little information on arterial wall deformation; therefore, the rigid wall assumption is no longer acceptable. The flexible wall assumption will be further investigated in Chapter 4 of this thesis.

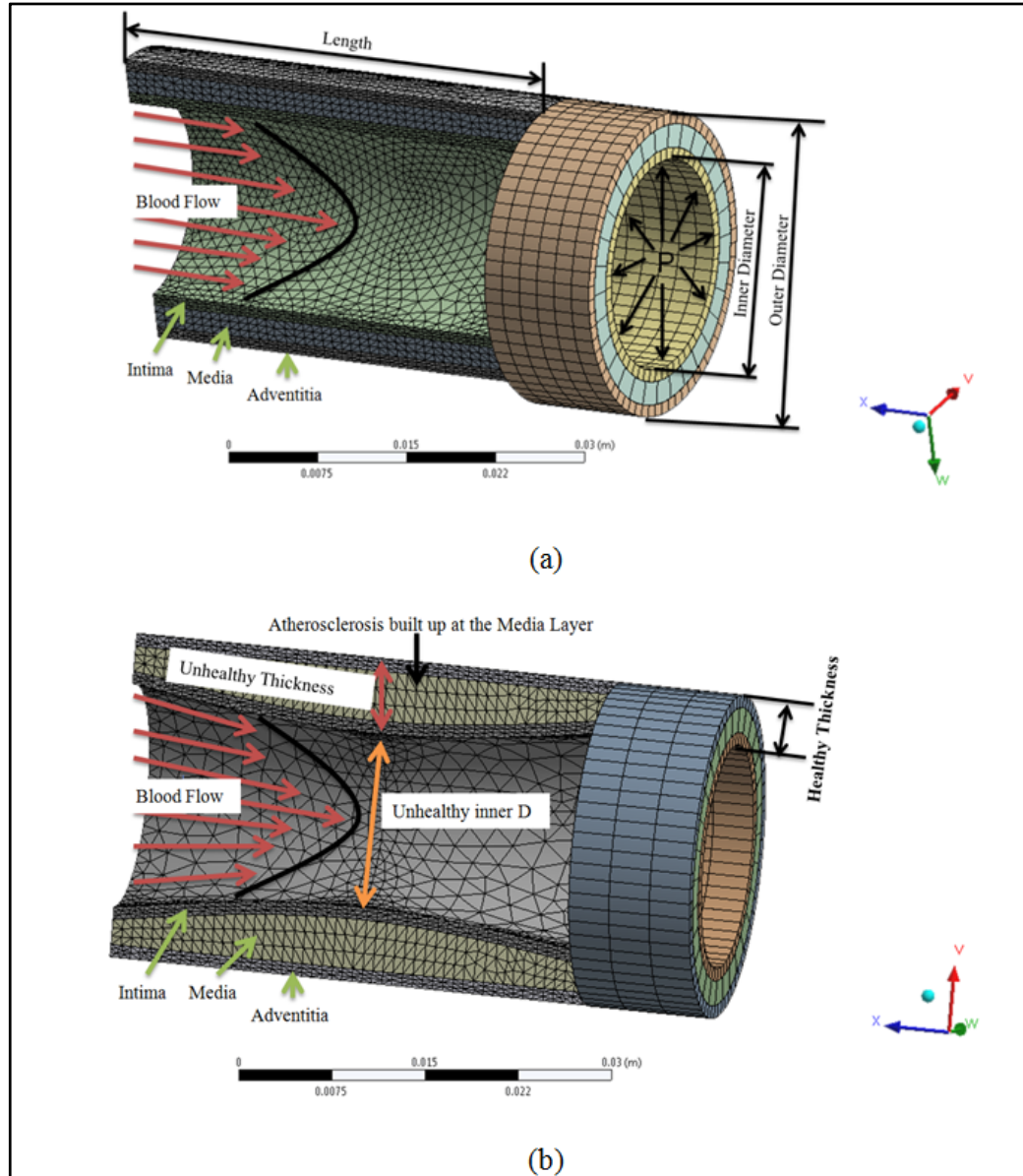
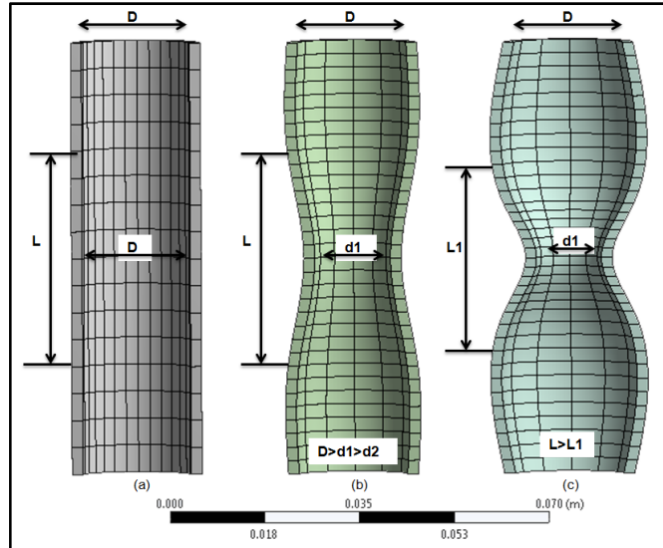


Figure 3-4: Arterial wall in (a) healthy artery and (b) diseased artery (atherosclerosis) showing the inner and outer diameters, the change of the thickness in both healthy and unhealthy conditions and how the length of the artery changes in atherosclerosis

### 3.2.3 Arterial Length

Changes to the length of the arterial wall in unhealthy conditions using CFD/FE modelling have a significant impact on the stresses and strains affecting the artery wall [59-64]. From the perspective of CFD modelling, modelling arteries using a short length assumption will impact on the initial and boundary conditions and affect pulse wave results. The reason for this is that the cardiovascular system is a closed system and each artery has its own conditions. Therefore, for better TSM and CFD modelling, the true lengths are recommended so as to reach the fully developed flow.



*Figure 3-5: Different types of arterial length condition: (a) healthy condition; (b) unhealthy condition with the same length,  $L$ ; and (c) unhealthy condition with shorter length,  $L_1$*

TSM modelling also allows us to investigate the change in the length parameter between the healthy and the unhealthy conditions [59-64]. Figure 3-5 shows the length of the artery in a healthy condition (a) and two other arteries with different unhealthy conditions, having lengths  $L$  (b) and  $L_1$  (c), respectively. Varying the length of the

artery allows us to investigate the relationship between length and disease progression, which will be investigated in Chapter 4.

### 3.2.4 Cross-Section

Transient Structural Mechanic (TSM) modelling enables us to depict a cross-section of the arterial wall [90]. This cross-section illustrates the effect of blood flow on the artery wall and vice versa. This effect shows the stress/strain characteristics and wall deformation affecting the artery wall [59-69]. Creating cross-sections could help to identify stiffness in the longitudinal and circumferential directions. This may help in identifying the risk of cardiovascular disease.

Figure 3-6 shows the different types of longitudinal cross sections along three different geometries which were shown in Figure 3-2. These show the domains of the fluid-solid bodies in more detail, and their mesh quality.

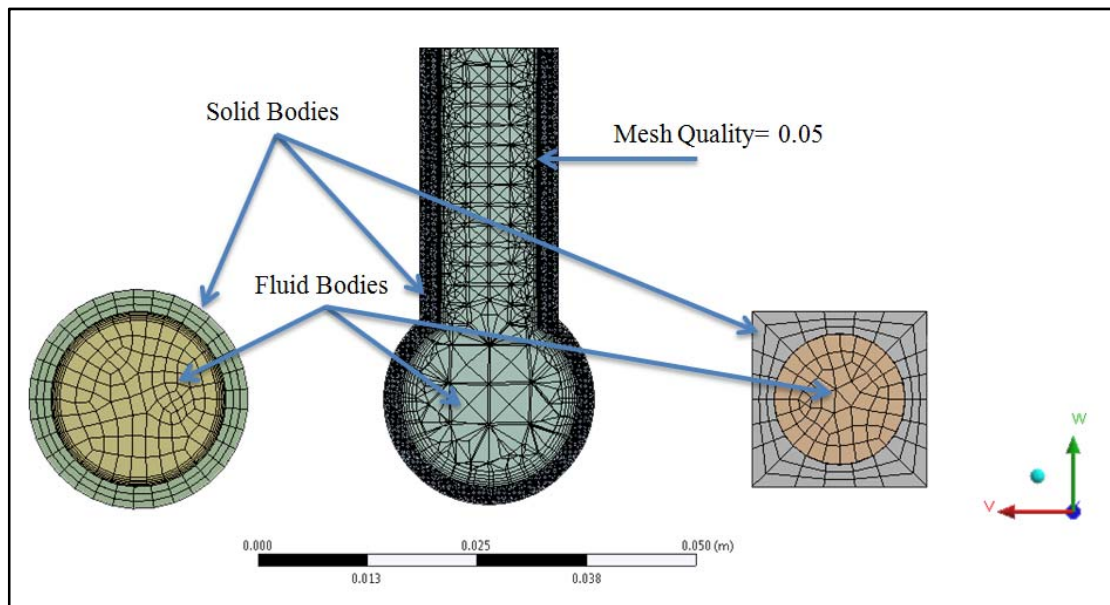


*Figure 3-6: Three different cross sections for the geometries in Figure 3-2 using different types of mesh method*

### 3.3 Computational Meshes

The mechanical model and fluid flow bodies each require different types of mesh methods and techniques. Before the meshing process, the model is reconstructed by DM as discussed in Section 3.2.

There are many different mesh methods which could be used by TSM and CFD in ANSYS® 14.0 such as: sweep, tetrahedrons and multi-zone [90]. These methods are used for both solid and fluid bodies and the choice of a suitable method depends on the degree of geometric complexity. Figure 3-7 shows the structure of the three different methods of mesh generation. Panels (a) and (b) show two cuboids meshed using sweep and tetrahedrons, respectively. However, the cylindrical geometry (c) is better meshed using the multi-zone method.

There are also many techniques to improve the mesh quality, such as, inflation, mapped face, resizing and refinement tools. These tools are validated by checking mesh quality such as its skewness with acceptable mesh metric ranges (0.05-0.85) [90].

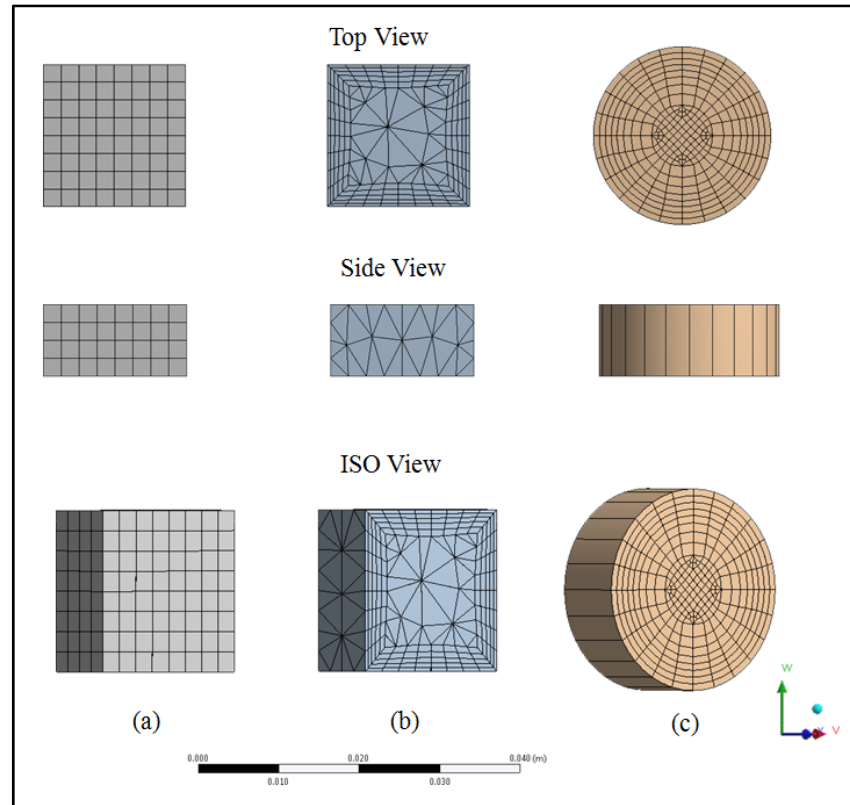


*Figure 3-7: Computational mesh methods for three-dimensional domains in ANSYS®: (a) sweep method for cuboid; (b) Tetrahedron method for cuboid; and (c) multi-zone method for cylindrical*

### 3.4 Fluid-Structure Interaction Method

The fluid-structure interaction (FSI) [90] technique is used to provide an understanding of the relationship between the blood flow and the artery wall. The application of FSI into the pulsatile blood flow models generates important information such as the location of the arterial lesions and how they occur based on hemodynamic stresses. This will help in diagnosing the development of potentially fatal cardiovascular diseases.

The FSI method could be used into two forms: one-way FSI and two-way FSI. In the following sections the two-way FSI method and the Arbitrary Lagrangian Eulerian (ALE) method are discussed in detail.



### 3.4.1 Two-Way FSI

Modelling of the complete cardiac cycle is better performed using the FSI approach. This technique allows us to study aorta fluid-mechanics by accounting for both the instantaneous fluid forces acting on the wall and the effects of wall motion on the fluid dynamic field [90]. The objective of this thesis is to investigate the two-way impact of the blood on the artery wall and the artery wall on the blood simultaneously; this is achieved using the two-way FSI method.

Figure 3-8 is a flow-chart illustrating the numerical modelling of the aorta geometry using the two-way FSI method. The left-hand side shows the TSM method used to set up the FSI conditions and to mesh the model of the artery wall. The right-hand side shows the Command Field Exercise (CFX) meshing and setting up of the boundary conditions and generating the FSI interface for the blood-flow body. The CFX results are then exported to the TSM model to generate the two-way FSI solution.

CFX is a commercial CFD application in ANSYS® 14.0, which uses the finite volume (FV) method to generate the mesh to represent the blood flow [90]. This software solves the pair of algebraic multi-grid equations to give robust solutions for complex flow fields (Equation 3-1) which employ complicated structures, multi-block, body-fitted coordinates and support grid movement.

$$\frac{d}{dt} \int_{(t)} \rho dV = \int_V \frac{\partial \rho}{\partial t} dV + \int_S \rho \mathbf{W}_j dn_j \quad (3-1)$$

where  $V$  and  $s$  represent the volume and surface regions of integration.  $dn_j$  represents the differential cartesian components of the outward normal surface vector and  $\mathbf{W}_j$  represents the velocity of the control volume boundary.

The FSI solver is an automated tool which uses the ANSYS® Fluid Solver for the fluid domain and the ANSYS® TSM solver for the solid domain. The two solvers solve the equations for the fluid and solid domains independently of each other [90]. The FSI solver transfers fluid forces (pressure) and velocities across the fluid-solid interface.

The algorithm continues to loop through the solid and fluid analyses until convergence is reached for that time-step. Convergence in the stagger loop is based on the quantities being transferred at the fluid-solid interface [90].

Figure 3-9 shows the two bodies which are considered in ANSYS® TSM and CFD modelling using the FSI approach, in the mesh perspective (a) and total deformation (b). The sub-section which follows describes the Lagrangian and Eulerian schemes which have been combined into one method called the ALE (Arbitrary Lagrangian-Eulerian) method which is appropriate for numerical modelling [90].

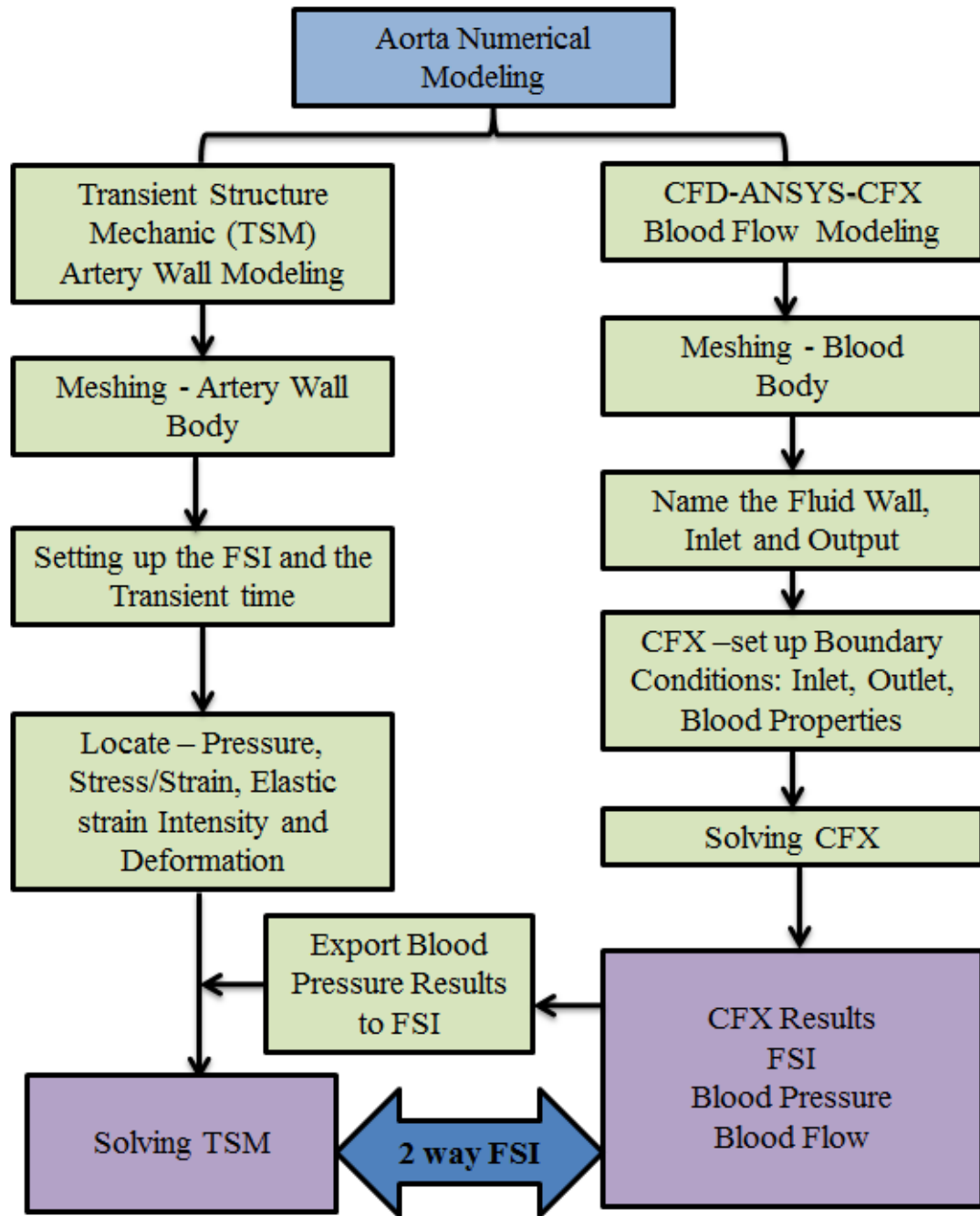


Figure 3-8: Flow chart of Aorta CFD/FE modelling using ANSYS® showing the steps followed to model any artery

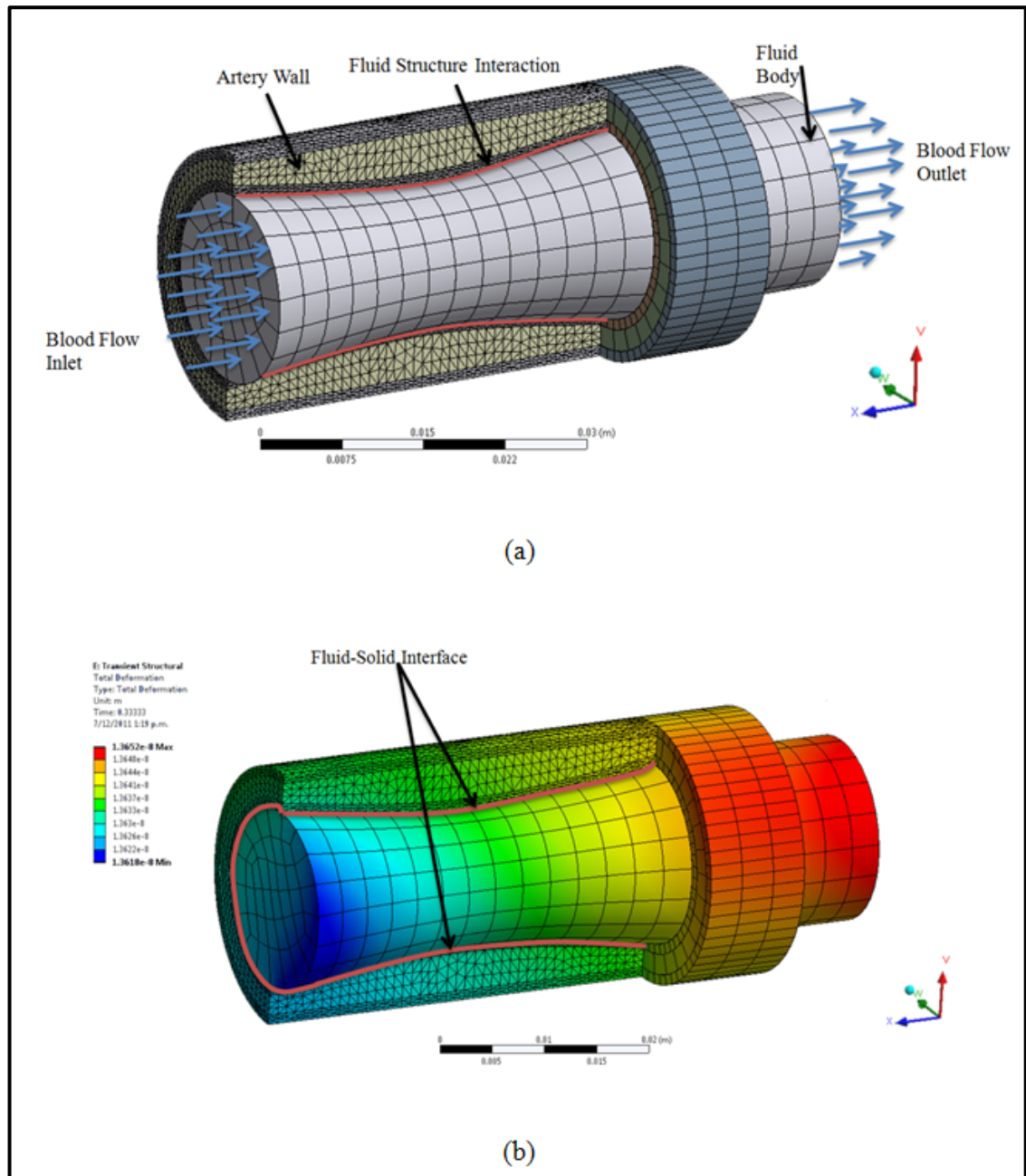


Figure 3-9: Blood flow-artery wall interaction: (a) Mesh generation and (b) total deformation

### **3.4.2 Arbitrary Lagrangian Eulerian Method**

The Arbitrary Lagrangian Eulerian (ALE) method is the most applicable method for modelling geometries involving FSI bodies [30]. This method is suitable for arteries that have large deformations resulting from the pulsatile flow because it allows the grid to track the movement of the material by adjusting the grid size and measures the flux of the material when the grid deforms excessively [90]. However, smaller grids provide more accurate results but require longer simulation time [90]. As computing power improves, grid-size can be reduced, enabling the software to solve more complex geometries.

CFD and TSM modelling of the FSI aorta geometry using ALE requires the equations of conservation of energy, momentum and mass to be solved simultaneously [90]. ALE analyses the fluid domain and the interface of the FSI geometry; however, the Eulerian scheme is used for the fluid frame only. The ALE equations [90] are provided in Appendix I.

### **3.5 Governing Equations**

There are many restrictions in blood flow modelling that limit the accuracy in the design and setting of boundary conditions which solve the two-way FSI model. These restrictions depend on the assumptions made regarding the blood flow, such as single phase, incompressible and Newtonian, as well as the transition from a laminar (healthy condition) to turbulent (unhealthy condition) flow profile. To overcome these assumptions, CFD and TSM equations are applied to govern the analysis of the aorta modelling in both its solid and fluid domains.

### 3.5.1 Blood Flow Equations

The blood flow in arteries is analysed with assumptions such as free surface and non-linear interaction with the artery structure. To solve models with this assumption computationally, the blood flow in this thesis for all models is governed and assumed as a pulsatile flow (laminar transition to turbulent), an incompressible, adiabatic and Newtonian fluid using the Navier-Stokes equations. The models are solved numerically and computationally using: (i) the mass continuity (Equation 3-2) and (ii) equation of momentum (Equation 3-4) [90]. The mass continuity equation in differential form is:

$$\frac{\partial \rho}{\partial t} + \nabla \cdot (\rho \vec{v}) = 0 \quad (3-2)$$

where  $\rho$  represents the density of the blood, the term  $\frac{\partial \rho}{\partial t}$  represents the incompressibility and unsteady blood flow and  $\nabla \cdot$  is the divergence of the flow velocity vector field  $\vec{v}$ . The blood is assumed incompressible and having a constant density, therefore the mass continuity equation becomes  $\nabla \cdot (\vec{v}) = 0$  which is the volume continuity equation. This means that the divergence of the velocity field is zero at any location, or in physical terms, the local volume dilation rate is zero [91] which is not a realistic assumption for arterial modelling.

For modelling symmetrical geometries the mass continuity equation [90] becomes:

$$\frac{\partial \rho}{\partial t} + \frac{\partial}{\partial x}(\rho \vec{v}_x) + \frac{\partial}{\partial r}(\rho \vec{v}_r) + \frac{\rho \vec{v}_r}{r} = 0 \quad (3-3)$$

where  $x$  is the axial coordinate,  $r$  represents the radial coordinate,  $\vec{v}_x$  and  $\vec{v}_r$  are the axial and radial vector velocities, respectively. The terms  $\frac{\partial}{\partial x}(\rho \vec{v}_x)$  and  $\frac{\partial}{\partial r}(\rho \vec{v}_r)$  represent

the partial differential equation of the vector velocity on the x-axis and r-axis, respectively, as shown in Figure 3-10. This figure illustrates the artery wall and the pulsatile blood flow (laminar profile) which causes stress on the wall.

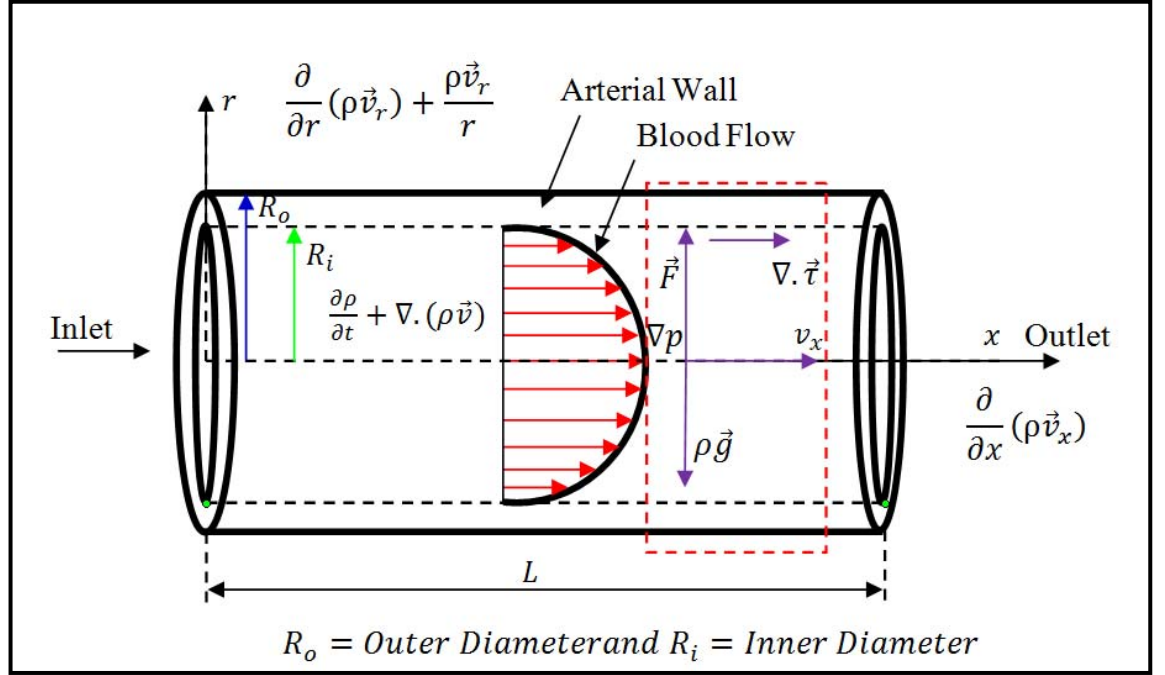


Figure 3-10: Inlet and outlet blood flow through the artery

The momentum conservation equation [90] represented in terms of the vector partial differential equation is:

$$\frac{\partial}{\partial t}(\rho \vec{v}) + \nabla \cdot (\rho \vec{v} \vec{v}) = -\nabla p + \nabla \cdot \vec{\tau} + \rho \vec{g} + \vec{F} \quad (3-4)$$

where  $p$  is the static pressure and the term  $\nabla p$  represents the divergence of the pressure,  $\vec{\tau}$  is the stress tensor (described in Equation 3-5), and the terms  $\rho \vec{g}$  and  $\vec{F}$  represent the gravitational body force and external body forces, respectively [91], as shown in Figure

3-10. The term  $\nabla \cdot \vec{\tau}$  represents the divergence of the stress tensor  $\vec{\tau}$  as shown in Figure 3-10 which is:

$$\vec{\tau} = \mu \left[ (\nabla \vec{v} + \nabla \vec{v}^T) - \frac{2}{3} \nabla \cdot \vec{v} I \right] \quad (3-5)$$

where  $\mu$  is the molecular viscosity,  $I$  represents the unit tensor, and the term  $[(\nabla \vec{v} + \nabla \vec{v}^T) - \frac{2}{3} \nabla \cdot \vec{v} I]$  represents the effect of volume dilation [90].

The conservation of momentum equations for symmetrical geometries in axial and radial coordinates are expressed in Equations (3-6) and (3-8) respectively as follows:

$$\begin{aligned} \frac{\partial}{\partial t}(\rho \vec{v}_x) + \frac{1}{r} \frac{\partial}{\partial x}(r \rho \vec{v}_x \vec{v}_x) + \frac{1}{r} \frac{\partial}{\partial r}(r \rho \vec{v}_x \vec{v}_r) = - \frac{\partial p}{\partial x} \\ + \frac{1}{r} \frac{\partial}{\partial x} \left[ r \mu \left( 2 \frac{\partial v_x}{\partial r} - \frac{2}{3} (\nabla \cdot \vec{v}) \right) \right] \\ + \frac{1}{r} \frac{\partial}{\partial r} \left[ r \mu \left( \frac{\partial v_x}{\partial r} + \frac{\partial v_r}{\partial x} \right) \right] + \vec{F}_x \end{aligned} \quad (3-6)$$

rearrange Equation 3-6:

$$\begin{aligned} \frac{\partial}{\partial t}(\rho \vec{v}_x) + \underbrace{\frac{\partial}{\partial x}(r \rho \vec{v}_x \vec{v}_x) + \frac{\partial}{\partial r}(r \rho \vec{v}_x \vec{v}_r)}_{\text{Convection for Volume Friction}} \\ = \underbrace{- \frac{\partial(r p_x)}{\partial x}}_{\text{Pressure}} + \underbrace{\frac{\partial}{\partial r} \left( r \mu \frac{\partial v_x}{\partial r} \right)}_{\text{Shear Stress}} + \underbrace{r \vec{F}_x}_{\text{Interfacial Drag}} \end{aligned} \quad (3-7)$$



and

$$\begin{aligned}
& \frac{\partial}{\partial t}(\rho \vec{v}_r) + \frac{1}{r} \frac{\partial}{\partial x}(r \rho \vec{v}_x \vec{v}_r) + \frac{1}{r} \frac{\partial}{\partial r}(r \rho \vec{v}_r \vec{v}_r) \quad (3-8) \\
& = -\frac{\partial p}{\partial x} + \frac{1}{r} \frac{\partial}{\partial r} \left[ r \mu \left( \frac{\partial v_r}{\partial x} + \frac{\partial v_x}{\partial r} \right) \right] + \\
& \frac{1}{r} \frac{\partial}{\partial r} \left[ r \mu \left( 2 \frac{\partial v_r}{\partial r} - \frac{2}{3} (\nabla \cdot \vec{v}) \right) \right] - 2 \mu \frac{v_r}{r^2} + \frac{2}{3} \frac{\mu}{r} (\nabla \cdot \vec{v}) + \rho \frac{v_z^2}{r} + \vec{F}_r
\end{aligned}$$

Rearrange Equation 3-8:

$$\begin{aligned}
& \frac{\partial}{\partial t}(\rho \vec{v}_r) + \underbrace{\frac{\partial}{\partial r}(r \rho \vec{v}_r \vec{v}_r) + \frac{\partial}{\partial x}(r \rho \vec{v}_x \vec{v}_r)}_{\text{Convection for Volume Friction}} \quad (3-9) \\
& = \underbrace{-r \frac{\partial(p_r)}{\partial r}}_{\text{Pressure}} + \underbrace{\left( 2r \mu \frac{\partial v_r}{\partial r} \right) + \frac{\partial}{\partial x} \left( r \mu \frac{\partial v_r}{\partial r} \right) - \frac{2 \mu v_x}{r}}_{\text{Shear Forces}} + \underbrace{r \vec{F}_r}_{\text{Interfacial Drag}}
\end{aligned}$$

Investigation of the fluid forces is governed by the viscosity equation for an incompressible, Newtonian fluid where the shear stress is proportional to the rate of the deformation tensor  $\left( \frac{\partial u_j}{\partial x_i} + \frac{\partial u_i}{\partial x_j} \right)$ . The viscosity equation [90] is:

$$\tau_{ij} = \mu \left( \frac{\partial u_j}{\partial x_i} + \frac{\partial u_i}{\partial x_j} \right) \quad (3-10)$$

where  $\mu$  is the viscosity, which is independent of the rate of deformation as shown in Figure 3-11, and  $i$  and  $j$  represent the tensor vectors. This figure shows how an element acts when the deformation occurs due to the shear stress resulting from the pulsatile

flow. For some non-Newtonian fluid, the shear stress can similarly be written in terms of non-Newtonian viscosity:

$$\tau_{ij} = \eta \left( \frac{\partial u_j}{\partial z_i} + \frac{\partial v_i}{\partial r_j} \right) \left( \frac{\partial v_j}{\partial z_i} + \frac{\partial u_i}{\partial r_j} \right) \quad (3-11)$$

where  $\eta$  is a function of all three invariants of the rate-of-deformation tensor  $\left( \frac{\partial u_j}{\partial x_i} + \frac{\partial u_i}{\partial x_j} \right)$ . However, in the non-Newtonian models available in ANSYS<sup>®</sup> 14.0 [90],  $\eta$  is considered to be a function of the shear rate  $\dot{\gamma}$  only, which is related to the second invariant of  $\left( \frac{\partial u_j}{\partial x_i} + \frac{\partial u_i}{\partial x_j} \right)$  and is defined as:

$$\dot{\gamma} = \sqrt{\left( \frac{\partial u_j}{\partial z_i} + \frac{\partial v_i}{\partial r_j} \right) : \left( \frac{\partial v_j}{\partial z_i} + \frac{\partial u_i}{\partial r_j} \right)} \quad (3-12)$$

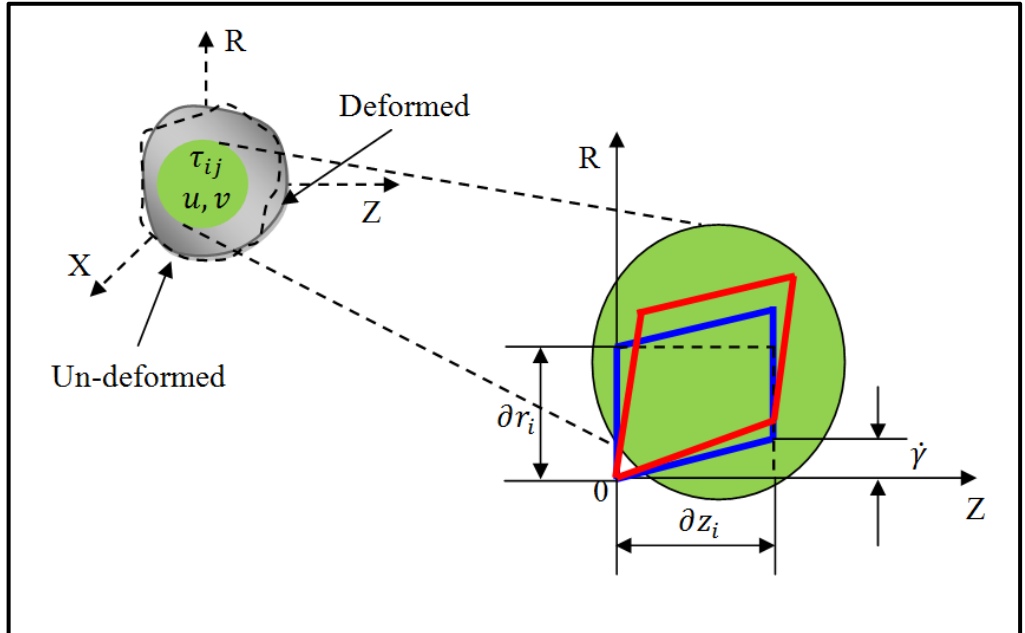


Figure 3-11: Engineering strain of deformation for a sample of the artery wall

### 3.5.2 Elastic Vessel Wall Modelling

The governing equations of motion of an elastic solid [90] are mathematically described by the following equations:

$$\rho_w \frac{\partial^2 \varepsilon_{ij}}{\partial t^2} = \frac{\partial \sigma_{ij}}{\partial x_j} + \rho_w F_i \quad (3-13)$$

$$\text{for } i = 1, 2, 3$$

where  $\varepsilon_{ij}$  and  $\sigma_{ij}$  are the components of the displacement and stress tensor in a solid respectively,  $\rho_w$  is the arterial density,  $F_i$  are the components of the body force acting on the solid as shown in Figure 3-12. The stress tensor  $\sigma_{ij}$  can be obtained from the constitutive equation of the material, whereas the arterial wall deformation is governed by the conservation of energy of blood flow, as illustrated in Figure 3-12. The energy will be stored inside the artery wall as the strain energy density function  $W$ . This is measured through the energy stored in the artery wall resultant from the deformation as shown in Equation 3-14 [90].

$$S_{ij} = \frac{\partial W}{\partial \varepsilon_{ij}} \quad (3-14)$$

$$i, j = 1, 2, 3$$

where  $S_{ij}$  and  $\varepsilon_{ij}$  represent the second Piola-Kirchhoff stress tensor and the Green-Lagrange strain tensor, respectively. The infinitesimal deformation conditions and the stresses are identical, therefore the Second Piola-Kirchhoff stress tensor [90] is related to Cauchy and total stress tensors as follows:

$$\tau_{ij} = -p'\bar{I}' + \sigma_{ij} \quad (3-15)$$

where  $\tau_{ij}$  and  $\bar{I}'$  represent the total stress and unit tensors for solid, respectively. However,  $p'$  represents the hydrostatic pressure [90].

The artery wall is assumed and modelled as a single layer throughout the entire model as a Neo-Hookean elastic non-linear arterial material dependent on stress-strain behaviour with large deformations [90]. This assumption is used for realistic material properties and is governed by strain energy and density which is considered a special case of a Cauchy elastic wall as shown in Equation 3-16 [90].

$$W = \frac{G}{2}(\bar{I} - 3) \frac{k}{2}(J - 1)^2 \quad (3-16)$$

where  $G$  and  $k$  are the shear and bulk modulus of the arterial wall, respectively,  $J$  represents the ratio of the deformed elastic volume over the un-deformed volume, and  $\bar{I}$  is the first invariant of the left Cauchy-Green deformation tensor.

The most widely used criterion for modelling arterial wall deformation is the Von Mises Stress distortion energy for a ductile material [8, 9, and 90].  $\sigma_{Von\ Mises}$ , is a scalar stress value that can be computed from the stress tensor and predicts the degree to which the material stretches under different loads [8, 9, and 90]. According to the Von Mises theory, although no individual stress may cause deformation to the material, the material may yield from the combined stresses [8, 9, and 90]. The Von Mises stress combines the three individual stresses into a combined, ‘equivalent’ stress, which is then compared to the ‘yield’ stress (at which deformation occurs) [8, 9, and 90].

The equation for Von Mises stress [90] is given as:

$$\sigma_{Von\ Mises} = \frac{\sqrt{2}}{2} \sqrt{(\sigma_{11} - \sigma_{22})^2 + (\sigma_{22} - \sigma_{33})^2 + (\sigma_{33} - \sigma_{11})^2} \quad (3-17)$$

where,  $\sigma_{11}$ ,  $\sigma_{22}$  and  $\sigma_{33}$  are the three principal stresses as shown in Figure 3-12.

ANSYS® 14.0 supports all the equations presented in this chapter and these can be recalled depending on the type of problem to be simulated and analysed. For example, to simulate incompressible, homogeneous, symmetrical 3D flow, ANSYS® 14.0 [90] will automatically select Equations 3-2 to 3-12; and will calculate the results using equations 3-13 and 3-15, for determining WSS and strain respectively.

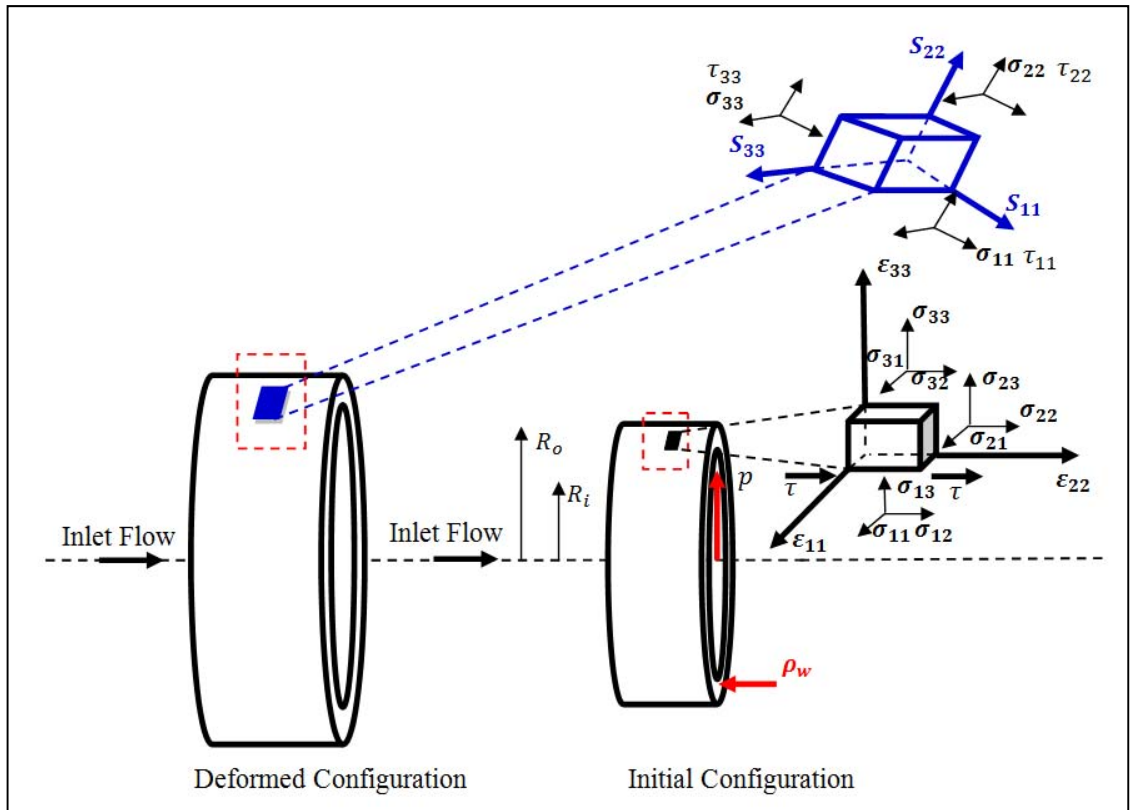


Figure 3-12 Analysis of shear stresses, normal strain rate and strain rate of deformation analysis of the artery wall for (right) diastolic and (left) systolic deformations

### 3.6 Closure

There are many advantages of using the CFD and TSM mathematical modelling methods for simulating and investigating the interactive domain between blood flow and artery wall. In this chapter set the theoretical CFD/FE methods followed for modelling two-way FSI geometries set could be used for the interaction between the blood flow and artery wall deformation. The equations presented in this chapter (3-1 to 3-9) are already set in ANSYS® 14.0 and will be chosen according to our assumptions as mentioned in Sections 3.5.1 and 3.5.2. For example, ANSYS® 14.0 knows which equation matches a 3D aorta geometry analysis as laminar flow, adiabatic, incompressible and Newtonian. The outcome from this chapter will be employed in modelling the development of atherosclerosis in the animal model and atherosclerosis and aneurysm in the human model within the abdominal aorta, in Chapters 4 and 5 respectively. Atherosclerosis will be examined and analysed using experimental and computational methods in Chapter 4. The systolic and diastolic blood pressure at the disease's location (abdominal aorta) and at the right femoral artery (which can be measured non-invasively) will also be investigated in Chapter 4.

## Chapter 4 Animal Model

### 4.1 Introduction

The main objective of this chapter is to investigate the practicability of CFD/FE modelling on a living being. Since it is very difficult if not impossible to validate CFD/FE modelling by conducting experiments on humans with the disease, an animal model is adopted to justify the computational findings. Literature indicates that it is possible to investigate cardiovascular diseases in animals such as rats and mice [113-117]. In this study, Wistar strain rats were chosen as the literature recommended these animals due to the similarity of their cardiovascular system to that of humans [113-117]. However one issue in this investigation is the difficulty in measuring blood pressure at the axillary artery (which represents the brachial artery in humans) due to the difficulty of finding an appropriately sized catheter to suit. Therefore, the CFD/FE models constructed in this chapter are validated against the *in vivo* data based on measuring the blood pressure waveform at the right femoral artery for both healthy and unhealthy conditions.

A narrowing of the artery due to disease or infection without any early diagnosis or treatment will cause a blockage which will reduce the oxygen delivery by the blood to the organs. From a medical perspective, this blockage results from atherosclerosis disease at the artery wall and many doctors are seeking an early diagnostic method to

assess it. In this chapter, an investigation of the effect of arterial blockages (atherosclerosis at the abdominal aorta) on blood pressure waveforms is performed using CFD/FE modelling validated against the clinical trials using rats. The rat models for both the *in vivo* and *in vitro* investigations are discussed in Section 4.2. A computational model is developed based on measured animal data and is tested to investigate the risk of atherosclerosis development at the abdominal aorta (Section 4.3). The CFD/FE model results and analysis are discussed in Section 4.4. Validation of the CFD/FE results against the animal model is discussed in Section 4.5.

## **4.2 Animal Model Background**

Animal experimental models have been studied by biomedical engineers and scientists for a long time to enhance the understanding of diseases in humans. The understanding and analysis of diseases developed in animals enable the discovery of treatments to preserve human lives [114-117]. Previous studies show that animal models have allowed for meaningful investigations into the early stages of disease development, although the selection of the animal was important to the disease under investigation [115-117]. For example, an ideal animal for the investigation of cardiovascular disease in humans should produce symptoms which are predictable and controllable as well as satisfies economical, technical and animal welfare considerations. Therefore, the use of Wistar strain rats was deemed acceptable for the animal model in this thesis due to the techniques which have been developed for these animals to measure relevant parameters. The Wistar strain rats developed at the Wistar Institute in 1906 [119] (coded 003, with a white coat colour (albino)) were found to be acceptable for cardiovascular and infectious disease research [114-117]. This strain is used to investigate



cardiovascular diseases such as hypertension and heart failure in humans, develop surgical procedures and test the effects of pharmaceutical drugs [117-123]. Larsen et al. [120] examined the use of Hylan gel to create cardiovascular diseases in rats by injecting the gel through the femoral artery to create a clot [120]. Rentschler and Baxter [121] investigated the development of abdominal aortic aneurysm (AAA) in rats in terms of the stresses affecting arterial wall compliance and stiffness [121]. This investigation resulted in the development of a laboratory system for assessing the pressure–diameter correlation to non-linear material properties of the artery wall [121].

The literature presented in this chapter supports the use of the Wistar rat for investigating the development of arterial blockages at the abdominal aorta. The rat experiments and data collected will be used to generate a 3D CFD/FE model which is discussed in the following sections.

### **4.3 Animal Model**

The CFD/FE modelling processes require data for setting the material properties of the artery wall and the boundary conditions such as blood pressure waveforms. With the intention of investigating atherosclerosis (arterial blockages) at the abdominal aorta, this chapter aims at assessing this disease using CFD/FE results validated against the animal model experimental measurements in terms of the pulse wave.

The animal experiments were performed following appropriate ethical protocols on Wistar rats weighing between 250-350g. An arterial blockage was created surgically at the abdominal aorta of healthy animals to generate unhealthy conditions [122-123]. Blood pressure was measured by a catheter (BD Vialon<sup>TM</sup> Material product (8360515,

F1754-4 B (9-09)) at the right femoral artery of the rat. This measurement was performed at the baseline (healthy condition) and for four different severities of arterial blockages created at the abdominal aorta for the same specimen. An *in vitro* measurement of the arterial diameter and wall thickness was also performed using microscopic and MRI techniques. These data were then implemented in CFD/FE models to investigate the development of a new non-invasive method for assessing arterial blockages.

The *in vivo* experiments and observations show that any disturbance (decreasing the lumen diameter) in the shape of the abdominal aorta has a large impact on blood pressure at further locations. These lumen diameter changes have been correlated to the blood pressure waveforms to establish a new formula to assess the development of early stage arterial blockage.

#### **4.4 Data Collection**

Arterial blockage lesions have one of the highest rates of disease fatality in humans and are very difficult to diagnose before they have advanced to a high-risk stage. Many scientists, physiologists and engineers are focusing on developing new methods for early, non-invasive diagnostic tools for these diseases [114-123].

For a better understanding of such diseases, it is ideal to compare their development on the same specimen from a healthy condition. This is impossible to perform on healthy human beings. Animal models are normally used as an alternative for performing this investigation. Abdominal aorta blockages can be clinically created on rats of the Wistar strain.

This section aims to describe the experimental procedure for collecting the physiological data and the pressure pulse waves for both healthy and unhealthy conditions. This section also clinically determines whether any change occurring at the abdominal aorta, such as the surgically created arterial blockage, can be detected at the right femoral artery in terms of blood pressure waveforms.

#### **4.4.1 *In vivo* Investigations**

The *in vivo* experiments involved a surgical procedure which simulated the creation and development of arterial blockages representing atherosclerosis at four different severities (20%, 50%, 80% and 100% of the lumen diameter) at the abdominal aorta in rats. These experiments were performed and set up to make possible the required measurements, such as blood pressure at both locations (the abdominal aorta and the right femoral artery) for the healthy and unhealthy conditions. This section presents the experimental design setup and the measured data.

##### **4.4.1.1 Experimental Design**

The design of this experiment was based on 10 Wistar rats which were used for conducting the *in vivo* experiments involving the creation of arterial blockages representing atherosclerosis. As previously mentioned, the main reason for selecting this rat was the similarity of the circulatory system, as shown in Figure 4-1 to that of humans, and the fact that it is favoured in the literature for heart disease investigation. In this study, the abdominal aorta was chosen as it is the most common location of cardiovascular diseases in humans; thereby being the ideal site to simulate the disease in rats.

Before performing the experiments, all applicable ethical protocols were followed. The rats were housed in the Vernon Jansen Unit (VJU) warehouse area Building 502 at the University of Auckland. The surgical procedure was performed at the VJU facilities and service using Surgery Bubble 3. Ten rats were anaesthetised as per the Institutional Drug Administration Order (IDAO as shown in Appendix III) which was approved by the University of Auckland ethics committee on 15/08/2011 approval number R915 (as shown in Appendix III).

The animals were anaesthetised during the whole procedure, so experienced no pain or distress. The preparation of the anaesthesia according to the IDAO was a mix 0.75 mL Ketamine, 0.5 mL Xylazine and 0.75 mL water [122-123]. This mixture was injected at the intraperitoneal region with 0.2 mL/100g dosage using a syringe with < 26g needle [122-123]. The method of injection used a gentle manual restraint technique. The frequency of dosage was once, however, there was a second dose to top up after 45-60 minutes if needed [122-123].

Firstly, a pilot study of five rats was conducted to develop the surgical procedure of creating arterial blockages at the abdominal aorta. This study was based on testing the proposed method as described in the ethical approval application (R915 see Appendix III) to achieve the main objectives of this thesis. Based on observations from the pilot study, the technique was modified to use a plastic cable for narrowing the artery instead of injecting gel. The reason for this change was that the injection of the gel at the abdominal aorta caused full blockage of the artery wall due to the small size of the vessel. Moreover, the gel technique did not allow the animal to recover after the blockage; however the plastic cable technique did allow this ( reversing the procedure).

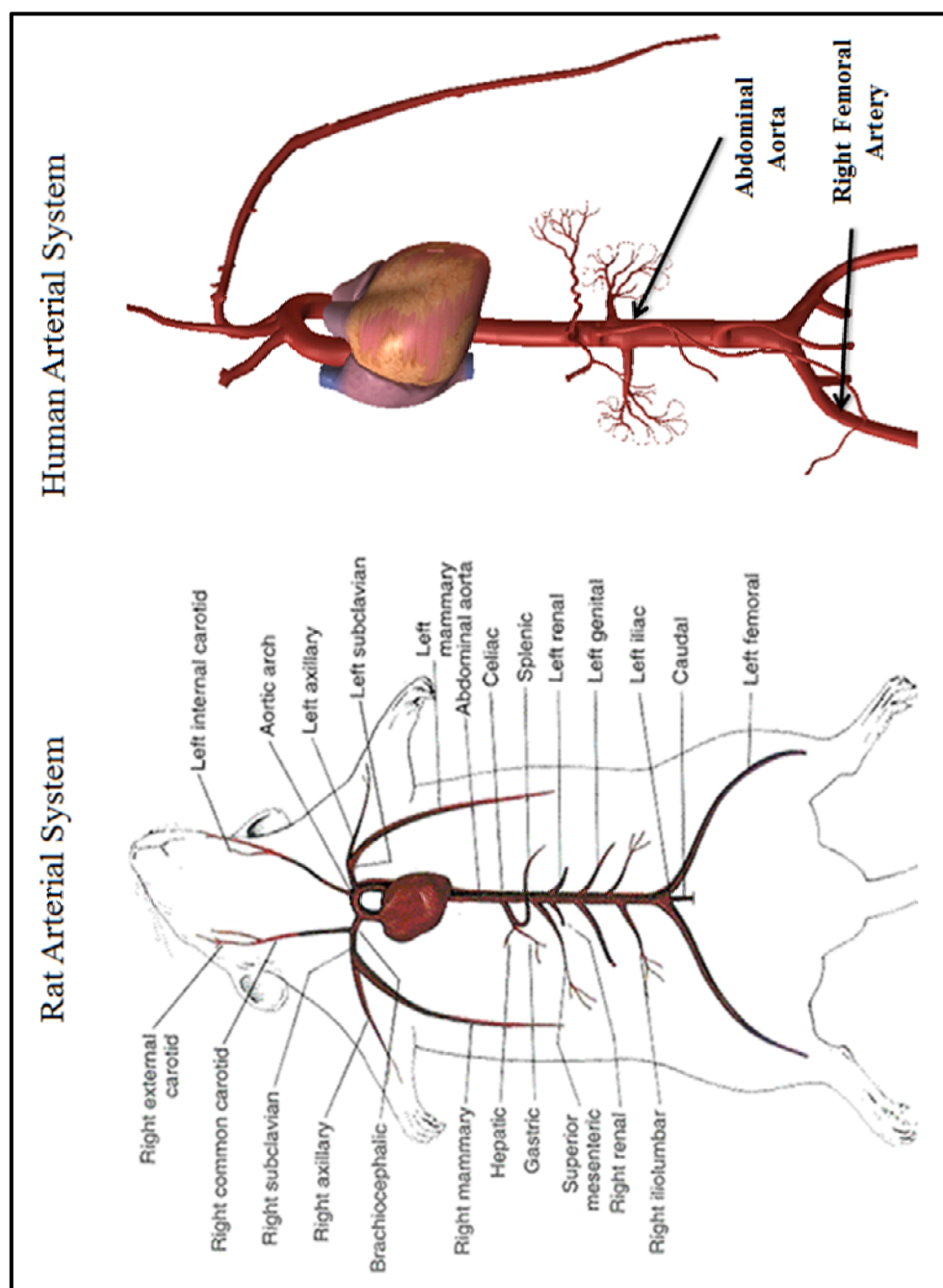
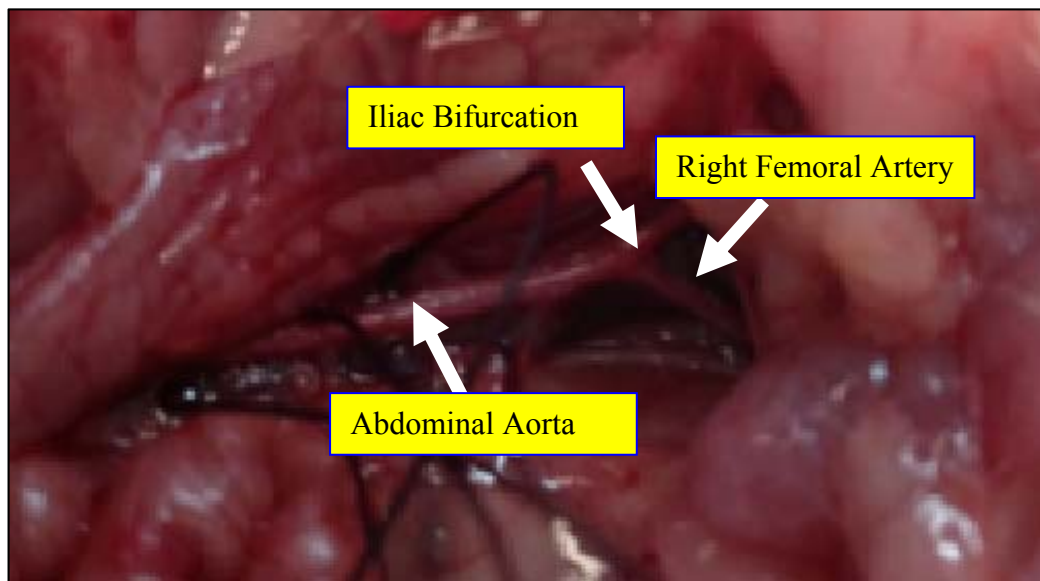


Figure 4-1: Cardiovascular system for rat (left) and for human (right) localizing the area of interest in this investigation (adapted from [118])

The arterial blockage is assumed to occur at the abdominal aorta. Four degrees of severity were created: 1) 20%, slight blockage; 2) 50% medium blockage; 3) 80%, heavy blockage; and 4) 100%, complete blockage. A small-lumen catheter (brand BD Vialon™ Insyte 8360515,F1754-4 B(9-09) made in USA) 24GA 0.75IN was injected at the right femoral artery to conduct the blood pressure measurements as shown in Figures 4-2 and 4-3.

Figure 4-2 shows the localization of both the abdominal aorta and the right femoral artery. Figure 4-3 shows the injection of the catheter into the abdominal aorta to measure healthy blood pressure. This measurement was used in the CFD model as an inlet boundary condition as well as for comparison with unhealthy conditions.



*Figure 4-2: Localizing the abdominal aorta, iliac bifurcation and right femoral artery*

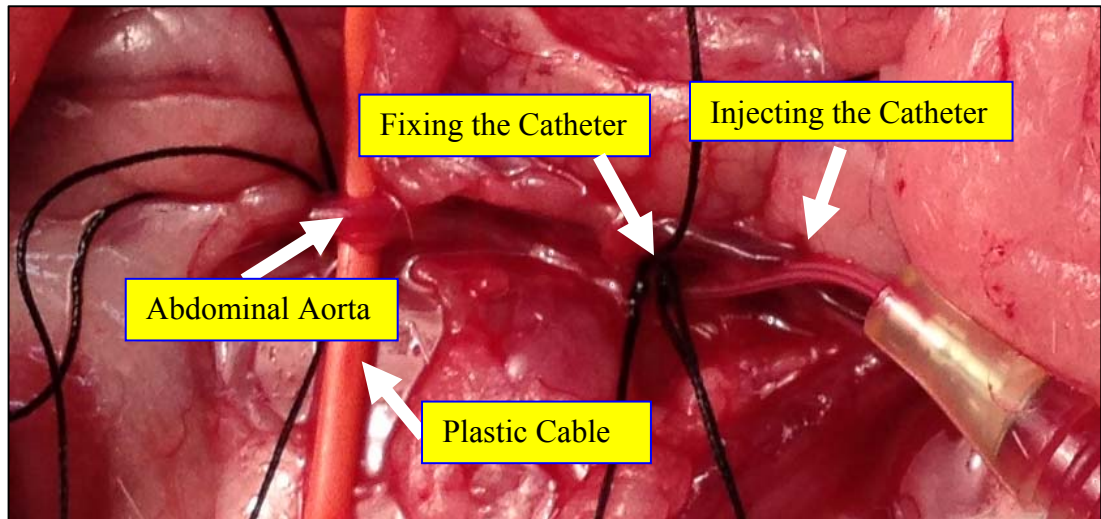


*Figure 4-3: Plastic cable for creating arterial blockages at the abdominal aorta*

The arterial blockages were assessed by a scale located at the plastic cable and a microscopic measurement examination as shown in Table 4-1. Blood pressure was measured at the abdominal aorta and the right femoral artery using a liquid-filled catheter. Once all the measurements were taken, all animals were euthanized via cervical dislocation without recovery from anaesthetic. The dead animals were dissected and the extent of plug formation in the artery was visualized using microscopic techniques.

*Table 4-1: The different controlled arterial blockages at the Abdominal Aorta*

<b>Severity at Abdominal Aorta</b>	<b>20% Severity 1</b>	<b>50% Severity 2</b>	<b>80 % Severity 3</b>	<b>100% Severity 4</b>
Diameter - D (mm)	0.8	0.5	0.2	0.0
Thickness - t (mm)	0.1	0.1	0.1	0.1
Length - L (mm)	0.25	0.25	0.25	0.25

**Magnetic Resonance Imaging Technique:** Figure 4-4 shows the MRI measurements performed on a non-random rat using MRI-4.7 Teslor. This measurement shows the right and left femoral arteries in Figure 4-4 (a). Figure 4-4 (b) shows the iliac

bifurcation cross-sectional images, (c) shows the longitudinal-section of the right and left femoral arteries and (d) shows the longitudinal section of the abdominal aorta.

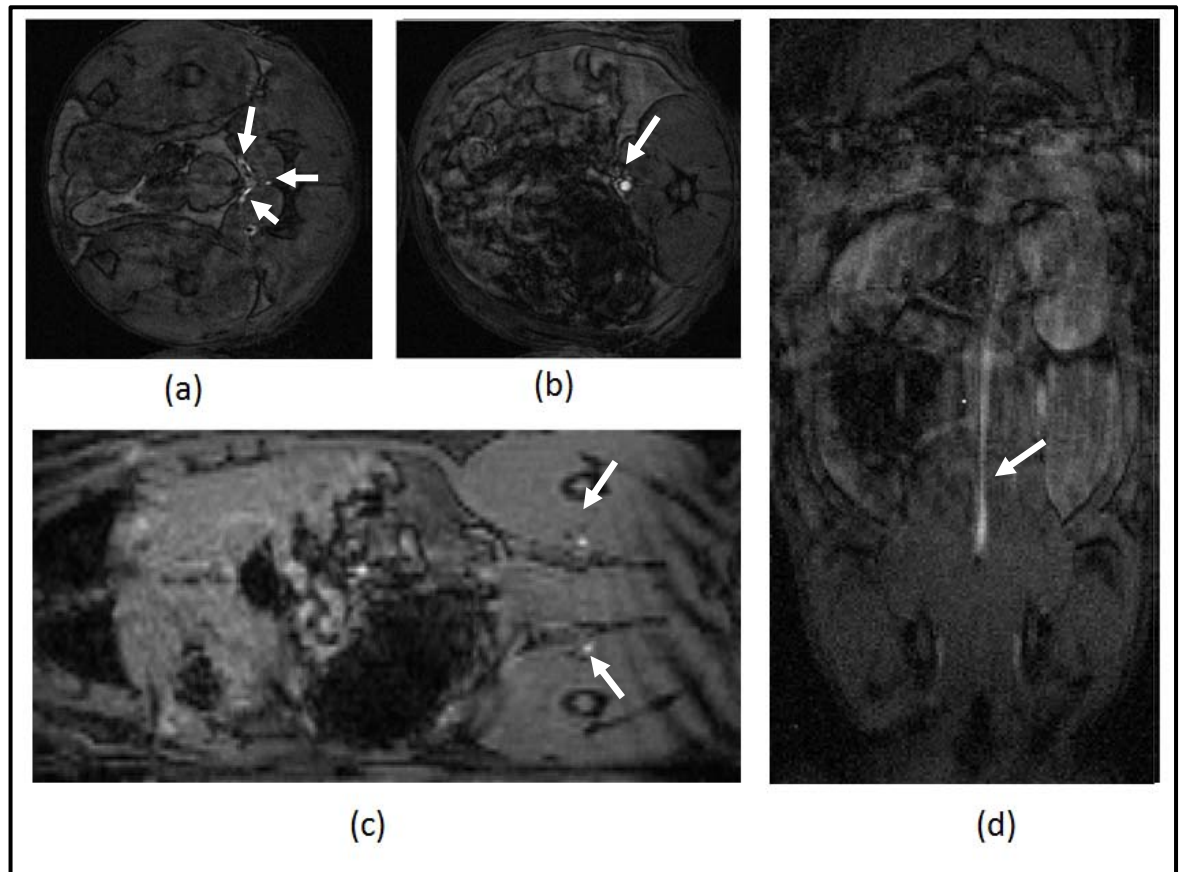


*Figure 4-4 MRI images for rat using MRI-4.7T illustrating (a) cross-sectional image showing the iliac bifurcation, (b) the abdominal aorta, (c) the longitudinal section illustrating the right and left femoral arteries and (d) the abdominal aorta*

As previously mentioned, the measurement of blood pressure waveform was used as an outlet boundary condition in the CFD/FE analysis. The relationship between arterial blockages at the abdominal aorta and arterial stiffness was analysed and validated in the CFD/FE models (Section 4.6) by investigating how any change to abdominal aorta diameter affected systolic pressure, diastolic pressure and AI.



#### 4.4.1.2 Experimental Setup

The setup for the *in vivo* experiment is illustrated in Figure 4-5. Firstly, Lab Chart was set up and the blood pressure transducer calibrated to mmHg units; the rat had already been anaesthetised, by this time.

The instruments used in this experiment were:

- 1- Computer- for connecting Lab Chart and recording the measured data.
- 2- Lab Chart amplifier from PowerLab Ltd (Electric Strength tests up to  $6.6\text{kV} \pm 1\%$  of reading and above  $6.6\text{kV} \pm 3\%$  of reading).
- 3- Voltage Transducer (sample rate 5-10 KHz) made by the University of Auckland Faculty of Medical and Health Sciences.

<http://www.adinstruments.com/solutions/research/applications/blood-pressure-intravascular#method>

- 4- Blood Pressure mercury device for calibration (Accosson Sphygmomanometers).
- 5- Catheter. (BD Vialon<sup>TM</sup> Insyte 8360515, F1754-4 B(9-09) made in USA) 24GA 0.75IN.
- 6- Surgical Equipment (operating scissors, straight, sharp blunt, needle holder, forceps (curved and straight) and rodent cannulate kit).

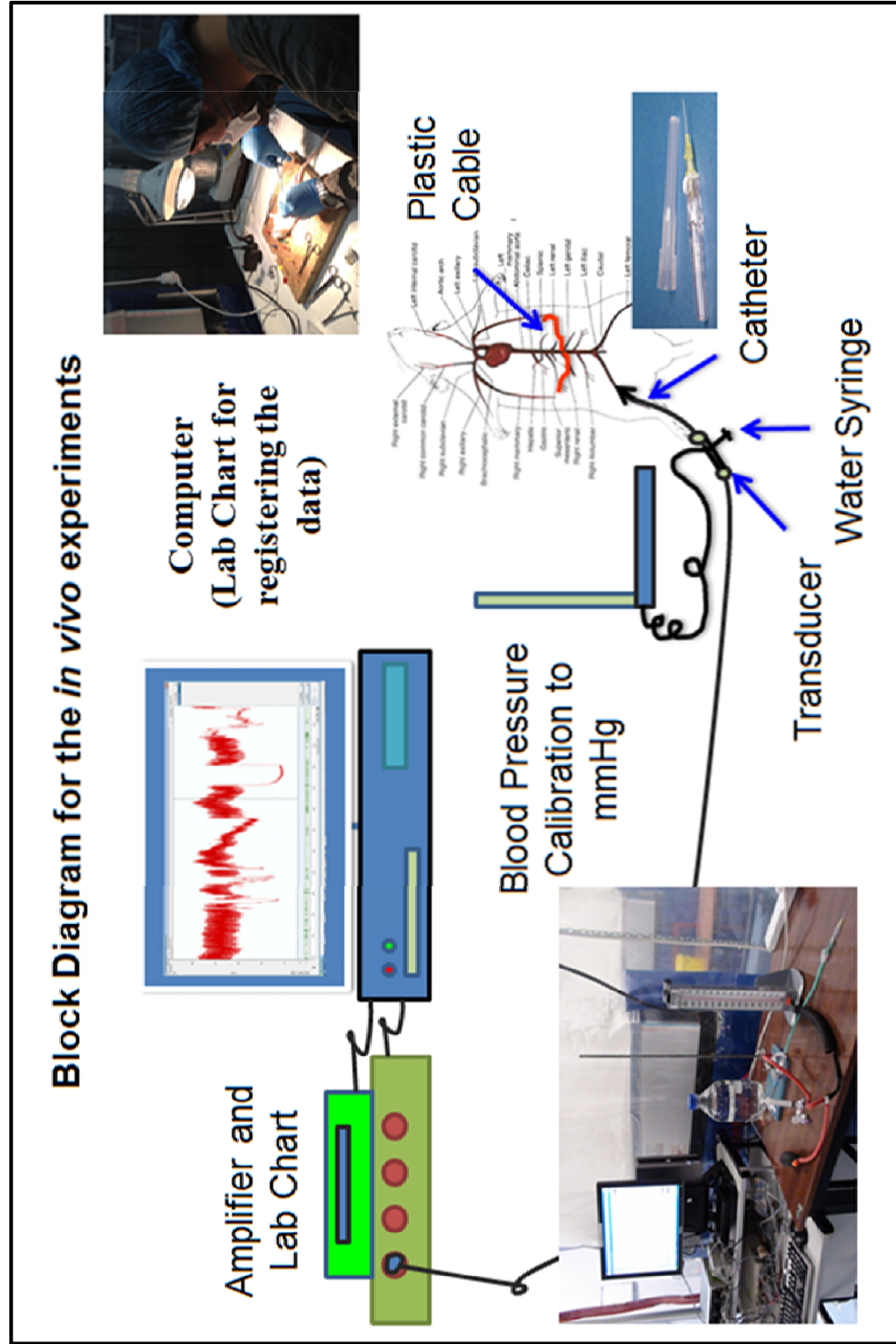
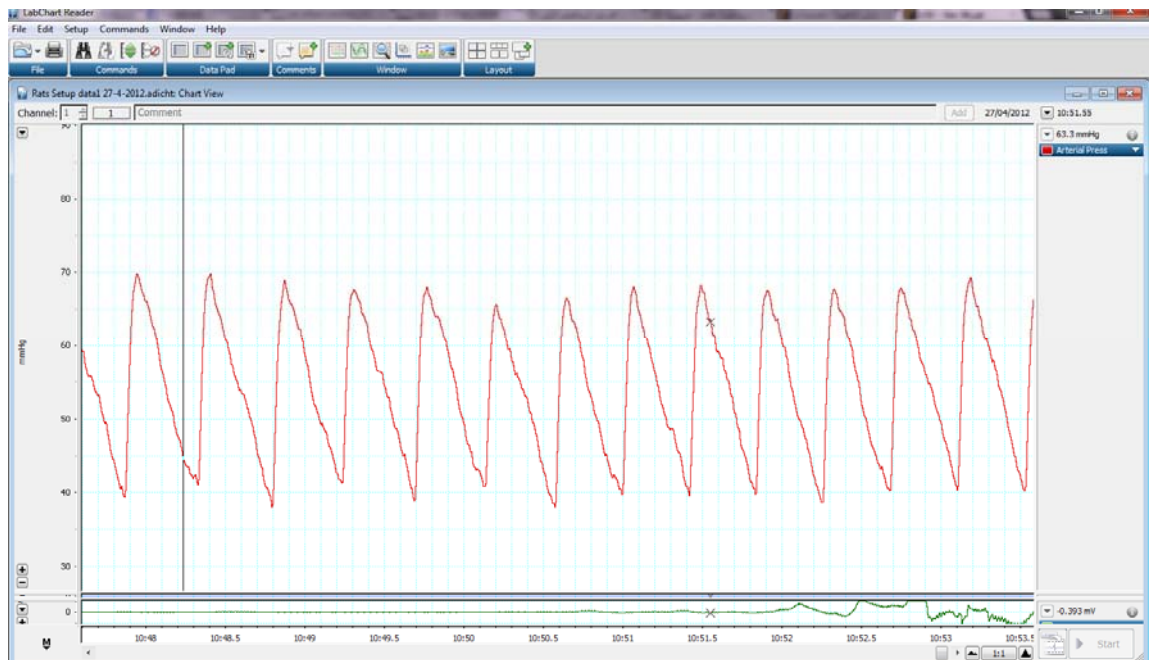


Figure 4-5: Block diagram of the experimental set up to perform *in vivo* experiments on rats

#### 4.4.1.3 Measurement Data

This section presents the data collected from the experiments; the material properties (Young's Modulus) and the blood pressure pulse wave.

The *in vivo* experiments consisted of measuring blood pressure at the abdominal aorta and the right femoral artery. Blood pressure was measured in both healthy and unhealthy conditions in the same specimen using the transducer through the catheter. This was an invasive measurement and was used as the outlet boundary condition for validating the CFD/FE model. Lab Chart was used to record blood pressure as shown in Figure 4-6. Figure 4-7 shows the blood pressure measurements for one rat in a healthy condition (P-H) and four different unhealthy conditions (P-U) measured invasively at the right femoral artery.



*Figure 4-6: The Lab Chart viewer showing the calibrated blood pressure measurement in mmHg*

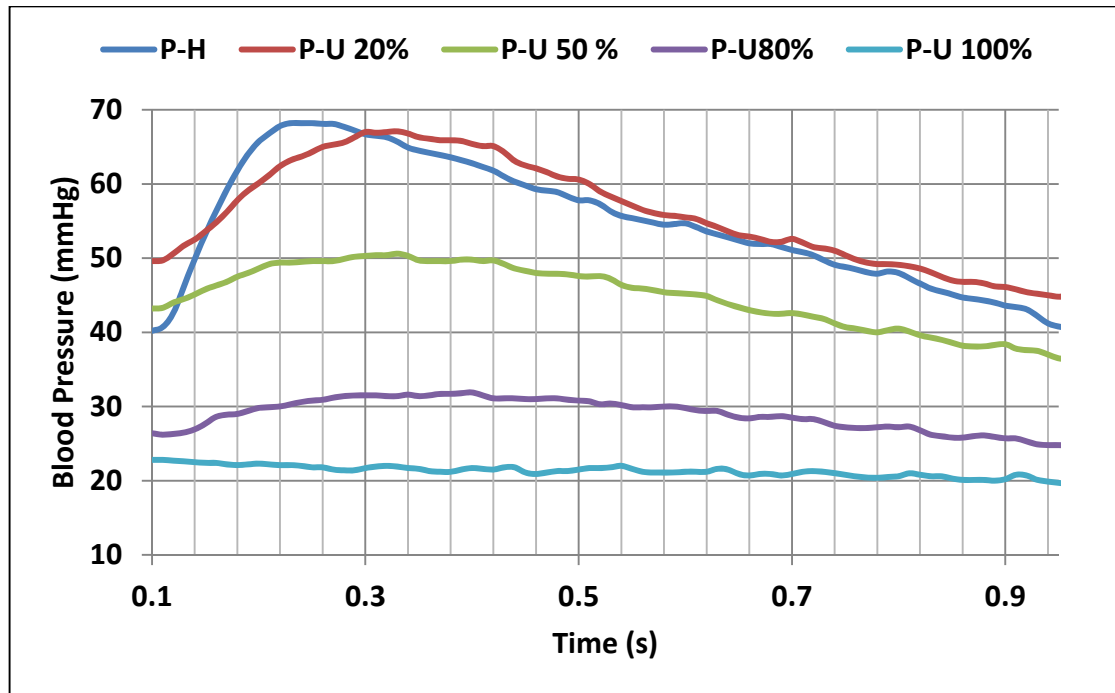
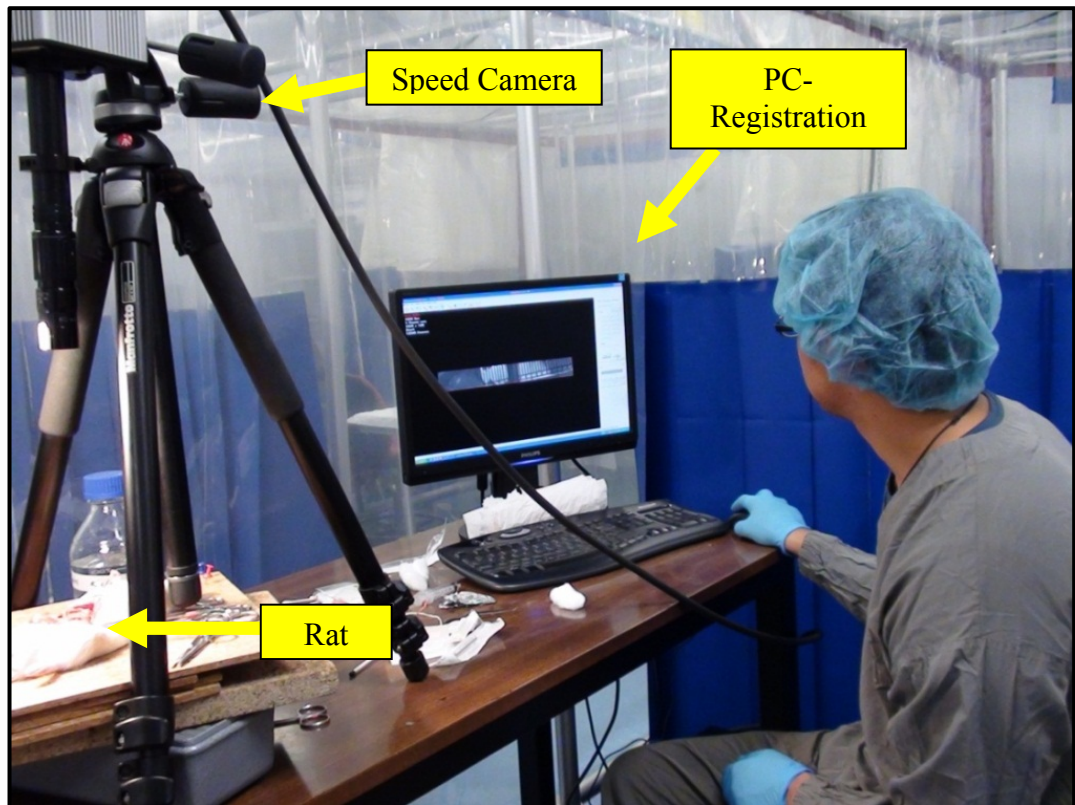


Figure 4-7: Blood pressure for a healthy specimen and four different arterial blockages representing the unhealthy conditions for the same rat (P-H: healthy blood pressure) and (P-U: unhealthy blood pressure) taken at the right femoral artery

**High Speed Camera Technique:** In addition to blood pressure waveform measurements, an arterial wall deformation was measured using a high-speed camera technique performed *in vivo* while simultaneously measuring blood pressure, as shown in Figures 4-8, 4-9 and 4-10. Figure 4-10 shows the speed camera software which has an application to measure arterial wall deformation using a pixel measurement; the scale is 1 pixel to 0.02 mm. This measurement is essential to the CFD/FE model's material properties as a realistic simulation of the non-linear material properties of the experiment. This enables our model to accurately reflect the non-linearity of the arterial wall which many studies have missed in their modelling processes, resulting in those studies [35-41] having some unrealistic assumptions.



*Figure 4-8: Setup of the speed camera for measuring the deformation of the arterial wall*

The deformable radius of the artery wall is located with the speed camera using the zoom-in technique. This was then calculated with the strain equation (4-1) and correlated to the stress equation (4-2) which is calculated from the blood pressure, as shown in Figures 4-9 and 4-11. All of the data was measured invasively and simultaneously with the pulsatile blood pressure waveforms. The calculation is validated against Rentschler et. al. (2008) [121] and shows good agreement. This measurement has been implemented as a Young's modulus curve between the stress and strain in the FE model (material set up) of the artery wall, as having non-linear material properties affecting the arterial wall deformation and compliance.

$$Strain = \frac{\Delta r}{r} \quad (4 - 1)$$

$$Stress = \frac{Pr}{2t} \quad (4 - 2)$$

where  $r$  represents the original radius of the artery which was measured from MRI experiments and evaluated with the microscopic measurement (Section 4.4.2).  $\Delta r$  represents the deformation of the artery wall.  $P$  represents systolic blood pressure measured at the abdominal aorta and  $t$  represents the thickness of the artery wall. The calculation of Young's Modulus was conducted at the abdominal aorta for the healthy condition (at the location where the disease was to be created) by Equation (4-3) as shown in Figure 4-9.

$$Young's\ Modulus = \frac{Strain}{Stress} \quad (4 - 3)$$

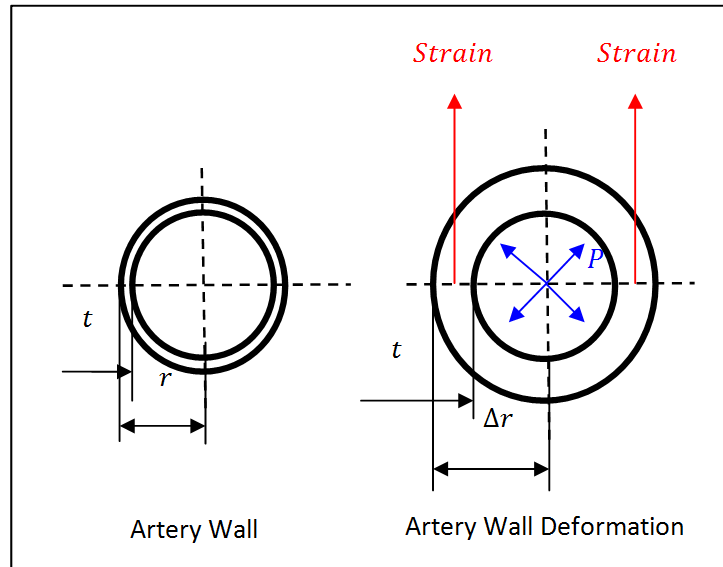


*Figure 4-9: Artery wall deformation for systolic and diastolic pulse and the stresses affecting the artery wall.*

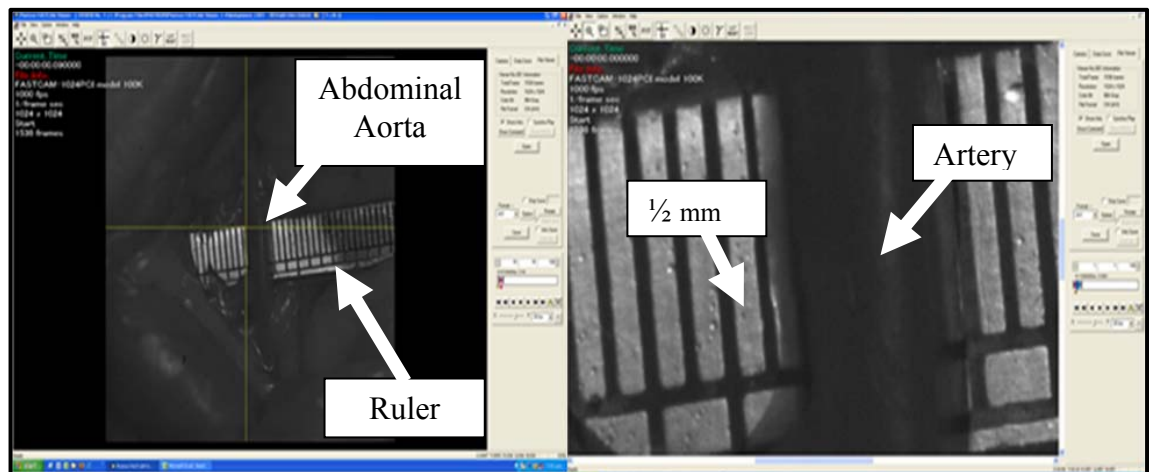


Figure 4-10: Speed Camera Technique for measuring deformation of the arterial wall in vivo experiments

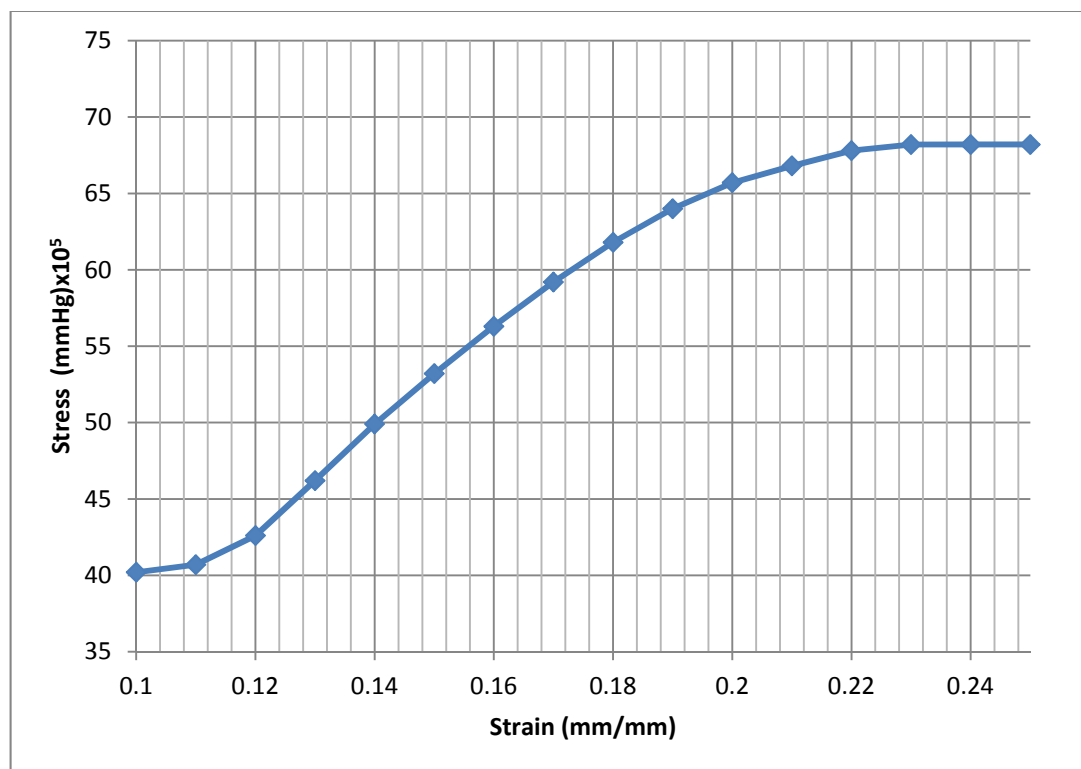


Figure 4-11: Stress vs Strain for the artery wall at the abdominal aorta



#### 4.4.2 *In vitro* Investigations

The *in vitro* experiment was based on taking a cross-section of the abdominal lumen in order to investigate the dimensional parameters for the artery wall. A microscopic technique was used to accurately determine the dimensional parameters of the abdominal aorta geometry, such as the inner and outer diameters, length and thickness. After completion of the *in vivo* experiments, the rat was further investigated by measuring the length and diameters of the abdominal aorta, iliac bifurcation, left and right femoral arteries. This data was then used to create the idealized geometry using the CFD/FE methods. Simulation of the geometry and its results were then validated and compared against the *in vivo* blood pressure measurements. The abdominal aorta measurements were undertaken using the microscopic study for the same randomly selected rat as shown in Figure 4-12. This figure shows the *in vitro* measurement for the descending aorta, abdominal aorta and right femoral artery. Figure 4-12 and Table 4-2 show the diameter, thickness and the length of the arteries.

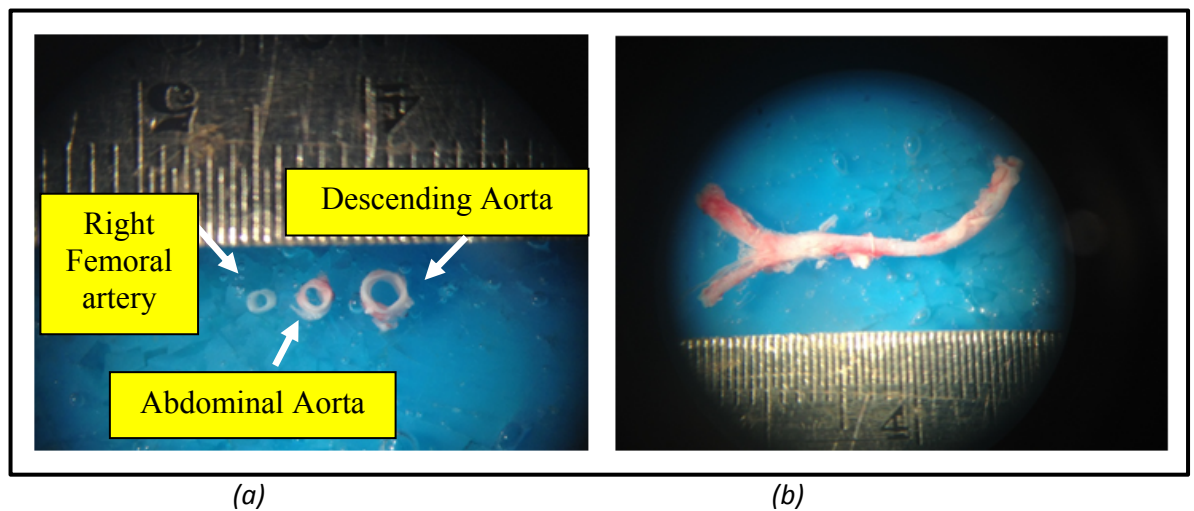


Figure 4-12: The *in vitro* measurement of (a) the descending aorta, abdominal aorta and right femoral artery in cross section and (b) the whole aortic body



Table 4-2 The measured *in vitro* data

Location	Diameter D (mm)	Thickness t(mm)	Length L (cm)
Abdominal aorta	1	0.1	0.5
Iliac Bifurcation	1	0.1	0.5
Right femoral	0.6	0.09	0.5
Left femoral	0.6	0.09	0.5

## 4.5 Computational Modelling

The CFD/FE methods for modelling arteries, discussed in detail in Chapter 3, are implemented in this chapter to investigate any narrowing in the abdominal aorta which affects blood pressure measurements at the right femoral artery. The investigated geometry in this section is the abdominal aorta, iliac bifurcation and the right and left femoral arteries. A healthy 3D model was simulated by ANSYS® 14.0 a with the two-way FSI approach, based on *in vivo* and *in vitro* measured data as described in Section 4.4. Four unhealthy 3D models were simulated computationally with each one representing a different severity of arterial blockage at the abdominal aorta (20%, 50%, 80% and 100% severities).

### 4.5.1 Abdominal Aorta Geometry

The data for constructing the rat geometry was gained from *in vivo* and *in vitro* experiments for 10 healthy specimens described in section 4.4. The modelling of those geometries is divided into two main parts. The first part represents the abdominal aorta geometry which is considered a solid body (artery wall) with non-linear material properties and is modelled using FE methods in the Transient Structure Mechanic (TSM). The second part represents the blood flow modelled and interpreted based on CFD methods.

#### 4.5.1.1 Transient Structure Mechanic

The mechanical modelling for the artery wall was performed by solving the FE method for analysing and preparing the model to be connected to the CFD model. This connection was implemented as a two-way FSI approach.

Figure 4-13 shows the flow chart for aorta modelling using the mechanical structure modelling process. The mechanical modelling was performed using ANSYS® 14.0 [90]. The TSM were based on setting the mechanical properties for the artery wall [9] (this will be discussed in Section 4.5.3). Then the second step was to unsuppress the blood body (blood flow) to keep the aorta body (aorta wall) isolated so as to apply mesh generation methods which are explained in more detail in the next section (4.5.2 Mesh Generation). The next step was setting the FSI and the fixed ends of the inlets and outlets of the aorta geometry. TSM's tools were used to set the FSI location and set the transient initial conditions and analysis support. The analysis support was essential to control the steps of the simulation which work in parallel with the computational fluid CFX's tools [90]. The aorta model was initially solved as being in a steady state condition by setting the number of steps to 1, current step 1, step end time 1s using a number of substeps 1. The results from the steady state were used as the initial condition to solve the transient model and boundary conditions which were gained from *in vivo* and *in vitro* trials and literature data [8, 9]. The TSM model was connected to the CFX model to analyse the effect of aorta shape and deformation on blood flow, using the FSI scheme. After finishing TSM modelling, different scenarios could be modelled, for example changing the material properties of the artery wall and dimensions (compliance) of the geometry to predict cardiovascular diseases.

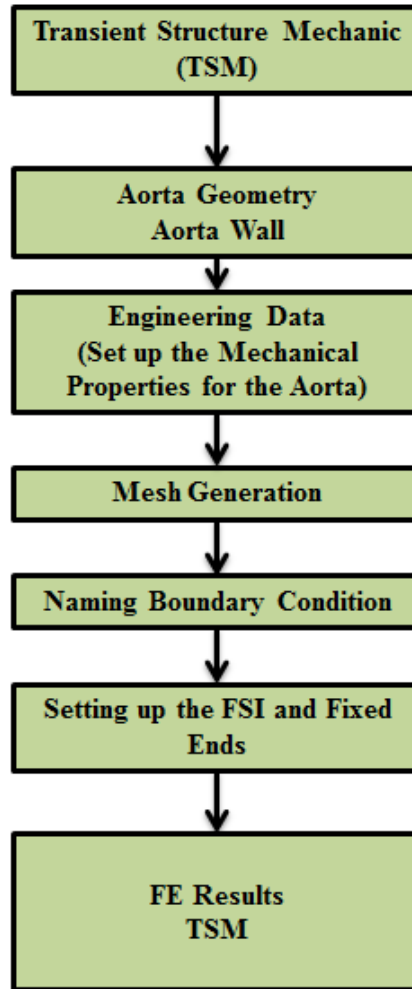


*Figure 4-13: Flowchart of the Transient Structure Mechanic (TSM)*

Arterial blockage conditions located at the abdominal aorta is indicated for four different severities; 20%, 50%, 80% and 100% of the lumen diameter. These unhealthy severities are compared with the healthy condition of 0% (no blockage).

Figure 4-14 shows the constructed models for the healthy abdominal aorta and the four unhealthy models. These models are developed based on the experimental model results starting with a healthy abdominal lumen diameter of 1 mm and decreasing it to 0.8, 0.5, 0.2 and 0 mm according the severities created in the surgical procedure.

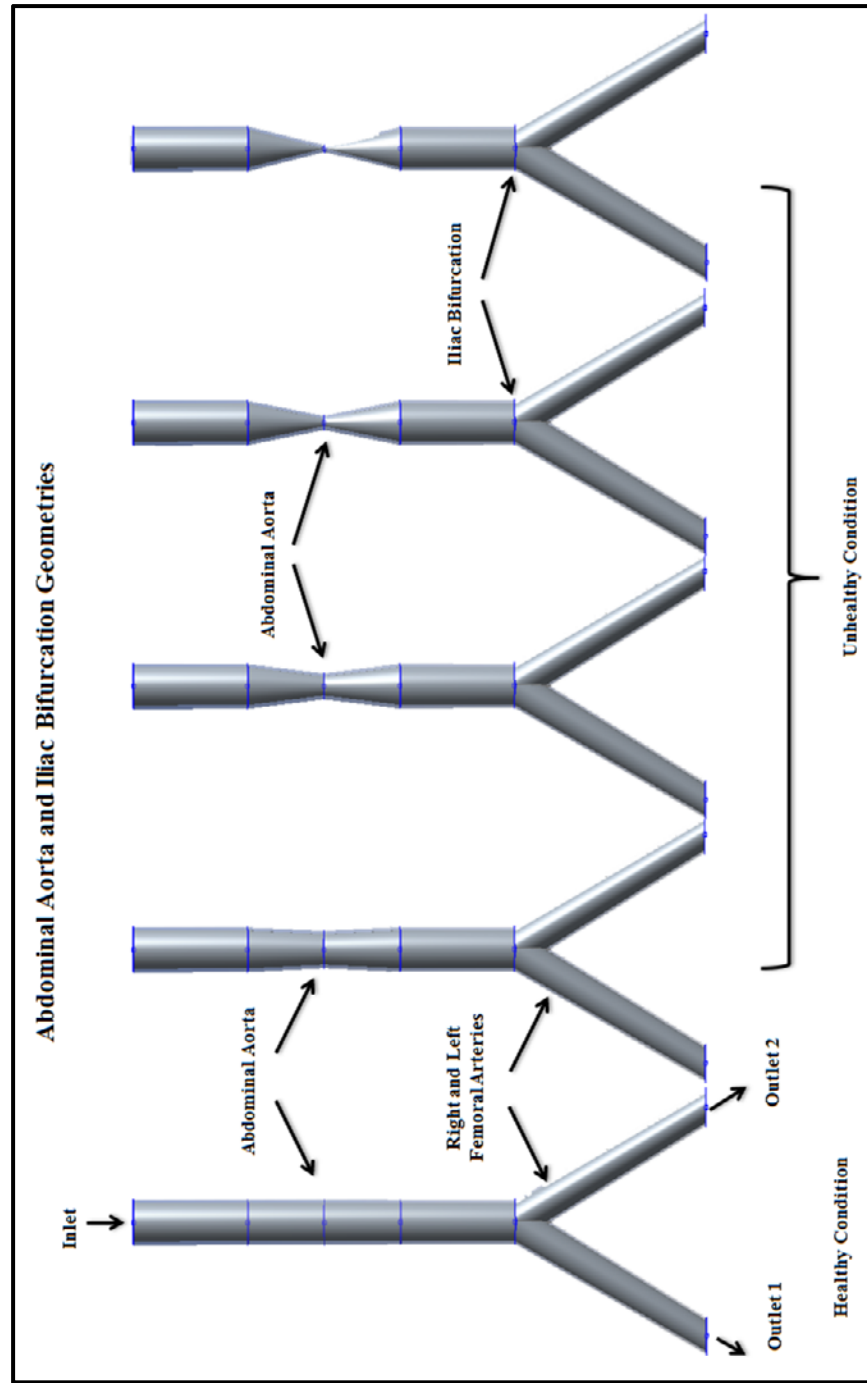
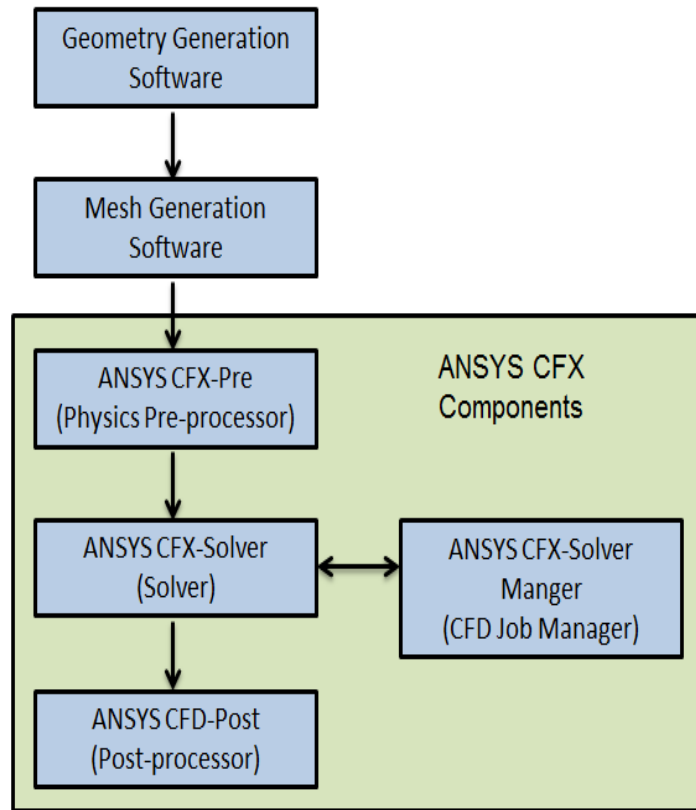


Figure 4-14: Abdominal aorta, iliac bifurcation and femoral arteries in healthy and unhealthy (20%, 50%, 80% and 100%) conditions

#### 4.5.1.2 Computational Fluid Dynamic

CFD with CFX are used to analyse difficult geometries with an existing component and lead to an improved reconstruction of the geometry. Figure 4-15 shows the flowchart of ANSYS®14.0 modelling which includes the analysis and solving of CFD problems using CFX's tools according to the following steps:

- 1- Geometry Generation: construct the geometry and suppress the fluid body.
- 2- Mesh Generation: after suppressing the fluid body, rename the fluid wall, inlet and outlets and choose a suitable method to mesh the fluid body [90].
- 3- ANSYS CFX-Pre 14.0: set up the default domain; the initial conditions, boundary conditions, the material properties of the blood flow, the interaction (FSI), type of the analysis (steady or transient), and fluid model, including shear stress transport (SST), laminar or *K-Epsilon* options [90].
- 4- ANSYS CFX-Solver: set up the solver control to solve the problem using Second Order Backward Euler equations (see Appendix I) for the transient model [90]. Also, set up the maximum and minimum iterations [90]. The output control is used to set the transient results; the total mesh displacement, pressure, velocity and WSS. The CFX solver is also used to monitor coefficient loop convergence; the total mesh displacement and the force in any direction which affect the FSI wall.
- 5- ANSYS CFD-Post 14.0: is used to provide state-of-the-art interactive post-processing graphics tools to analyse and present the ANSYS CFX simulation results [90]. This is presented in terms of quantitative post-processing, report generation, command line and generation of a variety of graphical objects [90].



*Figure 4-15: Flowchart structure of ANSYS CFX [90]*

The CFD modelling steps for analysing the aorta blood body are shown in Figure 4-16 and explained as follows:

- 1- After constructing the aorta geometry bodies (solid and fluid) using DM as discussed in Section 3.2, they are imported into CFX and the solid body is unsuppressed to site and rename the inlet and outlets of the fluid body.
- 2- Mesh generation is performed using the Sweep method by solving FV equations for meshing the blood body and using some techniques (as discussed in the next section) to improve the mesh quality.
- 3- CFX allows for the set up of the initial and boundary conditions such as a velocity waveform as an inlet and a pressure waveform as an outlet.
- 4- Set up FSI model and equations for the aorta wall and the blood flow body [90].

- 5- Set the time iteration and convergence of the solution [90]. This step is repeated many times in the case of any update.
- 6- CFD pressure results are exported to the TSM to see the effect of the FSI model on the artery wall.

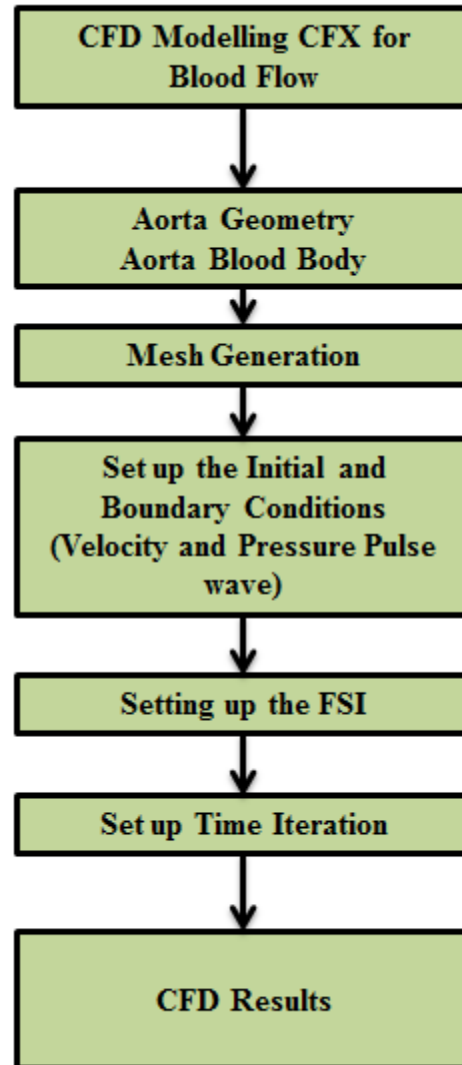


*Figure 4-16: Flow chart of Computational Fluid Dynamic method using CFX*

#### 4.5.2 Mesh Generation

Mesh generation of both the artery wall and the blood flow models is performed using the Patch Independent method. The number of elements and nodes in the abdominal aorta geometry for those models are: elements of range (145,359- 147,368) and nodes of range (240,386- 240,456). However, the blood geometries are meshed with elements of range (54,190- 56,195) and nodes of range (23,252- 24,747) as shown in Figure 4-17. The skewness feature, available within ANSYS® 14.0, is used to check and assess the mesh quality [90]. Skewness is a measure of the relative distortion of an element compared to its ideal shape and is scaled from 0.0 - 1.0, where a Skewness measure of 0.0 is excellent and 1.0 is unacceptable [90]. In the present models, the skewness shows a quality value range with a maximum accepted values of 0.73 from 0.85.

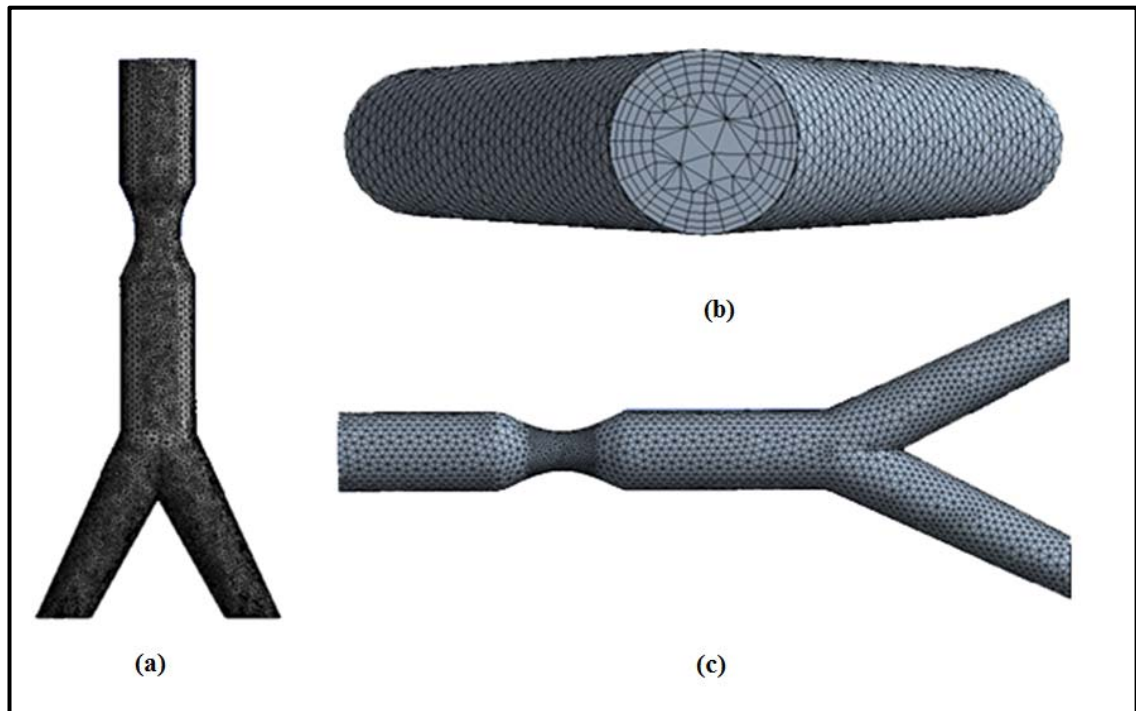


*Figure 4-17: 3D model of unhealthy abdominal aorta (a) the artery wall and (b) the blood body (top view) and (c) the side view of the blood body*



### 4.5.3 Material Properties and Boundary Conditions

The healthy abdominal aorta is modelled with non-linear properties measured invasively as described in Section 4.4. The Young's modulus was measured experimentally as shown in Figure 4-11, the Poisson's ratio ( $\nu=0.45$ ) and density  $\rho=1050 \text{ Kg/m}^3$  [9]. The inlet and outlet boundary conditions were assumed to be blood pressures which were measured invasively as seen in Section 4.4.1.

### 4.5.4 Fluid-Structure Interaction

In the FSI solving process, the fluid equations (which are described in Chapter 3 from Equation 3-2 to 3-9) and the solid equations (which are also described in Chapter 3 from Equation 3-13 to 3-16) are solved individually at each time step [90]. This means that the fluid model is solved with the latest displacement and velocity conditions provided by the solid part of the last time step. The obtained stress and pressure measurements are employed as boundary and loading conditions for the structure model used in the next time step. These two steps will be repeated until the final time step is reached [90].

ANSYS<sup>®</sup> application supports the two types of FSI approaches:

One-way FSI: The resultant blood pressure from the blood flow in the CFD analysis at the FSI is applied as a load for FE analysis [90]. The artery wall displacement from the FE analysis is not passed back to CFX analysis; that is, the result from the deformation of the artery wall is not considered to have a significant impact on blood analysis [90].

Two-way FSI: In this approach the results of the artery wall FE analysis are transferred to the CFX blood flow analysis as a load. Similarly, the results of the pulsatile blood flow and pressure analysis are passed back to the FE analysis as a load on the FSI

surface [90]. The analyses continue until overall equilibrium and divergence of the solution between the FE and CFX analysis are reached, as shown in Figure 4-18. Two-way FSI is only supported between ANSYS® and CFX solvers [90].

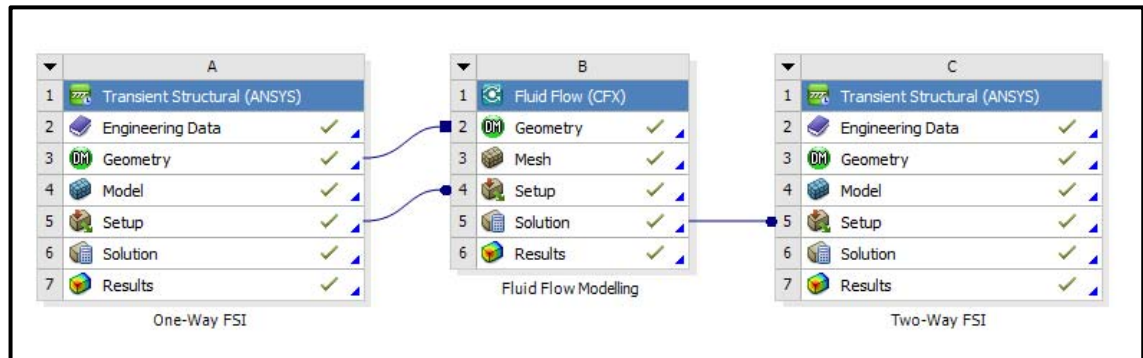


Figure 4-18: Two-way FSI using ANSYS® 14.0 [90]

## 4.6 Validation and Results

The models were analysed from a 3D geometrical form using CFD/FE methods. This section presents the results of the clinical experiments and the CFD/FE models.

### 4.6.1 In vivo Results

Blood pressure measured at the abdominal aorta for four healthy rats is shown in Figure 4-19. This figure shows blood pressures for four different rats of weights (300-350g). These data will be used for validating the CFD/FE results.

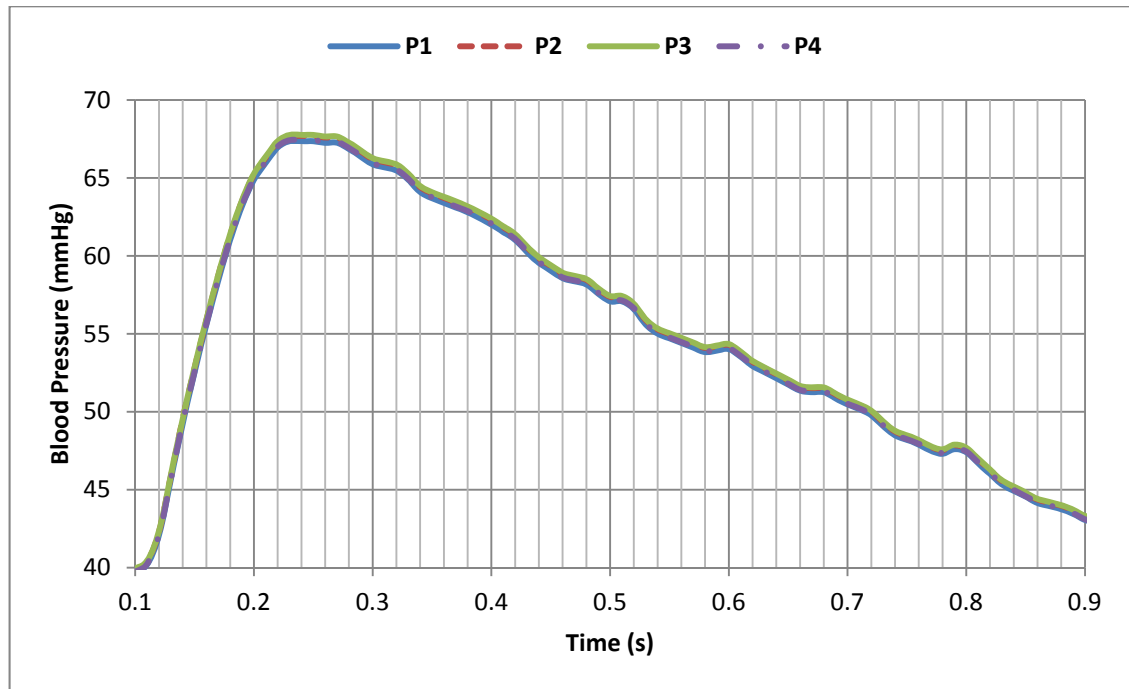
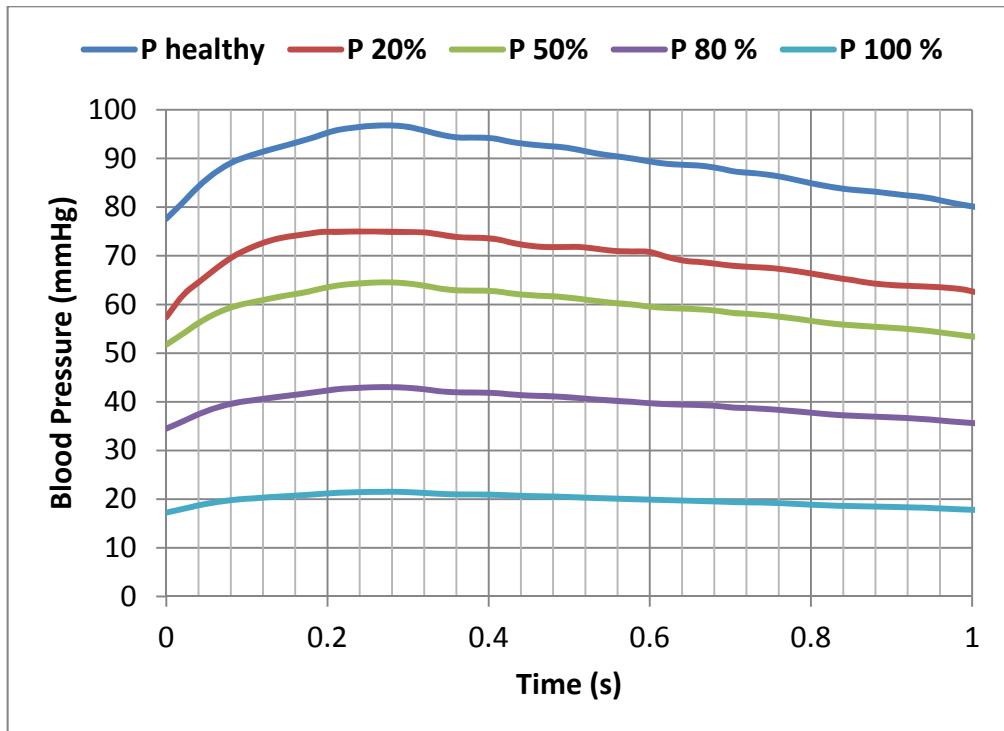
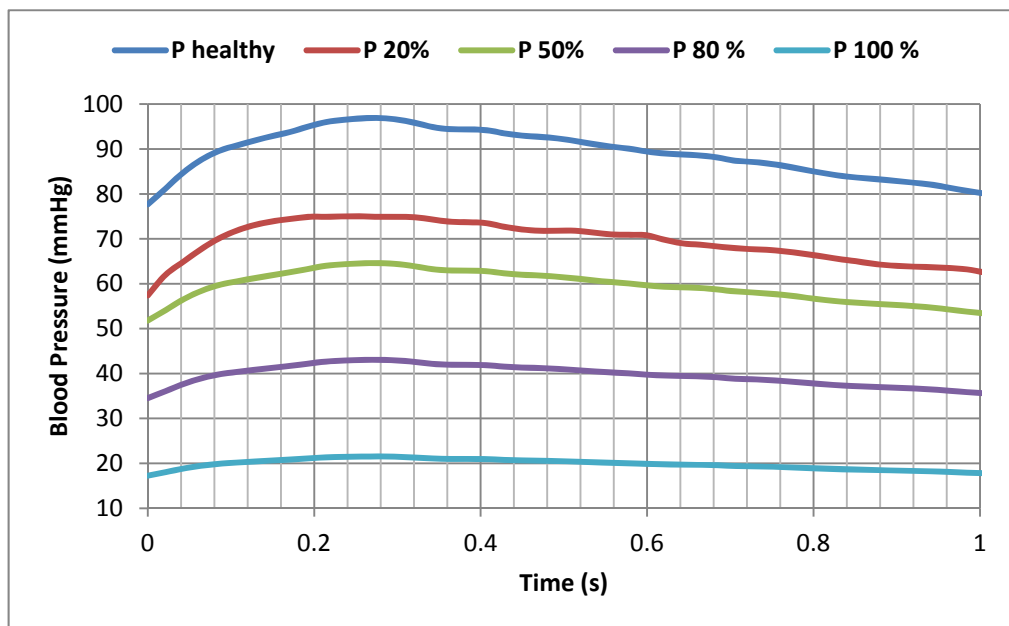


*Figure 4-19: Blood pressure at the abdominal aorta for four different rats in a healthy condition, using a catheter method*

Blood pressure is also measured at the right femoral artery for 10 rats of a weight between 300-350g, in both healthy and unhealthy conditions. The unhealthy conditions represent the four different arterial blockages as shown in Table 4-1. Figure 4-20 shows blood pressure measured invasively at the right femoral artery for one rat in both healthy and unhealthy conditions. This measurement is repeated for the other nine rats, and shows the same observed change, that blood pressure is affected by changes in arterial compliance/stiffness at the abdominal aorta.



(a)



(b)

Figure 4-20: The healthy blood pressure and four unhealthy blood pressures measured invasively at the right femoral artery for rats weighing (a) 350g and (b) 300g

#### 4.6.2 CFD/FE Results

The results of blood pressure equations at the abdominal aorta from CFD/FE simulation agree very closely (0.94 % error) with the invasive data collected from the *in vivo* measurements for healthy rats as shown in Figure 4-21. The main reason for this would be the realistic control boundary conditions assumed in the CFD/FE modelling.

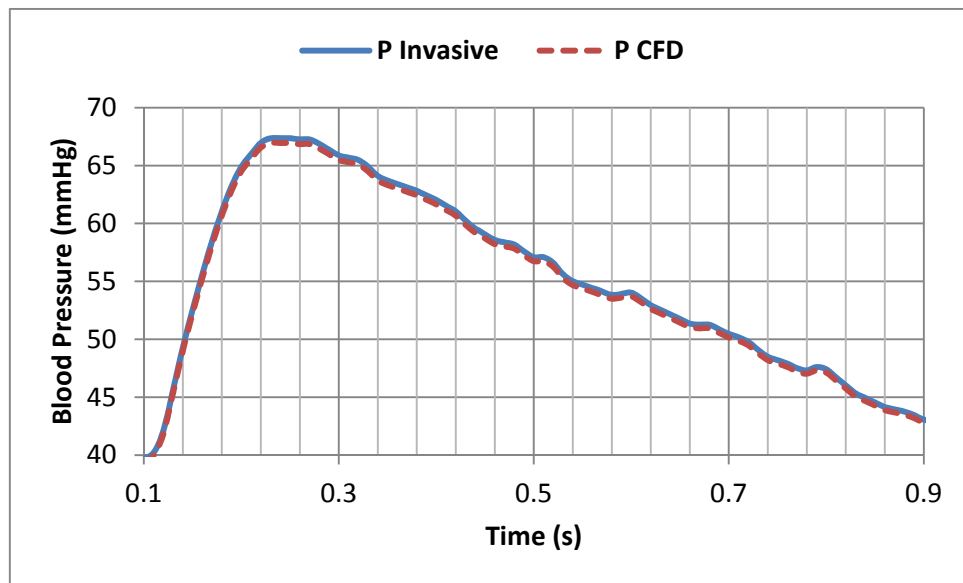
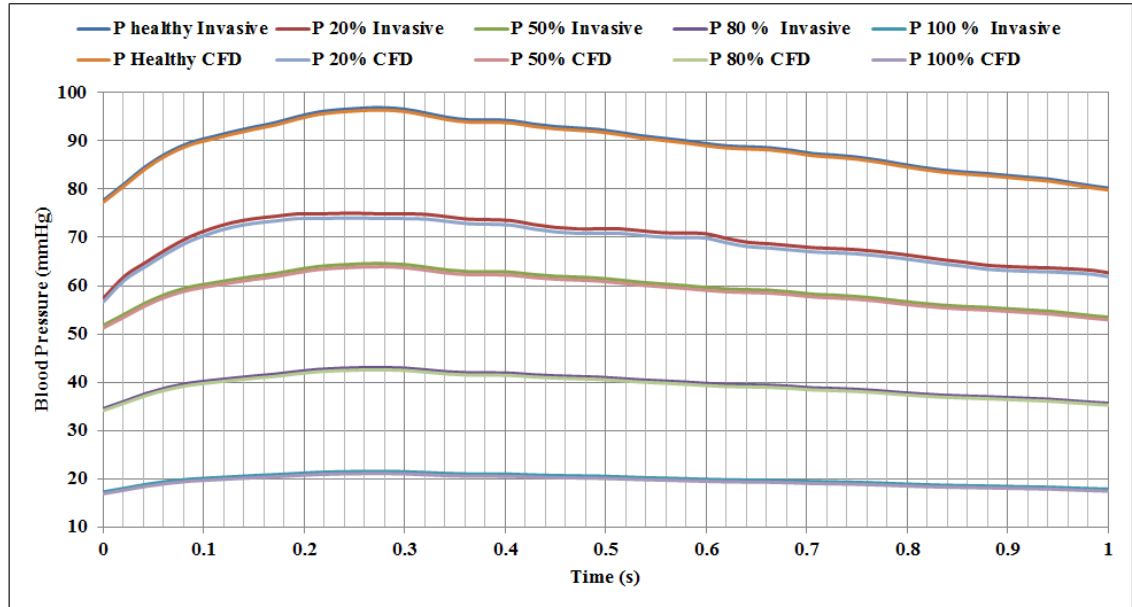


Figure 4-21: Blood pressure measured invasively at the abdominal aorta compared to the CFD/FE results

Figure 4-22 shows a comparison between the CFD/FE results and the *in vivo* data measured at the right femoral artery. These pressure wave propagations are affected by the degree of arterial blockage created at the abdominal aorta. These results show that decreasing the diameter of the abdominal lumen will result in decreasing systolic and diastolic blood pressure, due to the increase in kinetic energy and reduction in pressure. In addition, these results show that arterial compliance is related to propagated pressure wave forms. This will be correlated and discussed in more detail in Chapter 6.



*Figure 4-22: The blood pressure at the right femoral artery for both the simulated (CFD) simulation results and the in vivo experiments(Invasive)*

Results calculated of blood pressure at the arterial blockages are determined using the CFD/FE model which was based on realistic assumptions and clinical data. Figure 4-23 shows the CFD/FE results at the abdominal aorta for the four arterial blockages for a 300g rat.

The results of the measured data at the abdominal aorta and the right femoral artery will be formulated to establish and develop a new method of diagnosing arterial blockages. This will be discussed in detail in Chapter 6.

The AI is a ratio calculated from the blood pressure waveform and indicates the wave reflection and arterial stiffness as shown in Equation 4-4 [9].

$$AI = \frac{P_s - P_i}{P_s - P_d} * 100 \quad (4 - 4)$$

where  $P_s$  represents the systolic pressure (the maximum peak of the pulse wave),  $P_d$  represents the diastolic pressure (the minimum value of the pressure) and  $P_i$  represents the inflection pressure which indicates the merging of the forward and backward pulse waves as discussed in Chapter 2 (Section 2.2, Figure 2-2). In this study, the AI is investigated at the abdominal aorta for two groups of rats. The first group, weighing between 310-350g, and the second group weighing between 270-300g, are simulated with four different severities of arterial blockages of (20%, 50%, 80% and 100%) as shown in Figure 4-24. At full blockage the abdominal aorta delivers no blood flow, completely impeding oxygen flow to dependent organs.

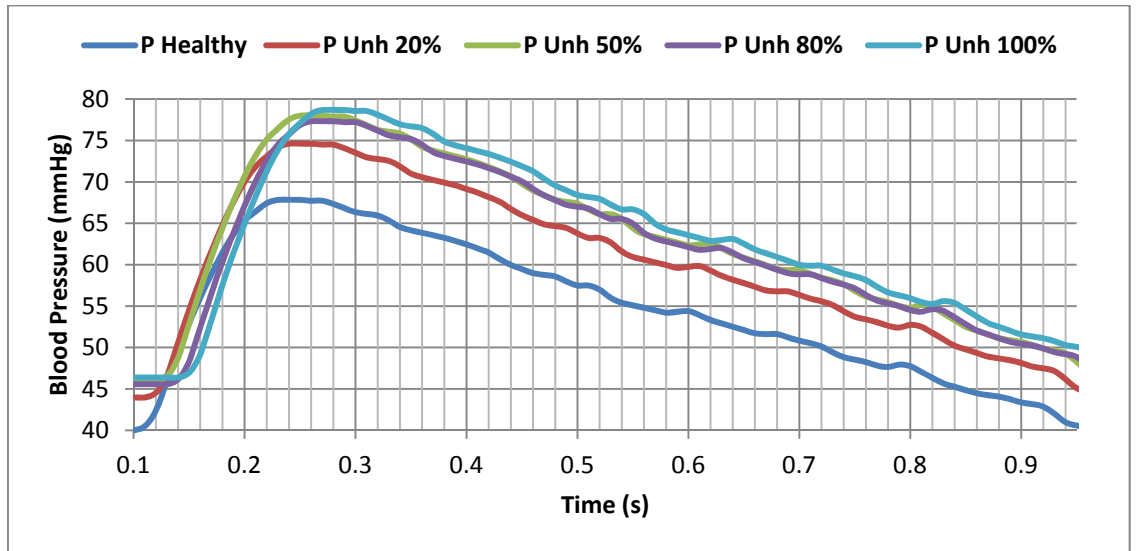
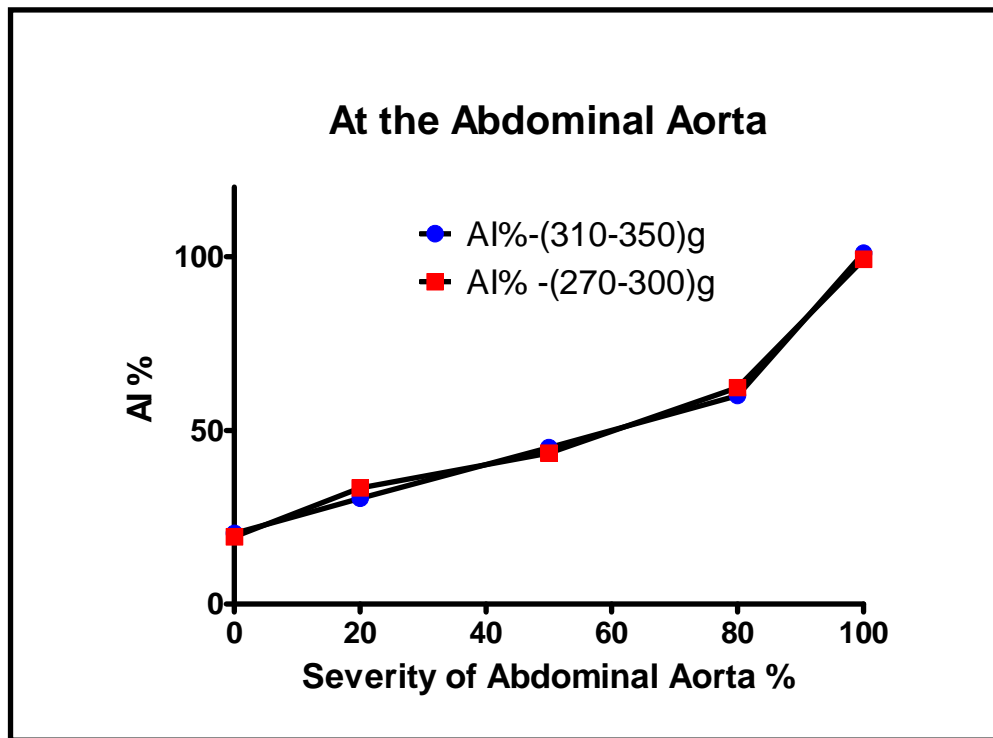


Figure 4-23: Blood pressure at the abdominal aorta for four arterial blockages compared with a healthy condition for a 300g rat from CFD/FE results ( $P$ = Pressure and  $Unh$ =Unhealthy)



*Figure 4-24: Augmentation Index (AI %) at the abdominal aorta for a group of rats 310-350g and a group 270-300g*

The development of arterial blockages starts with the deformation of atherosclerosis lesions at the abdominal aorta. This results in disturbance in blood flow and normal hemodynamic stresses attack the artery wall. Hemodynamic stresses can play an important role as a localizing factor in atherosclerosis.

The WSS and CS are determined and investigated at two locations using CFD/FE modelling with the two-way FSI scheme. Figures 4-25, 4-26 and 4-27 show the WSS and CS for an arterial blockage of 50% at both locations (a) the abdominal aorta and (b) at the right femoral artery. The result shows that the CS is shifted at the right femoral artery and this requires thorough investigation into the SPA. This could be correlated to the development of the arterial blockages, as will be discussed in Chapter 6.



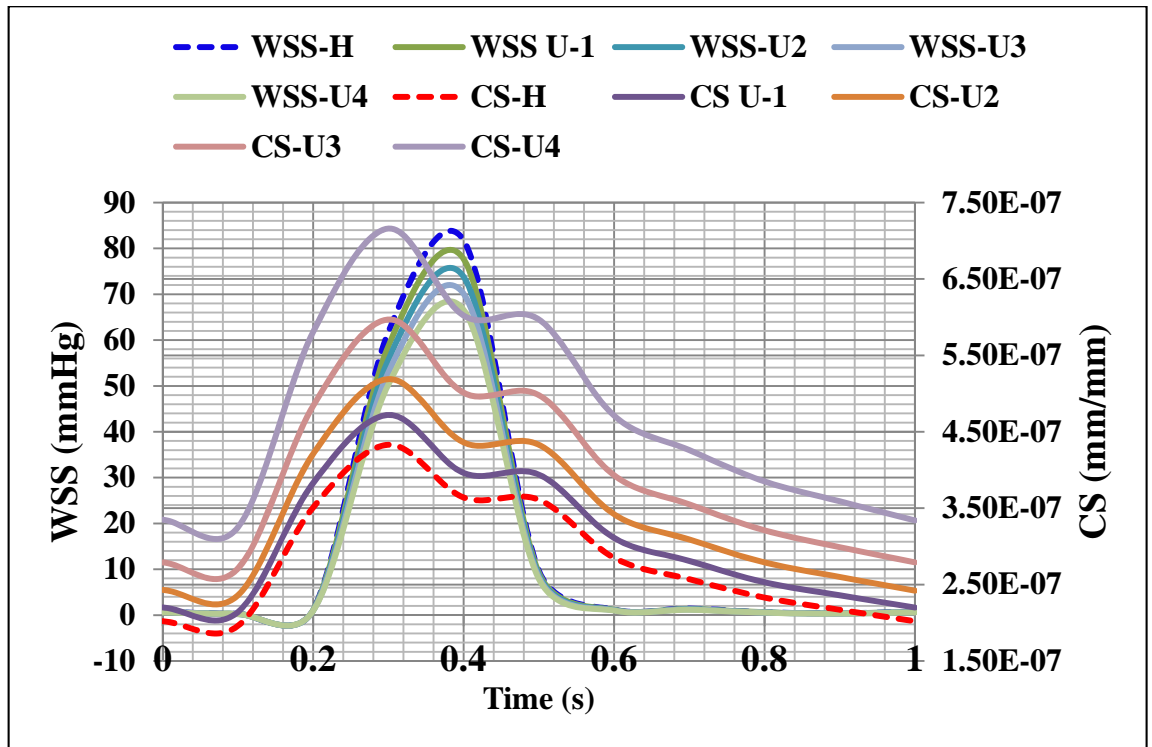


Figure 4-25: WSS and CS for 50% Arterial blockage at (a) the abdominal aorta and (b) the right femoral artery [H= Healthy and U=Unhealthy]

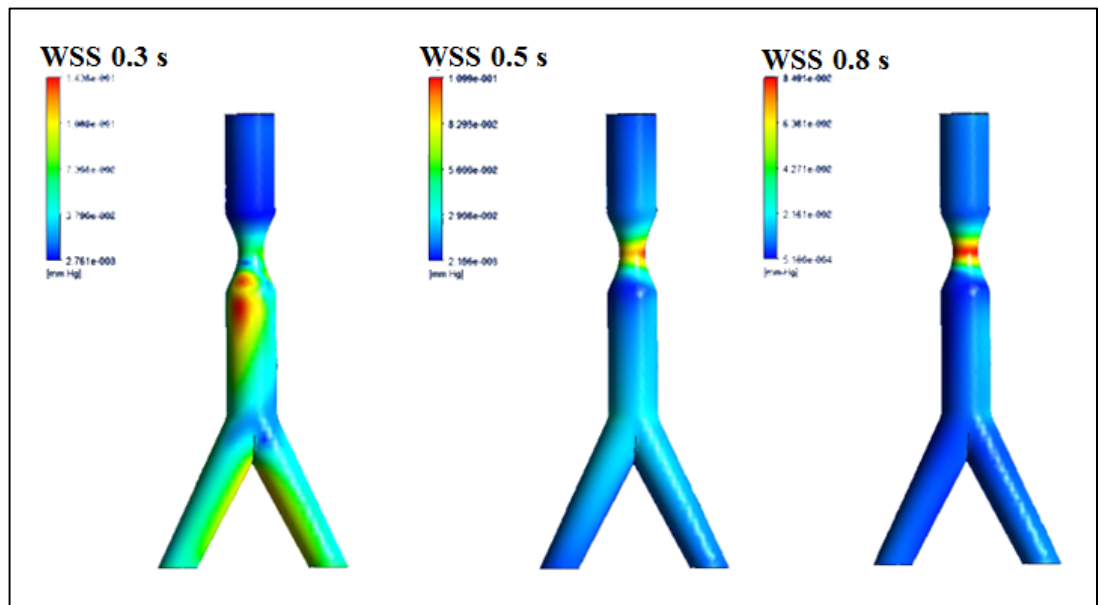


Figure 4-26: WSS for the FSI for atherosclerosis of 50% severity at the abdominal aorta at different times (0.3, 0.5 and 0.8s)

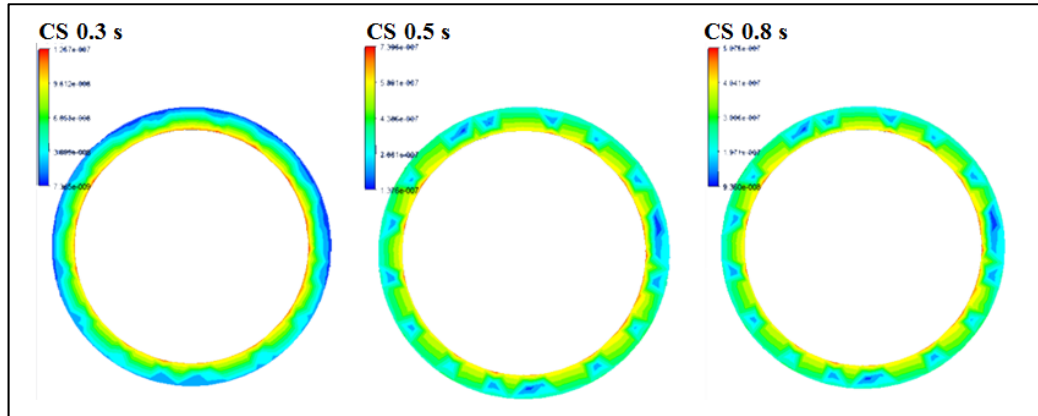


Figure 4-27: CS of the artery wall for atherosclerosis of 50% severity at the abdominal aorta at different times (0.3, 0.5 and 0.8s)

#### 4.7 CFD/FE Model Validation

The CFD/FE models are validated against the invasive right femoral artery blood pressure measurements. The CFD/FE models show an error of 1.1% when compared to the experimental results, due to the small size of the model, no significant alteration to the pulse wave was observed in the CFD/FE model. Figure 4-28 shows the validation of the results for four severities against blood pressure taken at the right femoral artery.

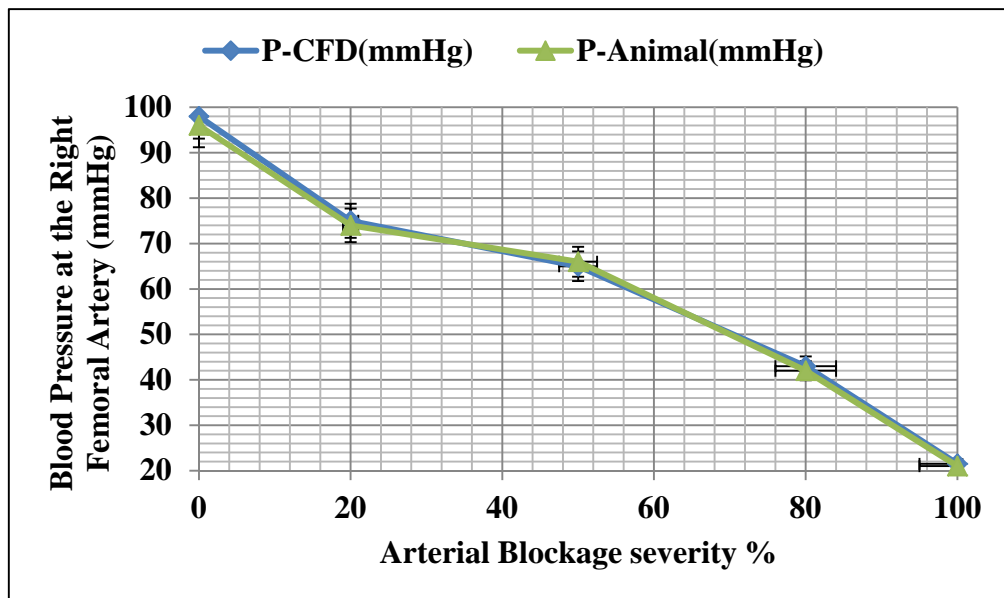


Figure 4-28: Comparison between the CFD/FE models against the experimental data

## 4.8 Closure

A series of *in vivo* animal experiments to investigate the development of arterial blockages that were developed and used to validate the CFD/FE models have been described in this chapter. The animal model results show that the CFD/FE modelling could be tested on human models. Therefore, the next chapter will examine CFD/FE methods on human models and will investigate how atherosclerosis and aneurysm occurring at the abdominal aorta are reflected in the measurement of blood pressure waveform at the brachial artery.

## **Chapter 5 The Human Model**

### **5.1 Introduction**

There are many processes involved in constructing a 3D aorta geometry and setting up the mesh generation for atherosclerosis or aneurysm occurring at the abdominal aorta. Aorta geometry consists of structure domain, fluid domain and a fluid-structure interaction (FSI). The use of the mesh method for 3D aorta geometry is important because it affects the convergence solution of the FSI model. However, the complex deformable aorta structure in both healthy and unhealthy (atherosclerosis or aneurysm) conditions presents various significant difficulties in processing mesh generation.

ANSYS® 14.0 is a valuable software package used to construct 2D and 3D geometries and generate the mesh for their multi-components and interactions [90]. This software is used to numerically investigate aorta geometry by: separating it into two bodies, solid (artery wall) and fluid (blood flow); and generating their FSI. The solid body is modelled using the Finite Element (FE) method under transient structure mechanic (TSM); however the fluid body is modelled using the Finite Volume (FV) method under computational fluid dynamic (CFD) methods.

In this chapter the aorta modelling and analysis processes and procedures are presented in detail and illustrated using specific data from literature [9, 59-67]. This modelling is performed using two-way FSI which shows the effect of stresses on arterial wall deformation as shown in Figure 5-1. These stresses are correlated in terms of the stress

phase angle (SPA) and augmentation index (AI). The SPA is used to develop a relationship between stresses and blood pressure, as measured non-invasively from the cuff.

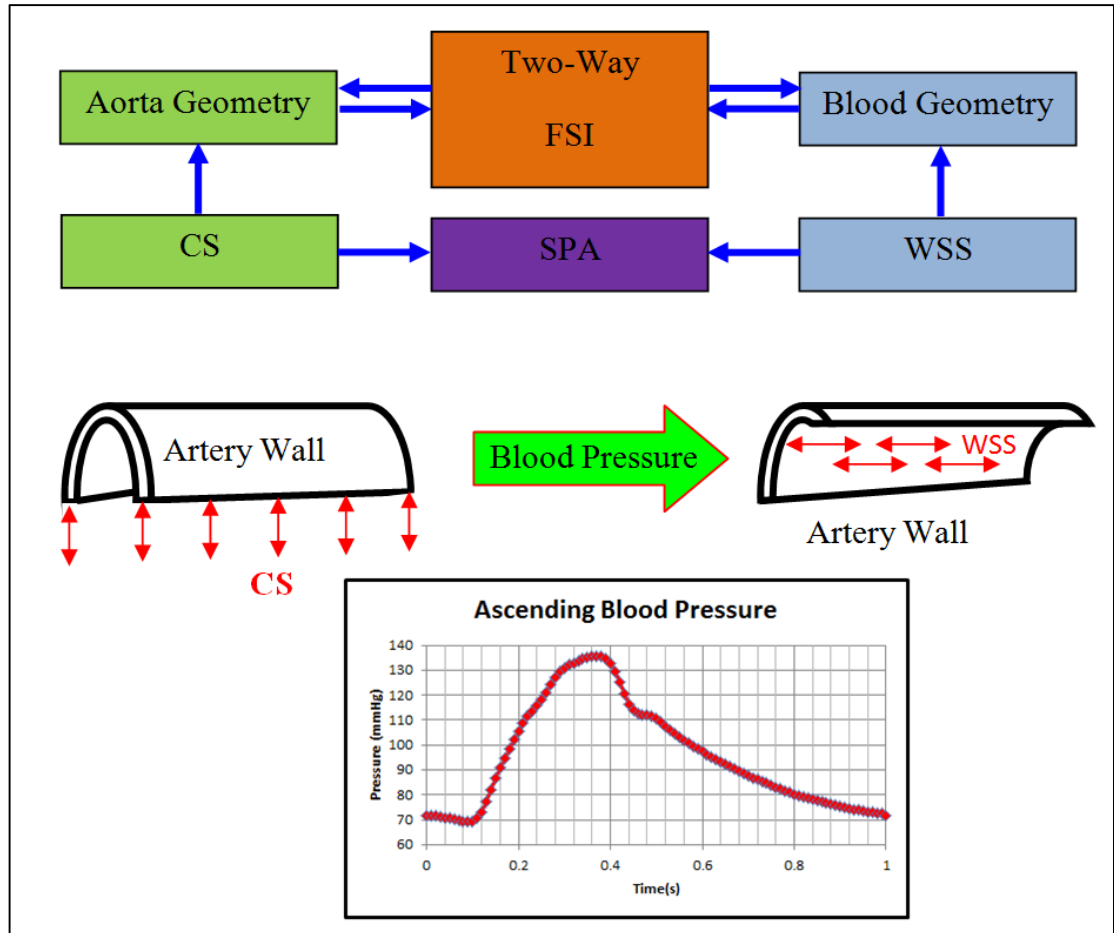


Figure 5-1: Block diagram of WSS and CS affecting the arterial wall

Aorta geometry is modelled in detail including the transient and two-way FSI scheme for both atherosclerosis and aneurysm (Section 5.2). The SPA is discussed in Section 5.3. The validation methods are discussed in Section 5.4 followed by the results in Section 5.5 and Section 5.6 contains the analysis of the results.

## **5.2 Model Development**

This section describes the physical models considered, starting from construction of the 3D geometry for both the solid and fluid bodies using DesignModeler (DM) [90]. The solid body is modelled using TSM. It is also used to set the material properties for the artery wall. The fluid body is then modelled using CFD using command field exercise (CFX).

### **5.2.1 Aorta Geometry**

As discussed in Chapter 3 Section 3.2, DM is used to construct the aorta geometry adopted from literature [9, 59-67] and after edit it to simulate disease development. In addition, as discussed in Chapter 3 (Section 3.2.1) under TSM, the DM tool converts 2D sketches to 3D geometries [90] and updates and modifies the aorta geometry dimensions. DM provides a technique for separating the multi-physical bodies i.e. the fluid and the solid, which helps to identify the FSI. This technique involves freezing the solid body which allows for the creation of a separate body representing blood volume. Figure 5-2 shows realistic aorta geometry in a healthy condition constructed from 3D anatomy images and Figure 5-3 shows simplified aorta geometry of both the solid body, representing the aorta wall (a), and the fluid body, representing the blood flow (b). In order to best construct the aorta geometry, DM provides the option of identifying the inlet and outlets of the aorta which helps to simplify the setup of the mesh generation of the geometry and the boundary conditions.

The healthy aorta geometry is constructed from literature data [9, 59-67] which indicates the range of aorta dimensions that are observed clinically for several healthy human subjects. The ascending aorta is constructed with an outer diameter  $D_o=24$  mm and an inner diameter  $D_i=20$  mm and thickness  $t=2$  mm [9, 59-6]. These diameters are applied along the aorta which includes the descending aorta, aortic arch and the iliac bifurcation. The aortic arch is constructed with an arch radius of 40 mm and the branches (Brachiocephalic, left common carotid and left subclavian artery) with an outer diameter  $d_o=12$  mm, inner diameter  $d_i=10$  mm and thickness  $t_1=1$  mm.

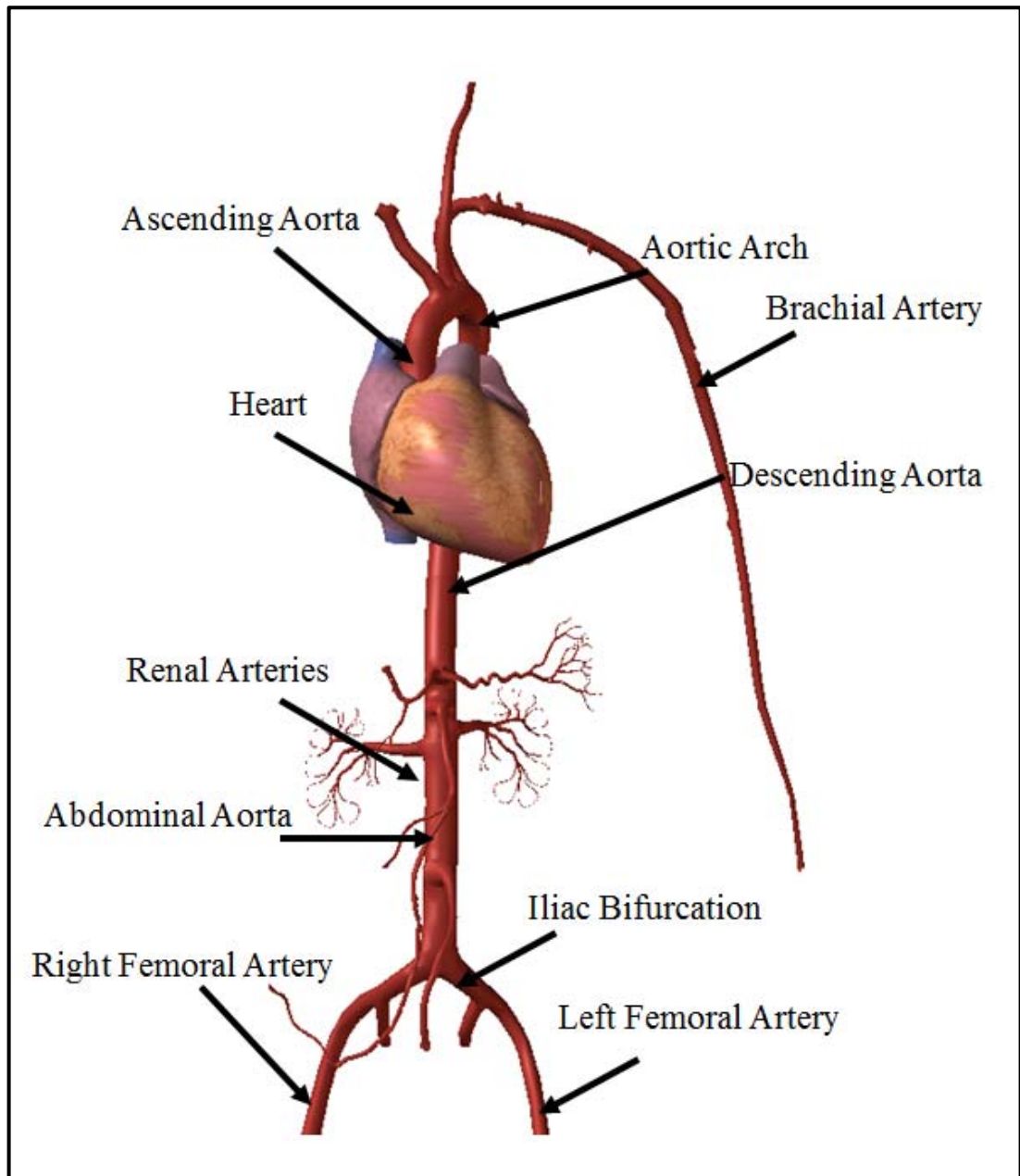


*Figure 5-2: A realistic 3D aorta geometry in a healthy condition*



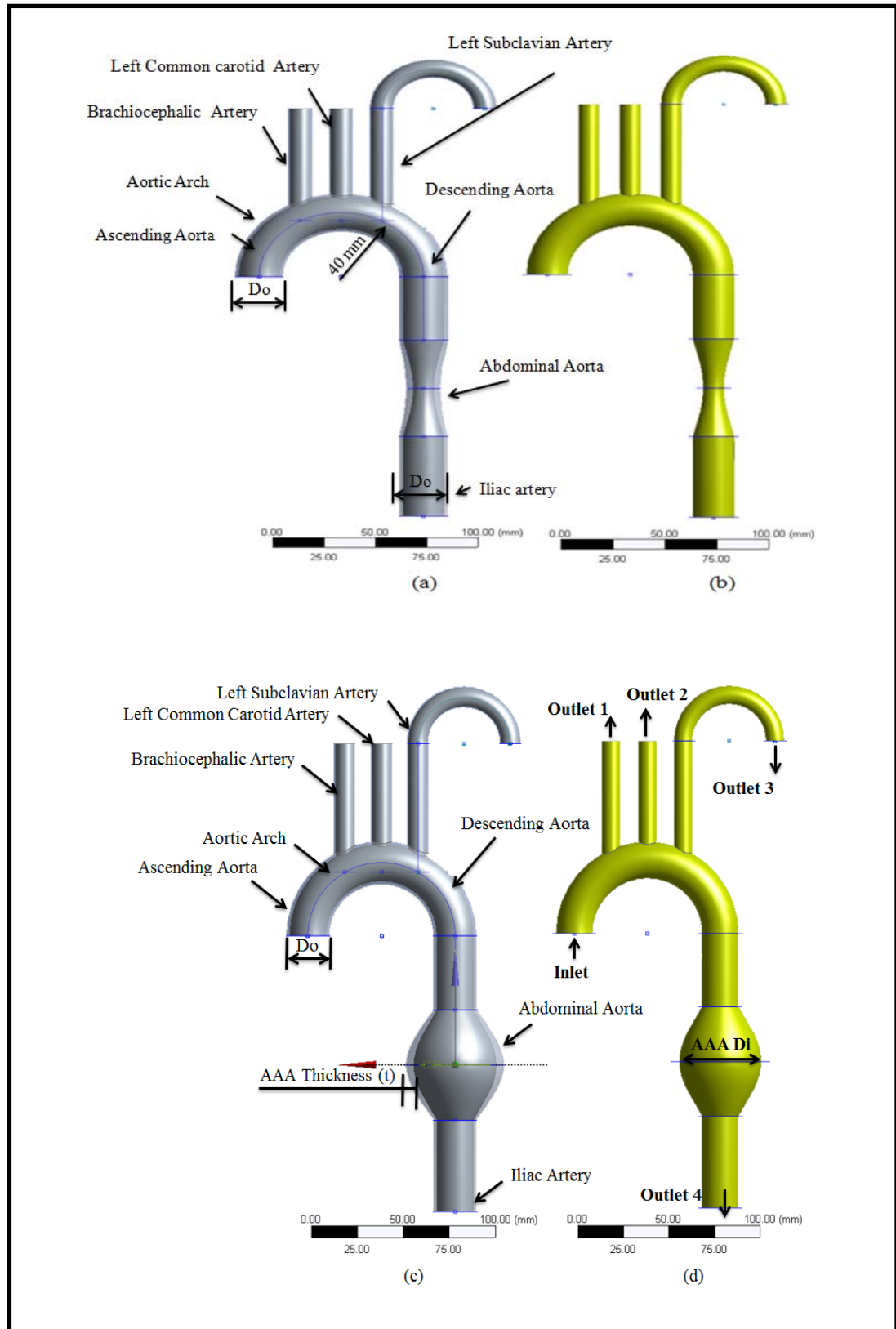


Figure 5-3: Aorta geometry of the artery wall and blood body for atherosclerosis (a) and (b), respectively; and abdominal aortic aneurysm (c) and (d), respectively

### 5.2.1.1 Atherosclerosis

In this investigation three main variables (inner diameter, wall thickness and length) of atherosclerosis are tested. To investigate the effect of each of these variables, three groups are conducted as follows:

Group-one (fixing thickness and length): containing one healthy aorta and eight diseased conditions with atherosclerosis implied at the abdominal aorta. The development of atherosclerosis is investigated by keeping the length of the diseased portion constant  $L=60\text{mm}$  and thickness of the abdominal aorta  $t=2\text{mm}$  as shown in Figure 5-4. However, the  $D_o$  and  $D_i$  are progressively decreased by  $2.5\text{ mm}$  to reach the stage of the full blockage of the abdominal aorta [9, 59-67].

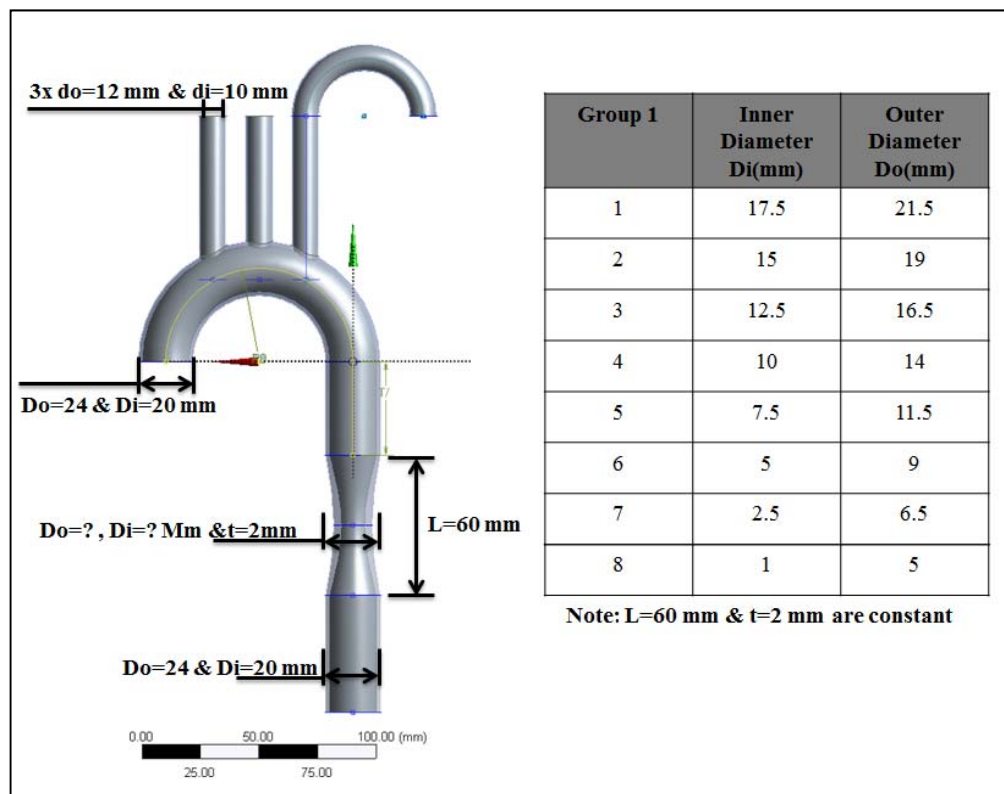
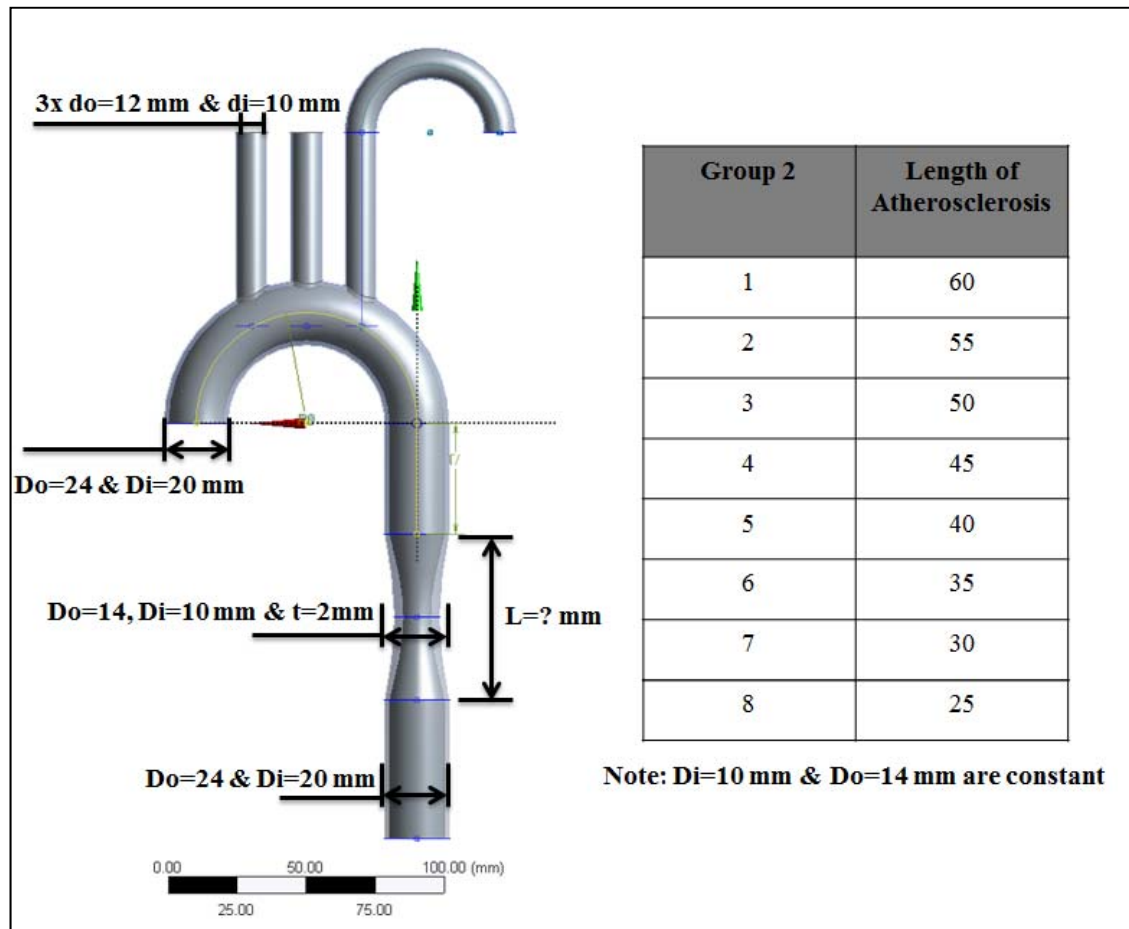


Figure 5-4: Aorta geometry and the scenarios of decreasing diameter of the aorta to simulate atherosclerosis development for Group one

Group-two (fixing the inner diameter and thickness): In which the  $D_i$  and  $D_o$  are constant with values of 10 mm and 14 mm, respectively. However, the length of the diseased portion is progressively reduced by 60 mm down to 10 mm for eight unhealthy aortas. In this group the thickness is kept constant at 2 mm as shown in Figure 5-5.



*Figure 5-5: Aorta geometry for the scenario of reducing the length of the diseased portion*

Group-three (fixing the inner diameter and length): In which the  $D_i$  and  $L$  of the atherosclerosis are kept constant with values of 10 mm and 60 mm, respectively. However, the  $D_o$  and  $t$  are variable as shown in Figure 5-6. This figure shows the design of eight unhealthy aorta models with increasing thickness from 0.5-4 mm at the abdominal aorta.

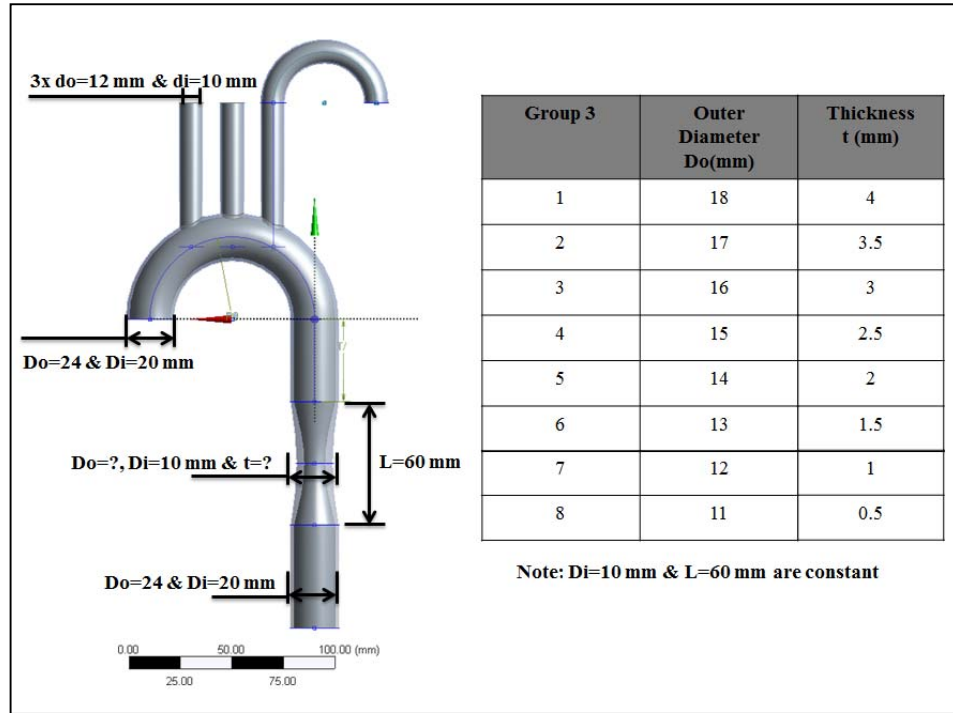


Figure 5-6: Aorta geometry for the scenario of increasing the thickness of the atherosclerosis

### 5.2.1.2 Abdominal Aortic Aneurysm

A healthy aorta control model is generated as discussed in Section 5.2.1 [9, 64-80]. Figure 5-7 shows the AAA model with disease length  $L=60$  mm. Twenty such abdominal aortic aneurysm models from literature [9, 59-73] are simulated in this study. Each model is made up of a fluid domain, representing the aortic lumen and a solid domain, representing the artery wall. This figure shows the fluid domain entities in healthy and diseased models.

For the current investigation, the proposed internal and external diameters of the aneurysm are increased by an increment of 2 mm from an inner diameter of 20 mm and an external diameter of 24 mm for a healthy model, to 60 mm and 64 mm, respectively, for the unhealthy case [9, 59-73].

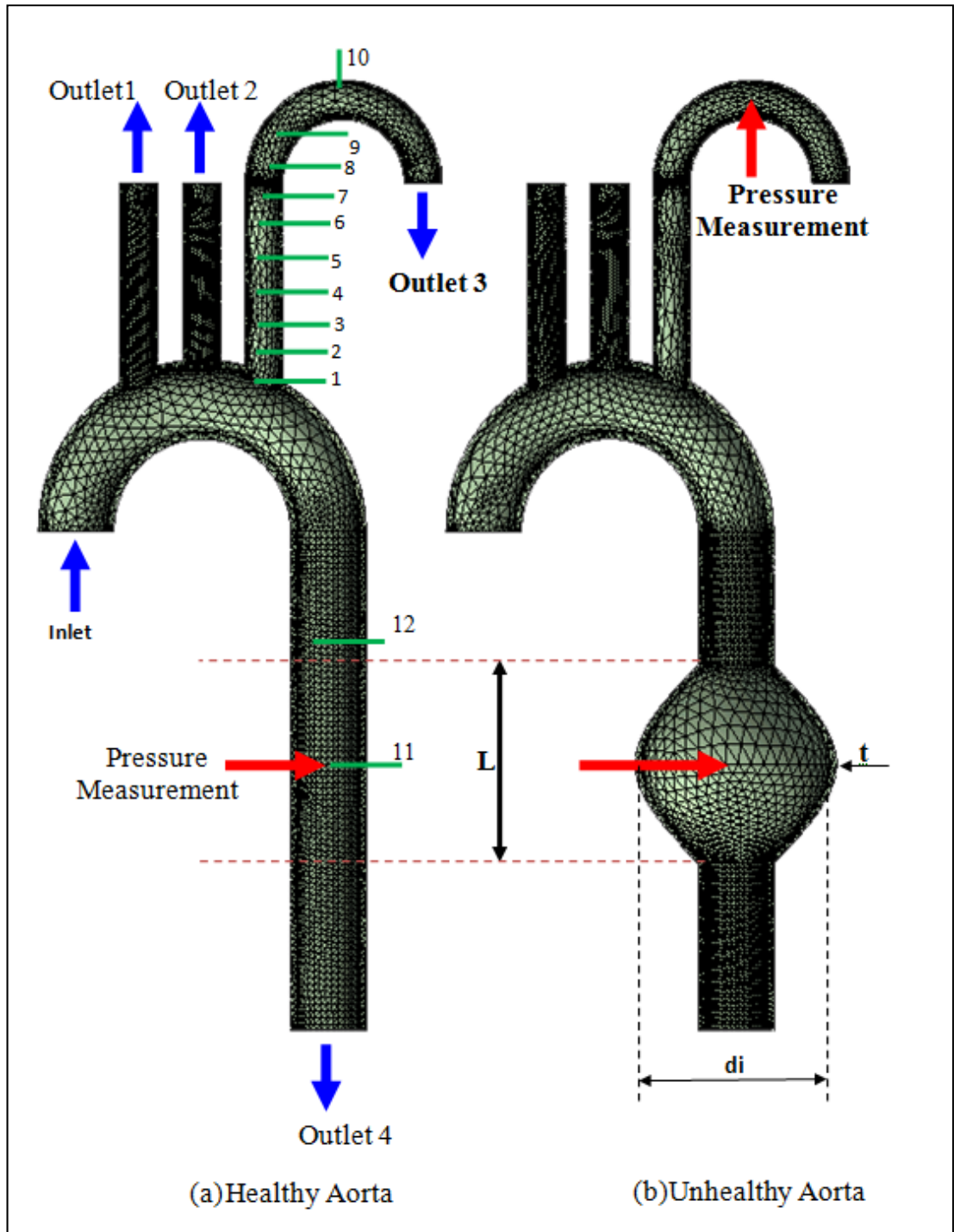


Figure 5-7: Design of the study of healthy and unhealthy aorta; (a) the healthy aorta measurement locations and (b) the unhealthy aorta

## **5.2.2 Transient Structure Mechanics**

Transient mechanical analysis is a preliminary tool used to analyse and investigate the physics of a problem [90]. This analysis requires a simpler model as a first step, such as a straight artery. The simplified model determines the dynamic response of the structure and is used to construct the more complex model. The process of this method was described in Chapter 4 in detail in Section 4.5.1.1.

### **5.2.2.1 Mesh Generation**

To select 3D element types for the aorta geometry, mesh density is assigned after several trials by specifying the proper numbers of division along the edges of volumes [90]. There are many different types of mesh methods which could be considered for aorta geometry. The Sweep method (as discussed in Chapter 3, Section 3.3) is used to generate the mesh for the solid body, as shown in Figure 5-8. The number of elements and nodes in the aorta geometry for the atherosclerosis condition are: elements (45,539) and nodes (90,877) for the solid body. However, in the AAA condition for the solid body, the number of elements are 53,351 and the nodes are 106,551. Figure 5-8 (a) and (b) respectively show a close up of mesh detail at the aortic arch and the branches for both atherosclerosis and aneurysm conditions in the abdominal aorta.

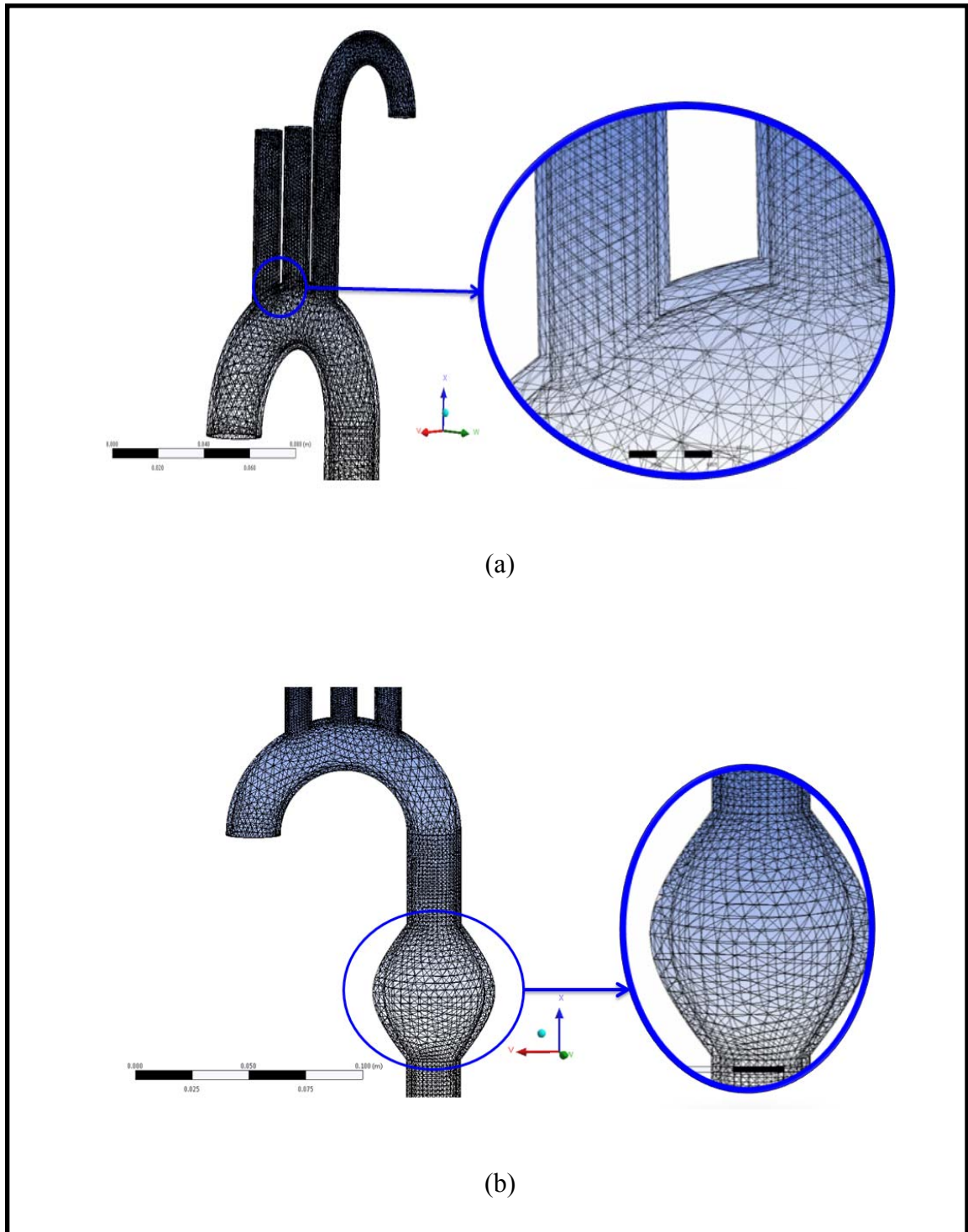


*Figure 5-8: Mesh generation for the aorta wall (a) at the aortic arch for an atherosclerosis condition and (b) for an abdominal aortic aneurysm condition*

To improve the quality of the mesh for both conditions, there are many tools that can be used to refine the 23 faces of the aorta wall with value 2 and Mapped Face meshing of 22 faces. To check the quality of the mesh, the Skewness tool (available with ANSYS®14.0) is used. This tool shows a quality value range of a minimum value 0.03 and maximum value of 0.8 which are considered very good within the range of mesh acceptance.

#### **5.2.2.2 Material Properties**

**Blood Properties.** The rheological properties are assumed to be in ranges that permit blood to be treated as an incompressible, homogeneous and Newtonian fluid [9]. The dynamic viscosity and density of the blood are 0.004 Ns/m<sup>2</sup> and 1100 kg/m<sup>3</sup> respectively [9].

**Artery Wall Properties.** The healthy artery wall is modelled assuming a Hyperelastic Neo-Hookean model with Young's modulus of  $E=0.5$  MPa and Poisson's ratio of  $\nu=0.45$  [90]. The healthy and unhealthy artery wall models' material properties are set as shown in Table 5-1. The boundary conditions are also set for the solid-fluid interface and the fixed ends of the inlet and outlets of the aorta geometry. These conditions combined with the CFD-CFX analysis provide great understanding of arterial wall displacement and deformation resulting through the pulsatile blood flow. The FSI model is used to investigate the effect of pulsatile blood flow on the aorta wall deformation, compliance and displacement for healthy and unhealthy conditions.



*Table 5-1: The material and boundary conditions of the arterial wall in healthy conditions and unhealthy (atherosclerosis and aneurysm) conditions (adapted from [8, 9, and 23])*

Condition	Characteristic	Artery Wall
<b>Healthy Artery</b>	Module	Material Properties
	Material Model	Hyperelastic Neo-Hookean
	Initial Shear Modulus	$G=1.74 \text{ MPa}$
	Initial Bulk Modulus	$K=34.7 \text{ MPa}$
	Young Modulus	$E=0.5 \text{ MPa}$
	Density	$\rho_w = 1050 \text{ Kg/m}^3$
	Poisson's Ratio	0.45
<b>Artery with Atherosclerosis</b>	Module	Material Properties
	Material Model	Hyperelastic Neo-Hookean
	Initial Shear Modulus	$G=2.5 \text{ MPa}$
	Initial Bulk Modulus	$K=40 \text{ MPa}$
	Young's Modulus	$E=1 \text{ MPa}$
	Density	$\rho_w = 1160 \text{ Kg/m}^3$
	Poisson's Ratio	0.4
<b>Artery with Aneurysm</b>	Module	Material Properties
	Material Model	Hyperelastic Neo-Hookean
	Initial Shear Modulus	$G=0.075 \text{ MPa}$
	Initial Bulk Modulus	$K=1.5 \text{ MPa}$
	Young's Modulus	$E=0.25 \text{ MPa}$
	Density	$\rho_w = 960 \text{ Kg/m}^3$
	Poisson's Ratio	0.33

### 5.2.3 Computational Fluid Dynamic and Command Field Exercise

The CFD modelling process was described in Chapter 4 Section 4.5.1.2 in detail. In this section blood flow is governed by the equations of momentum (Equation 3-1) and continuity (Equation 3-4 to 3-7) with boundary conditions set up at the inlet and outlets of the vessel. The blood is modelled using the fluid model shear stress transport (SST) scheme. The solver control is solved by the Second Order Backward Euler (SOBE) equations (see Appendix I) which set up the maximum and minimum iterations [90]. The output control is used to set the transient results; i.e. total mesh displacement, pressure, velocity and wall shear stress (WSS). The CFX solver is also used to monitor coefficient loop convergence; i.e. total mesh displacement and the force in any direction which affect the FSI wall.

### 5.2.3.1 Mesh Generation

CFD analysis is applied in terms of numerical discretization to develop approximations of the governing equations of fluid mechanics in the fluid region of interest [90].

For the aorta geometry several attempts are made to identify the size of the meshes to be used. Starting with simple geometry and gradually increasing the number of elements, we are able to identify the most suitable and accurate mesh for the current investigation. This leads to a mesh of 1,360,627 nodes and 702,712 elements for the blood body for atherosclerosis, as shown in Figure 5-9 (a) and 1,592,853 nodes and 832,763 elements for aneurysm, as shown in Figure 5-9 (b). The models are meshed using the tetrahedron path independent method, which has the advantage of producing uniformly sized meshes, especially for small arteries. Furthermore, there are several methods for assessing mesh element quality (mesh metrics) such as the element skewness, which is available within ANSYS® 14.0 [90]. In the present work the Skewness is between a minimum of 0.46 and a maximum of 0.75 which is within the acceptable range. The above mesh has demonstrated a good statistical measure for moving meshing nodes, and convergences are assessed as being in the acceptable range by comparing them with the literature [56-74]. In this computational model, a maximum number of iterations are performed, based on the level of residual reduction or absolute residual levels as a convergence criterion; that is iterations continue until an appropriate level of convergence is reached.

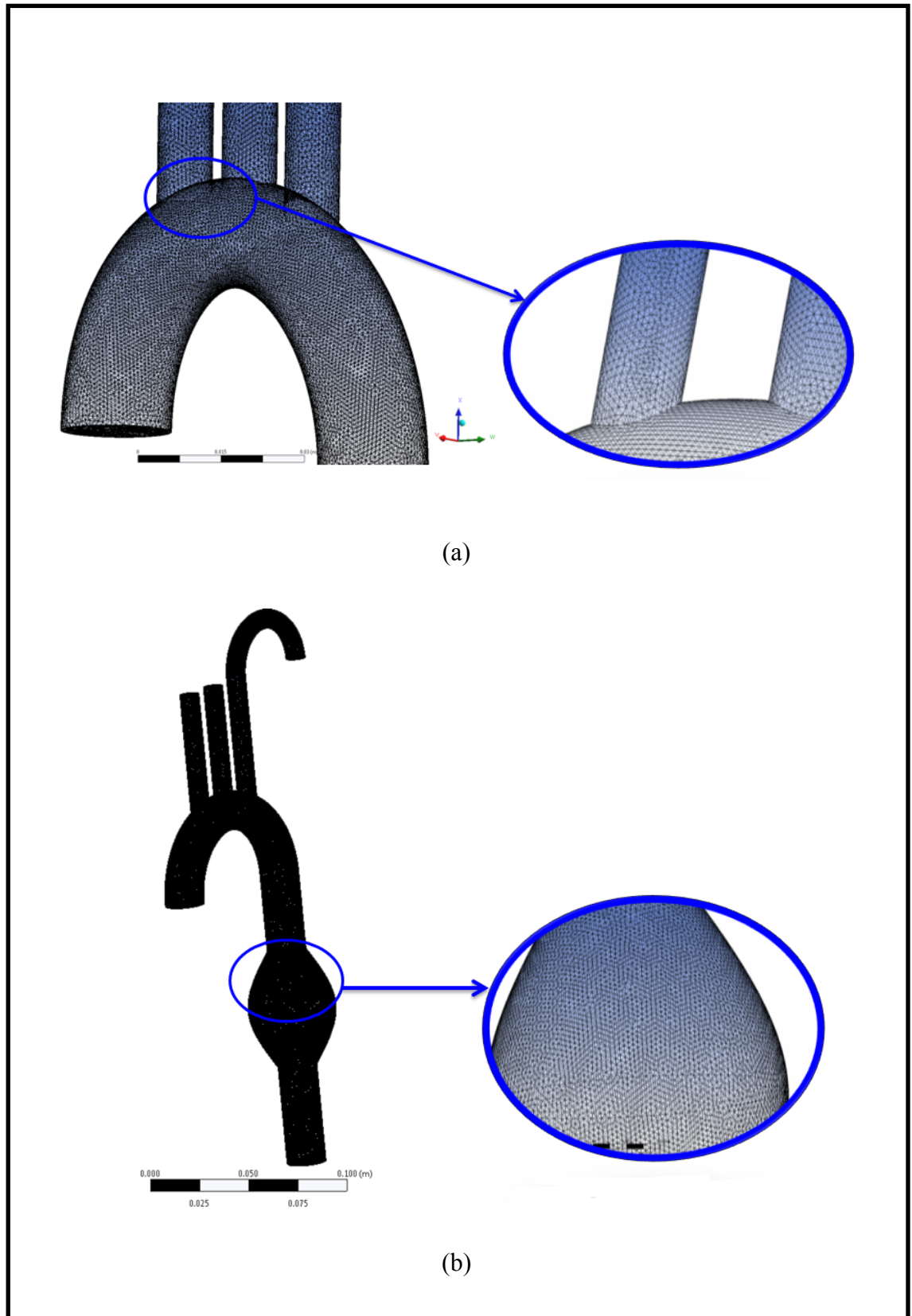


*Figure 5-9: Mesh generation for the aortic arch and three branches (a) blood flow in case of atherosclerosis and (b) in the case of abdominal aortic aneurysm*

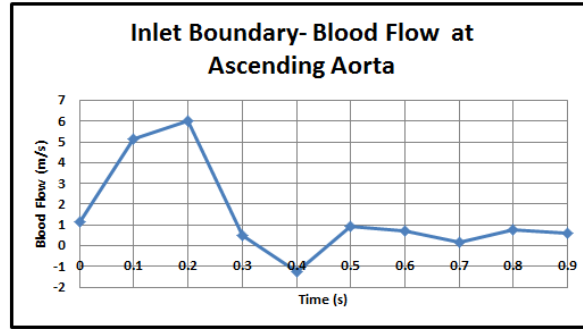
### 5.2.3.2 Boundary Conditions

The numerical simulations were performed using the ANSYS®14.0 software. This tool is based on the finite element method and numerically simulates partial differential equations as described in Chapter 3, equations 3-1 to 3-16, and Appendix I. For the fluid part, ANSYS solves Navier-Stokes equations inside the computational domain. The fluid is assumed incompressible, Newtonian of dynamic viscosity  $5 \times 10^{-3}$  Pa s and  $\rho=1060$  kg/m<sup>3</sup>.

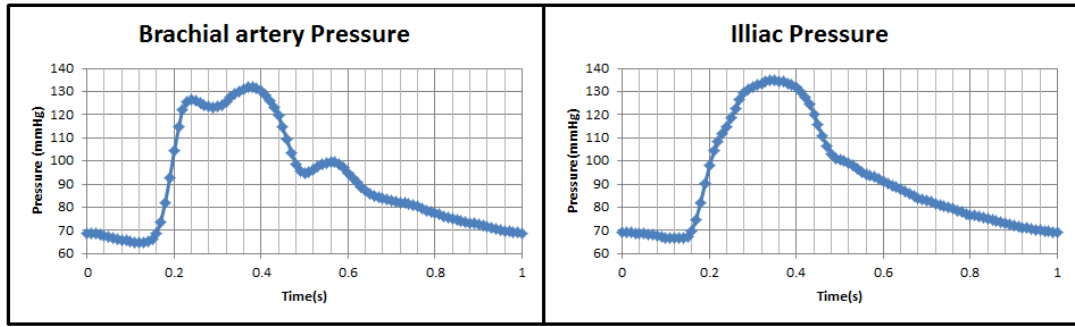
For the fluid domain, the inlet and outlet boundary conditions are expressed as follows in ANSYS:

- I. The inlet boundary condition is a waveform of blood flow velocity [8, 9, 23], as shown in Figure 5-10 (a).
- II. Three of the outlets' boundary conditions are brachial artery pressure waveforms, as shown in Figure 5-10 (b).
- III. The fourth outlet is an iliac pressure waveform as shown in Figure 5-10 (c). All of these waveforms were invasively measured in patients undergoing left heart catheterization at Green Lane Hospital under Ethics approval number (NTX/09/11/109). Figure 5-10 (d) also shows the free body diagram of the aorta geometry.

For the solid domain, a fluid-structure interaction face is set between the solid and fluid bodies. The solid body is assumed flexible and solved as an isotropic linearly elastic solid with only radial displacement because the inlet and outlets' ends are assumed fixed (with zero displacement and slope), as shown in Figure 5-10 (d).

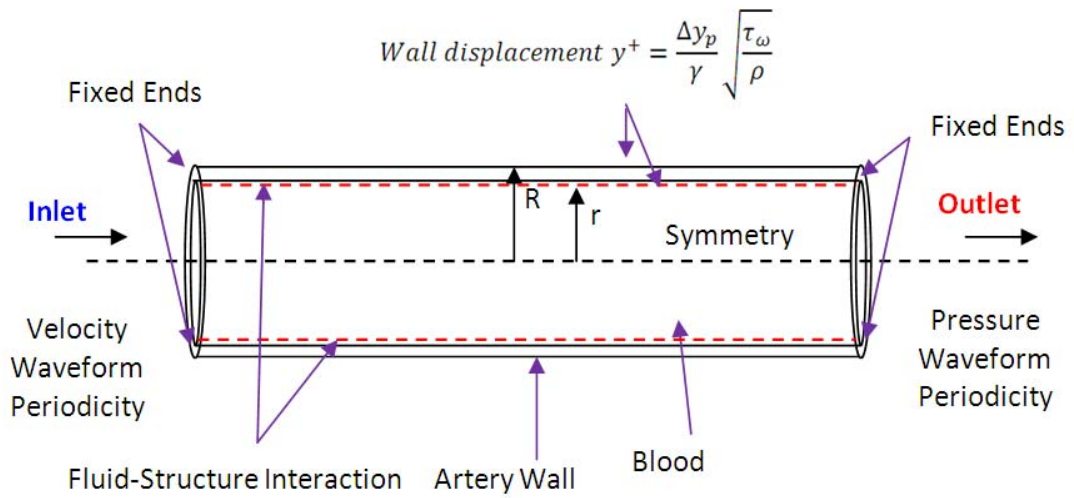


(a)



(b)

(c)



(d)

Figure 5-10: Boundary conditions for blood flow and pressure; (a) blood flow waveform at the ascending aorta; (b) blood pressure at the brachial artery; (c) at the iliac artery and (d) a free body diagram of the boundary conditions

### **5.2.3.3 Fluid-Structure Interaction Model**

Coupling between blood and the artery is due to the relatively low stiffness of the artery when compared to blood. Hence, the pressure exerted by the flowing blood on the artery wall can result in considerable deformations of the artery, and vice-versa [64]. To address this coupling, FSI is developed to combine a constitutive model describing the stress distribution in the vessel's wall with the computational analysis of the blood flow [58-7]. This method allows for solving the coupled fluid-solid phase problems by accounting for both the instantaneous fluid mechanical forces on the artery wall and the effects of wall displacement on the fluid motion. To address this in a 3D moving-boundary format, it is necessary to consider a suitable moving mesh method, such as the ALE approach [90]. ALE allows the grid to track the material by adjusting grid generation and measuring the flux of the material during the adjustment (as described in Chapter 3 Section 3.4.2).

The advantage of using the FSI approach (as shown in Figure 5-11) is the ability to investigate the effect of atherosclerosis and aneurysm conditions on the interface between blood flow and the artery wall. This method allows us to investigate the stresses and strains which are affecting the artery wall and blood flow. Consequently, CFX results have a big impact on the mechanical arterial wall function for example deformation, which we is being investigated in this thesis.

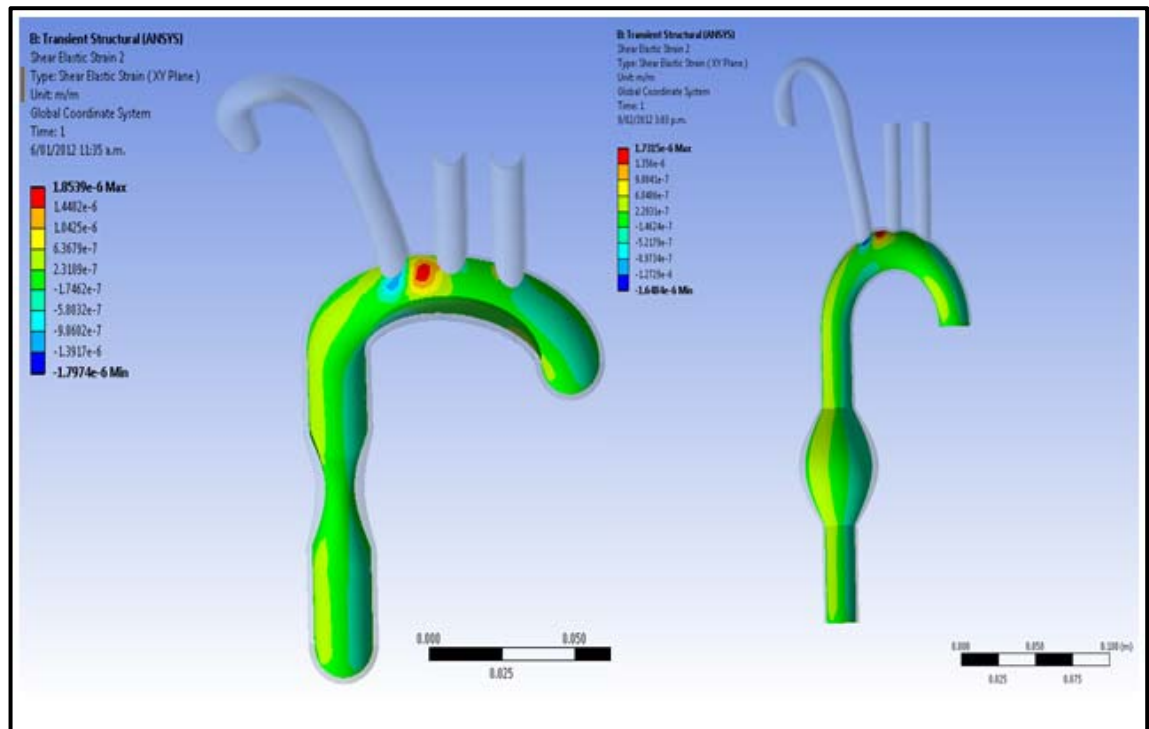


Figure 5-11: FSI approach effects on the wall-blood interaction for the atherosclerosis model (right) and abdominal aortic aneurysm (left)

## 5.2.4 Two-way FSI

The two-way FSI method is used to allow the modelling of the coupling between the blood flow and the artery wall (as described in Chapter 4 in Section 4.5.4). The FSI method is based on solving the ALE approach which allows the grid to track the material by adjusting grid generation and measuring the flux of the material during the adjustment as described in Chapters 3 and 4. These models are simulated for blood pressure for time equal to 30 seconds, and WSS, CS and AI are investigated. The aim of this section is to come up with a new form of diagnosis for arterial blockages based on the arterial wave propagation for the blood pressure. In addition, the results of the 3D model will be validated against the animal experimental model.

### 5.3 Stress Phase Angle

Stress phase angle (SPA) is the phase angle between circumferential strain (CS) which results from arterial wall deformation and wall shear stress (WSS) resulting from pulsatile blood flow. There are many reasons to investigate the SPA in arteries in terms of time lag and phase angle to correlate stresses and cardiovascular diseases as based on many studies [107-110]. These studies have reported that the production of endothelin by bovine aortic endothelial cells is strongly suppressed with an SPA=  $-180^\circ$  under asynchronous hemodynamic conditions compared to a SPA= $0^\circ$  under synchronous hemodynamic conditions [107-110]. Another reason to consider the SPA is to correlate the stresses and the development of atherosclerosis at the abdominal aorta. This correlation is based on three groups of aorta models based on clinical trials and comparing them to one healthy constructed aorta. Figure 5-12 shows the stresses, CS and WSS, which affect the artery wall and blood pressure (P) and flow rate (Q). There is a strong relationship between all these variables which can be investigated using the SPA.



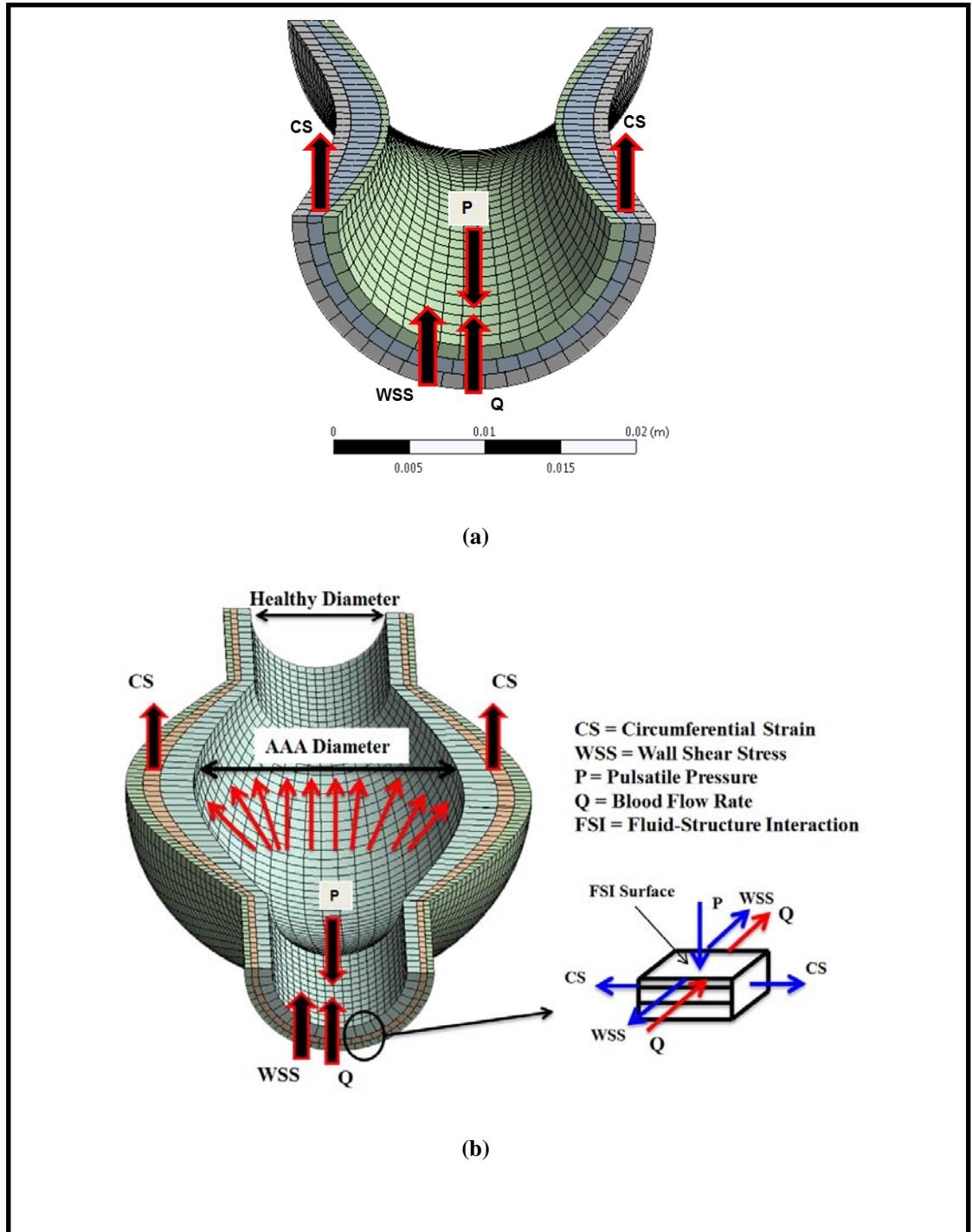


Figure 5-12: Stress Phase Angle (SPA); (a) in the case of atherosclerosis condition and (b) in the case of an aneurysm

For investigation purposes, two sites are considered in this study: locations A and B, as shown in Figure 5-13, (a) for atherosclerosis and (b) aneurysm, respectively. At each site, two points are investigated, one at the artery wall, the other at the fluid-solid interface region. Location A represents weaknesses where most disease (atherosclerosis or aneurysm) most commonly occurs in the abdominal aorta [107-110]. However, location B represents where it is possible to measure blood pressure non-invasively. WSS and CS, which are measured as a function of time, are determined at these points. This work intends to investigate the pulse waveform in terms of the SPA and the time phase delay ( $\Delta t$ ) for different groups of models of atherosclerosis and aneurysm in the abdominal aorta. The methodology for investigating the SPA is to find the  $\Delta t$  for a healthy aorta at locations A and B. The healthy  $\Delta t$  is then compared with the unhealthy aorta geometries.

The SPA is expressed as ( $\phi$ ) between the vessel diameter stretch in terms of CS (D) and WSS ( $\tau$ ). The SPA is separated into two parts related to the flow (Q) and pressure (P) as follows:

$$\phi(D-\tau) = \phi(D-Q) - \phi(\tau-Q) \quad (5-1)$$

$$\approx \phi(P-Q) - \phi(\tau-Q)$$

The difference in phase between P and Q represent the impedance phase angle (IPA) in terms  $\phi(P-Q)$ , and the  $\phi(\tau-Q)$  represents the WSS-flow rate phase angle.

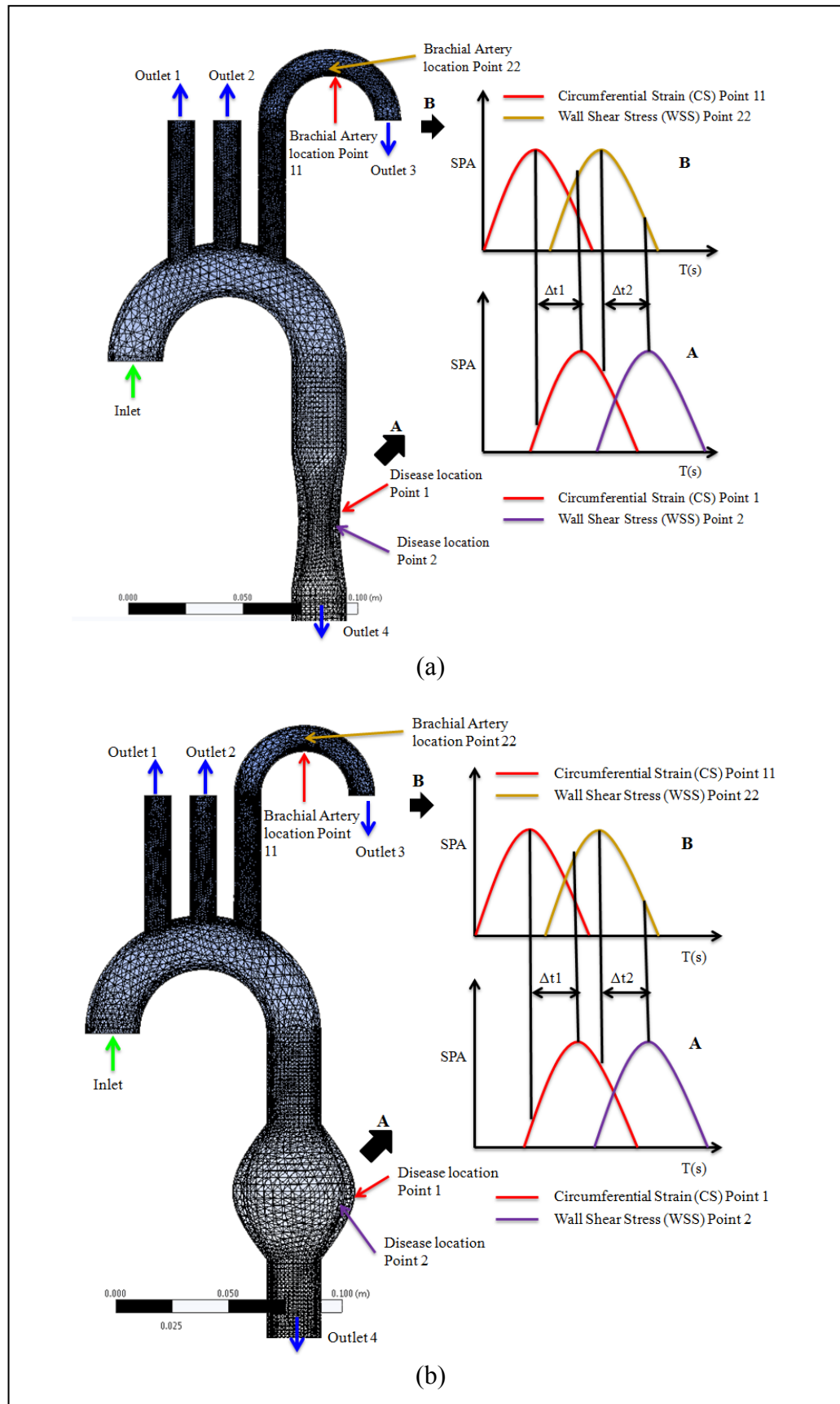


Figure 5-13: SPA for the (a) abdominal aorta when atherosclerosis occurs and (b) an abdominal aortic aneurysm

## 5.4 CFD/FE Results and Analysis

**Validation.** The models presented in this chapter are compared with the literature and validated against clinical trials on artery geometry. Firstly, the healthy model is validated against literature data and the clinical trial results. These validations are also performed by investigating the pressure pulse wave at different locations such as the ascending, descending and the renal arteries. Figure 5-14 shows the blood flow rate resulting from CFD/FE models validated against literature data [9, 23, 59-67]. This validation is performed at the inlet condition of the ascending aorta in healthy model. There is a good agreement between the literature and the presented CFD/FE results. The slight difference between these could be due to possible error in the CFD/FE modeling, for example, the material properties assumptions for the artery wall.

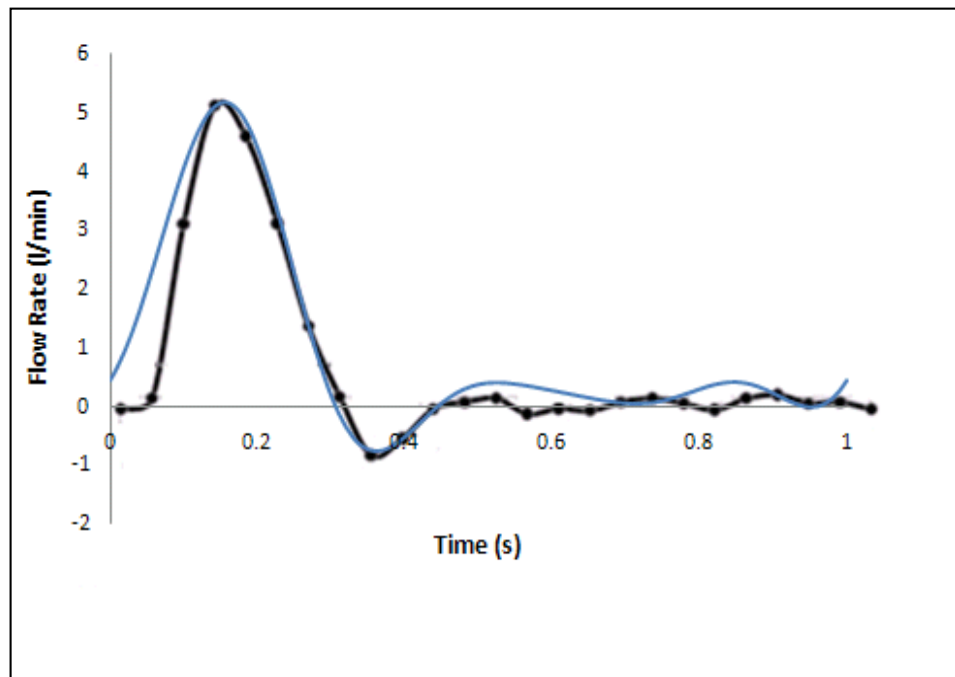
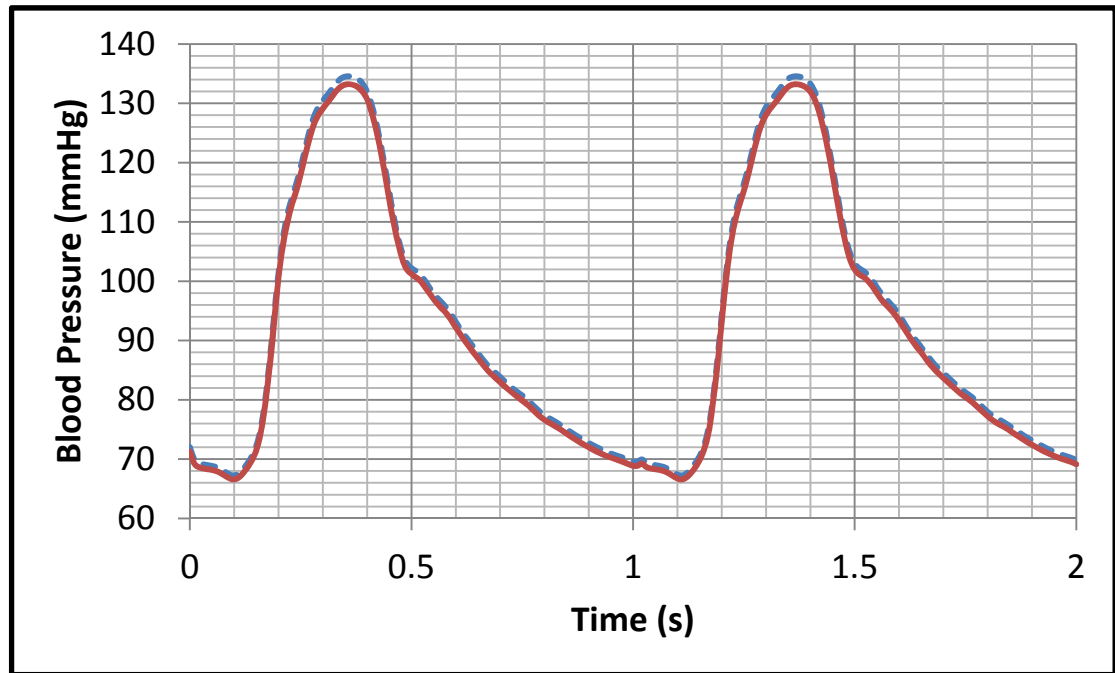


Figure 5-14: Flow Rate validations (for healthy condition) with literature data (black dotted) [17] and CFD model (blue)

Figure 5-15 shows the validation of the CFD/FE results against the invasive clinical data taken at the renal artery. There is a strong agreement between CFD/FE and the invasive clinical data obtained from healthy subjects at Green Lane Hospital.



*Figure 5-15: Validation of pressure wave forms located at the renal artery against the clinical trials: P invasive (solid) and P CFD/FE (dotted) in a healthy condition*

The results are discussed in detail in the next sub-sections. These sub-sections outline and discuss the results of the CFD/FE models for atherosclerosis and abdominal aortic aneurysm (AAA) in terms of hemodynamic stresses, WSS and pressure, the SPA and the arterial compliance/stiffness.

### **5.4.1 Atherosclerosis**

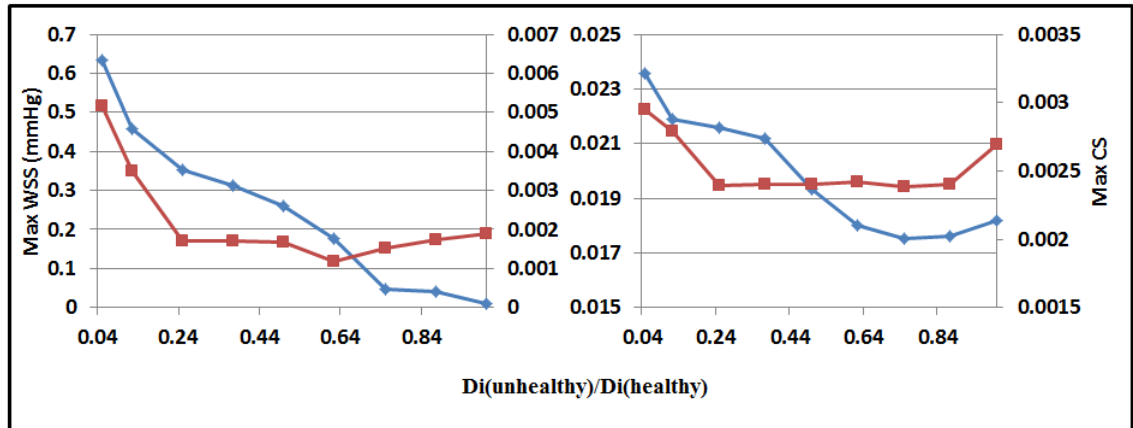
The ability to identify atherosclerosis, which is represented by a reduction in the lumen of the artery, would be most valuable to medical doctors for ideal clinical control of the disease. To obtain such information, this study investigates the WSS and CS in a healthy model and compares them against unhealthy models which are governed by relative compliance at the abdominal aorta. For this purpose, two sites are considered in this research, one at the abdominal aorta representing the location of the disease and the other at the brachial artery which represents an ideal location at which non-invasive measurements can be obtained (as discussed in Section 5.3). At each site, two points are investigated, one at the artery wall and the other at the fluid-solid interface. These two locations (at the abdominal aorta) represent sections of weakness where atherosclerosis occurs most commonly at the intima layer.

#### **5.4.1.1 Stress and Strain**

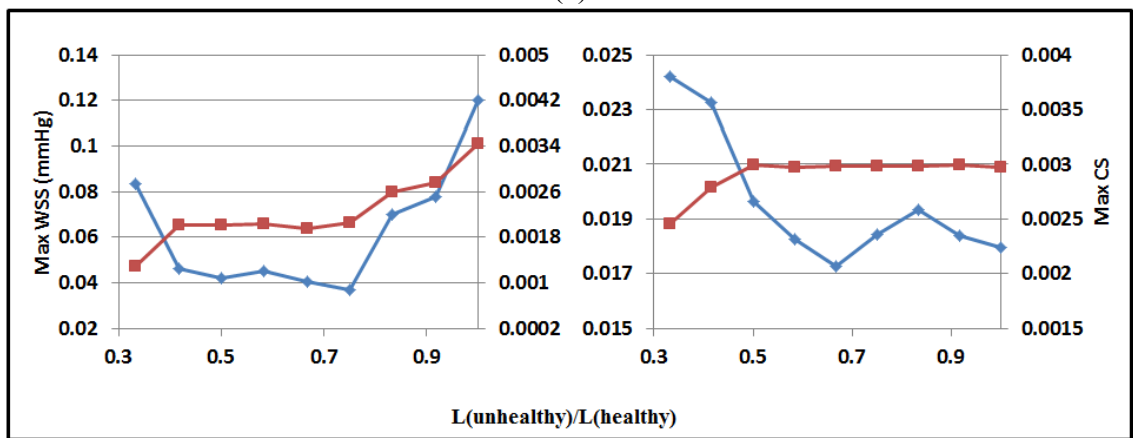
The effects on WSS and CS are investigated on the three groups of atherosclerosis conditions which are developed in this chapter (Section 5.2.1.1). The simulations of these models are compared against the healthy (control) condition. These stresses are determined at two locations as mentioned above in Section 5.4.1.

The values of the systolic WSS and CS at the brachial artery vary in a manner different from those at the abdominal aorta in abnormal conditions. The abnormal conditions are applied to the inner diameter, length of the disease and thickness of the artery wall as shown in Figure 5-16. Figure 5-16 (a) highlights that the systolic WSS and CS are increased with the decreasing of the cross sectional area of the abdominal lumen for

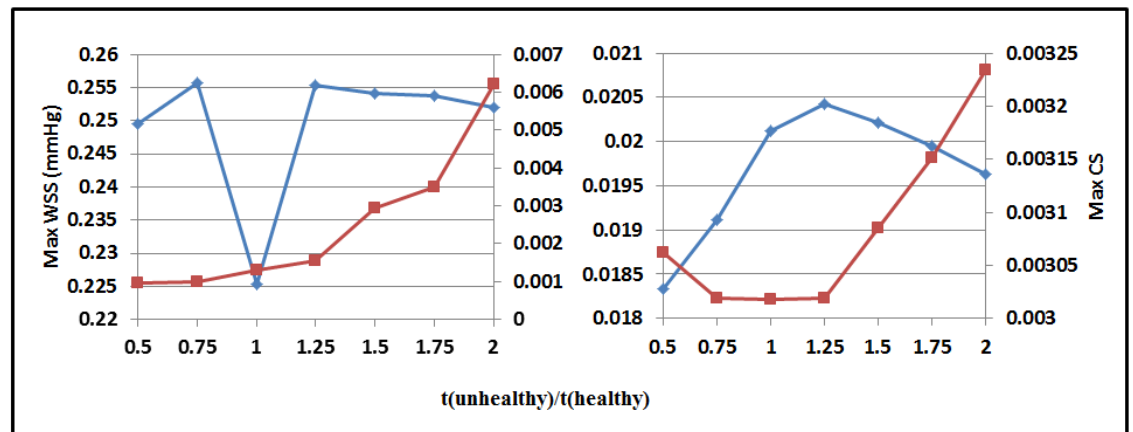
group-one against the ratio of Di unhealthy to Di healthy. This is attributed to the combination of high blood flow and pressure occurring due to stenosis and arterial narrowing. However, the results of group-two against the ratio of unhealthy to healthy lengths do not affect the systolic CS at either location; see Figure 5-16 (b). Figure 5-16 (c) shows the same trend for the systolic WSS and CS in the third group. This figure shows that systolic CS is affected and increased at both locations against the ratio of unhealthy to healthy thicknesses. The systolic WSS dropped at the abdominal aorta (left) when  $[t(\text{unhealthy}) = t(\text{healthy})]$  which indicates the healthy condition. However, the systolic WSS at the brachial artery in Figure 5-16 (c) (right) shows that an increase in the severity of the abdominal aorta blockage thickness increases the systolic WSS at the brachial artery compared to the low stiffness condition. These results demonstrate that any changes to the geometrical characteristics of the abdominal aorta impact on the impulse of WSS and CS waveforms at the brachial artery.



(a)



(b)



(c)

Figure 5-16: The max WSS (blue) and the max CS (red), at the brachial artery (right) and at the abdominal aorta (left) for: (a) Group One; (b) Group Two and; (c) Group Three



The comparison between the hemodynamic stresses in terms of waveforms (WSS and CS) at the disease location and at the brachial artery is summarized in Table 5-2 and Figure 5-17. Table 5-2 shows the time delay transferred from Figure 5-17 for the healthy condition and the two unhealthy conditions for each group. The time lag difference between the CS and WSS indicates a possible approach to detect diseases at the brachial artery. Figure 5-17 shows the same comparison between the healthy and two unhealthy conditions on the WSS and CS in the three atherosclerosis development groups. The comparison shows a clear change in the shape of the propagated stress, such as the shifting of the CS waveforms at the abdominal aorta. These results indicate a very high possibility of detecting the development of atherosclerosis from the brachial artery by making a correlation between the WSS and CS in terms of time lag and phase angle. This correlation requires a formula to describe the level of the cardiovascular disease risk. This data is correlated and formulated to the development of atherosclerosis in Chapter 6.

*Table 5-2  $\Delta t$  for the three groups of atherosclerosis disease compared with the healthy condition*

<b>Groups</b>	<b>Locations</b>	<b>Healthy</b>	<b>Unhealthy (Atherosclerosis 50%)</b>	<b>Unhealthy (Atherosclerosis 90%)</b>
<b>Group One</b>	Abdominal Aorta	$\Delta t_1=0.14$ s	$\Delta t_2=0.16$ s	$\Delta t_3=0.19$ s
	Brachial Artery	$\Delta t_{11}=0.19$ s	$\Delta t_{12}=0.19$ s	$\Delta t_{13}=0.2$ s
<b>Group Two</b>	Abdominal Aorta	$\Delta t_1=0.14$ s	$\Delta t_2=0.15$ s	$\Delta t_3=0.19$ s
	Brachial Artery	$\Delta t_{11}=0.19$ s	$\Delta t_{12}=0.19$ s	$\Delta t_{13}=0.2$ s
<b>Group Three</b>	Abdominal Aorta	$\Delta t_1=0.14$ s	$\Delta t_2=0.12$ s	$\Delta t_3=0.19$ s
	Brachial Artery	$\Delta t_{11}=0.19$ s	$\Delta t_{12}=0.19$ s	$\Delta t_{13}=0.19$ s

Healthy Condition	Unhealthy Condition 5	Unhealthy Condition 8
-------------------	--------------------------	--------------------------

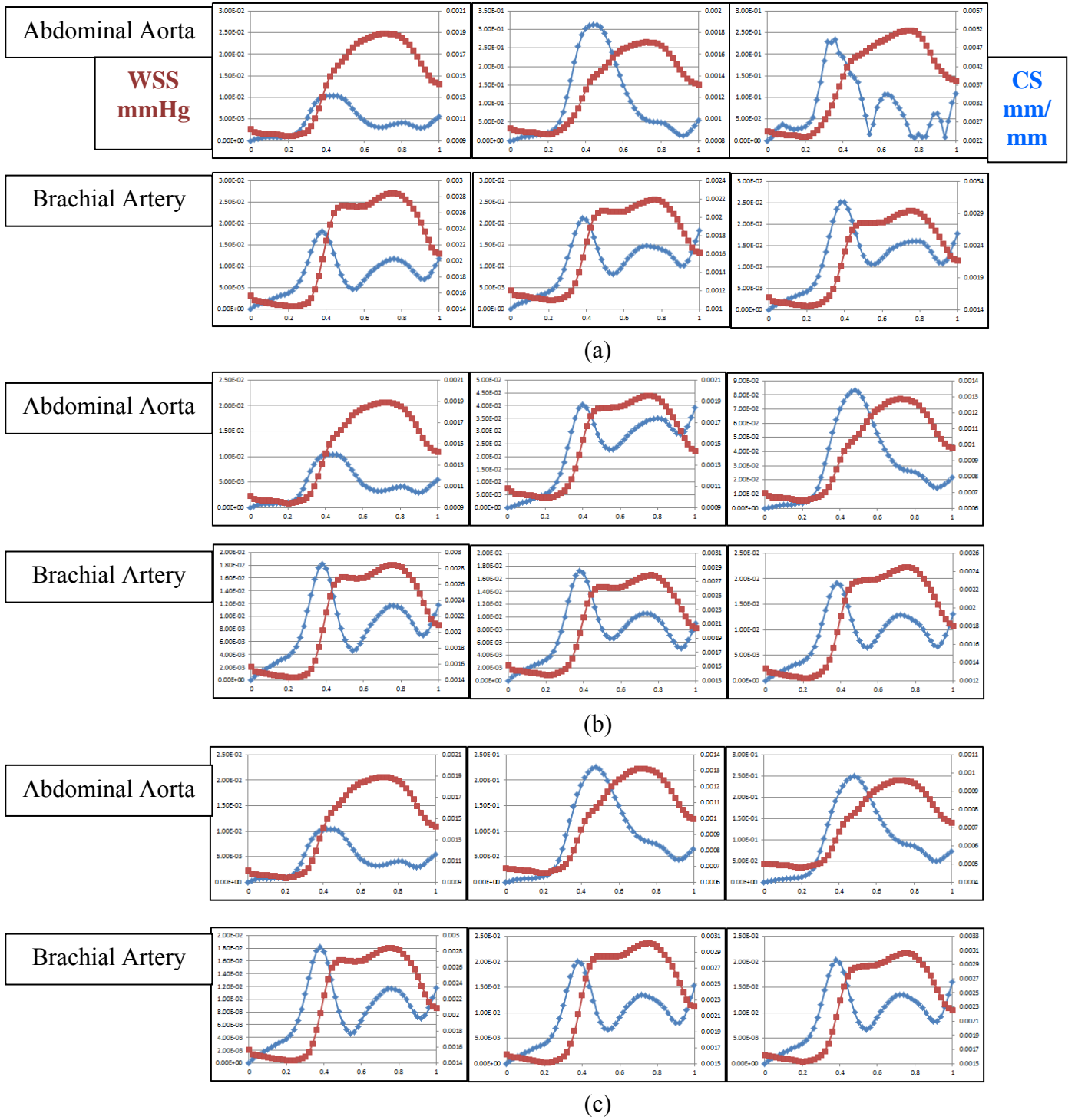


Figure 5-17: WSS and CS comparison between the healthy condition and (a) Group One, (b) Group Two and (c) Group Three unhealthy conditions. The upper left graphs represent the healthy data at the abdominal aorta and the lower left graphs represent these data at the brachial artery. The middle graphs represent the unhealthy condition (5) and the right graphs represent unhealthy condition (8)

The CFD/FE modelling analysis of WSS and CS counters along the aorta are illustrated in Figure 5-18. This figure shows WSS contours on the FSI model for two unhealthy conditions of lumen diameter ( $D_i=12.5$  and  $2.5$  mm) compared with the healthy condition of  $D_i=20$  mm. This figure also shows how WSS varies along the FSI with a changing diameter at different time domains of 0.3, 0.5 and 0.86s. The results indicate that the development of atherosclerosis affects the WSS contours at the brachial artery.

The critical time level is considered to be 0.3s, which coincides with systolic blood pressure, for investigating the distributions of WSS for a non-random atherosclerosis condition selected from group-one. Figure 5-18 shows that the contours of WSS for a very severe arterial blockage (100%) at the abdominal aorta impact significantly on the distribution of WSS at the aortic arch and its branches, compared to the control model. This finding will be investigated in-depth to determine the SPA for healthy and unhealthy conditions in Chapter 6.

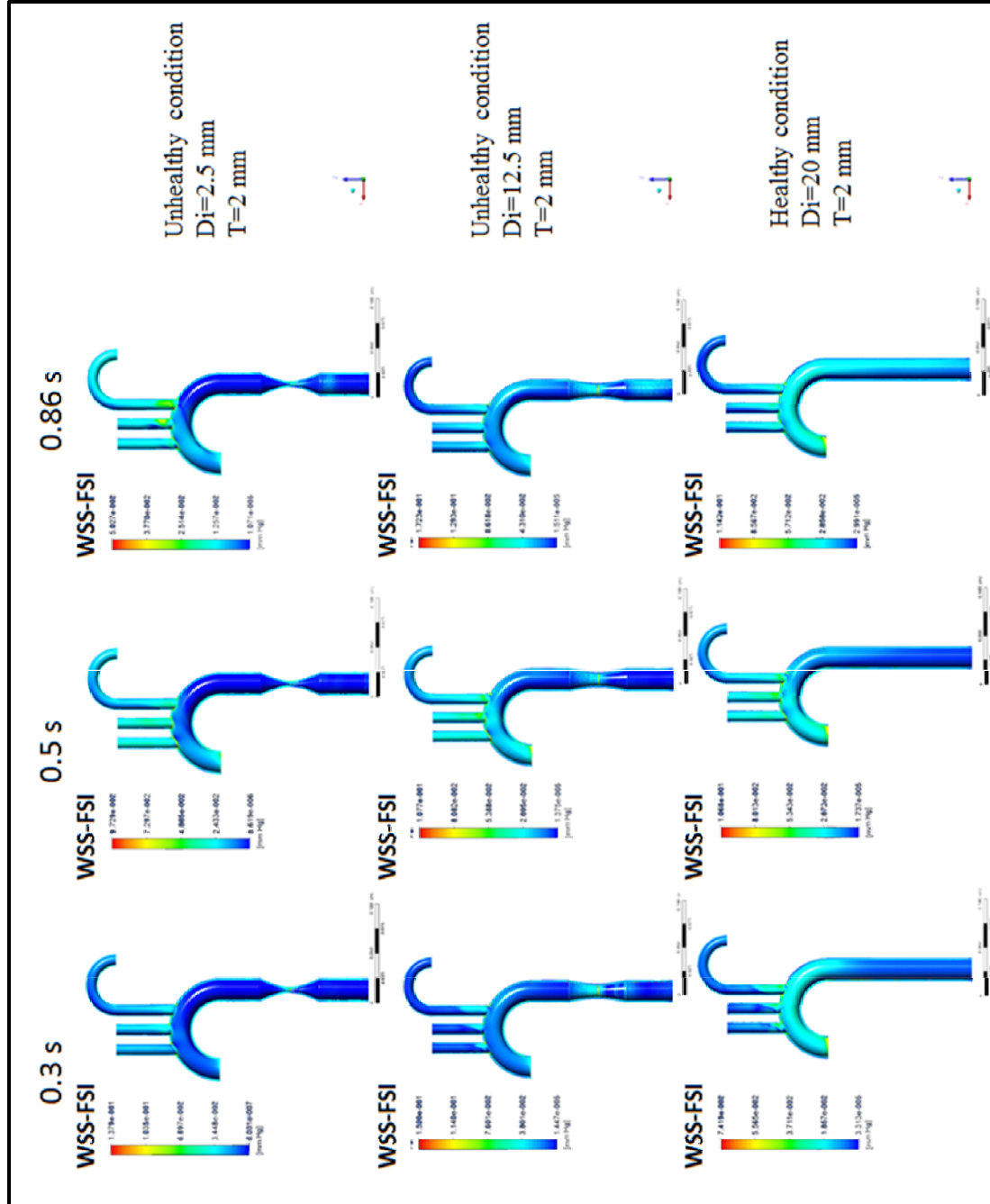
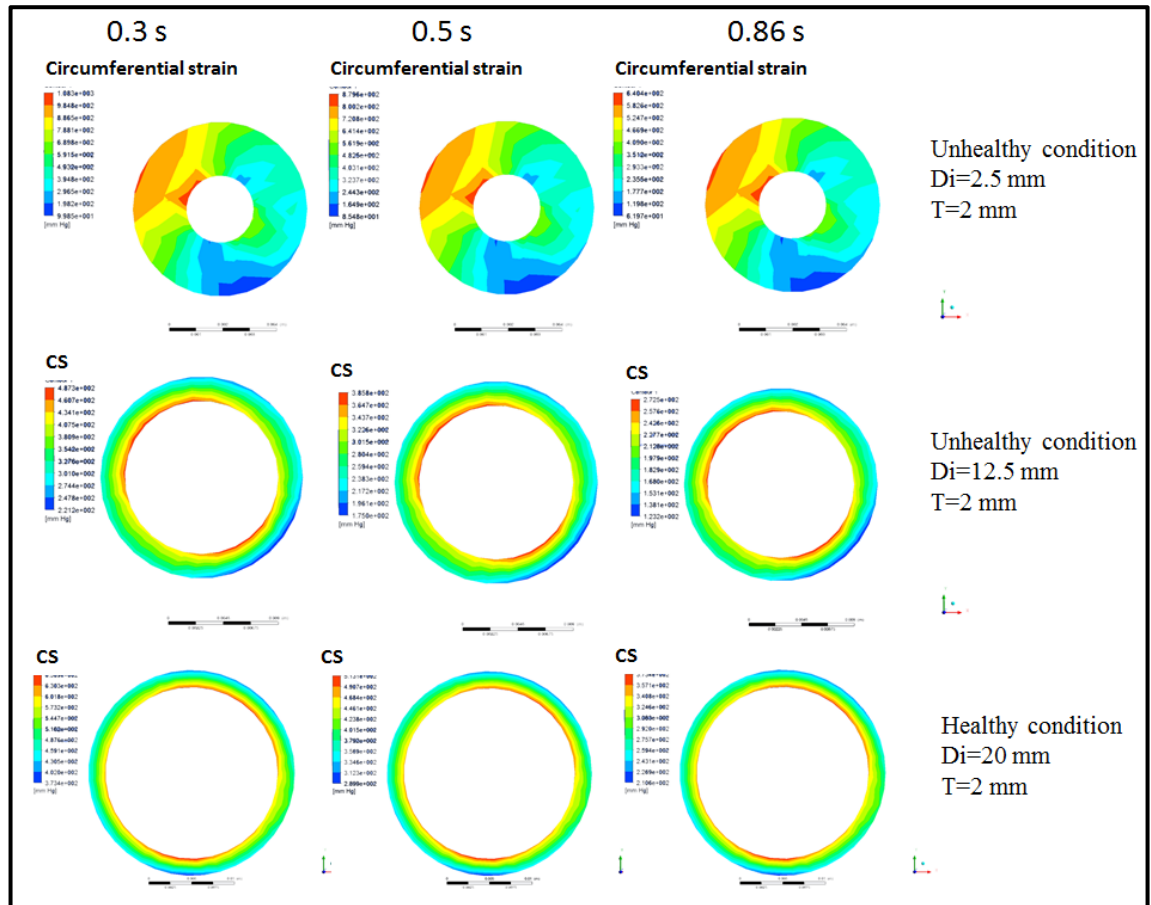


Figure 5-18: WSS-FSI for two unhealthy conditions ( $Di= 2.5$  mm and  $12.5$  mm) compared to the healthy condition, keeping the thickness constant

The findings of Figure 5-18 lead us to investigate the cross-sectional area of the disease. Figure 5-19 shows the cross-sectional contours of the CS at different times; 0.3, 0.5 and 0.86s, at the abdominal aorta for two arterial blockages of diameter conditions ( $D_i=12.5$  and 2.5 mm) compared to the healthy condition of  $D_i=20$  mm. This figure also shows that the high stiffness resulting from turbulent blood flow affects the artery wall and could injure it. This damage to the intima layer results in clot formation around the arterial infection site which could cause arterial blockages [40].



*Figure 5-19: CS at the abdominal aorta showing the development of arterial blockages in two unhealthy conditions as compared with the healthy condition*

#### 5.4.1.2 Stress Phase Angle

A comprehensive investigation of the results in Figure 5-16 was conducted to correlate the hemodynamic stress and strain waveforms in terms of the SPA. The SPA is used to compare healthy and unhealthy models for each group individually. Figure 5-20 shows the results of discrete Fourier transform (DFT) for the first harmonic which allowed for the calculation of the SPA through finding the fundamental frequency for WSS and CS from their magnitude and phase angle. Figure 5-20 (a and b) shows DFT for the healthy and unhealthy models in group-one. SPA for the healthy model at the abdominal aorta is  $0^\circ$  and the eight unhealthy conditions in this group are of a range between  $-45^\circ$  and  $-178^\circ$ . However, at the brachial artery location, the healthy SPA is  $-5^\circ$  and the unhealthy conditions are of a range between  $-10^\circ$  to  $-15^\circ$ . The SPAs in this group at the abdominal aorta indicate a negative phase caused by narrowing of the lumen diameter. Figure 5-20 (c and d in Appendix II) shows the results of the SPA for the second group of atherosclerosis conditions. These conditions have SPAs in the range of  $-99^\circ$  to  $-100^\circ$  at the abdominal aorta. However, the SPA at the brachial artery is  $-10^\circ$ . The SPAs for this unhealthy group indicate that there is no impact on hemodynamic stresses from varying the length of the disease on the hemodynamic stresses. The third group of atherosclerosis development shows a highly negative SPA of range ( $-95^\circ$  to  $-160^\circ$ ) at the abdominal aorta as shown Figure 5-20 (e and f in Appendix II). This figure also shows that the SPA at the brachial artery is in the range of  $-11^\circ$  to  $-14^\circ$ . The results of Figure 5-20 indicate that any changes occurring to the lumen diameter and thickness of the abdominal aorta could be screened non-invasively at the brachial artery. In another words, the results show that the elasticity and compliance of the arterial wall is limited

by effect of stresses and strains when a narrowing occurs and any sufficient changes to the elasticity could save the artery from blockage.

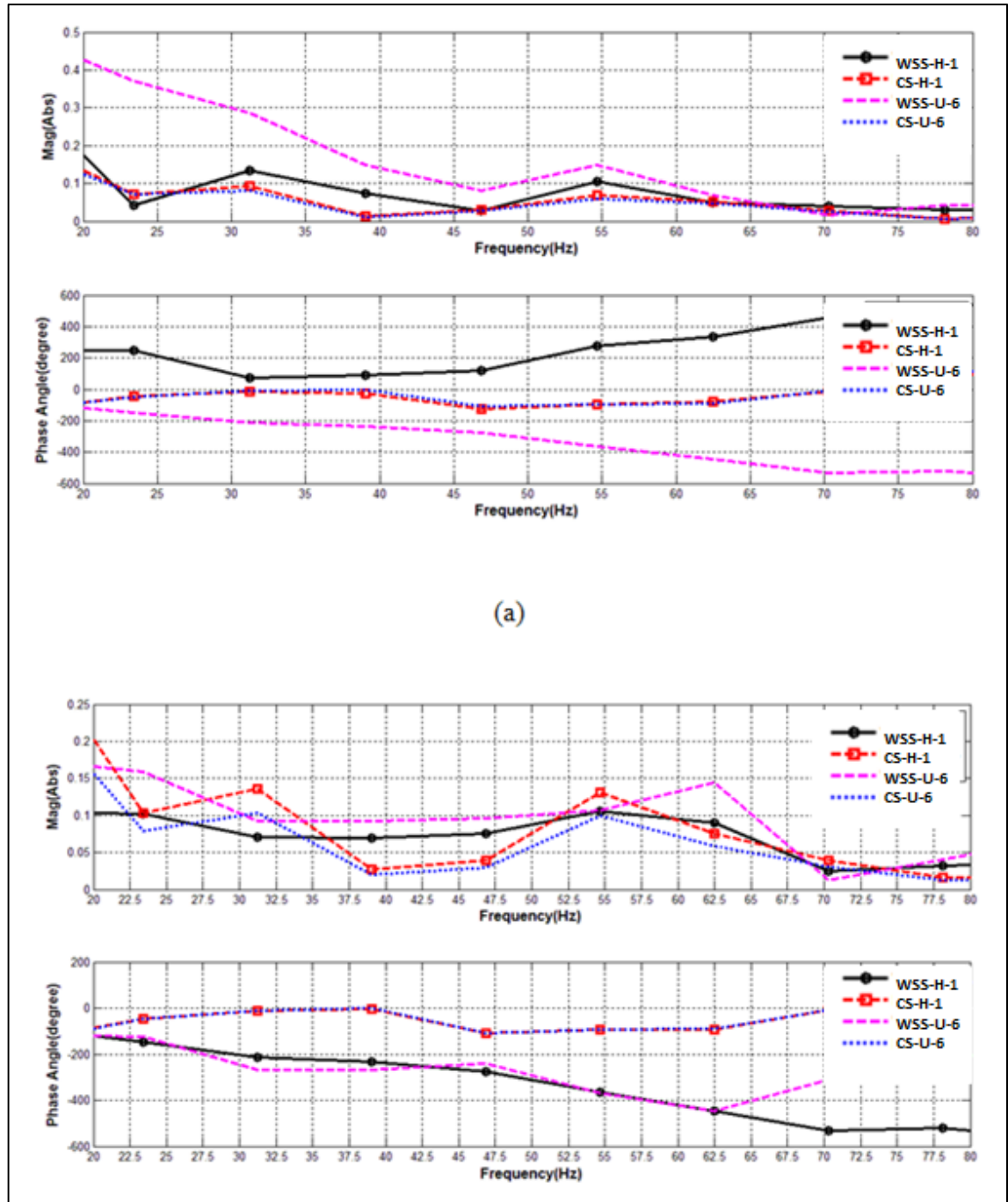


Figure 5-20: The DFT of healthy and unhealthy WSS and CS for Group One at (a) the abdominal aorta and (b) at the brachial artery (see Appendix II)

The results of Figure 5-20 are summarized in Table 5-3 illustrating the difference of SPA between the abdominal aorta and the brachial artery for the three groups.

*Table 5-3: SPA for the three groups at the abdominal aorta and brachial artery as compared to the healthy condition*

Group	SPA at the Abdominal Aorta		SPA at the Brachial Artery	
	Healthy	Unhealthy	Healthy	Unhealthy
One	0°	-45 to -178°	-5°	-10° to -15°
Two	0°	-99 to -100°	-5°	-10°
Three	0°	-95 to -160°	-5°	10° to -14°

This table will be analysed in more detail in Chapter 6 and will be validated and correlated against the *in vivo* observations.

#### 5.4.1.3 Artery Stiffness Variations

The CFD/FE healthy and diseased models adopted in this chapter are used to analyse blood pressure waveforms at two locations: the abdominal aorta and the brachial artery as shown in Figures 5-21 and 5-22, respectively. As mentioned previously, the presented models are adapted from literature and from invasive data. The results of their systolic and diastolic blood pressures are examined in terms of the arterial compliance using the augmentation index (AI). AI is a ratio calculated from the blood pressure waveform and is also a measure of wave reflection and arterial stiffness (as discussed in Chapter 4 Section 4.6.2). A previous study shows that a higher AI is associated with organ damage, so that it may be a predictor of adverse cardiovascular diseases [54-56]. AI is determined on sighting the systolic and diastolic blood pressures, the inflection point (a point on a pulse wave indicating the reflection of the backward wave as shown in Figures 5-21 and 5-22) at the abdominal aorta, and the brachial artery blood pressure waveforms as shown in Figures 5-21 and 5-22, respectively.



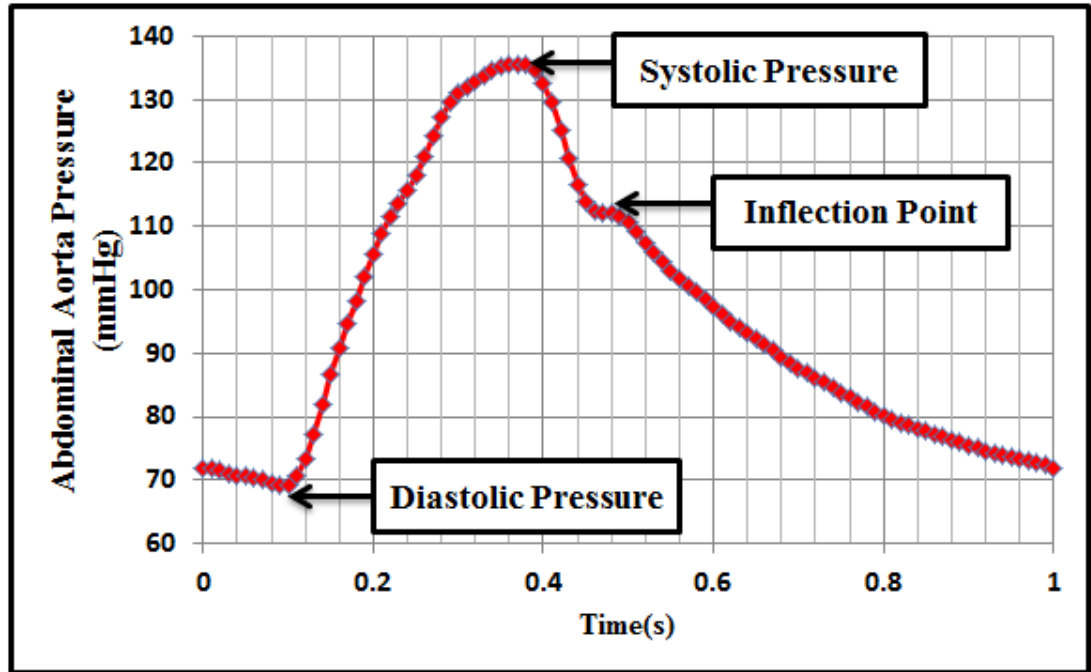


Figure 5-21: Simulated abdominal aorta pressure waveform for an unhealthy young adult (45 years old from Green Lane Hospital data)

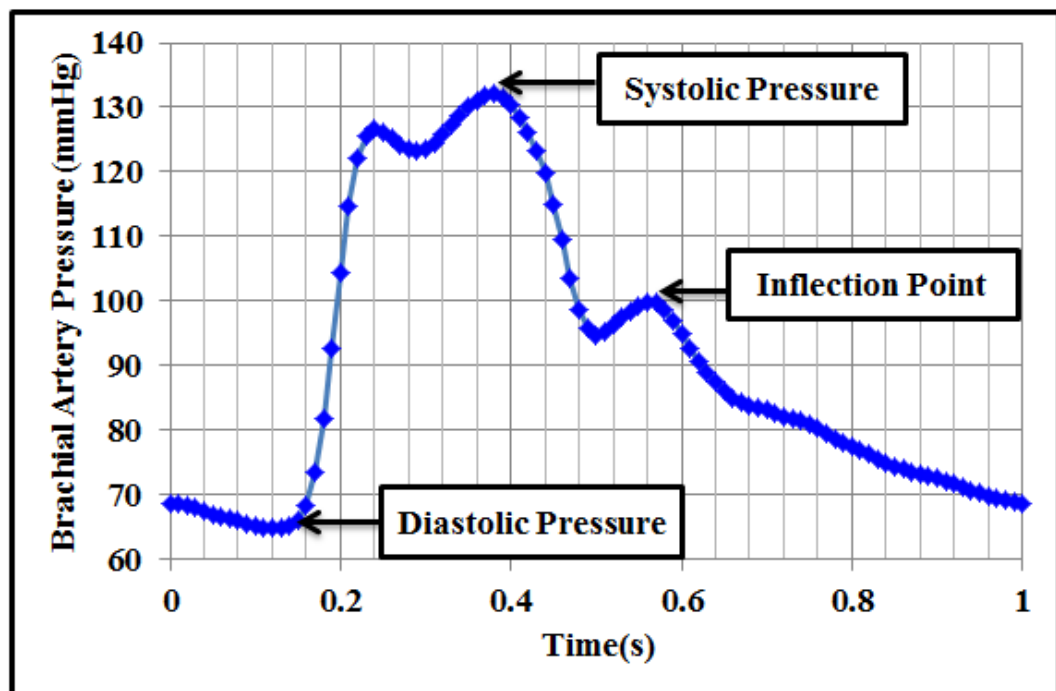


Figure 5-22: Simulated brachial artery pressure waveform for an unhealthy young adult (45 years old from Green Lane Hospital data)

These two figures are a sample of blood pressure waveforms selected from the three developed atherosclerosis groups. For each group the AI is determined at both locations, the disease site (abdominal aorta) and the brachial artery as shown in Figures 5-23, 5-24 and 5-25.

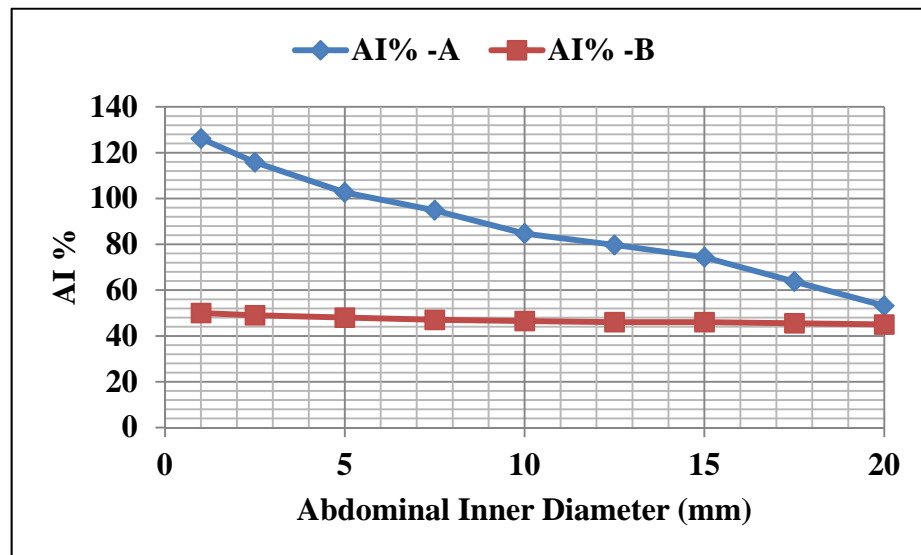


Figure 5-23: Augmentation Indices at the abdominal aorta and brachial artery for Group One, changing the inner diameter of the abdominal aorta. AI-A (Abdominal Aorta) and AI-B(Brachial artery)

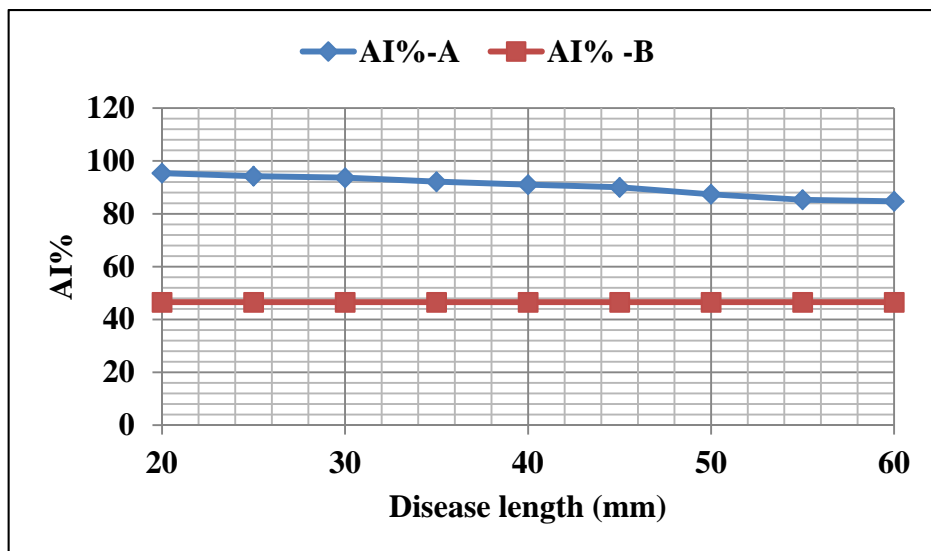


Figure 5-24: Augmentation Indices at the abdominal aorta and brachial artery for Group Two, changing the length of the atherosclerosis disease along the abdominal aorta. AI-A (Abdominal Aorta) and AI-B(Brachial artery)

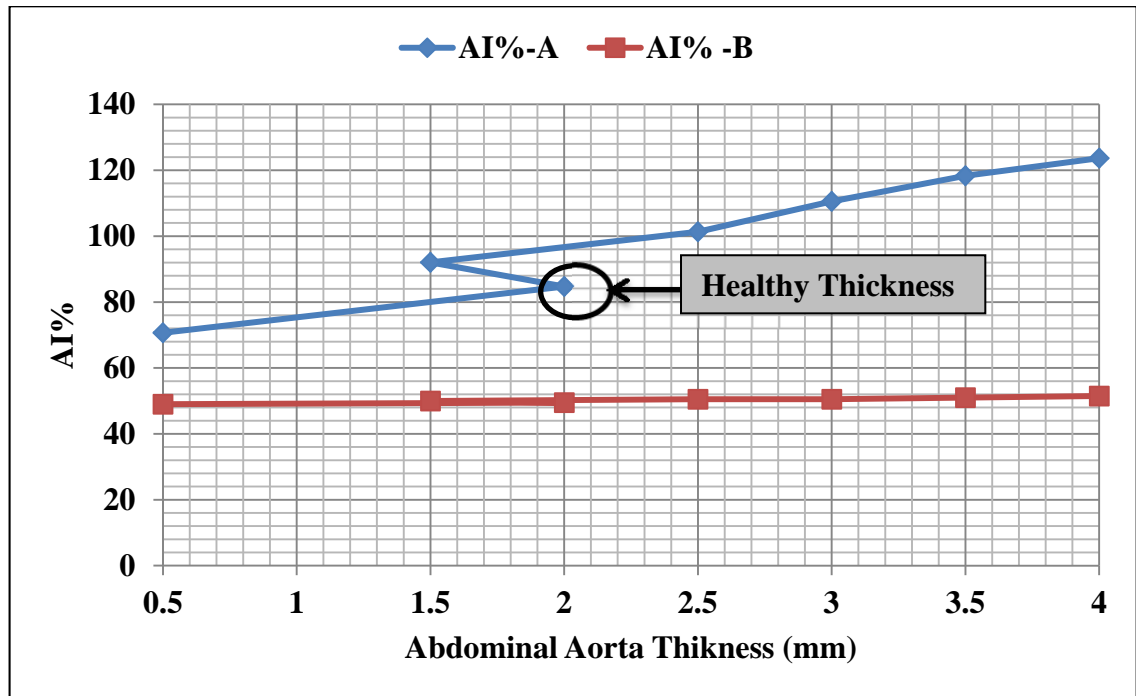


Figure 5-25: Augmentation Indices at the abdominal aorta and brachial artery for Group Three, changing the thickness of the atherosclerosis disease along the abdominal aorta. AI-A (Abdominal Aorta) and AI-B (Brachial artery)

The results of these three figures indicate that arterial wall compliance is governed by the severity of the development of atherosclerosis, which causes arterial blockages. These results will be correlated with the *in vivo* observations in Chapter 6.

#### 5.4.2 Abdominal Aortic Aneurysm

The healthy (control) model is used again to investigate the effect of a steadily growing aneurysm on systolic and diastolic blood pressures along with a calculation of the SPA. The aneurysm growth rate is simulated by increasing the inner and outer diameters for the abdominal aorta. Identifying how the aneurysm enlarges is one of the most valuable pieces of data required to perform optimal clinical management of the disease. This data is obtained by investigating the characteristics of the blood flow dynamics in healthy

and unhealthy conditions which are governed by relative compliance of the abdominal aorta vessel.

For the models under investigation, the idea is to computationally study the systolic and diastolic pressure variations for several points along the left subclavian artery. These points are spaced at 10mm distances. Figure 5-26 shows systolic pressure for the healthy model of  $D_i=20$  mm and the unhealthy model of  $D_i=26$  mm along points 1-10 of Figure 5-27. The figure indicates that systolic pressure is slightly affected by the size of the aneurysm, while other conditions (such as the material properties of the wall) that affect the pressure waveforms are held constant. However, points 1 and 2 show lower systolic pressure values compared with those of 5-27. This may be attributed to the fact that these two points are closer to the aortic arch and are affected by the vortices and circulation of the flow. Also, blood flow impacts the inlet edges of the left subclavian artery which effects the blood pressure contour. Figure 5-27 shows the pressure contour along the left subclavian artery. This shows low pressure areas at locations 1 and 2 compared with locations 3 to 10.

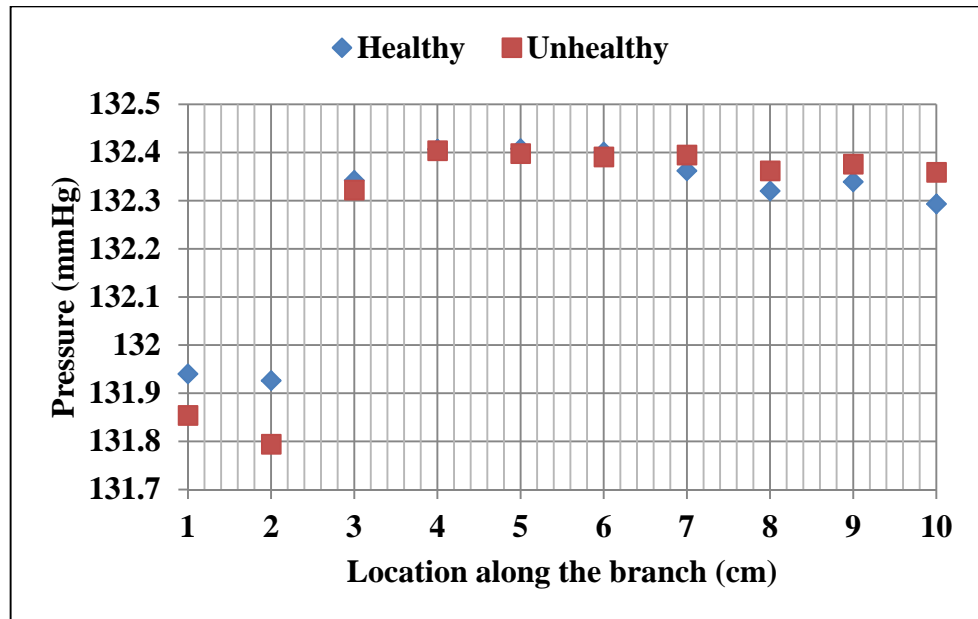


Figure 5-26: Systolic blood pressures along the left subclavian artery: Unhealthy ( $D_i=24$  mm) and unhealthy ( $D_i=26$  mm) conditions

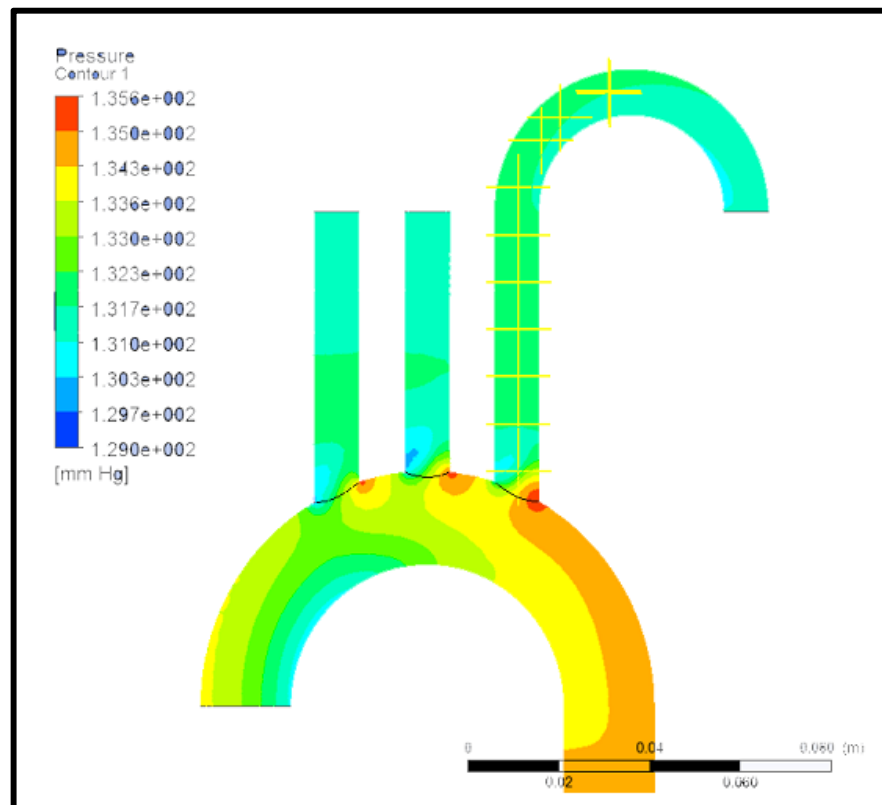
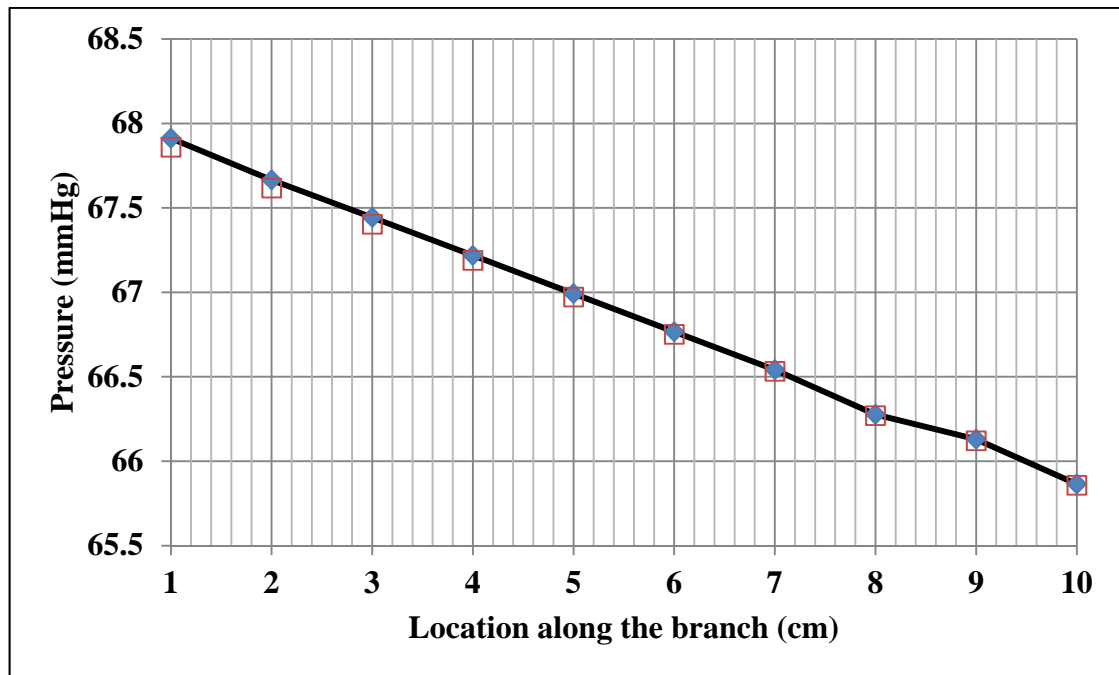


Figure 5-27: Pressure contour at the aortic arch and along the branches (left subclavian artery) to the brachial artery for an unhealthy diameter ( $D_i=26$  mm) and time = 0.3s

Figure 5-28 shows that the diastolic pressure along the left subclavian artery for healthy and unhealthy models have similar decreasing values along the distance from the branch root; however, these values need further investigation. It is very difficult to reinforce the wave at location 11 and investigate the changes of the wave at location 10 due to the system complexity and the unavailability of clinical trials to prove the accuracy of the results.



*Figure 5-28: Diastolic blood pressures along the branch as shown in Figure 5-7: for healthy ( $D_i=20$  mm) and unhealthy ( $D_i=22$  mm) conditions*

#### 5.4.2.1 Stress and Strain

Clinical observations indicate that the increase in the abdominal aorta systolic pressure in older patients with hypertension is the result of faster waves travelling down the artery and merging with stronger reflected waves [71-74]. This together with the increase in the ratio of lumen diameter, results in an increase in systolic pressure in the abdominal aorta. This obviously causes an increase in the wall stresses. In this study, the variation of WSS (representing the shear stress attacking the inner wall) and CS (representing the stretching of the artery wall due to the pulsatile blood flow) waveforms in terms of propagation time delay are presented in Figure 5-29 for healthy and unhealthy models at the brachial artery (a & b) and at the abdominal aorta (c & d), respectively.

Figure 5-29 also shows that CS precedes WSS for an unhealthy model with indication of an increase in the maximum elasticity at the artery wall (location 11) for the abdominal aortic aneurysm. This means that an aneurysm growth does occur at regions of low WSS [104-105]. Furthermore, the luminal hemodynamics and the resulting pressure distribution induce WSS and contribute to the stress developing within the aneurismal wall, thus increasing the risk of rupture. This may imply a possibility of a rupture due to an increase in CS values at the location of the aneurysm. These results show that the elasticity of the arterial wall is limited to the effect of stresses when a rupture occurs and any sufficient changes to the elasticity could save the artery from rupture.

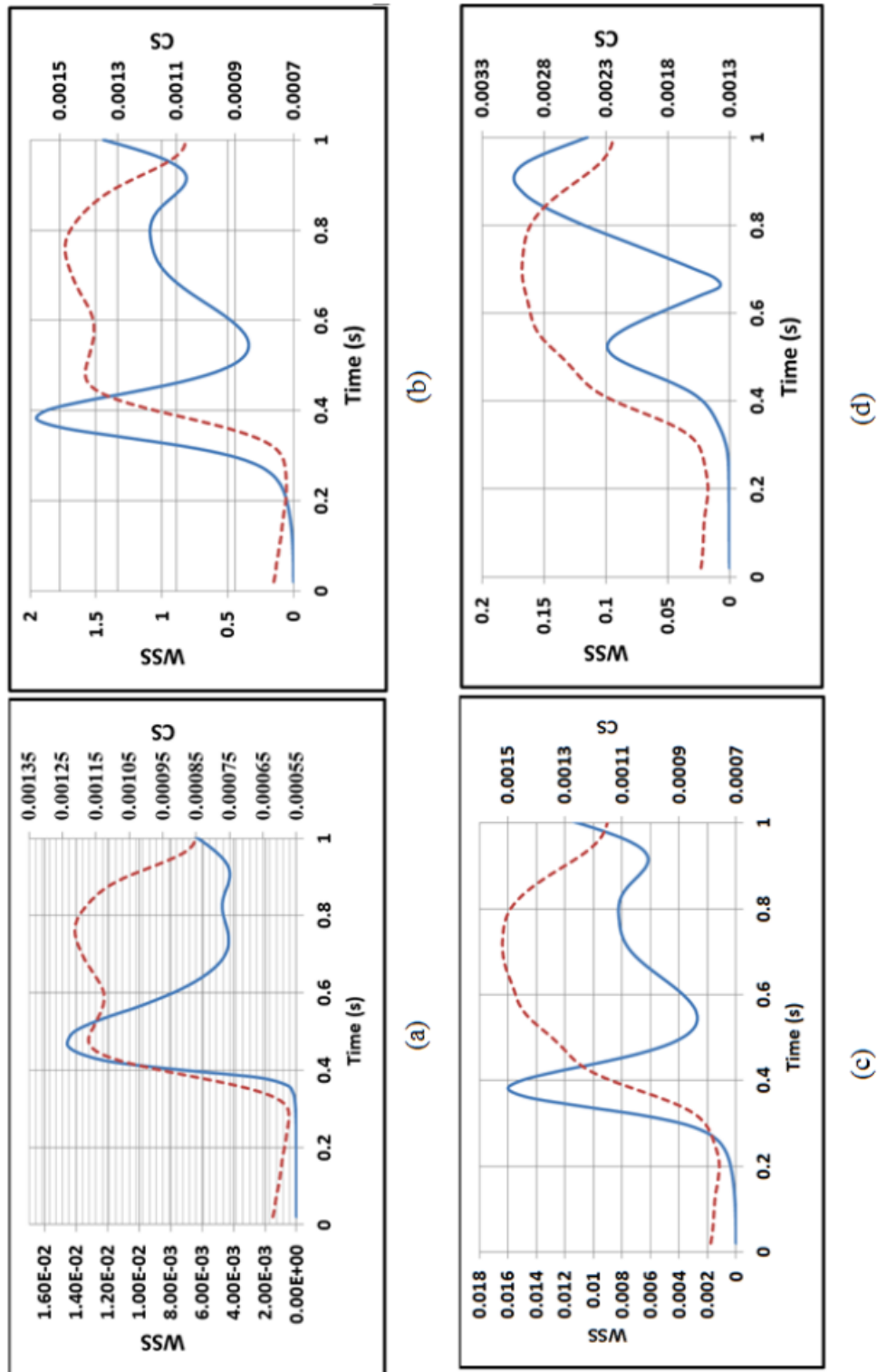


Figure 5-29: WSS (solid) mmHg and CS (dotted) in terms of  $\Delta t$  for (a) healthy and (b) unhealthy models at location 10 brachial artery (c) or healthy and (d) for unhealthy model at location 11 abdominal aorta



#### **5.4.2.2 Stress Phase Angle**

To have an insight into the relationship between SPA and the pulse wave, further analysis of Figure 5-29 is performed using the DFT transfer function (as discussed in Section 5.4.1.2) as shown in Figure 5-30. Figure 5-30 compared the SPA of the healthy and unhealthy conditions at the abdominal aorta range ( $0^\circ$  to  $-0.05^\circ$ ) and at the brachial artery of range ( $-5^\circ$  to  $-7.5^\circ$ ). The SPA for unhealthy conditions increases proportionally to the enlargement of the abdominal lumen diameter and developing aneurysm. For example, the mild stage of aneurysm has a range of SPA at the abdominal aorta of  $-30^\circ$  to  $-56^\circ$ . Increasing the diameter of the abdominal aorta while keeping its thickness constant, the SPA ranges are  $-60^\circ$  to  $-79^\circ$ , which indicates moderate risk. SPA indicates a very high risk when the abdominal aorta diameter extends to the range of 52 - 60 mm with a stress phase range of  $-125^\circ$  to  $-164^\circ$ . These results are investigated and compared in depth in Chapter 6.

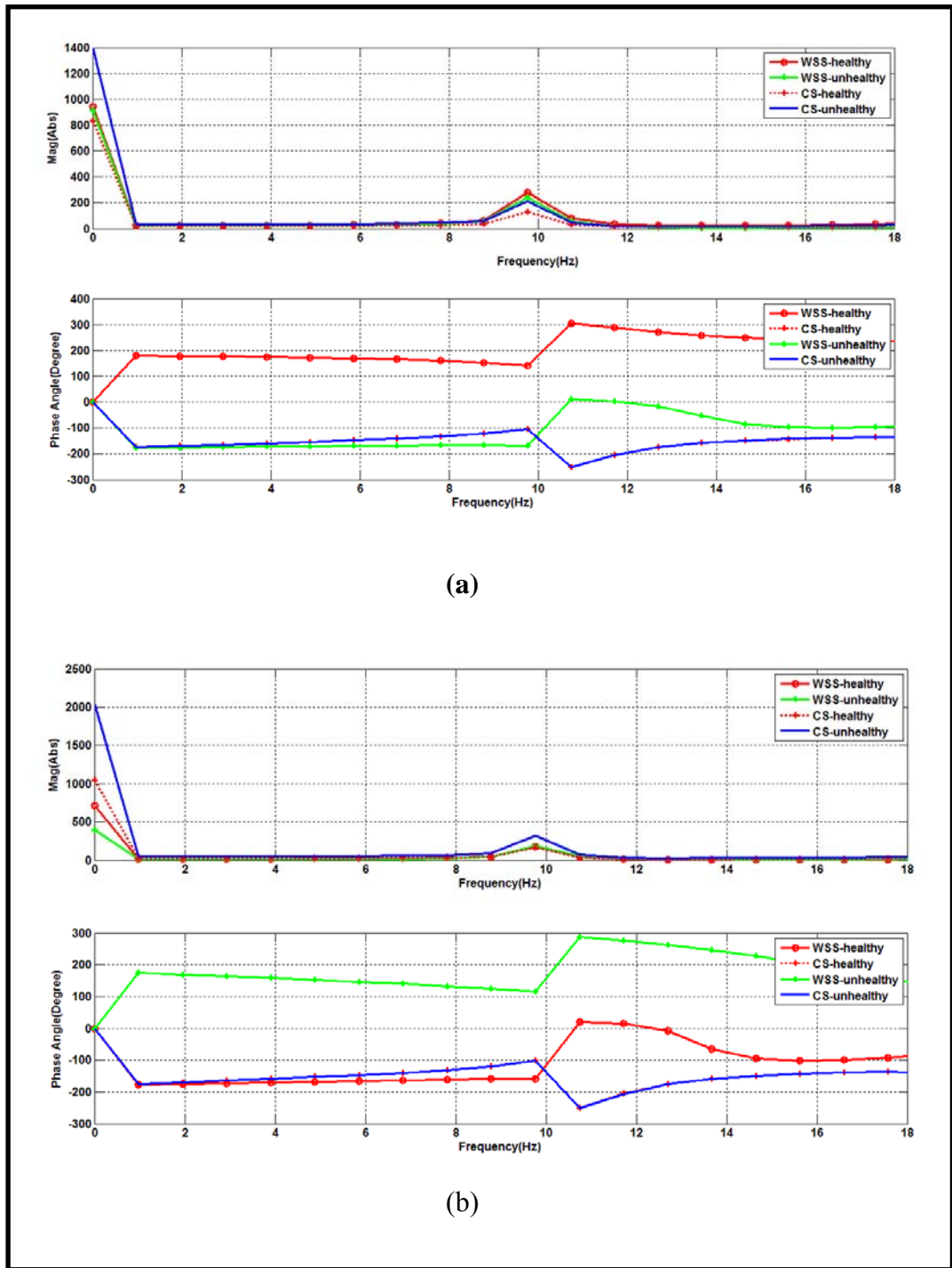


Figure 5-30: Amplitude and phase angle vs. frequency at (a) location 10 brachial artery (b) location 11 abdominal aorta: WSS-healthy (-o-), WSS-unhealthy (-I-), CS-healthy ('+') and CS-unhealthy (solid)

### 5.4.2.3 Arterial Wall Stiffness Variation

Age is the leading factor in AAA. It seems reasonable to assume that the primary cause of AAA lies in the coupling between the specific shape changes of the vessel (length, diameter and wall structure) which normally result from the aging process and the hemodynamic changes [89-91]. Arterial stiffness is investigated in terms of the Augmentation Index (AI), which is a measure of wave reflection and arterial stiffness. In this study, stiffness is investigated at constant arterial wall material elasticity whilst changing the shape and geometry of the aneurysm.

Figure 5-31 shows the AI in reference to the development of aneurysm size for both locations 10 (brachial artery) and 11 (abdominal aorta) as in Figure 5-7. It is clearly indicated that AI variation is highly significant at location 11 and minimal at location 10. This indicates that the changes in aneurysm size have more impact on the wave shape at the abdominal aorta than at the left subclavian artery. This may imply development of an abdominal aortic aneurysm rupture at location 11, due to reduced values of AI which indicate very low stiffness. This can be further investigated by considering the systolic pressure as a function of lumen diameter, as shown in Figure 5-32. This figure indicates that small changes in the systolic pressure at location 11 may have a slight effect on pressure at location 10, but is not significant enough to detect an aneurysm by measuring pulse waves only at location 10. Further work is needed to investigate how it is possible to reinforce the wave at location 11 so that a change at location 10 can be detected.

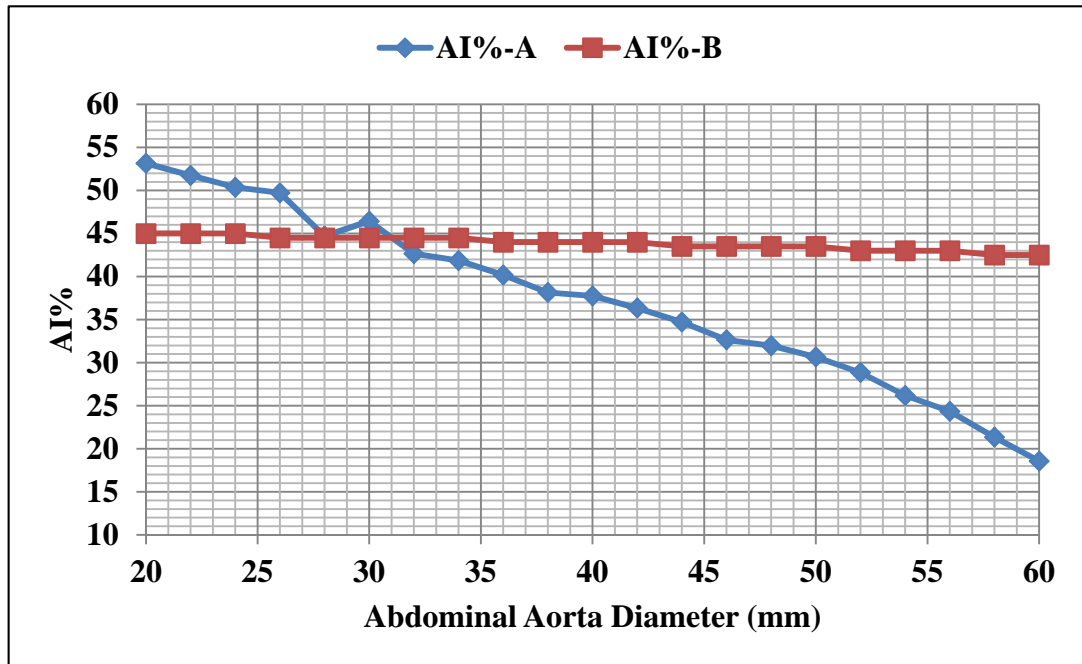


Figure 5-31: Augmentation Indices (AI) for the twenty abdominal aortic aneurysm developments at the abdominal aorta (A) and at the brachial artery (B)

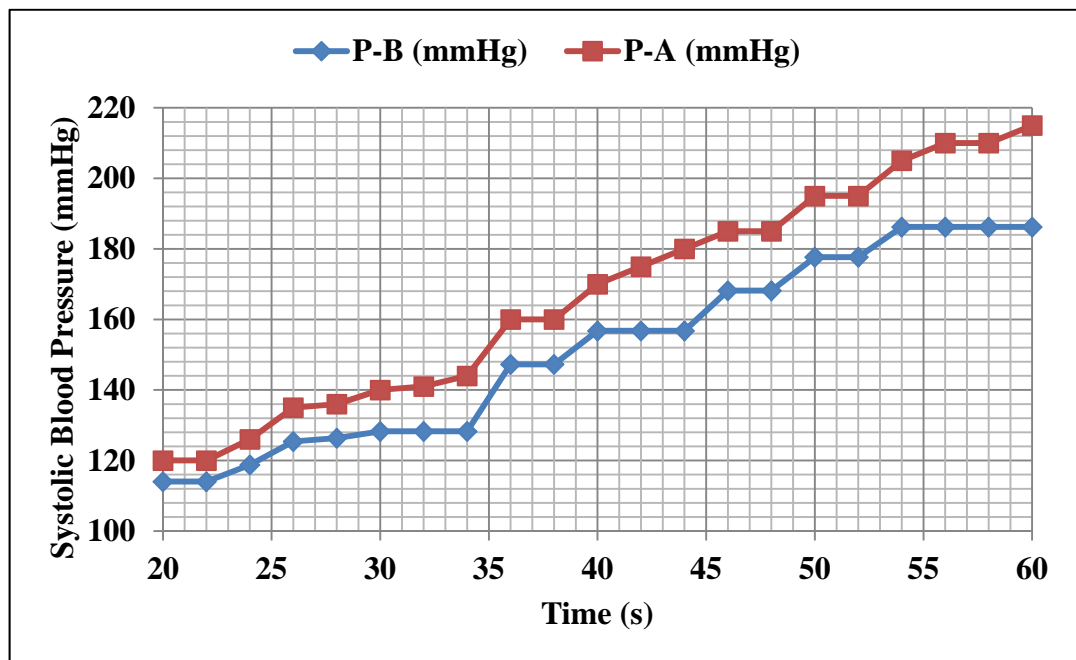


Figure 5-32: Systolic blood pressures at the abdominal aorta (A) and at the brachial artery (B)

## **5.5 Closure**

The CFD/FE models for atherosclerosis and abdominal aortic aneurysm diseases are used to simulate abdominal blood pressure waveforms and the SPA on arterial wall compliance in human models. A number of models are developed to analyse the early stages of disease development. The models' sensitivity to variations of important parameters is then investigated by changing one parameter at a time and observing the changes in waveforms feature points and indicators. These results will be correlated and analysed in more detail in Chapter 6. Chapter 6 will correlate the findings of the CFD/FE models and establish a new formula for non-invasively diagnosing cardiovascular disease based on any changes occurring to arterial wall compliance.

## **Chapter 6 Discussion and Analysis**

### **6.1 Introduction**

The computational and experimental results given in Chapter 4 for the animal model and the computational results of the human model given in Chapter 5 are discussed in detail in this chapter.

The significance of the models developed in this thesis is examined and we discuss how they may be used to investigate the effect of atherosclerosis and aneurysm at locations further from the disease sites.

The consequences of the atherosclerosis CFD/FE models at the abdominal aorta correlated to the development of the disease in its earlier stages and is discussed in Section 6.2. Section 6.3 discusses the correlation of abdominal aortic aneurysm development with brachial artery blood pressure measurement. The animal CFD/FE model is compared to its experimental investigation and a formula and colour-coded chart for diagnosing cardiovascular diseases non-invasively are developed in Section 6.4.

### **6.2 Atherosclerosis Development Formula**

The results presented in Chapter 5 are investigated in more depth to derive a new formula for screening atherosclerosis in its early stages and are correlated to the non-

invasive measurement of blood pressure at the brachial artery. This formula is based on the results of the three scenario groups developed using CFD/FE methods in Chapter 5.

### **6.2.1 Atherosclerosis Group-One**

This group, as explained in Chapter 5 Section 5.2.1.1, consists of one healthy (control) condition compared to eight diseased conditions. The comparison leads to a formula illustrating the development of atherosclerosis based on the narrowing of the abdominal aorta by increments of 2.5 mm to reach full blockage. The results show that narrowing the lumen diameter at the abdominal aorta impacts blood pressure waveforms measured at the brachial artery. In addition, the results of this group are correlated to the compliance of the artery wall using the AI. This shows that AI increases with the development of arterial blockage as seen in an increase of SPA. These are correlated in a diagram which indicates the high risk of narrowing the abdominal aorta. From a mechanical perspective, the hemodynamic characteristics calculated at the abdominal aorta are investigated through non-invasive brachial blood pressure at the brachial artery as shown in Figure 6-1. This figure shows that systolic brachial blood pressure increases proportionally with increasing compliance of the abdominal aorta as the lumen diameter reaches the fully-blocked stage. Moreover, the SPA shows that the hemodynamic stresses impact the abdominal aorta and increase the risk of developing arterial blockages. These results are reflected in the brachial systolic blood pressure which any medical doctor could assess using the cuff blood pressure measurement method.

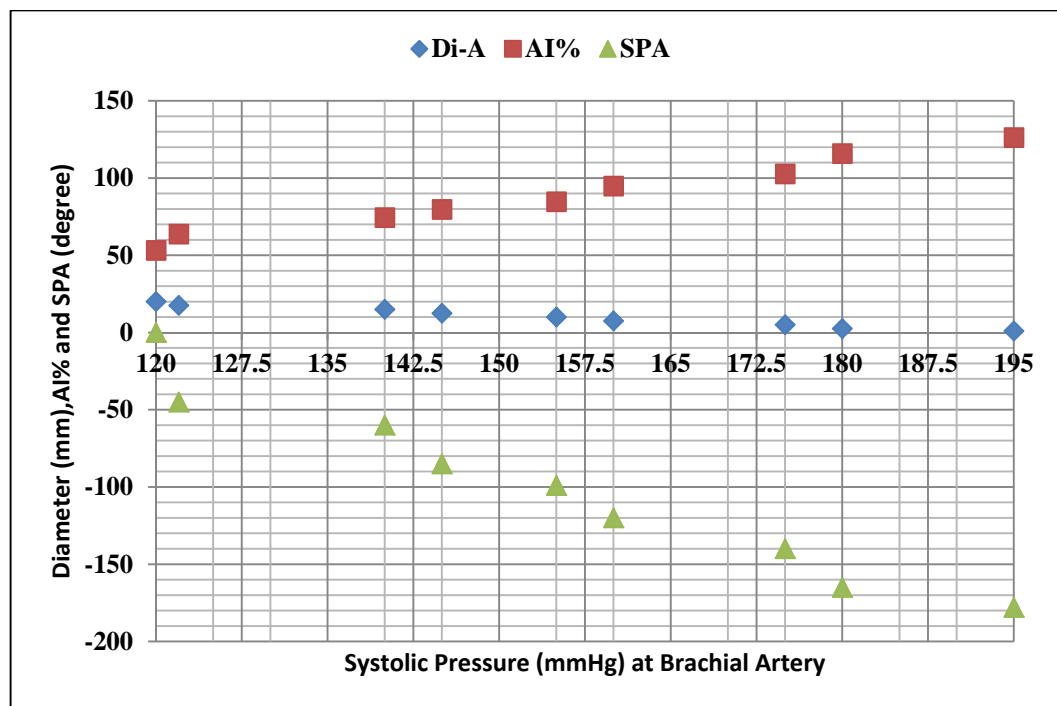


*Figure 6-1: Correlating brachial blood pressure with the lumen diameter, AI and SPA (at the abdominal aorta) for Group One of Atherosclerosis diseases*

Figure 6-1 does not help medical doctors to determine the amount of risk of any disease, therefore, these results need to be translated into medical terms to enable simple disease risk assessment. Figure 6-2 shows the combined results of group-one as a colour-coded chart, which could be referred to quickly and easily by any medical staff when screening for the risk of atherosclerosis. This figure correlates changes in the lumen diameter, the arterial compliance (AI) and SPA with brachial artery pressure. The brachial pressure is validated against the invasive data from Pulsecor (NTX/09/11/109) from seven non-random patients selected for this thesis. This figure indicates when it is most likely that atherosclerosis could occur in a male patient aged 45 by measuring the systolic and diastolic blood pressure non-invasively from the cuff. The results show the healthy values of blood pressure (120/75 mmHg), and the high risk value (195/110 mmHg) which indicates the patient is at significant risk of developing atherosclerosis.



The presented chart in Figure 6-2 could be used by any medical doctor to screen for abnormal cardiovascular disease development and, if found, further medical investigation could recommend to the patient.

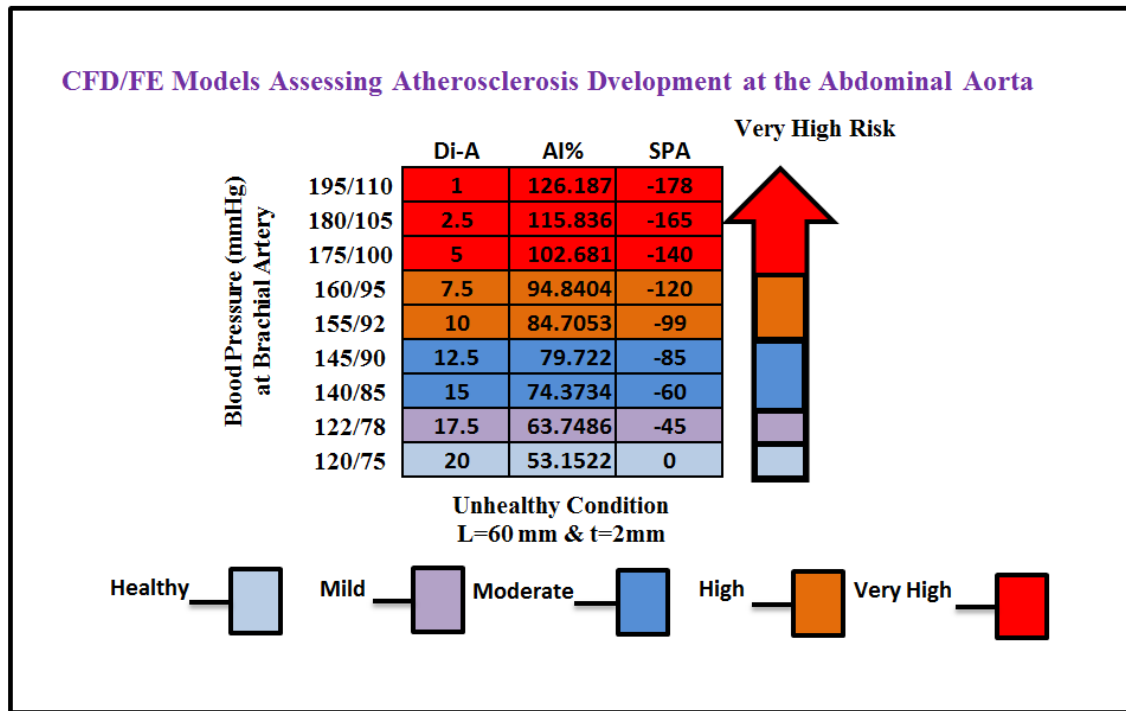


Figure 6-2: Diagram illustrating the amount of risk for developing atherosclerosis through narrowing the abdominal aorta

### 6.2.2 Atherosclerosis Group-Two

This group was developed and simulated in Chapter 5 and represents change to non-randomly selected atherosclerosis conditions caused by changing the length of the disease along the abdominal aorta. This CFD/FE model is tested on an unhealthy condition with  $D_i=10$  mm,  $D_o=14$  mm and  $L=60$  mm and decreasing  $L$  to reach 20 mm. The results of this model indicate that changes to the length of the disease condition do not have a measurable effect on the risk of atherosclerosis as shown in Figure 6-3. This figure illustrates the changes in length and the calculated AI% and SPA from CFD/FE

models. This figure could also be translated into a format useful for medical practitioners to identify risk for atherosclerosis diseases occurring at the abdominal aorta as shown in Figure 6-4.

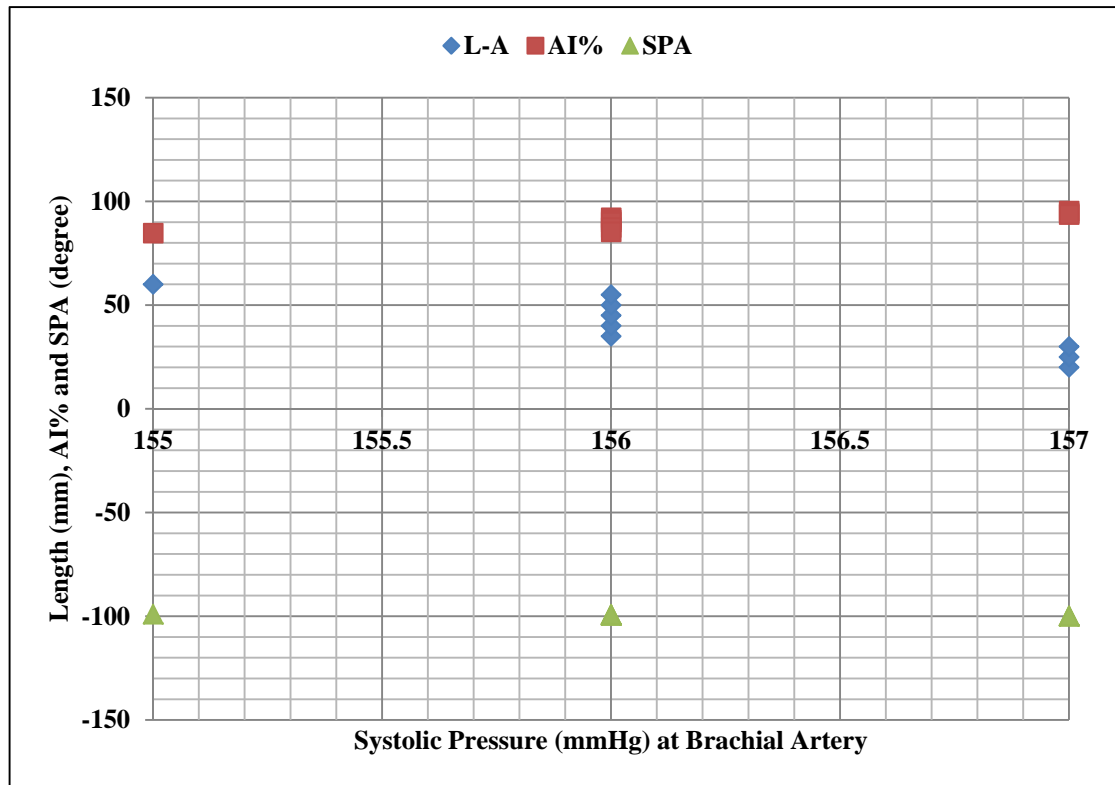


Figure 6-3: Correlating brachial blood pressure with the length of the disease along the abdominal aorta, AI and SPA calculated at the abdominal aorta for Group Two of Atherosclerosis with  $D_i=10$  mm,  $D_o=14$  mm and  $L=60$

Figure 6-4 shows the amount of risk of atherosclerosis development correlated to the length of the unhealthy condition. The systolic and diastolic brachial blood pressure indicates that changing the length of the disease does not affect the arterial compliance and SPA. This group indicates that the length of the diseased artery does not show any significant impact at the brachial artery using cuff blood pressure measurement method.

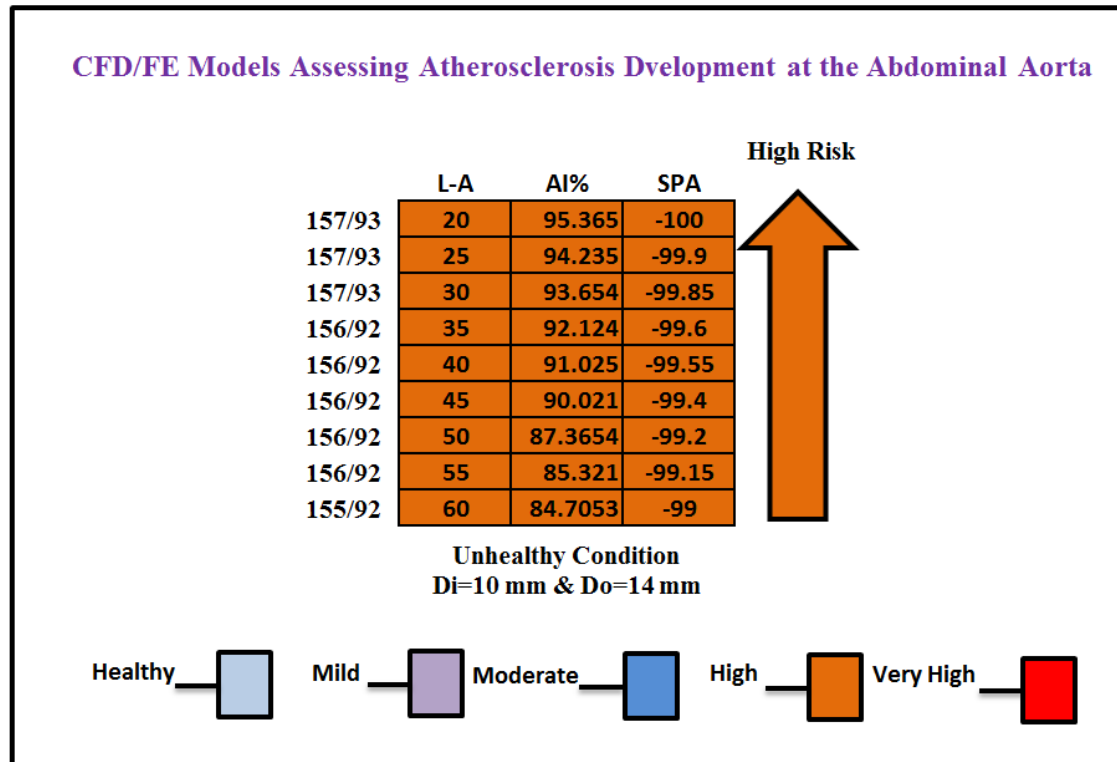


Figure 6-4: Diagram illustrating the risk of developing atherosclerosis from changing the length of the atherosclerosis condition at the abdominal aorta

### 6.2.3 Atherosclerosis Group-Three

In group-three changes to arterial wall thickness affecting blood pressure measurements at the brachial artery were tested. This group illustrates four different conditions tested from group-one, examining how arterial compliance at the abdominal aorta affects brachial artery blood pressure. The first group of unhealthy conditions represents  $D_i=7.5$  mm and  $L=60$ mm, changing the thickness of the abdominal aorta wall. Figure 6-5 (a) shows how compliance increases with an increase in systolic pressure. Moreover, the SPA is highly negative and with disease development becomes close to  $-160^\circ$ . This finding is tested for three other conditions of arterial blockages severities with  $D_i=10$ , 15 and 17.5 mm and shows that a small lumen diameter with a thick artery wall indicates a very high risk compared to the early stage of disease development. The

results also show that arterial compliance increases proportionally with the increasing severity of atherosclerosis and causes a high reading of systolic and diastolic blood pressure at the brachial artery. This is due to stress attacking the artery wall due to the highly negative value of the SPA which amplifies the shape of the pulse. This finding is interpreted as an illustration for medical practitioners as shown in Figure 6-6. This figure shows the four groups of developing atherosclerosis based on changes to arterial wall thickness at the abdominal aorta. In each one of these four groups any medical doctor could identify the risk of atherosclerosis development non-invasively by measuring brachial blood pressure.

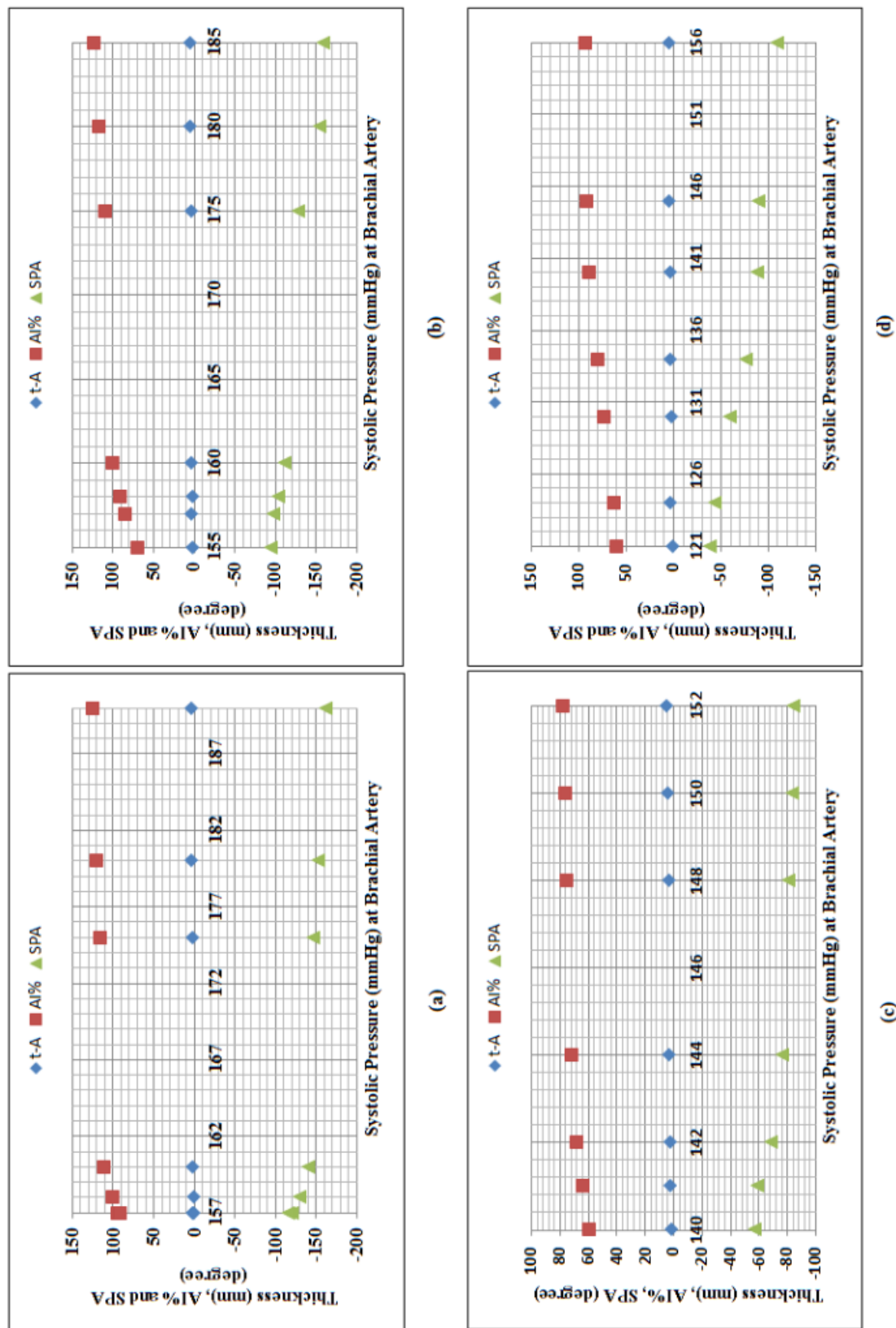


Figure 6-5: Systolic blood pressure at the brachial artery for unhealthy conditions (a)  $Di=7.5\text{ mm}$ , (b)  $Di=10\text{ mm}$ , (c)  $Di=15\text{ mm}$  and (d)  $Di=17.5\text{ mm}$

Figure 6-6 shows the assessment of atherosclerosis disease development for a 45 year old male patient (data collected from Green Lane Hospital with ethical approval number (NTX/09/11/109)) based on brachial blood pressure measurements. This is correlated to the compliance of the abdominal aorta by addressing changes to the arterial wall thickness, AI% and the SPA calculated from CFD/FE models.

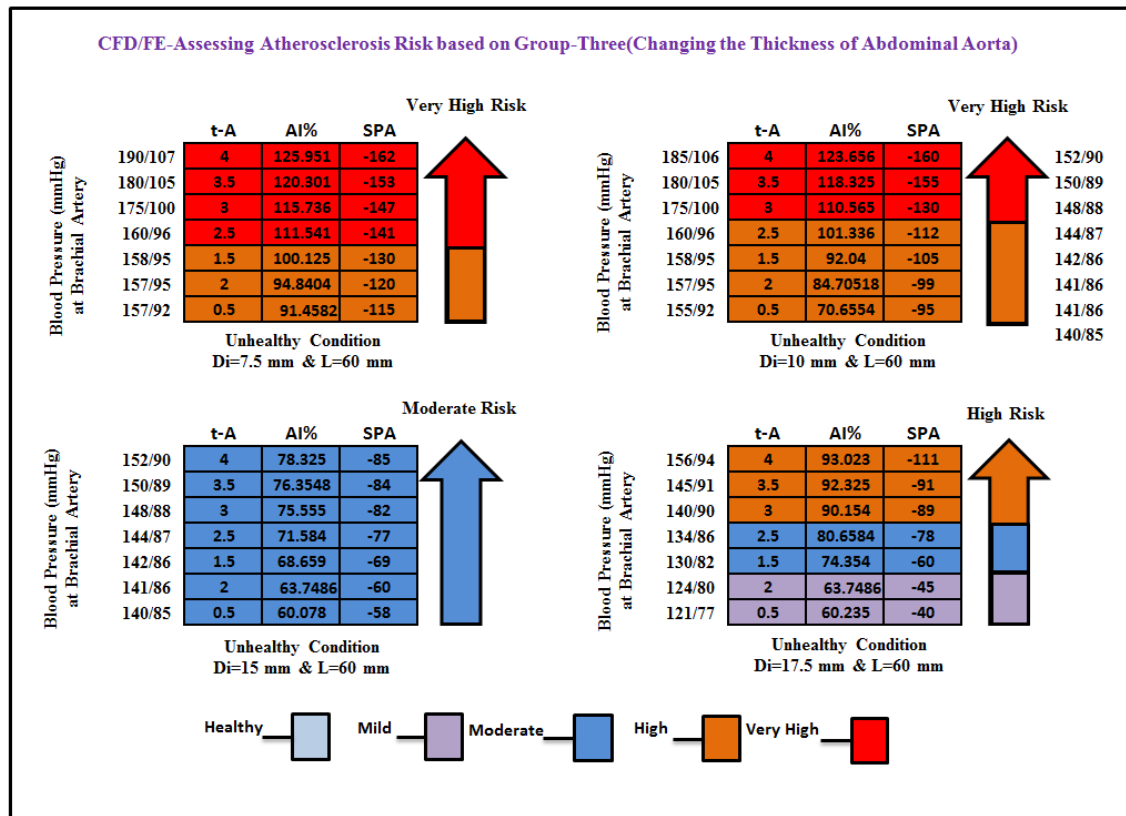


Figure 6-6: Diagram illustrating the risk of developing atherosclerosis through change to the thickness of the abdominal aorta wall in four unhealthy conditions with different lumen diameters

## 6.2.4 Atherosclerosis Risk Assessment

Biomechanically, atherosclerosis risk is assessed by determining the relationship between the hemodynamic stresses and the characteristics of the shape of the disease (diameter and thickness). From a mechanical perspective, analysing group one of atherosclerosis in its early stage is governed by two equations using the logarithmic

form: Equation 6-1 (from Figure 6-7) for assessing lumen diameter and Equation 6-2 (from Figure 6-4) for assessing the arterial compliance.

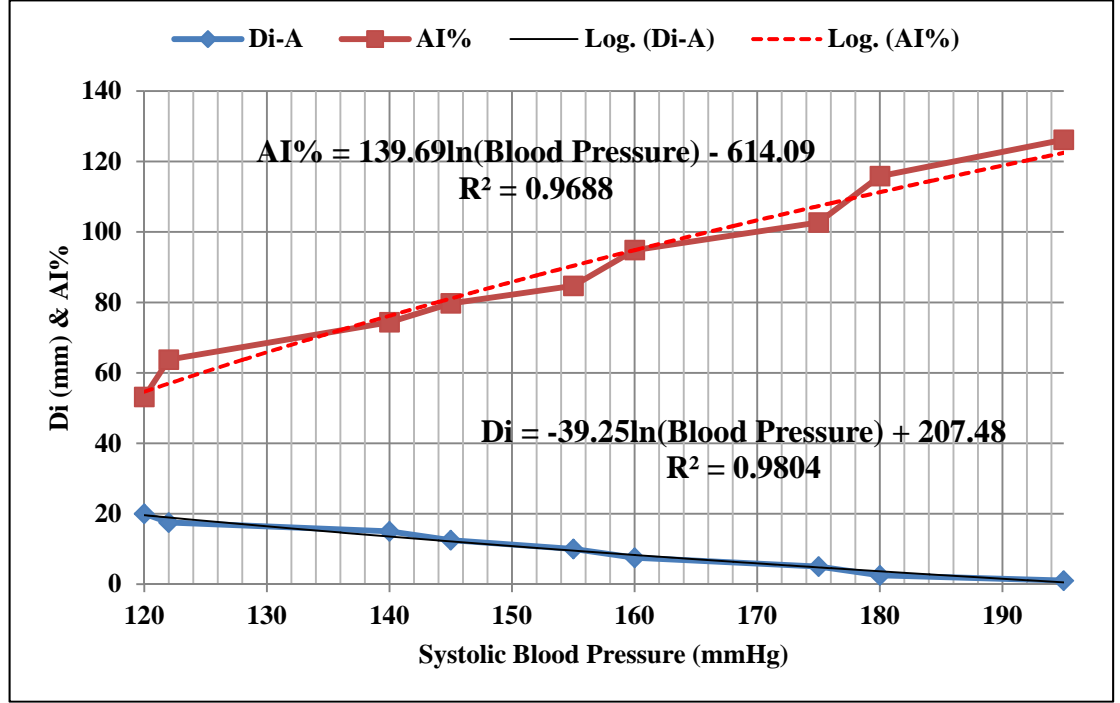


Figure 6-7: Correlation between the Di, AI (at the abdominal aorta) against the systolic blood pressure at the cuff for atherosclerosis

$$Di_{unhealthy} = -39.25 \ln (BP_{Measured\ at\ Brachial\ Artery}) + 207.48 \quad (6-1)$$

$$AI \% = 139.69 \ln (BP_{Measured\ at\ Brachial\ Artery}) - 614.09 \quad (6-2)$$

Solving these two equations simultaneously enables identification of atherosclerosis along the abdominal aorta for a particular patient aged 40-50 years old. These formulas require further investigation and clinical validation using data from humans, including the impact of weight, height and gender. In this thesis, they will be validated and tested using animal models in Section 6.4.1.

### **6.3 Abdominal Aortic Aneurysm Formula**

The 20 unhealthy conditions of abdominal aortic aneurysm are compared to the control model. The comparison shows that increasing the lumen diameter affects abdominal aorta compliance and results in increased blood pressure at the brachial artery. Figure 6-8 shows changes to the lumen diameter, AI% and the SPA correlated to systolic blood pressure at the brachial artery. Assessing the risk of arterial rupture using CFD/FE models has advantages and disadvantages which need to be discussed. The CFD/FE models have the capability of predicting when abdominal aortic aneurysm will occur based on changes to lumen diameter; however, the computational modelling has a margin of error equal to 1.1% due to the computational, mesh, geometrical and numerical errors.

Figure 6-8 also shows a drop in the negative values of the SPA from  $-60^{\circ}$  to  $-79^{\circ}$  which indicates the collagen degradation is largely balanced by collagen production. Very high values of SPA between  $-125^{\circ}$  to  $-164^{\circ}$  indicate that accelerated collagen degradation exceeds repair. This high negative value indicates that the abdominal aorta could rupture at any time, according to Figure 2-5 in Chapter 2, Section 2.2.2.



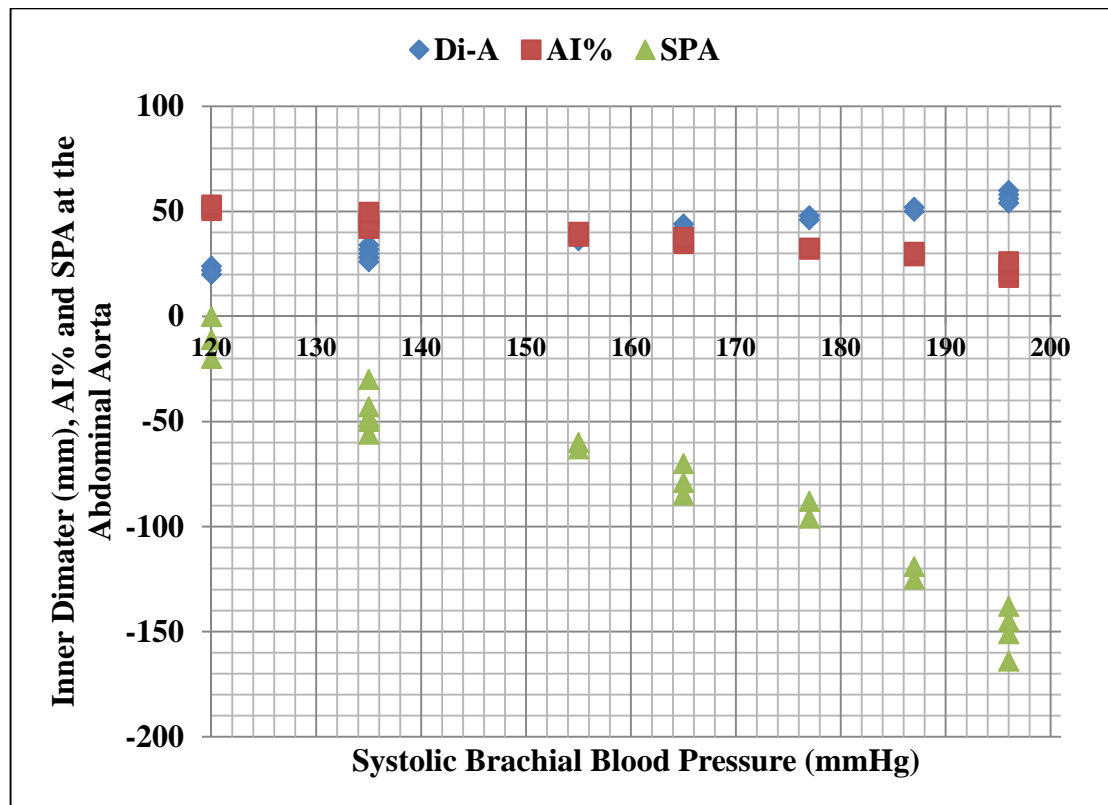


Figure 6-8: Correlating systolic brachial blood pressure with arterial wall thickness, AI % and SPA of an abdominal aortic aneurysm

The results of Figure 6-8 and Figure 2-5 are decoded in a diagram for ease of understanding in a clinical setting, which illustrates very high risk of abdominal aorta rupture (highlighted in red) as shown in Figure 6-9. This diagram could assist clinicians to screen for abdominal aortic aneurysms non-invasively based on blood pressure measurement at the brachial artery. This diagram requires further investigation and validation which could be performed on animal models; however, creating aneurysms is difficult in *in vivo* experiments on live specimens.

### CFD/FE Model

#### Abdominal Aortic Aneurysm

**Very High Risk**

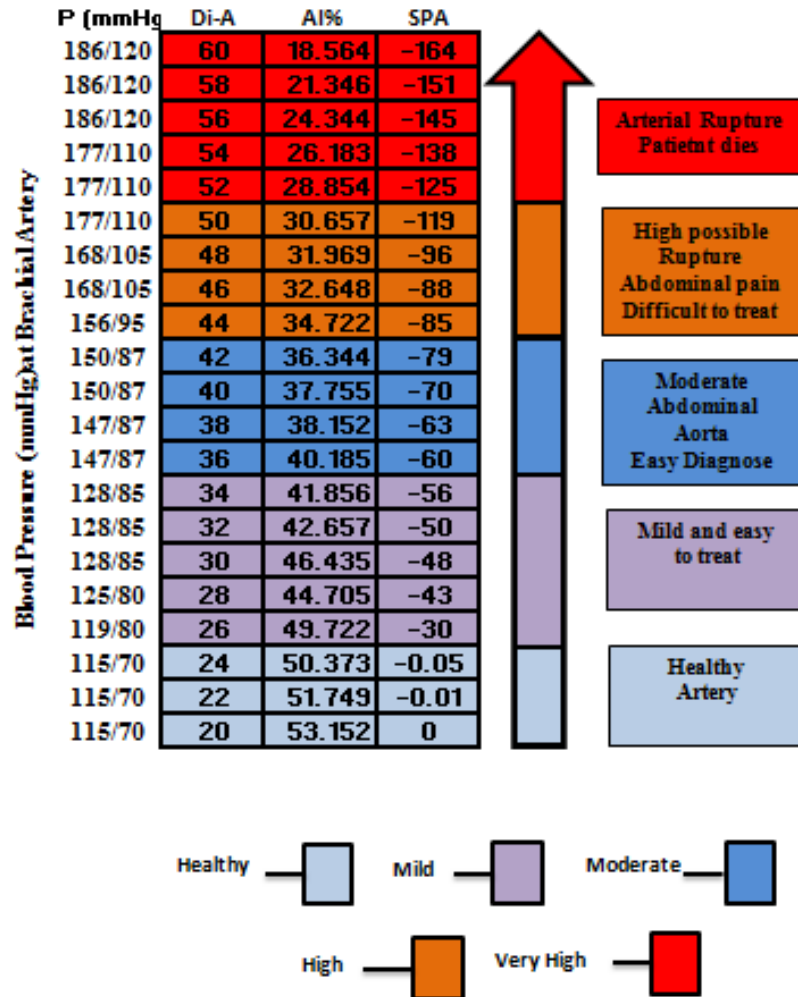


*Figure 6-9: Diagram illustrating the high risk of developing abdominal aortic aneurysm by changing lumen diameter of the abdominal aorta in twenty unhealthy conditions*

### 6.3.1 Abdominal Aortic Aneurysm Assessment

Biomechanically, AAA rupture is assessed and determined via the relationship between WSS and CS and the characteristics of the shape of the aneurysm (diameter and thickness). From a mechanical perspective, analysing Figure 6-10 for AAA in its early

stage is formulated with two equations using logarithmic form: Equation 6-3 for assessing lumen diameter and Equation 6-4 for assessing arterial compliance.

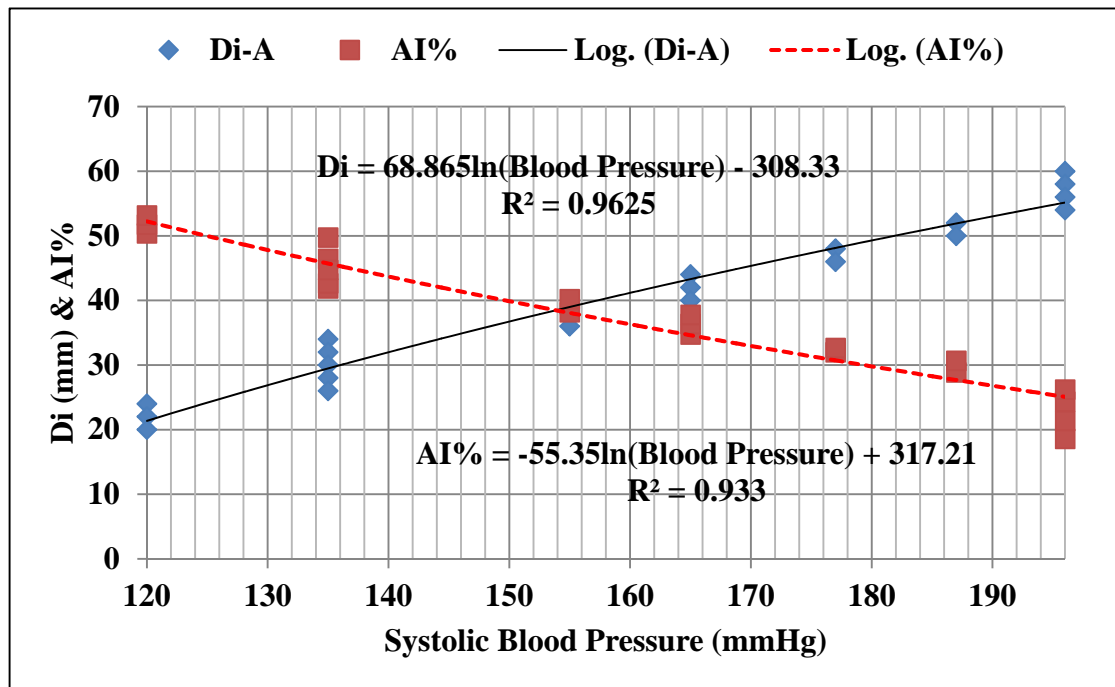


Figure 6-10: Correlation between the Di, AI (at the abdominal aorta) with systolic blood pressure at the cuff for abdominal aortic aneurysm

$$Di_{\text{Aneurysm}} = -55.35 \ln (BP_{\text{Measured at Brachial Artery}}) + 317.21 \quad (6-3)$$

$$AI \% = 68.865 \ln (BP_{\text{Measured at Brachial Artery}}) - 308.33 \quad (6-4)$$

Solving these two equations helps to identify aneurysm risk along the abdominal aorta at its early stage, based on non-invasive blood pressure measurement at the brachial artery.

#### 6.4 Assessing Arterial Blockages Using Animal Models

The *in vivo* experiments presented in Chapter 4 are divided into two groups of Wistar strain rats. The first group represents five rats with high body fat and their results indicate that arterial wall compliance and severity are inversely proportional to blood pressure measurement at the right femoral artery as shown in Figure 6-11. At the same time, high negative SPA value indicates the risk of development of abdominal aorta blockages.

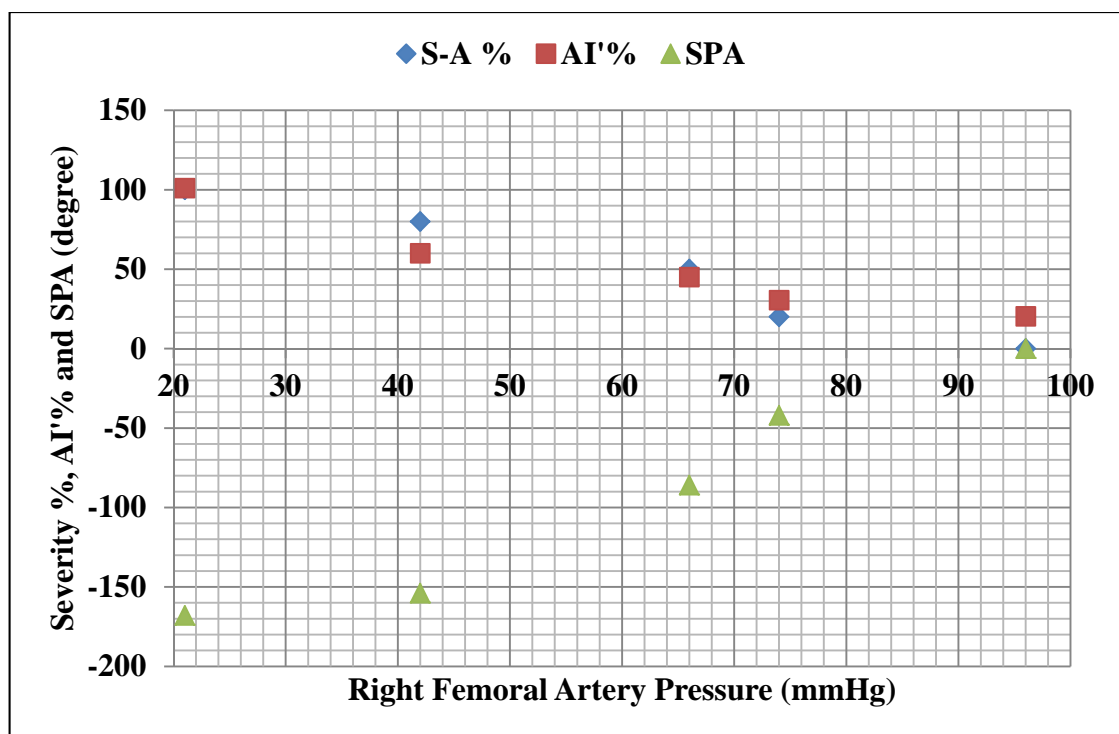


*Figure 6-11: Blood pressure measurement at the right femoral artery for five rats with high body fat compared with the severity of abdominal aorta blockages, AI' % and SPA at the abdominal aorta*

Figure 6-11 shows how the severity of the arterial blockages at the abdominal aorta and arterial compliance affects the measurement at the right femoral artery. The non-random group with high body fat indicates higher risk and lower blood pressure measurement.

The results for the second group of five low fat rats show that the risk effects of development of arterial blockages are smaller for this group compared to Group One as shown in Figure 6-12.

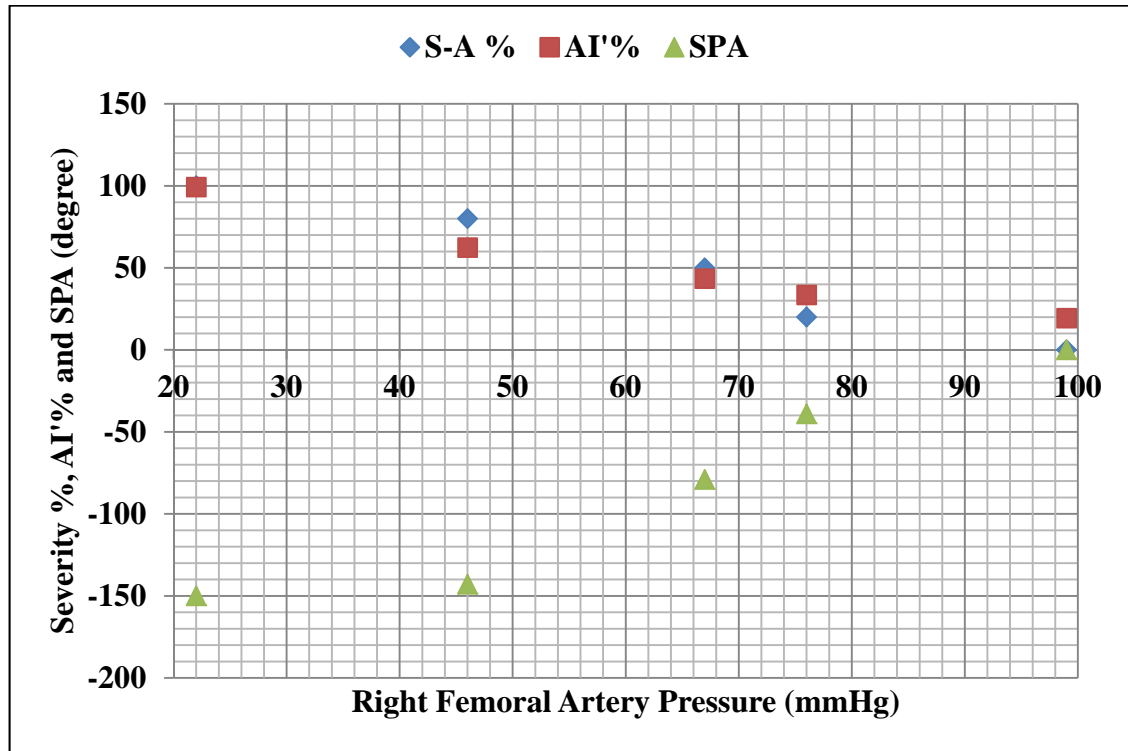


*Figure 6-12: Blood pressure measurement at the right femoral artery for five rats with low body fat compared with the severity of abdominal aorta blockages, AI' % and SPA at the abdominal aorta*

The results of Figures 6-11 and 6-12 are converted into a diagram for medical screening of arterial blockages as shown in Figure 6-13. Figure 6-13 shows based on animal data when the abdominal aorta will be at high risk of arterial blockage. These data will be correlated to the data from the Group-One CFD/FE models to assess arterial blockages non-invasively. This analysis is based on both Figures 6-2 and 6-13, and will be discussed in more detail in the next section.

## Assessing Arterial Blockages in Animal Models

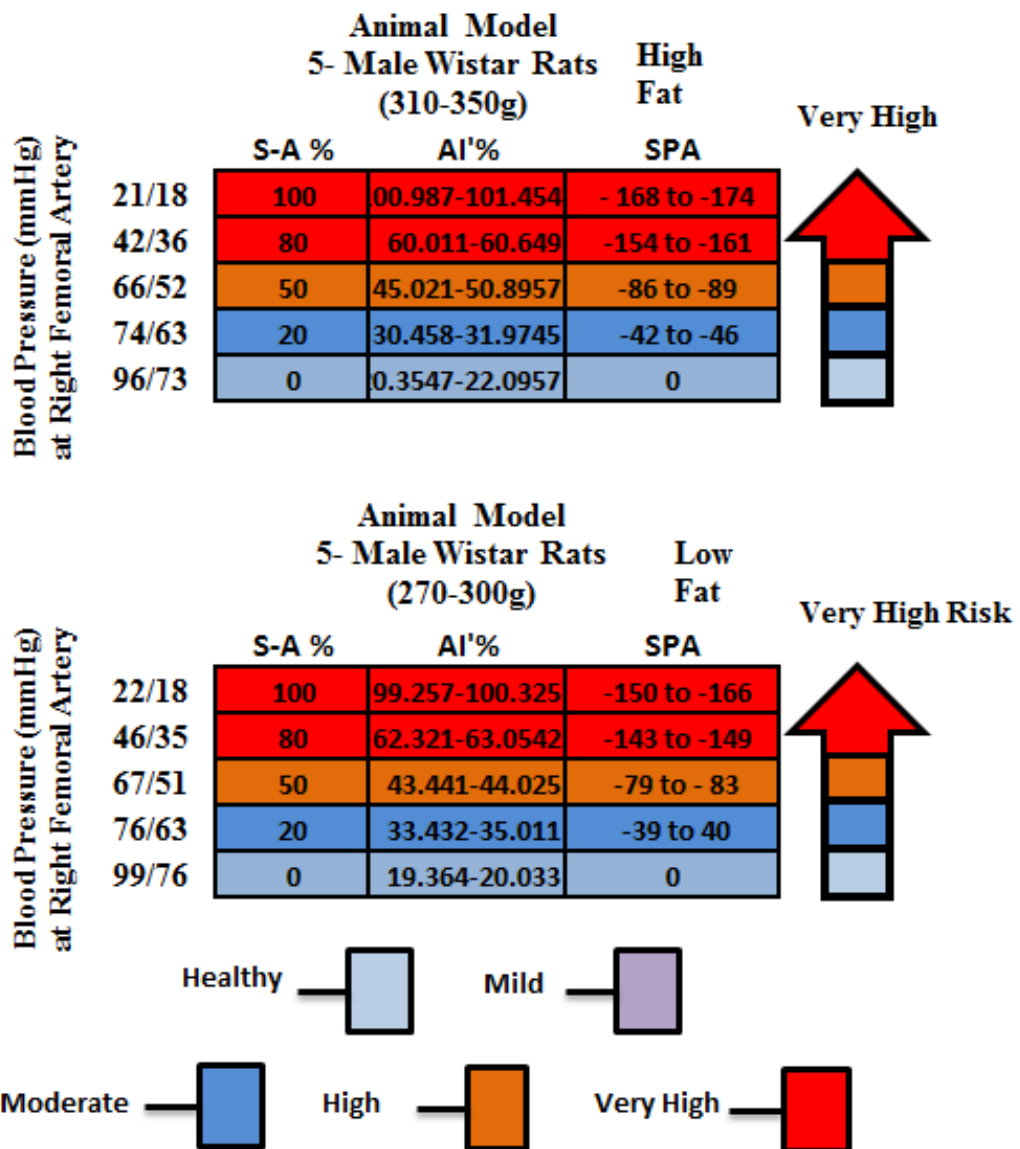


Figure 6-13: Diagram illustrating the assessment of arterial blockages in ten rats divided into two groups of 5 high body fat rats and 5 low body fat rats of Wistar strain

#### **6.4.1 Arterial Blockage Formula Based on Animal Model Validations**

The animal experiments and CFD/FE models of Group-One are correlated together to achieve a new, non-invasive diagnostic method for cardiovascular diseases. This diagnosis will be undertaken either at the brachial artery (the arm) or the right femoral artery (the leg). The animal models and their invasive results prove that any weakening and reduction of lumen diameter significantly impacts on blood pressure measurement at the right femoral artery. In addition, the CFD/FE models in Group-One demonstrate that any changes occurring at the abdominal aorta, such as arterial blockage, impacts on the computational measurements of brachial artery blood pressure.

Figure 6-14 shows that blood pressure at the brachial artery is proportional to the increase in arterial wall compliance (in physiology, wall compliance represents the tendency of the artery to resist recoil toward its original dimensions) and decrease in lumen diameter of the abdominal aorta. However, the experimental model indicates that the narrowing of the abdominal aorta results in a reduction of blood pressure in the right femoral artery. This is an indication that blood pressure waveforms increase their reflection waves in the upper body and reduce them in the lower body.

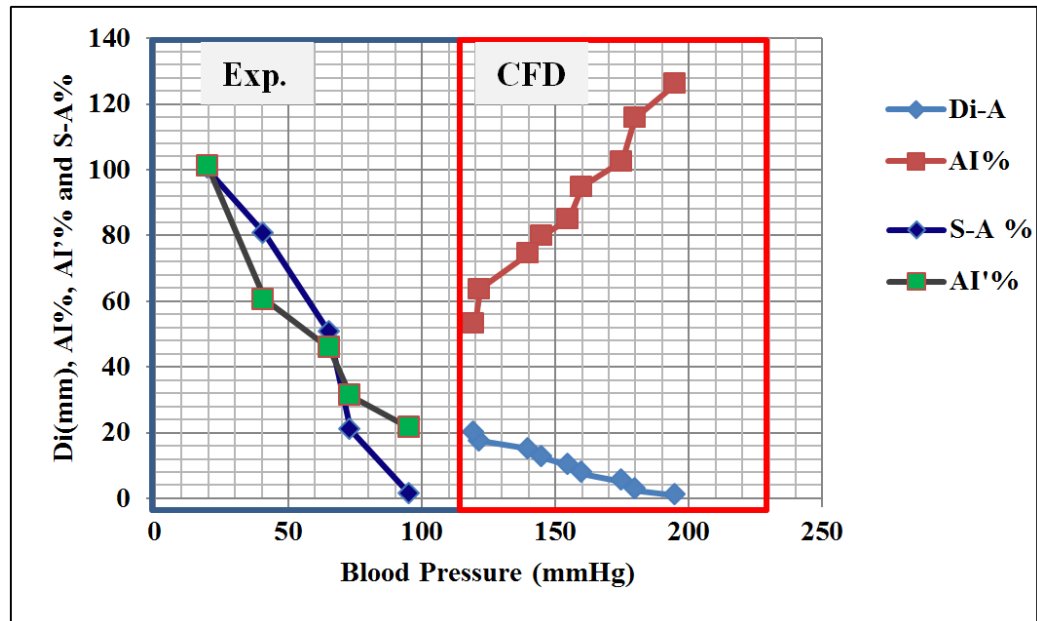


Figure 6-14: Comparison between animal models and the CFD/FE models

## 6.5 Closure

This chapter shows that a correlation does exist between the presence of cardiovascular disease and blood pressure at both the brachial and femoral arteries that can be used to assess the risk of cardiovascular diseases. The new finding in this thesis is that any change occurring at the abdominal aorta can be assessed using the SPA, AI and systolic blood pressure taken from easy to reach, and therefore non-invasive locations such as the brachial and femoral arteries. These findings can be used to develop a reference chart to assist medical practitioners in assessing the degree of risk of cardiovascular disease development in their patients. In addition, a software can be developed in which clinical data such as the systolic and diastolic blood pressure values could be extended as input and the output will be an estimate of the dimensions of the lumen of the abdominal aorta. However, for more accuracy, this investigation requires further medical trials to identify further characteristics that influence the development of cardiovascular diseases, such as weight, height and gender.



## Chapter 7 Conclusion and Future Work

### 7.1 Summary

The main aim of this study was to investigate the relative contributions of blood pressure, and arterial compliance using SPA and AI to the development of atherosclerosis and aneurysm for the purpose of developing a method for non-invasive diagnosis of these diseases. Four objectives were identified to address this aim. This thesis described the results of the investigation for these objectives. In Chapters 1 and 2 the circulatory system physiology was described, cardiovascular diseases affecting it were presented and a literature review of existing knowledge and models for disease diagnosis was conducted. Mathematical and computational theories in Chapter 3 provided the necessary approach to develop and model atherosclerosis and aneurysm. In Chapter 4, an animal CFD/FE model was validated against an experimental study, which identified the risk of arterial blockages and validated the *in vivo* and *in vitro* experiments in CFD/FE models. A CFD/FE two-way FSI model for different scenarios of atherosclerosis and aneurysm was developed in Chapter 5 using clinical invasive and available literature data. Chapter 6 described how these results were used to adjust and validate the computational models based on clinical observations.

## 7.2 Conclusions

In this section the conclusions of the investigation into each of the four objectives formulated in Chapter 2 Section 2.6 are presented.

*1- To investigate hemodynamic stresses in both atherosclerosis and aneurysm affected samples and healthy samples.*

After developing an unhealthy condition experimentally and computationally in animal models and computationally in human models, the results for each model were compared to their control (healthy) model. Four different arterial blockages were investigated in rats and three groups of atherosclerosis and one group of aneurysm were investigated in human models. The comparison was in terms of the WSS and CS at the disease site and at the site of possible non-invasive measurement such as the right femoral artery for the animal model and the brachial artery for the human model. The process of such a correlation and comparison was highly complex to develop, due to the lack of quantitative data in the literature and the lack of understanding of the growth of disease in the arteries. The novel approach here was to use the response of the WSS and CS resultant from pulsatile blood pressure and arterial compliance to develop a relationship with predictive capabilities for early diagnosis of cardiovascular disease based on hemodynamic stress and the deformation of the artery wall. This approach involved changing one parameter (i.e. the shape of the disease) at a time (e.g. inner diameter) while keeping the other parameters constant (e.g. thickness, length) and the experimental and CFD/FE results indicated the presence of early disease development in the animal models. However, the human models were developed using the CFD/FE methods based on literature

and clinical invasive data. The outcome of simulating those models was not sufficient to achieve realistic results due to the number of independent parameters in the models and the lack of physiological evidence for atherosclerosis and aneurysm development. The atherosclerosis CFD/FE models led to the development of a relationship to assess the risk of atherosclerosis development non-invasively, based on the brachial artery systolic blood pressure correlated to arterial compliance. The aneurysm CFD/FE models led to the development of a new formula to assess the high risk of arterial rupture based on brachial artery blood pressure measurement.

*2- To discover the correlation between the stress phase angle (SPA) and the development of atherosclerosis and aneurysm.*

An extensive literature review was presented which revealed that despite a century of research into atherosclerosis and aneurysm, many aspects of their hemodynamic behaviour are not yet fully understood. The experimental and computational analysis involved in modelling atherosclerosis and aneurysm characteristics were identified as: blood pressure, AI and SPA. Existing research on the development of cardiovascular disease components of the SPA response was found to be insufficient for the purposes of quantitative modelling for non-invasive diagnoses. Consequently an initial experimental animal study was conducted to investigate the SPA further. A relationship between the negative phase angle of the SPA and disease development was found in this study which corresponded with the literature data.

- 3- *To investigate arterial wall compliance and severity in both diseased and healthy conditions.*

Experiments were conducted to validate the models for assessing the risk of arterial blockages based on measuring arterial wall compliance. A close agreement between the experiments and CFD/FE model predictions was found, although further improvements can be made. The CFD/FE arterial blockage models are likely to require adjustment of governing parameters, but the experimental data strongly suggests that any change to the arterial wall stiffness plays an important, if not leading, role in non-invasive diagnosis of atherosclerosis.

- 4- *To investigate the hypothesis of non-invasively assessing the risk of arterial blockages and aneurysm, based on systolic and diastolic blood pressure measurement from the cuff using pulse wave transmission.*

The principle of screening cardiovascular diseases based on pulse wave propagation proposed in this work was partially confirmed, and with some minor adjustment the model, was capable of simulating lumen diameter change at the abdominal aorta. A comparison between the CFD/FE and the *in vivo* and *in vitro* experiments indicated that the CFD/FE model was closer to clinical observation due to the indication of the systolic and diastolic blood pressure measured experimentally and computationally.

The main aim of this work, to understand the relative contributions of the SPA, AI and lumen diameter on the early development of cardiovascular diseases, has been fulfilled to a great extent in this work. The experiments and CFD/FE modelling work have

shown that any change to the shape of the abdominal aorta plays an instrumental role in narrowing of the artery.

### **7.3 Future Work**

A major factor in assessing the risk of cardiovascular diseases is the difference in physiological components of each patient (such as weight and gender). In this thesis, many simplified assumptions have been implemented for modelling the complex aorta geometry (such as constant weight and one gender). Model validation indicated that the majority of these assumptions were justifiable. However a more detailed model would require additional investigation to provide insight into the impact of other physical factors on the biomechanics and hemodynamics of atherosclerosis and aneurysm. The improvement of the risk assessment tool for those diseases for different patients requires a secure deployment clinically, and future work could include:

#### **7.3.1 Blood Pressure Device**

The measurements at the brachial or the right femoral arteries show that any disease that affects the abdominal aorta is reflected on the oscillation waveforms, which vary according to the type of the disease. In particular, in experimental results arterial blockages show a clear difference in pressure waveforms shapes when the disease forms and becomes more severe. This phenomenon indicates the feasibility of getting non-invasive measurement waveform features at the femoral artery to determine the development of cardiovascular diseases. This investigation could be carried out when a new transfer function and sensor for various specimens has been developed and could be tested on multiple patients.

This thesis presents a feasibility study investigating the possibility of detecting cardiovascular diseases at the brachial artery non-invasively. The animal experiments

show the possibility of detecting a gradual arterial blockage growing at the abdominal aorta based on the blood pressure waveform measured by the transducer connected to the catheter. Material properties were collected to test our clinical data in the CFD/FE model. The material properties for the animal model were obtainable upon dissection of the animal. However, in the human case it is difficult to collect accurate material properties for the artery wall. Therefore an estimate of the material properties for each patient would need to be determined, based on statistical analysis performed across hospital patients having different disease severities, and taking into account characteristics such as age, gender, height and weight. For future work, more thorough investigation has to be undertaken to determine accurate human material characteristics.

### **7.3.2 Improving the CFD/FE Model**

Several suggestions can be made for future work on CFD/FE modelling processes and assumptions. One of them is improving the boundary conditions of the presented models. In this thesis the CFD/FE models assume the artery wall consists of one layer, representing the intima layer. To improve this, an assumption of three-layers of artery wall could be made, taking into consideration their physiological material properties to model aorta geometry. This assumption could enhance the screening tool for diagnosing cardiovascular disease development at an early stage. In addition, the new assumptions could allow the CFD/FE modelling processes to analyse WSS and CS at each layer for further investigation into where the weakness of a developing disease occurs. This modelling could be performed using animal models in both *in vivo* and *in vitro* experiments. This study should be conducted on 70 female and 70 male rats of the

Wistar strain, in different weight groups. The measurement would be performed on the axillary artery (equivalent to the brachial artery in humans) for assessing the risk of developing atherosclerosis and aneurysm at four different locations: the ascending aorta, aortic arch, descending aorta and the abdominal aorta. Those models may help to formulate new equations for assessing cardiovascular disease occurring at any location using non-invasive cuff-sensor techniques. These animal models could also be interpreted by the CFD/FE model which could determine the cause of disease development by calculating WSS and CS.

## REFERENCES

1. **Ebrahim, S., D. Montaner, and D.A. Lawlor.** *Clustering of risk factors and social class in childhood and adulthood in British women's heart and health study: cross sectional analysis.* BMJ, 2004. **2004**: p. 328:861.
2. **Mendis, S.,** *Cardiovascular Risk Assessment and Management in Developing Countries.* Vascular Health and Risk Management 2005.
3. **Chan, W.C., C. Wright, T. Riddell, S. Wells, A. J. Kerr, G. Gala, and R. Jackson.** *Ethnic and socioeconomic disparities in the prevalence of cardiovascular disease in New Zealand.* Journal of the New Zealand Medical Association, 2008. **121 (1285)** .
4. **Wells, S., J. Broad, and R. Jackson.** *Estimated prevalence of cardiovascular disease and distribution of cardiovascular risk in New Zealanders: data for healthcare planners, funders, and providers.* THE NEW ZEALAND MEDICAL JOURNAL, 2006. **119 (1232)**.
5. [http://en.wikipedia.org/wiki/File:Circulatory\\_System\\_en.svg](http://en.wikipedia.org/wiki/File:Circulatory_System_en.svg)
6. <http://www.medicalhistology.us/twiki/bin/view/Main/Cardiovascular>
7. **Willmer, W.N.,** Clinical Measurement of Arterial Stiffness Obtained From Non-invasive Pressure Waveforms. American Journal of Hypertension, **2005. 18: p. 3S-10S.**
8. **Yahya, M.,** " Three Dimensional Finite-Element Modelling of Blood Flow in Elastic Vessels: Effects of Arterila Geometry and Elasticity on Aneurysm Growth and Rupture" Master of Science thesis: Ryerson University, Toronto, Ontario, Canada, 2010
9. **Nichols, W. W., O'Rourke, M., F., and C. Vlachopoulos.** McDonald's Blood Flow in Arteries, 6th ed: Theoretical, Experimental and Clinical Principles, USA
10. **Wellnhofer, E., L. Goubergrits, U. Kertzscher, K. Affeld, and E. Fleck.** Novel non-dimensional approach to comparison of wall shear stress distributions in coronary arteries of different groups of patients. Atherosclerosis, 2009. 202 p. 483– 490.
11. **Grigioni, M., C. Daniele, U. Morbiducci, C. Del Gaudio, G. D'Avenio, A. Balducci, and V. Barbaro.** *A mathematical description of blood spiral flow in vessels: application to a numerical study of flow in arterial bending.* Journal of Biomechanics, 2005. **38** p. 1375–1386.
12. **Kagadis, G.C., E.D. Skouras, G.C. Bourantas, C.A. Paraskeva, K. Katsanos, D. Karnabatidis, and G.C. Nikiforidis.** *Computational representation and hemodynamic characterization of in vivo acquired severe stenotic renal artery geometries using turbulence modeling.* Medical Engineering & Physics, 2008. **30**: p. 647–660.
13. **Ross, R.** *Atherosclerosis an inflammatory disease.* New England Journal of Medicine, 1999. **340**: p. 115–126.
14. **Blacher, J., A. Asmar, S. Djane, G.M. London, and M.E. Safar.** *Aortic pulse wave as a marker of cardiovascular risk in hypertensive patients.* Hypertension, 1999. **33**: p. 1111–1117.
15. [http://en.wikipedia.org/wiki/File:Endo\\_dysfunction\\_Athero.PNG](http://en.wikipedia.org/wiki/File:Endo_dysfunction_Athero.PNG)
16. **Safar, M.E., G.M. London, R. Asmar, and E.D. Frohlich.** *Recent Advances on large arteries in hypertension.* Hypertension, 1998. **32**: p. 156–161.
17. **Fronck, A., K.H. Johansen, R.B. Dille, and E.F. Bernstein.** *Noninvasive physiologic tests in the diagnosis and characterization of peripheral arterial occlusive disease.* American Journal of Surgery, 1973. **126**: p. 205-214.
18. **Laurent, S., P. Boutouyrie, R. Asmar, I. Gautier, B. Laloux, L. Guize, P. Ducimetiere, and A. Benetos.** *Aortic stiffness is an independent predictor of all-cause and cardiovascular mortality in hypertensive patients.* Hypertension, 2001. **37**: p. 1236–1245.
19. **Lowe, G.D.O.** *Different Locations of Atherosclerosis - Different Risk Factors, Different Therapies.* Pathophysiology of Haemostasis and Thrombosis 2004. **2003/2004; 33: 262-267.**
20. **Mitchell, J.R.A. and C.J. Schwarz,** *Arterial disease.* Oxford: Blackwell Scientific, 1965.
21. **Abraham, J.P., E.M. Sparrow, and R.D. Lovik.** *Unsteady, three-dimensional fluid mechanic analysis of blood flow in plaque-narrowed and plaque-free arteries.* International Journal of Heat and Mass Transfer, 2008. **51**: p. 5633–5641.
22. **Ito, S., K. Akutsu, Y. Tamori, S. Sakamoto, T. Yoshimuta, H. Hashimoto, and S. Takeshita S.** *Differences in Atherosclerotic Profiles Between Patients With Thoracic and Abdominal Aortic Aneurysms.* The American Journal of Cardiology, 2008. **101(5)**: p. 696-699.



23. **Li, Z.** Computational Analyses and Simulations of Fluid-Structure Interactions Applied to Stented Abdominal Aortic Aneurysms. PhD Thesis, North Carolina State University, NC, 2005. USA.
24. **Tan, F.P.P., A. Borghi, R.H. Mohiaddin, N.B. Wood, S. Thom, X.Y. Xu.** *Analysis of flow patterns in a patient-specific thoracic aortic aneurysm model.* Computers and Structures, 2009. **87**(11-12): p. 680-690.
25. **Mantha, A., C. Karmonik, G. Benndorf, C. Strother, and R. Metcalfe.** *Hemodynamics in a cerebral Artery before and after the formation of Aneurysm.* American Society of Neuroradiology, 2006. **27**: p. 1113-1118.
26. **Gebbers, J.** *Atherosclerosis, cholesterol, nutrition, and statins – a critical review.* German medical science, 2007. **5**: p. 1612-3174.
27. [http://www.cookmedical.com/zenith\\_patient\\_guides/flex\\_patient/intro.html](http://www.cookmedical.com/zenith_patient_guides/flex_patient/intro.html)
28. **Botnar, R.M., M. Stuber, K.V. Kissinger, W.Y. Kim, E. Spuentrup, and W.J. Manning.** *Noninvasive coronary vessel wall and plaque imaging with magnetic resonance imaging.* Circulation, 2000. **102**(21): p. 2582-2587.
29. **Laffon, E., V. Bernard, M. Montaudon, R. Marthan, J.L. Barat, and F. Laurent.** *Tuning of pulmonary arterial circulation evidenced by MR phase mapping in healthy volunteers.* Journal of Applied Physiology, 2001. **90**: p. 469-474.
30. **Johnson, K., P. Sharma, and J. Oshinski.** *Coronary artery flow measurement using navigator echo gated phase contrast magnetic resonance velocity mapping at 3.0T.* Journal of Biomechanics, 2008. **41**: p. 595-602.
31. **Laffon, E., N. Valli, V. Latrabe, J.M. Franconi, J.L. Barat, and F. Laurent.** *A validation of a flow quantification by MR phase mapping software.* European Journal of Radiology, 1998. **27**(2): p. 166-172.
32. **Foster, F.K., and D. Turney.** *Oscillometric Determination of Diastolic, Mean and Systolic Blood Pressure- A Numerical Model.* Journal of Biomechanical Engineering, 1986. **108**: p. 359-364.
33. **Bickley, L.S.** *Bates' Guide to Physical Examination and History Taking.* 7th edition J.B. Lippincott Company, Philadelphia, USA, 1999. **Philadelphia, USA.**
34. **Wilson, K., MacCallum, H., Wilkinson, I.B., Hoskins, P., R., Lee, A., J., and A.W. Bradbury.** *Comparison of Brachial Artery Pressure and Derived Central Pressure in the Measurement of Abdominal Aortic Aneurysm Distensibility.* European Journal of Vascular and Endovascular Surgery, 2001. **Vol. 22**(355-360).
35. **Sorvoja, H.** *The development of the transducer for the measurement of blood pressure pulse and blood pressure on the wrist.* Licentiate Thesis, 1998. **University of Oulu.**
36. **Hyman, C., R.L. Paldino, and E. Zimmermann.** *Local Regulation of Effective Blood Flow in Muscle.* Circulation Research, 1965. **XII.**
37. **Hong, H. and M. Fox.** *Noninvasive detection of cardiovascular pulsations by optical Doppler techniques.* Journal of Biomedical Optics, 1997. **2**: p. 382-385.
38. **Riva, C., B. Ross, and G.B. Benedek.** *Laser Doppler measurements of blood flow in capillary tubes and retinal arteries.* Investigative Ophthalmology 1972. **11**: p. 91-102.
39. **Lee, B.K., H.M. Kwon, D. Kim, Y.W. Yoon, J.K. Seo, I.J. Kim, H.W. Roh, S.H. Suh, S.S. Yoo, and H.S. Kim.** *Computed Numerical Analysis of the Biomechanical Effects on Coronary Atherogenesis Using Human Hemodynamic and Dimensional Variables.* Yonsei Medical Journal 1998. **39**(2) p. 166-174.
40. **Deshpande, M.D., B. Vinay, S.R. Shankapal, V.M.D. Prabhu, and M.G. Srinath.** *Subject-specific blood flow simulation in the human carotid artery bifurcation.* CURRENT SCIENCE, 2009. **97**(9): p. 1303-1312.
41. **Cornelius, T.L.,** *Biomechanical Systems: Biofluid methods in vascular and pulmonary systems.* Library of Congress Cataloging-in-Publication Data, 2001.
42. **Bogren, H.G., and M.H. Bounocore.** *Complex flow patterns in the great vessels: a review.* International Journal of Cardiac Imaging, 1999. **15**: p. 105-113
43. **Pythoud, F., N. Stergiopoulos, and J.J. Meister.** *Modelling of the wave transmission properties of large arteries using nonlinear elastic tube.* Journal of Biomechanics, 1994. **27**: p. 1379-1381.
44. **Karamanoglu, M., M.F. O'Rourke, A.P. Avolio, and R.P. Kelly.** *An analysis of the relationship between central aortic and peripheral upper limb pressure waves in man.* European Heart Journal, 1993. **14**: p. 160-167.

45. **Hamilton, W.F.** *The patterns of the arterial pressure pulse.* American Journal of Physiology, 1944. **141**: p. 235-241.
46. **Kroeker, E.J. and E.H. Wood.** *Comparison of simultaneously recorded central and peripheral arterial pressure pulses during rest, exercise and tilted position in man.* Circulation Research, 1955. **3**: p. 623-632.
47. <http://mytreatmentabroad.co.uk/arteriograph>
48. **Sugimachi, M., T. Shishido, K. Miyatake, and K. Sunagawa.** *A new model-based method of reconstructing central aortic pressure from peripheral arterial pressure.* The Japanese Journal of Physiology, 2001. **51**: p. 217–222.
49. **Lowe, A., W. Harrison, E. El-Aklouk, P. Ruygrok, and A.M. Al-Jumaily.** *Non-invasive model-based estimation of aortic pulse pressure using suprasystolic brachial pressure waveforms.* Journal of Biomechanics 2009. **42**: p. 2111-2115.
50. **Al-Aklouk, E., A. Al-Jumaily, and A. Lowe.** *Acoustic Wave Technology as a Diagnostic Tool for Cardiovascular Disease.* World Congress on Medical Physics and Biomedical Engineering, 2006. **14**(1): p. 3386-3389.
51. **Al-Aklouk, E., A. Al-Jumaily, and A. Lowe.** *Pressure Waves as a Non-Invasive Tool for Artery Stiffness Estimation.* Journal of Medical Devices, 2008. **2**: p. 021001-021008.
52. **Pontrelli, G.,** *Blood Flow Through an Axisymmetric Stenosis* Journal of Engineering in Medicine, 2001. **215**(1): p. 1-10.
53. **Varghese, S.S., S.H. Frankel, and P.F. Fischer.** *Direct numerical simulation of stenotic flows, Part 2: Pulsatile flow.* Journal of Fluid Mechanics, 2007. **582**: p. 281-318.
54. **Giddens, D.P., C.K. Zarins, and S. Glagov.** *The role of fluid mechanics in the localisation and detection of atherosclerosis.* Journal of Biomechanical Engineering, 1993. **115**(4): p. 588–594.
55. **Cebal, J.R., M.A. Castro, and C.M. Putman.** *Numerical simulation of flow alterations after carotid artery stenting from multi-modality image data.* Computational Fluid and Solid Mechanics, 2005. **Third MIT Conference on Computational Fluid and Solid Mechanics**: p. 607-611.
56. **Ivankovic, A., A. Karac, E. Dendrinis, and K. Parker.** *Towards Early Diagnosis of Atherosclerosis: The Finite Volume Method for Fluid-Structure Interaction.* Biorheology, 2002. **39**: p. 401-411.
57. **Bathe, M. and R.D. Kamm.** *A fluid-Structure Interaction Finite Element Analysis of Pulsatile Blood Flow Through a Compliant Stenotic Artery.* Journal of Biomechanical Engineering, 1999. **121**: p. 361-369.
58. **Tang, D., C. Yang, S. Kobayashi, and D.N. Ku.** *Steady Flow and Wall Compression in Stenotic Arteries: A Three-Dimensional Thick-Wall Model With Fluid–Wall Interactions.* Journal of Biomechanical Engineering, 2001. **123**: p. 548-557.
59. **Sulaiman, A., L. Bousset, F. Taconnet, J.M. Serfaty, H. Alsaïd, C. Attia, L. Huet, and P. Douek.** *In vitro non-rigid life-size model of aortic arch aneurysm for endovascular prosthesis assessment.* European Journal of Cardio-thoracic Surgery, 2008. **33**: p. 53-57.
60. **Leung, J.H., A.R. Wright, N. Cheshire, J. Crane, S.A. Thom, A.D. Hughes, and Y. Xu.** *Fluid structure interaction of patient specific abdominal aortic aneurysms: a comparison with solid stress models.* BioMedical Engineering OnLine, 2006. **5**(33)(1-15).
61. **Gao, F., O. Ohta, and T. Matsuzawa.** *Fluid structure interaction in layered aortic arch aneurysm model assessing the combined influence of arch aneurysm wall stiffness.* Australian Physical & Engineering Sciences in Medicine, 2008. **31**: p. 32-41.
62. **Zhao, S.Z., X.Y. Xu, A.D. Hughes, S.A. Thom, A.V. Stanton, B. Ariff, and Q. Long.** *Blood flow and vessel mechanics in a physiologically realistic model of a human carotid arterial bifurcation.* Journal of Biomechanics, 2000. **33** p. 975-984.
63. <http://www.tree.com/health/aneurysms.aspx>
64. **Scotti, C.M., J. Jimenez, S.C. Muluk, and E.A. Finol.** *Wall stress and flow dynamics in abdominal aortic aneurysms: finite element analysis vs. fluid–structure interaction.* Computer Methods in Biomechanics and Biomedical Engineering, 2008. **11**(3): p. 301–322.
65. **Vito, R.P., and S.A. Dixon.** *Blood Vessel Constitutive.* Annual Review of Biomedical Engineering, 2003. **5**: p. 413-439.
66. **Kim, Y., S. Sookkyung, S. V.Raman, O. P. Simonetti, and A. Friedman.** *Blood Flow in a Compliant Vessel by the Immersed Boundary Method.* Annals of Biomedical Engineering, 2009. **37**(5): p. 927–942.

67. **Demiray, H. and R.P. Vito.** *On large periodic motions of arteries.* Journal of Biomechanics, 1983. **16**(8): p. 643-648.
68. **Steinman, D.A., J.B. Thomas, H.M. Ladak, J.S. Milner, B.K. Rutt, and J.D. Spence.** *Reconstruction of carotid bifurcation hemodynamics and wall thickness using computational fluid dynamics and MRI.* Magnetic Resonance in Medicine, 2002. **47**(1): p. 149-159.
69. **Weydahl, E.S. and J.E. Moore.** *Dynamic curvature strongly affects wall shear rates in a coronary artery bifurcation model.* Journal of Biomechanics, 2001. **34**(9): p. 1189-1196.
70. **Chandran, K.B. and T.L. Yearwood.** *Experimental Study of Physiologic Pulsatile Flow in a Curved Tube.* Journal of Fluid Mechanics, 1981. **111**: p. 59-85.
71. **Perktold, K., D. Hilbert.** *Numerical simulation of pulsatile flow in a carotid bifurcation model.* Journal of Biomedical Engineering, 1986. **8**: p. 193-199.
72. **Atabek, H.B.** *Wave propagation through a viscous liquid contained in a tethered, initially stressed, orthotropic elastic tube.* Biophysical Journal, 1968. **8**: p. 626-649.
73. **Yilmaz, F., and M.Y. Gundogdu.** *A critical review on blood flow in large arteries; relevance to blood rheology, viscosity models, and physiologic conditions.* Korea-Australia Rheology Journal, 2003. **Vol. 20, No. 4, December 2008 pp. 197-211.**
74. **Womersley, J.** *Oscillatory motion of a viscous liquid in a thin walled elastic tube: The linear approximation for long waves.* Philosophical Magazine, 1955. **46**(373): p. 199-221.
75. **Peiro, J., and S.J. Sherwin.** *Automatic reconstruction of a patient-specific high-order surface representation and its application to mesh generation for CFD calculations.* Medical & Biological Engineering & Computing, 2008. **46**: p. 1069-1083.
76. **Ku, D.N. and D.P. Giddens.** *Laser Doppler anemometer measurements of pulsatile flow in a model carotid bifurcation.* Journal of Biomechanics, 1987. **20**(4): p. 407-421.
77. **Ojha, M., R.S.C. Cobbold, K.W. Johnstom, and R.L. Hummel.** *Pulsatile flow through constricted tubes: an experimental investigation using photochromic tracer methods.* Journal of Fluid Mechanics 1989. **203**: p. 173-197.
78. **Li, H.J., J.H. Haga, and S. Chien.** *Molecular basis of the effects of shear stress on vascular endothelial cells.* Journal of Biomechanics, 2005. **38**(10): p. 1949-1971.
79. **Valencia, A. and F. Baeza.** *Numerical simulation of fluid-structure interaction in stenotic arteries considering two layer nonlinear anisotropic structural model.* International Communications in Heat and Mass Transfer, 2009. **36** p. 137-142.
80. **Cox, R.H.** *Comparison of linearized wave propagation models for arterial blood flow analysis.* Journal of Biomechanics, 1969. **2**: p. 251-265.
81. **Avolio, A.P., M.F. O'roukre, and M.E.D. Webster.** *Pulse-Wave Propagation in the Arterial System of the Diamond Python Morelia Spilotes.* AJP - Regulatory, Integrative and Comparative Physiology, 1983. **245**: p. 831-836.
82. **Thurston, G.B.** *Effect of viscoelasticity of blood on wave propagation in the circulation.* Journal of Biomechanics, 1976. **9**: p. 13-20.
83. **Cox, R.H.** *Wave propagation through a Newtonian fluid contained within a thick-walled viscoelastic tube: the influence of wall compressibility.* Journal of Biomechanics, 1970. **3**: p. 317-335.
84. **Misra, J.C., and K. Roychoudhuri.** *Effect of initial stresses on the wave propagation in arteries.* Journal of Mathematical Biology, 1983. **18**: p. 53-67.
85. **Atabek, H.B. and H.S. Lew.** *Wave propagation through a viscous incompressible fluid contained in an initially stressed elastic tube.* Biophysical Journal, 1966. **6**: p. 481-503.
86. **Chow, J.C., and J.T. Apter.** *Wave propagation in a viscous incompressible fluid contained in flexible viscoelastic tubes.* Journal of the Acoustical Society of America, 1968. **44**: p. 437-443.
87. **Freudenburg, H., and P.R. Lichtlen.** *The normal wall segment in coronary stenosis-a postmortem study.* Kardiologie, 1981. **70**: p. 863-869.
88. **Stergiopoulos, N., M. Spiridon, F. Pythoud, J.J. Meister.** *On The Wave Transmission and Reflection Properties of Stenoses.* Journal of Biomechanics, 1996. **29**: p. 31- 38.
89. **Olufsen, M.S.** *Structured tree outflow condition for blood flow in larger systemic arteries.* American Physiological Society, 1999. **276**: p. H257-H268.
90. <http://www.ansys.com/>
91. **Liu, B.** *Computer simulations of flow in curved tubes with stenosis, in COMSOL Multiphysics User's Conference.* 2005: Boston.

92. **Liu, B.** *Flow patterns in curved atherosclerotic arteries.* Far East Journal of Applied Mathematics, 2004. **14**(2): p. 157-177.
93. **Soulis, J.V., G.D. Giannoglou, Y.S. Chatzizisis, K.V. Seralidou, G.E. Parcharidis, and G.E. Louridas.** *Non-Newtonian models for molecular viscosity and wall shear stress in a 3D reconstructed human left coronary artery.* Medical Engineering & Physics, 2008. **30** p. 9-19.
94. **Lee, S.E., S.W. Lee, P.F. Fischer, H.S. Bassiouny, and F. Loth.** *Direct numerical simulation of transitional flow in a stenosed carotid bifurcation.* Journal of Biomechanics 2008. **41**: p. 2551-2561.
95. **Morris, L., P. Delassus, A. Callanan, M. Walsh, F. Wallis, P. Grace, and T. McGloughlin.** *3-D Numerical Simulation of Blood Flow Through Models of the Human Aorta.* Journal of Biomechanical Engineering, 2005. **127**: p. 767-775.
96. **Stroud, J.S., B.A. A, and D. Saloner.** *Numerical Analysis of Flow Through a Severely Stenotic Carotid Artery Bifurcation.* Journal of Biomechanical Engineering, 2002. **124**: p. 9-20.
97. **Zeng, D., Z. Ding, M.H. Friedman, and C.R. Ethier.** *Effects of Cardiac Motion on Right Coronary Artery Hemodynamics.* Annals of Biomedical Engineering, 2003. **31**: p. 420-429.
98. **Jung, J., R.W. Lyczkowski, C.B. Panchal, and A. Hassanein.** *Multiphase hemodynamic simulation of pulsatile flow in a coronary artery.* Journal of Biomechanics, 2006. **39**(11): p. 2064-2073.
99. **Nguyena, K.T., C.D. Clark, T.J. Chancellor, and D.V. Papavassiliou.** *Carotid geometry effects on blood flow and on risk for vascular disease.* Journal of Biomechanics, 2008. **41** p. 11-19.
100. **Kenjereš, S.,** *Numerical analysis of blood flow in realistic arteries subjected to strong non-uniform magnetic fields.* International Journal of Heat and Fluid Flow, 2008. **29**: p. 752-764.
101. **Torii, R., J. Keegan, N.B. Wood, A.W. Dowsey, A.D. Hughes, G.Z. Yang, D.N. Firmin, S.A. Thom, and X.Y. Xu.** *A CFD Study on Coronary Artery Hemodynamics With Dynamic Vessel Motion Based on MR Images.* Journal of Biomechanics (Abstracts of the 16th Congress, European Society of Biomechanics), 2008. **41**: p. S212.
102. **Fayad, Z.A. and V. Fuster.** *The human high-risk plaque and its detection by magnetic resonance imaging.* American Journal of Cardiology, 2001. **88**(2A): p. 42E-45E.
103. **Chen, J. and X. Lu.** *Numerical investigation of the non-Newtonian blood flow in a bifurcation model with a non-planar branch.* Journal of Biomechanics, 2004. **37** p. 1899-1911.
104. **Qui, Y., and J.M. Tarbell.** *Interaction between Wall Shear Stress and Circumferential Strain Affects Endothelial Cell Biochemical Production.* Journal of Vascular Surgery, 1999. **37**: p. 147-157.
105. **Lee, B.K., H.M. Kwon, B.K. Hong, B.E. Park, S.H. Suh, M.T. Cho, C.S. Lee, M.C. Kim, C.J. Kim, S.S. Yoo, and H.S. Kim.** *Hemodynamic Effects on Atherosclerosis-Prone Coronary Artery: Wall Shear Stress/ Rate Distribution and Impedance Phase Angle in Coronary and Aortic Circulation.* Yonsei Medical Journal, 2001. **42**: p. 375-383.
106. **Wang, D.M. and J.M. Tarbell,** *Nonlinear analysis of flow in an elastic tube (artery): steady streaming effects.* The Journal of Fluid Mechanics, 1992. **239**: p. 341-358.
107. **Dancu, M.B., D.E. Berardi, J.P. Vanden Heuvel, and J.M. Tarbell.** *Asynchronous Shear Stress and Circumferential Strain Reduces Endothelial NO Synthase and Cyclooxygenase-2 but Induces Endothelin-1 Gene Expression in Endothelial Cells.* Arteriosclerosis, Thrombosis, and Vascular Biology, 2004. **24**(11): p. 2088-2094.
108. **Tada, S. and J.M. Tarbell.** *A Computational Study of Flow in a Compliant Carotid Bifurcation-Stress Phase Angle Correlation with Shear Stress.* Annals of Biomedical Engineering, 2005. **33** (9): p. 1202-1212.
109. **Dancu, M.B. and J.M. Tarbell.** *Large Negative Stress Phase Angle (SPA) attenuates nitric oxide production in bovine aortic endothelial cells.* Journal of Biomechanical Engineering, 2006. **128**(3): p. 329-34.
110. **Torii, R., N.B. Wood, N. Hadjiloizou, A.W. Dowsey, A. Wright, A.D. Hughes, J. Davies, D.P. Francis, J. Mayet, G. Yang, S.A. Thom, and X.Y. Xu.** *Stress phase angle depicts differences in coronary artery hemodynamics due to changes in flow and geometry after percutaneous coronary intervention.* Am J Physiol Heart Circ Physiol, 2009. **296**: p. H765-H776.
111. **Urbina, E.M., S.R. Srinivasan, R. Tang, M.G. Bond, L. Kieltyka, and G.S. Berenson.** *Impact of multiple coronary risk factors on the intima-media thickness of different segments of carotid artery in healthy young adults (The Bogalusa Heart Study).* American Journal of Cardiology, 2002. **90**: p. 953-958.

112. **Tada, S., C. Dong, and J.M. Tarbell.** *Effect of the Stress Phase Angle on the Strain Energy Density of the Endothelial Plasma Membrane.* Biophysical Journal, 2007. **Volume 93:** p. 3026–3033.
113. **Abassi, Z., I. Goltzman, T. Karram, J. Winaver, and A. Hoffman.** Aortocaval Fistula in Rat: A Unique Model of Volume-Overload Congestive Heart Failure and Cardiac Hypertrophy. Journal of Biomedicine and Biotechnology 2010, vol.2011.
114. **Langeveld,B.,A.J.Roks, R.A.Tio, A.J.VanBoven,J.J. VanderWant,R.H. Henning, H.M.Van Beusekom,W.J. Van der Giessen,F. Zijlstra,and W.H.Van Gilst.** Rat Abdominal Aorta Stenting: A new and Reliable Small Animal Model for In-Stent Restenosis” Journal of Vascular Research, 2004.vol,41,pp.377-386.
115. **Wronska-Nofer, T., S. Szendzikowski, and M. Oberebska-Parke.** Influence of chronic carbon disulphide intoxication on the development of experimental atherosclerosis in rats. British Journal of Industrial Medicine, 1980. vol.37,pp387-393.
116. **Russell, J., C.** Of mice and men, rats and atherosclerosis” Cardiovascular Research,vol.59(2003),pp.810-811.
117. **Still, W., S., and R.M. O’Neal.**Electron Microscopic Study of Experimental Atherosclerosis in the Rat.Atherosclerosis in the Rat, 1962. vol.40 No.1.
118. [http://www.biologycorner.com/worksheets/rat\\_circulatory.html](http://www.biologycorner.com/worksheets/rat_circulatory.html)
119. [http://en.wikipedia.org/wiki/Laboratory\\_rat](http://en.wikipedia.org/wiki/Laboratory_rat)
120. **Larsen, N., E., E.A. Leshchiner, E.G. Parent, J. Hendrikson-Aho, and E.A. Balazs.** Hylan gel composition for percutaneous embolization Cardiovascular. Journal of Biomedical Materials Research,vol.25(1991),pp.699-710.
121. **Rentschler, M., E., and B.T. Baxter.**Screening Aortic rug Treatments Through Arterial Compliance Measurements. Current Vascular Pharmacology,2008. vol.6, pp. 250-257.
122. **Hedenqvist, P.** Anaesthesia and analgesia for surgery in rabbits and rats: A comparison of the effects of different compounds. PhD thesis, Karolinska Institutet, Stockholm 2008, Sweden.
123. **Marshall, S., A. Milligan, and R. Yates, R.** Experimental Techniques and Anaesthesia in the Rat and Mouse. ANZCCART Fact Sheet, 1994. vol.7, No 1, March 1994.

## **APPENDIX**

**Appendix I**

**Mathematical Modelling  
Equations**

**Appendix II**

**Result Images**

**Appendix III**

**Ethical approval**

## Appendix I

### A-1 Arbitrary Lagrangian Eulerian (ALE)

In this thesis, the ALE scheme is used as a numerical approach to calculate the large strain deformation of the artery wall and the impact from the blood flow. The ALE equations are derived by substituting the relationship between the material time derivative and the reference configuration time derivative [15].

$$\frac{\partial f(X_i, t)}{\partial t} = \frac{\partial f(x_i, t)}{\partial t} - w_i \frac{\partial f(x_i, t)}{\partial x_i} \quad (\text{A-1})$$

where  $X_i$  is the Lagrangian coordinate,  $x_i$  the Eulerian coordinate, and  $i$  the referential coordinate. Given relative  $w = v - u$ , the conservation of mass equation is reformulated [15] as:

$$\frac{\partial \rho}{\partial t} = -\rho \frac{\partial v}{\partial x_i} - w_i \frac{\partial \rho}{\partial x_i} \quad (\text{A-2})$$

The Navier-Stokes equations using ALE formulation [15] are:

$$\frac{\partial v}{\partial t} = -(\sigma_{ij,j} + \rho b_i) - \rho w_i \frac{\partial v}{\partial x_j} \quad (\text{A-3})$$

The stress tensor  $\sigma_{ij}$  is given as:

$$\sigma_{ij} = -p\delta_{ij} + \mu(v_{i,j} + v_{j,i}) \quad (\text{A-4})$$

Boundary conditions and initial conditions are:

$$v_i = U_o \text{ on } \Gamma_1 \text{ and } \sigma_{ij}n_i = 0 \text{ on } \Gamma_2$$

where:

$$\Gamma_1 \cup \Gamma_2 = \Gamma, \quad \Gamma_1 \cap \Gamma_2 = 0$$

$\Gamma$  is the whole boundary of the calculation domain;  $\Gamma_1$  and  $\Gamma_2$  are partial boundaries of  $\Gamma$ ,  $n_i$  is the outward unit normal vector on the boundary and  $\sigma_{ij}$  is Kronecker's delta function [15].

The velocity field is assumed in the whole domain  $\Omega$  at  $t = 0$ ,  $v_i(x, 0) = 0$ .

The energy equation of ALE is:

$$\frac{\partial E}{\partial t} = -(\sigma_{ij,j}v_{i,j} + \rho b_i v_j) - \rho w_i \frac{\partial E}{\partial x_j} \quad (\text{A-5})$$

Eulerian equations are derived by assuming that the velocity of the reference configuration is zero and that the relative velocity,  $w$ , is the material velocity. The term in the relative velocity is usually referred to as the advective term, which accounts for the transport of material past the mesh. The ALE equilibrium equations [15] are given as:

$$\frac{\partial v_i}{\partial t} = \sigma_{ij,j} + \rho b_i \quad (\text{A-6})$$

$$\frac{\partial E}{\partial t} = \sigma_{ij,j}v_{i,j} + \rho b_i v_i \quad (\text{A-7})$$



## A-2 Second Order Backward Euler

For the transient solution, the Second Order Backward Euler (SOBE) scheme is used to define the discretization algorithm. ANSYS CFX supports this scheme which is applicable for constant and variable time-step domains. In this thesis, SOBE runs the turbulent transient blood flow using the First-Order scheme and the volume fraction using the Second-Order scheme [90].

Modelling the blood flow in a controlled volume is governed using the general discrete equation [90] in terms of the transient condition for a number of times steps, and is written as:

$$\frac{\partial}{\partial x} \int_V \rho \varphi dV \approx V \frac{(\rho \varphi)^{n+\frac{1}{2}} - (\rho \varphi)^{n-\frac{1}{2}}}{\Delta t} \quad (\text{A-8})$$

where  $V$  represents the volume,  $\rho$  represents density and  $\varphi$  represents the nodal integration points using the finite-element shape function at the start  $n + \frac{1}{2}$  and end  $n - \frac{1}{2}$  of the time step as described in Equations A-9 and A-10 [90].

$$(\rho \varphi)^{n-\frac{1}{2}} = (\rho \varphi)^o + \frac{1}{2} (((\rho \varphi)^o - (\rho \varphi)^{oo}) \quad (\text{A-9})$$

$$(\rho \varphi)^{n+\frac{1}{2}} = (\rho \varphi) + \frac{1}{2} (((\rho \varphi) - (\rho \varphi)^o) \quad (\text{A-10})$$

The solution of Equation A-9 and A-10 are substituted into Equation A-8 as shown:

$$\frac{\partial}{\partial x} \int_V \rho \varphi dV \approx V \frac{1}{\Delta t} \left( \frac{3}{2} (\rho \varphi) - 2(\rho \varphi)^o + \frac{1}{2} (\rho \varphi)^{oo} \right) \quad (\text{A-11})$$

In this thesis, SOBE is considered robust, time-conservative and successfully simulates long time steps. However it can sometimes generate non-physical solution oscillations and computational errors.

## Appendix II

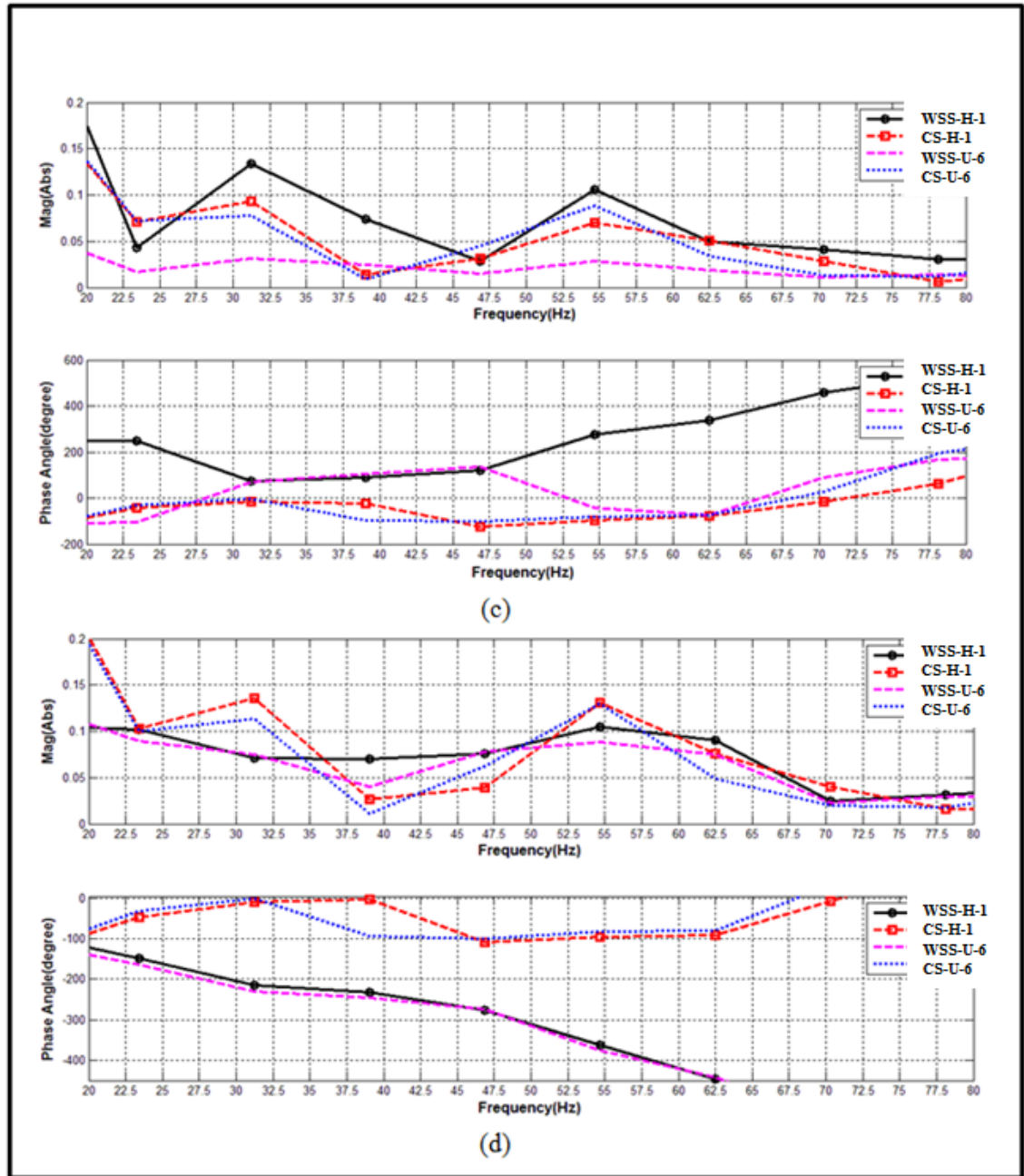


Figure II-1 The DFT of healthy and unhealthy WSS and CS for Group Two at (c) the abdominal aorta and (d) at the brachial artery

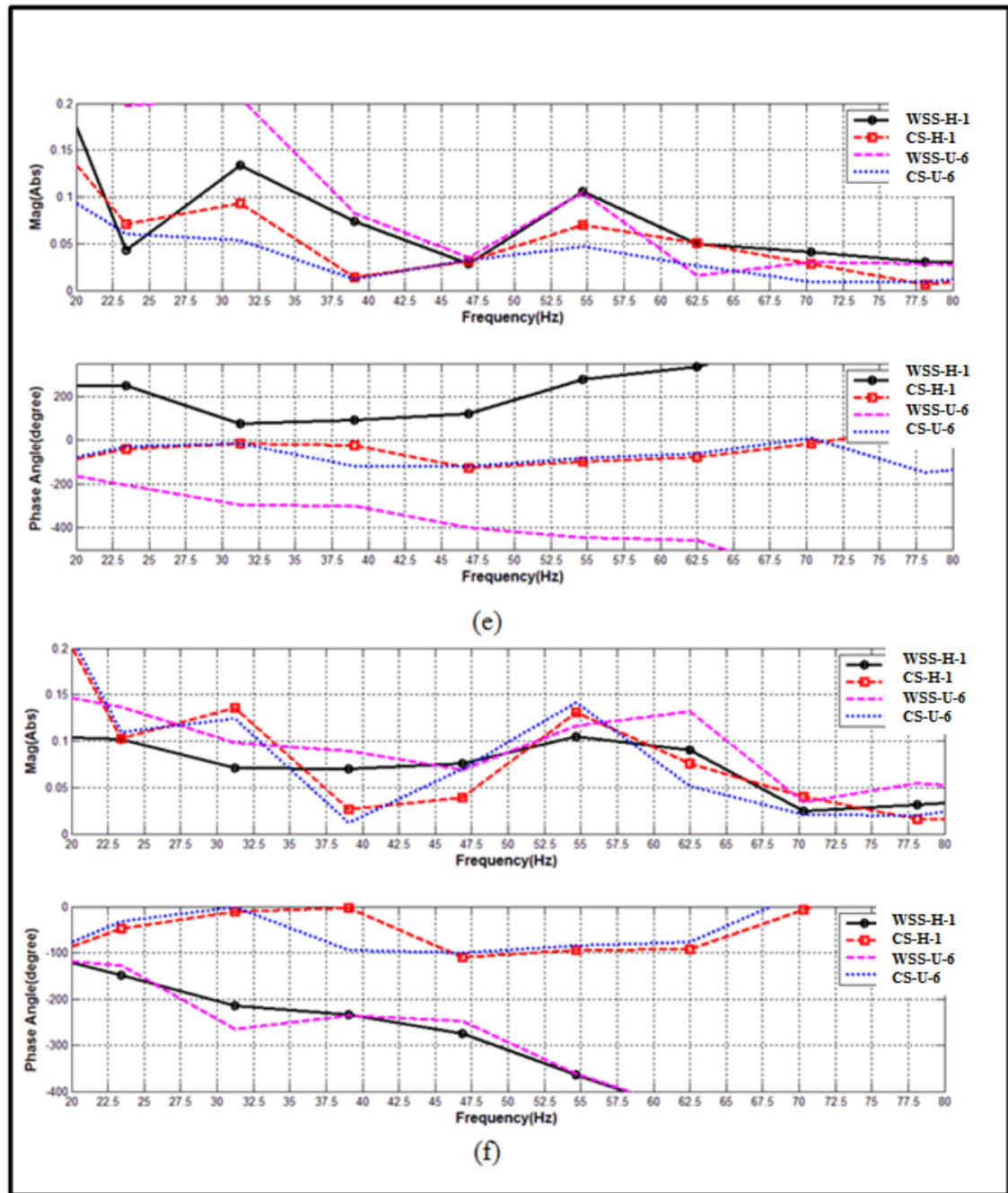


Figure II-2 The DFT of healthy and unhealthy WSS and CS for Group Three at (e) the abdominal aorta and (f) the brachial artery

## Appendix III

ANIMAL ETHICS COMMITTEE



Based at:  
Research Office  
Level 3, 76 Symonds St  
Auckland, New Zealand  
Telephone 64 9 373 7599 ext. 86356  
Facsimile 64 9 373 7432 or ext 85432  
email [aec-secretary@auckland.ac.nz](mailto:aec-secretary@auckland.ac.nz)

The University of Auckland  
Private Bag 92019  
Auckland

15/08/2011  
Ahmed Al-Jumaily  
AUT

Dear Ahmed Al-Jumaily,

### R915 - APPROVAL NOTICE

Predict arterial blockage using blood pressure measurement from left axillary artery in rats.

Your application to use animals in research was considered on 29/07/2011 and the committee is pleased to advise that this application has now been approved. Ethics approval was given for a period of 3 years.

Approval date 15/08/2011  
Expiry date 15/08/2014

#### Condition of Approval

All deaths which occur prior to the planned end of experiment must be notified to the AEC so that a post mortem may be performed if required by the Animal Welfare Officer. This includes all animals that are found dead or moribund, or killed due to abnormalities which make them not fit for purpose.

Training requirements for Mohammad Al-Rawi and Abd Halim Embong:

- Please attend a New Animal Users Legislation Training; contact the Animal Ethics Administrator to register.
- Please arrange to attend a Module 2a (Handling, Sexing, Euthanasia) training with Allan Gall (VJU).

Please note the requirement regarding reporting of animal use brought about by the Animal Welfare Act 1999. As Responsible Investigator it is your statutory responsibility to provide Animal Use Statistics to MAF, as outlined in section 2.6 of the Agreement between the University of Auckland (UoA) and the Auckland University of Technology (AUT) to allow the AUT to use the UoA Code of Ethical Conduct and UoA Animal Ethics Committee. In addition, on completion of the project please submit an end of approval report along with final animal use figures for the whole project to the AEC.

The required forms can be provided on request.

Regards,

Hiljanne van der Meer

Animal Ethics Administrator  
For the Animal Ethics Committee

### Institutional Drug Administration Order

This form applies to use of AEC approved prescription medicines (human or animal) and/or medicines for the direct management of the animals, such as anaesthetics, analgesics and prophylactic antibiotics.

<b>AEC OFFICE USE ONLY</b>	
IDAO no. 315/1	
Replaces IDAO no.	
AEC approval commencement date	15 AUG 2011
AEC/IDAO approval end date	15 AUG 2014
Cancellation date if replaced	
Replaced by IDAO no.	

<b>Reason for issue of IDAO (excessive detail is not required or expected)</b>
Summary of aim of trial: Predict arterial blockage using blood pressure measurement from left axillary artery in rats.
Reason for involvement of medicines: Anaesthesia for MRI scanning

<b>ANIMALS</b>	
Species/Breed	Rat
Gender	Male and Female
Age	3 - 6 months
Weight	280-350 g
Method of identification	Cage number
Number	70
Reproductive status	Non pregnant

<b>MEDICINES INFORMATION</b>	
Name (trade or generic)	Isoflurane
Active ingredient	Isoflurane
Strength	100%
Formula type	Liquid
Prescription Status	Restricted Veterinary Medicine
Is the medicine a controlled drug?	No
Product Type	Anaesthetic

<b>ADMINISTRATION DETAILS</b>	
Preparation (if required)	None
Dosage (e.g. mg/Kg)	1-5% as required (induce on 5% O2 4L/min, maintain on 2-2.5% O2 2L/min)
Dose (e.g. mL/Kg)	1-5% as required (induce on 5% O2 4L/min, maintain on 2-2.5% O2 2L/min)
Frequency of dosing	to effect
Site	gaseous
Equipment	Anaesthetic Machine and induction chamber, scavenging system
Technique used	allow rat to run free in induction chamber to induce. maintain on face mask

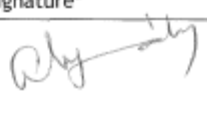

<b>EFFECTS AND OUTCOMES</b>	
Expected treatment outcome	Surgical plane of anaesthesia as judged by loss of paw pinch reflex or tail pinch reflex
Unexpected outcomes	Too light a plane of anaesthesia (start to react to stimuli) and too deep a plane of anaesthesia (irregular jerky breathing movements)
Possible adverse events	Respiratory depression (stop breathing)



Measures to be taken to correct adverse effects or unexpected outcomes	<p>If rat stops breathing - check head and neck are extended, administer 100% oxygen (flush circuit to get rid of residual circuitry gases), and it is possible to compress the chest gently to stimulate breathing.</p> <p>Too light: return to induction chamber if no face mask is being used, and turn vapouriser up to 5% until paw pinch reflex is abolished. If being maintained on face mask, increase gas to 5% until paw pinch reflex abolished and then reduce to maintenance requirements.</p> <p>Too deep: turn off vapouriser, consider ventilation with air + supplementary oxygen in case of overdose and if experimentally appropriate consider euthanasia.</p>
Actions to be taken in case of inadvertent self administration	<p>Skin: Wash splashes from skin with soap and water.</p> <p>Eyes: Wash contaminated eyes with water for 15mins and go to hospital without delay, leave contacts in place</p> <p>Oral: contact Poisons information centre 0800 764 766. Do not induce vomiting. Give water to rinse out mouth, then provide liquid slowly and as much as casualty can comfortably drink. Avoid giving milk, oils or alcohol. Seek medical advice</p> <p>Inhalation: Remove person from source of volatile anaesthetic to well ventilated area, symptomatic therapy as required</p>

<b>VET COMMENTS</b>
If the issuing veterinarian has any specific comments regarding this usage please enter here

FOOD SAFETY	
Will products from these animals enter the food chain of any other animal (i.e. human or animal)?	No
Does use of the medicine pose any threat to agricultural security?	No
If the answer to either of the above questions is 'yes', please provide detail	

STORAGE AND DISPOSAL	
Where will the medicine be stored?	VJU warehouse 502-611
How will un-used product be disposed of?	Unlikely to dispose of unused product

PERSONNEL			
Name	Skill/Qualification	Position	Signature*
Prof. Ahmed Al-Jumaily	11 years of active research for Fisher and Paykel Healthcare to develop, optimize and implement medical devices/ Bsc, MSC, PhD in mechanical engineering	Director of the Institute of Biomedical Technologies (IBTec)	A-M 
Dr. Jun Lu	Bsc, MSc, and PhD in Pharmacology, has extensive training and experience in animal handling and experimentation. Have experience in rat MRI.	Senior Lecturer	

Mohammad Al-Rawi	Bsc, MSc, Mechanical Engineering, has no experience in animal handling	PhD Candidate	
Abd Halim Embong	Bsc, MSc, Mechanical Engineering, has no experience in animal handling	PhD Candidate	

\*Signature confirms acceptance of this statement: "I have read, and agree to abide by, the RSNZ "Code of Practice for the Use of Veterinary and Human Medicines in Research, Testing and Teaching Organisations" and the Auckland University Institutional Operating Plan for the Direct management of Animals".

Authorisation by prescribing veterinarian

Date: 16/8/11

Signed: 

Name: T.E. DIXON BVM&S



### Institutional Drug Administration Order

This form applies to use of AEC approved prescription medicines (human or animal) and/or medicines for the direct management of the animals, such as anaesthetics, analgesics and prophylactic antibiotics.

<b>AEC OFFICE USE ONLY</b>	
IDAO no. 915/2	
Replaces IDAO no.	
AEC approval commencement date	15 AUG 2011
AEC/IDAO approval end date	15 AUG 2014
Cancellation date if replaced	
Replaced by IDAO no.	

<b>Reason for issue of IDAO (excessive detail is not required or expected)</b>
Summary of aim of trial: Predict arterial blockage using blood pressure measurement from left axillary artery in rats.
Reason for involvement of medicines: Anaesthesia for induction of arterial blockage.

<b>ANIMALS</b>	
Species/Breed	Rat
Gender	Male and Female
Age	3 - 6 months
Weight	280-350 g
Method of identification	Cage number
Number	70
Reproductive status	Non pregnant

<b>MEDICINES INFORMATION</b>	
Name (trade or generic)	Ketamine
Active ingredient	Xylazine 2% ketamine hydrochloride xylazine hydrochloride
Strength	ketamine 100mg/ml xylazine 20 mg/ml
Formula type	Injectable
Prescription Status	Restricted Veterinary Medicine
Is the medicine a controlled drug?	Yes
Product Type	Anaesthetic

<b>ADMINISTRATION DETAILS</b>	
Preparation (if required)	Mix 0.75 mL Ketamine, 0.5 mL xylazine and 0.75 mL water for injection.
Dosage (e.g. mg/Kg)	75mg/kg ketamine, 10 mg/kg xylazine
Dose (e.g. mL/Kg)	0.2 mL/100g
Frequency of dosing	once but may need top up after 45-60 min
Site	intraperitoneal
Equipment	syringe and <26G needle
Technique used	gentle manual restraint

<b>EFFECTS AND OUTCOMES</b>	
Expected treatment outcome	Maintenance on surgical plane of anaesthesia, measured by loss of withdrawal reflex (pinch of ear and hind leg).
Unexpected outcomes	Inappropriate level of anaesthesia a) Too light: positive tail movement to pinch, movement in response to surgical stimulus, rapid respiratory rate b) Too deep: very slow shallow or irregular breathing, cyanosis

Possible adverse events	respiratory depression, bradycardia, hypotension
Measures to be taken to correct adverse effects or unexpected outcomes	Anaesthesia: a) Inappropriately light: administer further 1/4 to 1/3 of original dose and observe for signs for adequate anaesthesia. b) Inappropriately deep: Consider assisted ventilation with air + supplementary oxygen if experimentally appropriate. Consider euthanasia if experimentally appropriate.
Actions to be taken in case of inadvertent self administration	Eye: wash with water thoroughly and seek medical review if pain develops Skin: wash thoroughly with soapy water Oral: induce vomiting with fingers if help >15min away only if conscious and seek medical attn immediately - ring poisons centre. Injected: small animal amounts unlikely to cause problems, treat symptomatically, if large amount then seek medical advice immediately or phone 0800 POISON

<b>VET COMMENTS</b>
If the issuing veterinarian has any specific comments regarding this usage please enter here

FOOD SAFETY	
Will products from these animals enter the food chain of any other animal (i.e. human or animal)?	No
Does use of the medicine pose any threat to agricultural security?	No
If the answer to either of the above questions is 'yes', please provide detail	

<b>STORAGE AND DISPOSAL</b>	
Where will the medicine be stored?	VJU warehouse dispensary 502-611
How will un-used product be disposed of?	flush down sink with running water

PERSONNEL			
Name	Skill/Qualification	Position	Signature*
Prof. Ahmed Al-Jumaily	11 years of active research for Fisher and Paykel Healthcare to develop, optimize and implement medical devices/ Bsc, MSC, PhD in mechanical engineering	Director of the Institute of Biomedical Technologies (IBTec)	A. M. Al-Jumaily
Dr. Jun Lu	Bsc, MSC, and PhD in Pharmacology, has extensive training and experience in animal handling and experimentation.	Senior Lecturer	Jun Lu
Mohammad Al-Rawi	Bsc, MSC Mechanical Engineering, has no experience	PhD Candidate	M. Al-Rawi
Abd Halim Embong	Bsc, MSC Mechanical Engineering, has no experience	PhD Candidate	Abd Halim Embong

"Signature confirms acceptance of this statement: "I have read, and agree to abide by, the RSNZ "Code of Practice for the Use of Veterinary and Human Medicines in Research, Testing and Teaching Organisations" and the Auckland University Institutional Operating Plan for the Direct management of Animals".

Authorisation by prescribing veterinarian

Date:.....16/8/2011.....

Signed:..........

Name:.....T E DIXON BVM&S.....